Development of Electrolyte Salts for Multivalent Ion Batteries

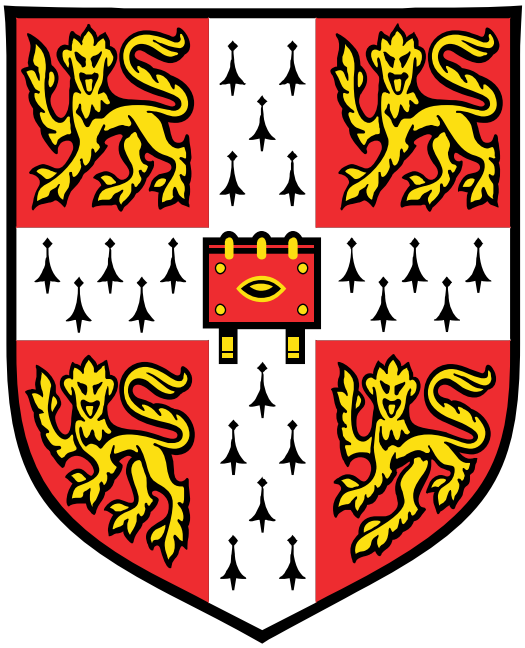

Evan N. Keyzer

Gonville & Caius College

University of Cambridge

Supervised by Profs. Dominic S. Wright and Clare P. Grey

August 2018

A dissertation submitted to the Degree Committee of the University of Cambridge, Board of Graduate Studies in partial fulfilment of the requirements for the degree of Doctor of Philosophy

Declaration

I hereby declare that this thesis entitled "*Development of Electrolyte Salts for Multivalent Ion Batteries*" is the result of work which was carried out at the University Chemical Laboratory at the University of Cambridge between October 2014 and August 2018. Credit for results obtained through collaboration with other members of the Wright and Grey groups is referenced directly in the text as well as in the acknowledgements section. Except where otherwise stated, either directly or by reference, the work is the authors own work. The work has not been submitted whether in part or as a whole for a degree or any other qualification at another university, and the text does not exceed 60,000 words in length.

Evan Keyzer

Cambridge, August 2018

This is a very complicated case, Maude. You know, a lotta ins, lotta outs, lotta what-have-yous.

- Lebowski

Acknowledgements

Firstly, I would like to thank Prof. Dominic Wright and Prof. Clare Grey for taking me on as a PhD student and challenging me with this project. Their encouragement, openness, good humour, and guidance throughout my PhD have been invaluable and it has been an honour to work with them.

I would like to thank Jae Lee and Dr. Zigeng Liu for useful discussions and guidance relating to electrochemistry and batteries and for their time spent collecting and interpreting solid-state NMR data. I would also like to thank Dr. Hugh Glass and Dr. Elizabeth Castillo Martinez for their help and guidance with setting up electrochemical measurements and troubleshooting. Many thanks also to Dr. Andrew Peel and Dr. Andrew Bond for their help and patience with crystal structure refinement. Further, I am very grateful to have been able to work in the Wright and Grey groups and alongside the Wheatley, Boss/Barker, Reisner, and Nitschke groups. The knowledge, support, and friendship provided by these people has been tremendously important to me during my time in the department and Cambridge.

During our time together in the Wright group, Dr. Pete Matthews was particularly encouraging and his persistence was motivating. He kept the ideas flowing and made working in the lab a pleasure and deserves special thanks.

Many thanks also to the Gonville Weights and Measures Society for many enlightening conversations against the Gate of Humility.

I am also very grateful to Ria and Robin Searle for generosity which enabled me to pursue my MPhil at Cambridge, which undoubtedly influenced my ability to continue my studies as a PhD candidate.

As the culmination of 28 years of encouragement for my academic and creative ability, this thesis would not have been dreamt of without the support of my mother. My gratitude for your dedication to my success is boundless, and as much as it doesn't do it justice, *thank you*.

Lily, you got me into this mess at Cambridge but you also got me out of it. The support you have given me has seen me through slumps and lulls and has encouraged me to keep going. Your motivation, confidence, and ability continue to inspire and challenge me to be a better person. Going through it all with you has made this time at Cambridge one incredible experience.

Abstract

This dissertation focuses on the synthesis and electrochemical testing of new electrolyte salts for rechargeable multivalent ion batteries.

In chapters 2 and 3 the synthesis of Mg and Ca hexafluoropnictogenate salts as well as the electrochemical behaviour of $Mg(PF_6)_2$ is presented. Pure samples of $Mg(EF_6)_2$ (E = P, As, and Sb) can be synthesized using Mg metal and $NOPF_6$/$NOSbF_6$ in CH_3CN or via a ammonium salt deprotonation route using Me_3NHAsF_6 and Bu_2Mg. The $NOPF_6$ method was extended to the Ca variant, but isolation of a pure $Ca(PF_6)_2$ material required the presence of a crown ether. Electrochemical and microscopy measurements of THF-CH_3CN solutions of $Mg(PF_6)_2$ show that the electrolyte good electrochemical stability and can facilitate the plating/stripping of Mg. Further, this electrolyte system can be cycled in a full cell using the Chevrel phase Mo_6S_8 cathode. The electrochemical stability of the AsF_6^- and SbF_6^- salts is lower than that of the PF_6^- salt and electrolyte decomposition is observed when cycling on Mg electrodes.

In chapter 4 the development of a series of Mg aluminates [$Mg(AlOR_4)_2$] using a general synthetic platform based on $Mg(AlH_4)_2$ and various alcohols is presented. Preliminary electrochemical studies performed on these aluminate salts in dimethoxyethane identify the phenoxy and perfluoro-*tert*-butoxy derivatives as promising electrolyte systems. Electrochemical cycling of these electrolytes using gold and Mg electrodes show that systems containing chloride, brought through to the product from the starting material in the form of NaCl, exhibit lower plating/stripping overpotentials and higher Coulombic efficiencies than systems from which chloride had been removed. Further, these two electrolytes can be used in Mg full cells containing the Chevrel phase cathode. Solid-state ^{23}Na NMR analysis as well as DFT calculations show that chloride-containing electrolytes facilitate the co-insertion of Na into the cathode material.

In chapter 5 the hydroboration of pyridines and CO_2 in the presence of pinacolborane is presented. An optimized system employing NH_4BPh_4 and HBpin is developed and a mechanism of pyridine hydroboration is proposed based on multinuclear NMR spectroscopy. The catalytic reaction was found to be catalyzed by a boronium salt, which was structurally characterized in the solid-state by single crystal X-ray diffraction. This new catalytic method is shown to be tolerant to a number of functional groups in the 3-position on pyridine as well as quinoline, and CO_2, producing the hydroboration products in good yields.

Abbreviations

CH_3CN	Acetonitrile
APC	All Phenyl Complex
Å	Ångstrom
A	Ampere
Ac	Acetyl
a.u.	Arbitrary Units
Ar	Aryl
ATR	Attenuated Total Reflection
BAr^{F-}	Tetrakis[3,5-bis(trifluoromethyl)phenyl]borate
BINOL	1, 1'-Bi-2-naphthol
$HMDS^-$	Bis(hexamethyldisilazide)
$TFSI^-$ or NTf_2^-	Bis(trifluoromethane)sulfonamide
$HNTf_2$	Bis(trifluoromethane)sulfonamide Protonated
Calc'd	Calculated
cat	Catalyst
ca.	*Circa* (approximately)
J	Coupling Constant (NMR) or Current Density
CP	Chevrel phase (Mo_6S_8)
CE	Coulombic efficiency (%) or Counter Electrode
CV	Cyclic Voltammetry
deg	Degrees
^oC	Degrees Celsius
DFT	Density Functional Theory
DMSO-d_6	Deuterated Dimethylsulfoxide
d_8-THF	Deuterated Tetrahydrofuran
1,2-DFB	1,2-Difluorobenzene
CH_2Cl_2	Dichloromethane
Et_2O	Diethyl ether
DHP	Dihydropyridine
DME	Dimethoxyethane
DMSO	Dimethylsulfoxide
DMC	Dimethyl Carbonate

e^-	Electron
eV	Electron Volt
EDX	Energy dispersive X-ray spectroscopy
ESI-MS	Electrospray Ionization Mass Spectrometry
e.g.	*exempli gratia* (for example)
Et	Ethyl
EC	Ethylene Carbonate
FLP	Frustrated Lewis Pair
FT	Fourier Transform
GC-MS	Gas Chromatography-Mass Spectrometry
GC	Glassy Carbon
Hz	Hertz
$^{i}Pr^{F}$	Hexafluoro-*iso*-propyl
HRMS	High-Resolution Mass Spectrometry
HOMO	Highest Occupied Molecular Orbital
i.e.	*id est* (that is)
IR	Infrared
K	Kelvin
LUMO	Lowest Unoccupied Molecular Orbital
NAD^+	Nicotinamide adenine dinucleotide
NADH	Reduced form of NAD^+
MAS	Magic Angle Spinning
MACC	Magnesium Aluminium Chloride Complex
m/z	Mass to Charge Ratio
MHz	Megahertz
Me	Methyl
MeTHF	2-methyltetrahydrofuran
mg	Milligram
mL	Millilitre
mmol	Millimole
mS	Millisiemen
M	Molar
MO	Molecular Orbital
nm	Nanometre

^{n}Bu	*N*-butyl
NMR	Nuclear Magnetic Resonance
R	Organic Alkyl or Aryl Group
ppm	Parts per million
Ph^{F}	Pentafluorophenyl
R^{F}	Perfluoro (where R is any alkyl/aryl group)
$^{t}Bu^{F}$	Perfluoro-*tert*-butyl
pin	Pinacol
Ph	Phenyl
Pn	Pnictogen
PTFE	Polytetrafluoroethylene
Py	Pyridine or pyridyl
RE	Reference Electrode
RT	Room temperature (ca. 25 °C)
SEM	Scanning electron microscopy
^{s}Bu	*Sec*-butyl
ss-316	Stainless Steel, 316 Grade
SEI	Surface Electrolyte Interphase
^{t}Bu	*Tert*-butyl
THF	Tetrahydrofuran
TMEDA	Tetramethylethylenediamine
tol	Tolyl
TREN	Tris(2-aminoethyl)amine
cm^{-1}	Wavenumber (in the context of infrared spectroscopy)
vs.	Versus
V	Volt
WCA	Weakly Coordinating Anion
WE	Working Electrode
XRD	X-ray Diffraction
XPS	X-ray Photoelectron Spectroscopy

Publications

1. *Regioselective 1,4-Hydroboration of Pyridines Catalyzed by an Acid-Initiated Boronium Cation*. **E. Keyzer**, S. Kang, S. Hanf, D. Wright, *Chem. Commun.*, **2017**, *53*, 9434.

2. *Reactivity of $Ca(PF_6)_2$ Formed via Nitrosonium Oxidation of Calcium and the Isolation of a Ca_4F_4 Cubanoid Cluster*. **E. Keyzer**, P. Matthews, Z. Liu, A. Bond, C. Grey, D. Wright, *Chem. Commun.*, **2017**, *53*, 4573.

3. *Insights into the Electrochemical Performances of Bi Anodes for Mg Ion Batteries Using ^{25}Mg Solid State NMR Spectroscopy*. Z. Liu, J. Lee, X. Guolei, H. Glass, **E. Keyzer**, S. Dutton, C. Grey, *Chem. Commun.*, **2017**, *53*, 743.

4. *$Mg(PF_6)_2$-Based Electrolyte Systems: Understanding Electrolyte-Electrode Interactions for the Development of Mg-Ion Batteries.* **E. Keyzer**, H. Glass, Z. Liu, S. Dutton, C. Grey, D. Wright. *J. Am. Chem. Soc.*, **2016**, *138*, 8682.

Contents

Declaration ..... **i**

Acknowledgements ..... **iii**

Abstract ..... **iv**

Abbreviations ..... **v**

Publications ..... **viii**

1. Introduction **1**

1.1 Sustainable Energy 1

1.2 Batteries 2

1.2.1 Li-Ion Batteries 3

1.2.2 Mg Batteries 4

1.3 Mg Electrolyte Systems 7

1.3.1 Development of Mg Electrolytes 7

1.3.2 Chloride in Mg Electrolytes 13

1.3.3 Summary 17

1.4 Project Aims 18

1.5 References 19

2. Synthesis and Electrochemical Analysis of Magnesium Hexafluoropnictogenate Salts **23**

2.1 Introduction 23

2.2 Results and Discussion 24

*2.2.1 Synthesis and Characterization of $(Py_2H)PF_6$ (**1**)* 24

*2.2.2 Synthesis and Characterization of $Mg(CH_3CN)_6(PF_6)_2$ (**2**)* 27

2.2.3 Electrochemistry of $Mg(CH_3CN)_6(PF_6)_2$ Solutions and Electrode Surface Analysis 29

*2.2.4 Synthesis and Electrochemistry of $Mg(CH_3CN)_6(SbF_6)_2$ (**3**)* 37

*2.2.5 Synthesis and Electrochemistry of $Mg(CH_3CN)_6(AsF_6)_2$ (**5**)* 40

2.3 Conclusions 44

2.4 Future Work 46

2.5 References 46

3. Synthesis of $Ca(PF_6)_2$, Formed via Nitrosonium Oxidation of Calcium 49

3.1 Introduction 49

3.2 Results and Discussion 50

3.3 Conclusions 58

3.4 Future Work 59

3.5 References 60

4. Magnesium Aluminate Electrolyte Systems for Mg Batteries 62

4.1 Introduction 62

4.2 Results and Discussion 64

*4.2.1 Synthesis of Magnesium Aluminate Salts **11-15*** 64

*4.2.2 Electrochemistry of Magnesium Aluminates **11-15*** 67

4.2.3 Analysis of Electrodeposited Magnesium 71

4.2.4 Battery Cycling and solid-state ^{23}Na NMR Analysis of the Chevrel phase (Mo_6S_8) Cathode 73

4.3 Conclusions 77

4.4 Future Work 78

4.5 References 80

5. Regioselective 1,4-Hydroboration of Pyridines Catalyzed by an Acid-Initiated Boronium Cation and CO_2 Hydroboration 83

5.1 Introduction 83

5.1.1 Dihydropyridines 83

5.1.2 Synthesis of Dihydropyridines 83

5.1.3 Hydroboration of CO_2 87

5.2 Results and Discussion 89

5.2.1 Catalytic 1,4-Hydroboration of Pyridines 89

5.2.2 Hydroboration of CO_2, Initiated by NH_4BPh_4 96

5.3 Conclusions 100

5.4 Future Work 101

5.5 References 103

6. Conclusions and Outlook 108

6.1 Conclusions 108

6.2 Outlook 112
6.3 References 114

7. Experimental 117
7.1 General Experimental Details 117
7.2 Synthetic Procedures and Characterization 120
7.2.1 Chapter 2 120
7.2.2 Chapter 3 122
7.2.3 Chapter 4 124
7.2.4 Chapter 5 127
7.3 Electrochemical Apparatus 133
7.4 Crystallographic Data 135
7.5 References 139

1. Introduction

1.1 Sustainable Energy

With surges in technological growth over the past 25 years as well as global population expansion placing greater demands on natural resources for the production of energy (coal, fossil fuels, natural gas, etc.), we are being faced with major challenges regarding our dependence on and continued use of non-renewable fuels.[1,2] The threat placed on us by the environmental consequences of climate change, influenced greatly by CO_2 emissions, as well as the prospect of a fossil fuel crisis has spurred enormous amounts of research into the development of efficient sustainable energy-production technologies such as wind turbines, inorganic and organic photovoltaics, and hydrogen fuel cells.[1,3] These technologies aim to use naturally occurring phenomena, such as light energy from the sun or kinetic energy from wind or tides, to generate useable electrical energy without the production of greenhouse gas emissions during energy generation. Despite the considerable research put into sustainable energy production methods, research into the storage of energy produced by these technologies is comparably lacking.[3] Whereas the burning of fossil fuels can be used to generate electricity to offset peaks in consumption, renewables do not offer such a convenient method of supplying energy on demand. Owing to the inherently intermittent nature of many renewable energy sources, high capacity energy storage technologies are required to decouple this intermittent energy supply from the scheduled or constant demand consumers are used to placing on the electrical grid. Many types of grid-scale energy storage technologies are being investigated for various energy storage requirements, including pumped hydro, flywheels, large-scale compressed gas, redox-flow batteries, and rechargeable batteries.[4,5] Rechargeable batteries are an attractive method of storing energy as their chemistries can be tuned to suit specific applications, they can be scalable for both mobile and grid storage applications, and they can be used to release stable energy over sustained periods.

On a smaller scale, batteries offer the opportunity to electrify our modes of transportation, allowing consumers to power their vehicles using electricity from the grid. Not only does this allow vehicles to be powered by electricity produced by renewables, when possible, but also eliminates the generation of pollutants at the site of energy consumption (e.g. when driving in densely populated areas). This could have a significant impact on the

health of residents of major cities and towns by reducing potentially fatal exposure to combustion by-products.[6] However, many current portable battery technologies, including leading Li-ion systems, exhibit only moderate capacities (ca. 140 and 150 $mAh \cdot g^{-1}$ for $LiCoO_2$ and $LiNi_{1/3}Mn_{1/3}Co_{1/3}O_2$ cells, respectively) and moderate cycle life (ca. 500 cycles depending on depth of discharge and thermal management).[7–9] Thus, the development of high energy density rechargeable batteries that possess a very long cycle life is of paramount importance and a key challenge for materials and chemical research.

1.2 Batteries

Batteries are a promising storage technology as they are able to directly store electrical energy harvested from wind and/or solar, without requiring chemical fuels (e.g., H_2 and O_2 for fuel cells). Furthermore, batteries enable the controlled release of that energy when desired and over long periods. A battery is composed of multiple electrochemical cells which are themselves comprised an anode and a cathode, current collectors, and an electrolyte (Figure 1.1). During the charging of the cell, electrons flow through an external circuit from the cathode to the anode (by way of the current collectors) where the 'active' electrolyte cation is reduced (M^{n+} to M^0). In a galvanostatic cycling experiment, in which a constant current is applied to the cell and the cell voltage is measured, the charging process is associated with an increase in cell potential as measured from the cathode side. During the discharge of the cell the opposite is true: electrons flow from the anode to the cathode and the active metal is oxidised (M^0 to M^{n+}) at the anode and travels as a cation to the cathode, which is reduced.[10] In the galvanostatic cycling experiment, the discharge process is associated with a decrease in cell potential as measured from the cathode side. The electrolyte conducts the active metal ions between the electrodes upon charge or discharge of the cell. Many different types of batteries have been developed based on a number of metals including Pb-acid, Ni-metal hydride as well as Li-, Na-, Mg-, Ca-, and Al-ion batteries.[3] The nature of the anode and cathode employed depend heavily on the active metal used in the battery and dictate the operating voltage of the cell, the rate at which the cell can be cycled, and the overall charge capacity of the cell. Further, the operation of the cell, especially the operating voltage of the anode and cathode, are heavily reliant on the electrochemical stability of the electrolyte.

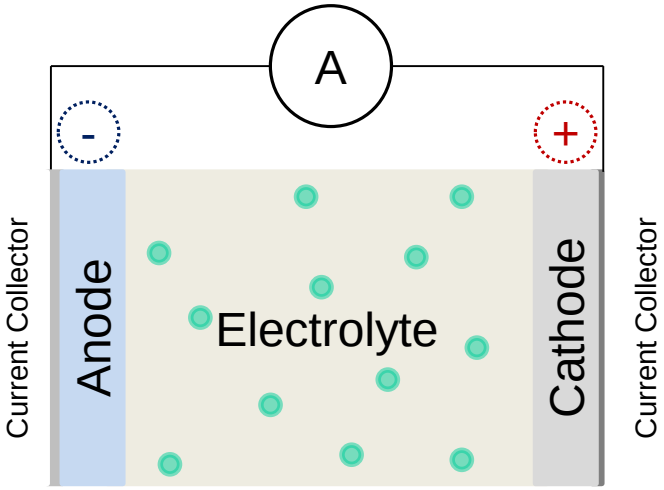

Figure 1.1 Schematic depiction of a generic electrochemical cell.

The electrochemical stability of the electrolyte solution is crucial to the performance of a given battery. Along with the electrochemical potentials of the electrodes (μ_A and μ_C), the potential range (V) over which an electrolyte is stable directly influences the voltage at which a battery can operate. Thus, to construct a battery with a high working voltage, it is desirable to have an electrolyte with the broadest possible electrochemical stability window. For a battery to be stable over the working range of the electrodes the electrolyte must have a HOMO that lies below the electrochemical potential of the cathode (to avoid *oxidation* of the electrolyte) and a LUMO that lies above the electrochemical potential of the anode (to avoid *reduction* of the electrolyte) (Figure 1.2).[10]

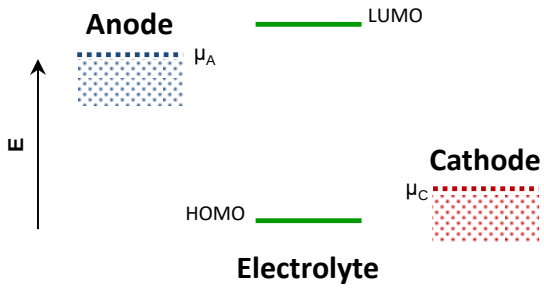

Figure 1.2 Relative energies of electrolyte HOMO/LUMO and electrode electrochemical potentials required to prevent electrolyte decomposition (shaded boxes represent electron filling in the electrode band structure).

1.2.1 Li-Ion Batteries

First developed for commercial use by SONY corp. in 1990, Li-ion batteries have become one of the most thoroughly developed and widely used rechargeable battery systems today, being implemented in many hand-held electronic devices, laptops, and electric/hybrid vehicles.[2,11] Current Li-ion batteries are typically composed of a graphite anode and a metal

oxide cathode, using a solution of $LiPF_6$ in mixed carbonate solvents as the electrolyte.[3] A graphitic carbon anode is used in place of Li metal due to of the propensity of Li to form dendrites—finger-like growths—during cycling on the surface of Li metal. These dendrites can grow large enough to span the anode and cathode to short-circuit the battery, resulting in battery failure or thermal runaway and fires, and are a serious concern in Li-ion battery development.[12] While Li metal has a greater propensity to form dendrites, graphite anodes are also able to develop dendritic growths on their surfaces, again causing safety issues.[12] Whereas Li can be plated directly onto Li metal during charge, in the case of carbon Li atoms intercalate between the layers of the graphite in the anode. This intercalation results in a lithiated carbon compound containing up to one lithium per six carbon atoms (C_6Li), thereby storing the Li until discharge when the Li is inserted into the metal oxide cathode material.[3]

The first few charge-discharge cycles are critical for the long-term performance of the Li-ion cell as the electrolyte solution (salt and carbonate solvent) breaks down on the active electrodes and current collectors, forming a protective film known as the surface electrolyte interphase (SEI). The highly reducing or oxidizing environments of the electrodes and current collectors during charge and discharge cause the electrolyte system to decompose at the surface to form the SEI which is composed of a complex mixture of both polymeric organic and inorganic phases.[7] The SEI is crucial to the operation of the cell as it prevents continuous decomposition and 'consumption' of the electrolyte during cycling. Despite being an insulating film, the SEI does not inhibit the cycling of the cell as Li^+ is able to traverse the SEI and penetrate the active electrode materials.[10] While Li-ion systems have well-established electrochemistry and widespread commercialisation, other metal-ion batteries, such as Mg, Ca, and Al, are predicted to possess higher volumetric capacities than Li systems as well as cost and safety benefits, making them attractive candidates for efficient energy storage.[13]

1.2.2 Mg Batteries

Magnesium holds great promise as an active ion in electrochemical cells. As Mg undergoes a two electron redox process ($Mg^0 \leftrightarrow Mg^{2+}$), it is able to carry more electrons per atom between electrodes. Thus, because of the divalent nature of Mg, Mg batteries have a theoretical volumetric capacity of 3833 $mAh \cdot cm^{-3}$ for the Mg metal anode, nearly twice that

of Li batteries[†] which have a theoretical capacity of 2062 mAh·cm^{-3} for a Li metal anode.[14,15] Mg is also significantly less expensive than Li due to its high natural abundance.[2,16] Furthermore, Mg is significantly less prone to the formation of dendrites during cycling on Mg metal and, thus, magnesium can be used directly and safely as an anode material.[14] The tendency for Mg to deposit without the formation of dendrites is not fully understood. A DFT calculation study performed by Ling and co-workers suggests that stronger Mg-Mg bonding resulted in preferential growth of 2D and 3D crystallites, with Mg preferring higher coordination numbers, whereas the weaker Li-Li bond is less preferential and facilitate the formation of 1D (dendritic) growths.[17] Another DFT study performed by Jäckle and Groß shows that Mg deposits in a hexagonally close packed (hcp) fashion whereas Li prefers the more open body centred cubic (bcc) arrangement.[18] This study again suggests that high coordination numbers drive smooth plating of Mg, rather than dendritic growth, at the anode. In addition, unlike Li systems, the formation of SEI layers on Mg electrodes typically completely passivates the surface and inhibits Mg transport to the electrode. This is both a result of the highly charge dense Mg^{2+} cation interacting strongly with the various components of the surface film as well as the generally large lattice energies of precipitated inorganic Mg species.[19]

Despite being a subject of synthetic and electrochemical investigations since 1990,[20] many challenges still face the development of Mg batteries that operate beyond the prototype stage and are competitive with Li-ion technology. Many of these challenges are a product of the high charge density of Mg, which results in large barriers to diffusion in cathodes and prevents the use of high voltage metal oxide cathode materials that have been established in the Li-ion field. Further, the charge density of Mg and the strong interactions it forms with many electrolyte solvents can introduce large overpotentials to the Mg plating (ca. 0.2 V on Mg) and intercalation (into the cathode) processes.[21] This means that larger overpotentials, positive or negative depending on the process, are required to 'de-solvate' Mg from solution than would typically be required for other ions. Another significant challenge facing Mg battery development is a lack of electrochemically stable electrolyte systems that facilitate highly reversible cycling. As the formation of an SEI is detrimental to the operation of the Mg cell, electrolytes that are stable below −0.5 V vs. Mg (to accommodate possible plating overpotentials) and above the cathode working potential are required to prevent the formation

[†] A Li or Mg battery is one in which the Li or Mg metal comprises the anode material whereas a Li-ion or Mg-ion battery is one in which an intercalation or alloying anode is used.

of passivating films. The development of electrolytes that are stable above 3.5 V vs. Mg is currently a very active area of investigation as lack of such electrolytes limits research on high voltage Mg cathodes. Thus far, many combinations of Mg salts and electrolyte solvents, along with various additives, have been examined but none have yet facilitated efficient cycling with cathodes other than Chevrel phase Mo_6S_8 (CP), operating below 2 V vs. Mg.[22] Further, many established electrolyte systems contain chloride which is known to result in corrosion of current collectors and cell casings.[15] The prevention of corrosion is another significant challenge as corrosion limits cell operating voltages and can result in cell failure over time.

The ability of the Chevrel phase to allow reversible insertion and deinsertion of Mg from its lattice has led to it being one of the most commonly employed cathode materials in Mg battery chemistry.[16] The CP structure is composed of octahedral Mo_6 clusters contained inside a cubic arrangement of eight sulfur atoms, which stack into Mo_6S_8 blocks and form an open framework (Figure 1.3).[23] The ability of the CP to facilitate reversible Mg electrochemistry with good Mg^{2+} mobility is largely due to its open structure and the polarizable Mo_6 metallic clusters, which can provide electron density to offset the presence of the 2+ charge of Mg. Further, the relatively soft and polarizable sulfur atoms contained within the structure allow the intercalated Mg^{2+} cations to move with lower energy barriers than would be observed for a metal oxide material owing to the ability of the electron cloud on sulfur to be distorted. Upon discharge, the Mo_6 cluster can accommodate up to 4 electrons involving the insertion of 2 Mg^{2+} cations per cluster, forming a $Mg_2Mo_6S_8$ phase with a corresponding capacity of 129 $mAh \cdot g^{-1}$.[24] Within the magnesiated CP Mg^{2+} occupies two distinct sites (inner and outer sites A and B, Figure 1.3) and insertion into these sites is reflected in the electrochemical charge/discharge profiles through the appearance of two distinct voltage plateaus.

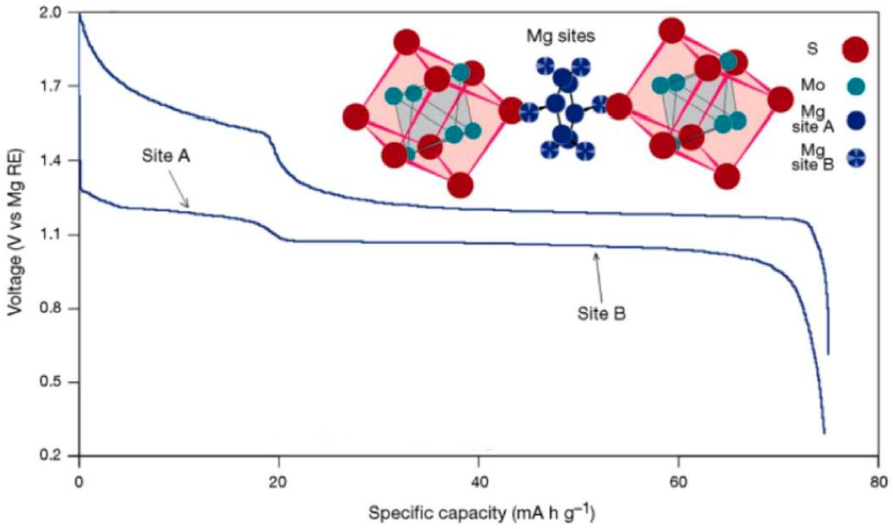

Figure 1.3 Structure and electrochemical charge/discharge profiles of a Chevrel phase Mo_6S_8 cathode. Figure adapted with permission from reference 29. Copyright 2000 Nature Publishing Group.

1.3 Mg Electrolyte Systems

1.3.1 Development of Mg Electrolytes

Amongst many other issues faced in the development of Mg-ion batteries, the preparation of electrochemically stable electrolytes that facilitate reversible electrodeposition of Mg over many cycles remains a considerable challenge.[19] The first breakthroughs in Mg-ion electrolyte development came from electrochemical investigations of Grignard solutions, which began in the early 1900s and demonstrated electrodeposition of Mg from ethereal solution of Grignard species. However, these highly nucleophilic systems exhibited poor oxidative stability (ca. 1.3 V vs. Mg for ^{n}BuMgCl) and reactivity with cathode materials.[25,26] Other organomagnesium species have been investigated, such as bis(η^5-cyclopentadienyl)magnesium, but have shown poor oxidative stability (<2 V vs. Mg).[27] In 1990, Mayer demonstrated that the addition of alkylaluminium reagents (e.g. $AlEt_3$ and $Al^{i}Bu_3$) to electrodeposition solutions of Bu_2Mg in Et_2O, solutions which did not otherwise facilitate Mg deposition, lead to an increase in conductivity and resulted in pure Mg electrodeposition.[28] This report founded a new class of Mg aluminate electrolytes which have continued to be the subject of development. Also in 1990, significant contributions were made by Gregory and co-workers with their use of Mg organoborates (e.g. $Mg(BPh_2Bu_2)_2$).[20] These borates were found to allow reversible electrodeposition of Mg while preserving the

chemical integrity of the electrolyte up to ca. 2 V vs. Mg. Further, the authors demonstrated that these electrolytes could facilitate the intercalation of Mg into cathodes such as ZrS_2.

A second significant study was presented by Aurbach and co-workers in 2000, which demonstrated the successful use of the Mg organohaloaluminate $Mg(AlCl_2EtBu)_2$, synthesized from Bu_2Mg and $EtAlCl_2$ in a 1:2 ratio in THF, as an electrolyte.[29] This electrolyte system opened the stability window of Mg-ion systems to 2.4 V vs. Mg on a Pt electrode and exhibited close to 100% plating/stripping efficiency over hundreds of cycles using the CP cathode in conjunction with a Mg anode (Figure 1.4).[30] Attempts to use $Mg(AlCl_2EtBu)_2$ above 2.4 V vs. Mg were found to result in β-hydride elimination of the organic substituents on Al, giving reactive Al-H species. Owing to the relatively low oxidative stability of the $Mg(AlCl_2EtBu)_2$ electrolyte, Aurbach and co-workers developed the aluminate 'all phenyl complex' (APC), $[Mg_2(\mu_2\text{-}Cl)_3{\cdot}6THF](AlPh_4)$, formed from $AlCl_3$ and PhMgCl (Figure 1.5a).[30,31] The presence of the phenyl groups removed the possibility of β-hydride elimination and extended the electrochemical stability of the electrolyte salt in THF to ca. 3.3 V vs. Mg while maintaining Coulombic efficiencies of close to 100% (Figure 1.4).[31]

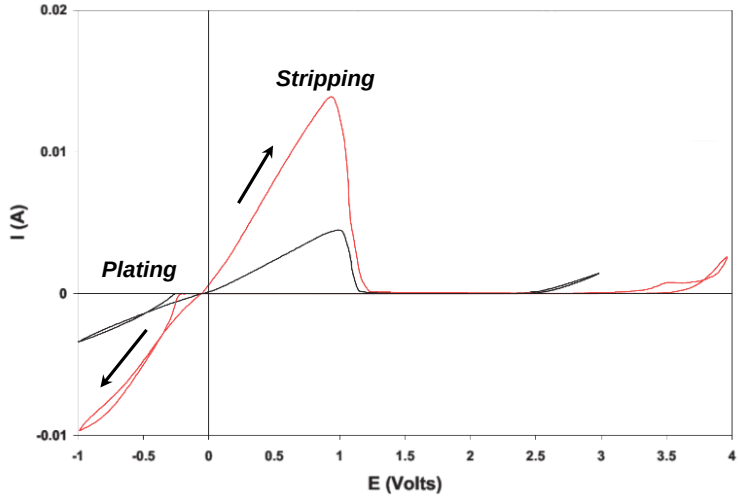

Figrue 1.4 Cyclic voltammograms of THF solutions containing a 1:2 mixture of Bu_2Mg and $EtAlCl_2$ (0.25 M, black line) and the APC electrolyte system (0.4 M, red line) using a Pt working electrode scanning at a rate of 25 $mV{\cdot}s^{-1}$. Figure adapted with permission from reference 30. Copyright 2007 WILEY-VCH Verlag GmbH & Co. KGaA, Weinheim.

The Muldoon and Zhao-Karger groups have reported the formation of a Mg aluminate formed from the reaction of the non-nucleophilic $HMDS^-$ anion (in the form of HMDSMgCl or $(HMDS)_2Mg$) and $AlCl_3$.[32,33] Not only does this electrolyte exhibit a stability window of ca. 3.2 V vs. Mg in THF and glymes, but also the non-nucleophilicity of $HMDS^-$ makes it

compatible with a sulfur cathode, an inexpensive conversion cathode material with high Mg capacity (ca. 1671 mhA·g^{-1}). Structural analysis by Muldoon and co-workers of the HMDS^{-}-based electrolyte salt by single crystal X-ray analysis isolated from THF showed that the compound has the formula [$Mg_2(\mu_2\text{-}Cl)_3$·6THF](HMDS$AlCl_3$). They propose that the [$Mg(\mu_2\text{-}Cl)_3$·6THF]$^{+}$ cation, a cation common to many Mg electrolytes, is the electrochemically active species in solution (Figure 1.5b).

A purely inorganic Mg aluminate, known as the Mg aluminium chloride complex (MACC), has also been investigated by a number of groups (Figure 1.5c).[34–37] This system is simple to prepare from the reaction of $MgCl_2$ and $AlCl_3$ in THF or glymes and has been shown to exhibit oxidative stability up to 3.4 V vs. Mg as well as excellent plating/stripping efficiencies.[34] However, the efficient plating and stripping of Mg facilitated by MACC is only possible through electrochemical conditioning of the electrolyte, whereby the electrolyte is cycled in a cell containing a Mg counter electrode. Detailed electrochemical investigations into this conditioning process by Gewirth and co-workers show that the initial cycling of the MACC electrolyte causes a re-equilibration of species in solution and results in an increased concentration of the [$Mg_2(\mu_2\text{-}Cl)_3$·6THF]$^{+}$ cation along with free Cl^{-}.[38,39] The generation of these two components has been found to be a key factor in the ability of chloride-containing electrolytes to plate/strip Mg with high efficiencies, which is discussed in more detail below.

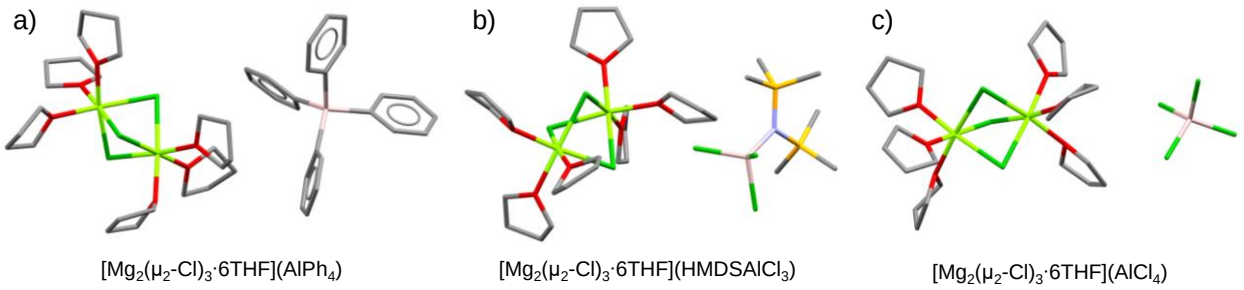

Figure 1.5 Solid state structures of the a) APC, b) HMDS-$AlCl_3$, c) and MACC Mg electrolyte salts. Protons and disorder have been removed for clarity (Mg, light green; Cl, dark green; Al, pink; Si, orange; N, blue; O, red; C, grey).

In 2014, Bartlett and co-workers employed $Al(OPh)_3$ as an alternative Lewis acid to $AlCl_3$ for the synthesis of Mg electrolytes.[40] By combining PhMgCl and $Al(OPh)_3$ in a 1:4 ratio in THF the authors were able to prepare an electrolyte system with apparent oxidative stability up to 5 V vs. Mg on Pt and stainless steel electrodes. A similar system has been developed by Arnold and co-workers by combining $Mg(O^{i}Pr^{F})_2$ ($^{i}Pr^{F}$ = hexafluoro-*iso*-

propyl) and $Al(O^iPr^F)_3$ in a 1:2 ratio in DME to form a $Mg[Al(O^iPr^F)_4]_2$-based electrolyte.[41] The weakly coordinating nature of these highly fluorinated anions, resulting from weak intermolecular dispersive interactions brought on by the low polarizability of C-F bond, makes salts containing these anions highly soluble as well as highly conductive.[42,43] Additionally, the electron withdrawing fluorine atoms lower the energy of the HOMO, thereby increasing oxidative stability (Figure 1.2). This system was found to exhibit oxidative stability over 3.5 V vs. Mg on a variety of electrodes, including Al and stainless steel. Further a 0.25 M solution of the electrolyte could be cycled on an inert glassy carbon electrode for 500 cycles with Mg plating/stripping Coulombic efficiencies close to 100%. However, cycling the electrolyte with a CP cathode was found to result in substantial capacity fade over 50 cycles. A second system developed by Arnold and co-workers utilized the Lewis acid $AlCl_3$ in conjunction with $Mg(O^iPr^F)_2$ in a 2:1 in DME.[44] While this electrolyte facilitated the efficient plating and stripping of Mg using an inert electrode it was also observed to be less stable than their previous system and exhibited a similar capacity fade when cycled with a CP cathode.

In addition to the system reported by Meyer discussed above, Mg borates have received considerable attention as electrolyte candidates, since they are highly stable with respect to oxidation. Mohtadi and co-workers found that solutions of $Mg(BH_4)_2$ in DME are stable up to 1.5 V vs. Mg and able to facilitate reversible deposition of Mg.[45] Additionally, the Mohtadi group found that the use of $LiBH_4$ as an additive in this system increased the plating/stripping efficiency to nearly 100%, an effect thought to result from the Lewis acidity of the Li^+ cation breaking-up tight ion pairing between Mg^{2+} and BH_4^-. Work by Muldoon and co-workers showed that phenyl-substituted borate anions, such as BPh_4^- and $B(C_6F_5)_3Ph^-$, paired with the $[Mg_2(\mu_2\text{-}Cl)_3\cdot 6THF]^+$ cation exhibit much greater oxidative stabilities than the more reducing $Mg(BH_4)_2$ salt, remaining stable up to 2.6 and 3.7 V vs. Mg, respectively.[19] The same group also demonstrated that high oxidative stability could be achieved using THF solutions of the highly fluorinated $Mg(BAr^F)_2$ (BAr^F = tetrakis[3,5-bis(trifluoromethyl)phenyl]borate) salt, which was oxidatively stable up to at least 4 V vs. Mg using a stainless steel electrode. However, the solutions of the $Mg(BAr^F)_2$ salt in THF were observed to exhibit poor reductive stability and decomposed at potentials above those required for Mg plating (i.e. 0 V vs. Mg), precluding its ability to deposit Mg at a Mg anode.[15]

In 2017, Zhao-Karger and co-workers reported a series of chloride-free Mg alkoxyborate salts, which were synthesized through the reaction of alcohols with $Mg(BH_4)_2$.[46] In this study the authors focus on a 0.6 M solution of the $Mg[B(O^iPr^F)_4]_2$ salt in DME and show that it is able to facilitate the reversible plating and stripping of Mg using Pt and Mg electrodes and exhibited oxidative stability over 4 V vs. Mg on stainless steel and aluminium electrodes. Further, this electrolyte could be cycled in cells containing a sulfur cathode, retaining reversible capacities of ca. 200 $mAh \cdot g^{-1}$ after 100 cycles. Solid-state X-ray diffraction analysis of single crystals grown from a concentrated solution of the salt in DME shows that the compound has the molecular formula $Mg(DME)_3[B(O^iPr^F)_4]_2$ and contains a tetrahedral alkoxyborate anion as well as the solvated Mg cation (anion shown in Figure 1.6a)

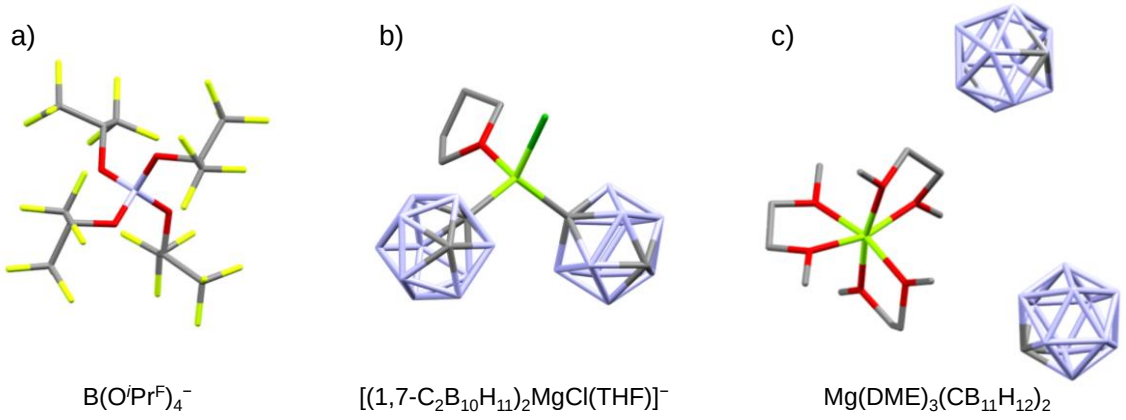

Figure 1.6 Solid state structures of the a) $B(O^iPr^F)_4^-$ anion, b) $MgCl(1,7\text{-}C_2B_{10}H_{11})_2$ anion, c) and $Mg(DME)_3(CB_{11}H_{12})_2$ salt. Protons and disorder have been removed for clarity (Mg, light green; Cl, dark green; B, purple; F, yellow; O, red; C, grey).

The Mohtadi group have also investigated a number of electrolyte systems based on Mg carborane salts. The first of these was based on the *m*-carboranyl ($1,7\text{-}C_2B_{10}H_{11}^-$) anion. The Mg salt was synthesized by stirring *m*-carborane with ^{i}PrMgCl in THF.[47] Upon crystallization from the reaction solution, the salt was found to comprise a $[(1,7\text{-}C_2B_{10}H_{11})_2MgCl(THF)]^-$ anion and the $[Mg_2(\mu_2\text{-}Cl)_3 \cdot 6THF]^+$ cation (Figure 1.6b). In THF this system exhibited oxidative stability up to 3.2 V vs. Mg on Al and stainless steel and facilitated efficient cycling with a CP cathode, with minimal capacity loss over 40 cycles and small overpotentials. In a second iteration of this electrolyte system Mohtadi and co-workers employed the monoanionic carborane $CB_{11}H_{12}$ as an anion as the negative charge is delocalized over the bonds within the cluster, rendering it weakly coordinating and relatively inert.[48] The Mg salt could be synthesized by metathesis between $AgCB_{11}H_{12}$ and $MgBr_2$ in THF, affording a halide-free electrolyte salt. Extraction of the solids retrieved from the

metathesis with DME afforded a Mg salt consisting of a $Mg(DME)_3^+$ cation and two non-coordinating carboranyl anions as determined by single crystal X-ray diffraction analysis (Figure 1.6c). Solutions of this salt in tetraglyme exhibit oxidative stability to ca. 3.5 V vs. Mg on Ni, Al, and stainless steel electrodes. Further, this group demonstrated that this electrolyte system can facilitate initial charging and discharging of the high voltage cathode material α-MnO_2 as well as reversible cycling with a CP cathode. While this electrolyte is highly stable and halide-free, which could have implications for limiting cell corrosion, the use of carboranes make this electrolyte costly and impractical.

The bis(trifluoromethane)sulfonamide ($TFSI^-$) anion has recently been the subject of a number of electrochemical studies in the context of Mg batteries. Owing to its delocalization of charge, the $TFSI^-$ anion is known to be highly oxidatively stable, making it an attractive electrolyte component. Initial studies of the commercially available $Mg(TFSI)_2$ salt in CH_3CN by Obrovac and co-workers showed that the electrolyte system resulted in corrosion of stainless steel coin cell components above 2.8 V vs. Mg, allowing it to be cycled only ca. 0.3 V higher than Grignard-based electrolytes which are also known to corrode stainless steel.[49] Further, this system was observed to decompose on the stainless steel electrode at ca. −0.2 V vs. Mg, which the authors attribute to CH_3CN breakdown. Both of these factors still ultimately limit the operational voltage window of the electrolyte in the presence of stainless steel. However, this system could be cycled reversibly with the CP cathode between 1.3 and 0.3 V vs. Mg with less capacity fade than has been observed for Mg organohaloaluminates.

Burrell and co-workers demonstrated that pure $Mg(TFSI)_2$ in THF does not exhibit typical plating/stripping behaviour in CV experiments conducted using a Pt working electrode; however, the addition of varying amounts of $MgCl_2$ to both THF and diglyme solutions of $Mg(TFSI)_2$ enabled plating/stripping of Mg (Figure 1.7).[50,51] Further, they showed that systems containing $MgCl_2$ exhibit oxidative stability over 3 V vs. Mg. Structural analysis conducted on a mixture of 2:1 $Mg(TFSI)_2$-$MgCl_2$ in THF using electrospray ionization mass spectrometry and single crystal X-ray diffraction showed that the salt in solution is composed of the $[Mg_2(\mu_2\text{-}Cl)_3 \cdot 6THF]^+$ cation and a $TFSI^-$ anion. The authors note that a 2:1 mixture of $Mg(TFSI)_2$-$MgCl_2$ in diglyme results in optimal plating/stripping behaviour and attribute this to equilibrium-driven and concentration-dependent formation of an electrochemically active species. Additionally, this optimized electrolyte system in THF can be cycled with a CP cathode with good capacity retention. Complementary to this work,

Ma and co-workers have shown that the addition of $Mg(BH_4)_2$ to solutions of $Mg(TFSI)_2$ in tetraglyme facilitates plating/stripping of Mg, albeit with Coulombic efficiencies around 80% using a variety of electrodes.[52] The plating/stripping behaviour of this electrolyte is attributed to the removal of trace amounts of water from the system by BH_4^-; however, the authors provide no indication of the influence of this anion on the oxidative stability of the system.

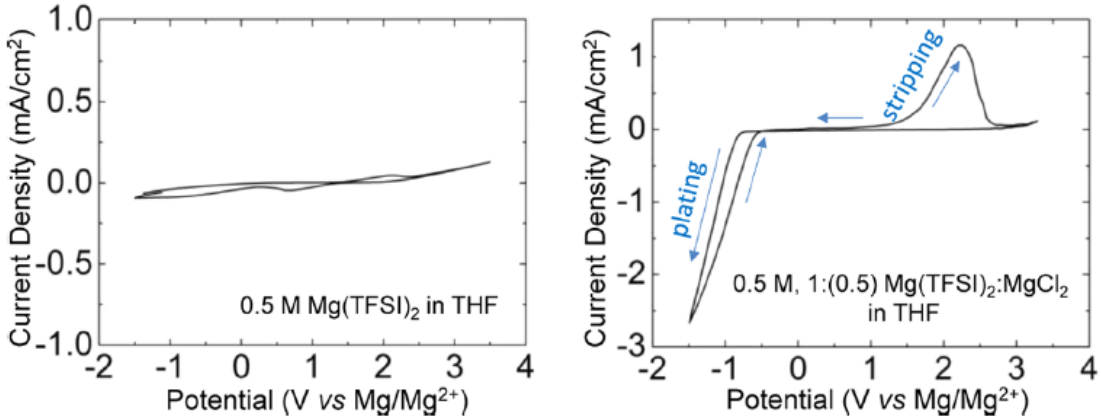

Figure 1.7 Cyclic voltammograms of $Mg(TFSI)_2$ electrolyte solutions in THF with (right) and without (left) $MgCl_2$ added. Figure adapted with permission from reference 50. Copyright 2016 American Chemical Society.

1.3.2 Chloride in Mg Electrolytes

Another challenge facing Mg battery electrolyte development is the identification of electrolyte preparation methods that limit corrosion within Mg cells. Specifically, the corrosion of current collectors such as Al, Ni, or stainless steel can have several negative effects on the cell. Corrosion can limit the charging voltage of the cell to below ca. 2.2 V vs. Mg, it can cause continuous decomposition of the electrolyte, and if corrosion is severe, contact between the cathode and the current collector can be broken resulting in battery failure.[53] It is believed that chloride is a major cause of corrosion in batteries and, as such, there has been a push to move away from chloride-containing electrolytes.[15] Accordingly, researchers have been making efforts to adopt synthetic methods that are free of chloride. A number of promising chloride-free electrolytes have been developed, including the $Mg[B(O^iPr^F)_4]_2$ and $Mg[Al(O^iPr^F)_4]_2$ systems developed by the Zhao-Karger[46] and Arnold groups,[41] respectively, as well as the highly stable carborane system developed in the Mohtadi group.[48]

However, it is becoming increasingly apparent that the presence of chloride in Mg electrolytes is beneficial to Mg plating/stripping efficiencies and overpotentials for these processes.[34,39,50,54,55] The Gewirth group has investigated in detail the impact of chloride in Mg cells in detail using the $Mg(AlCl_2EtBu)_2$ and MACC systems in THF, by a combination of analytical techniques including Raman spectroscopy, NMR spectroscopy, and X-ray total scattering methods. Both of these systems are known to require 'conditioning' to enable efficient plating and stripping of Mg.[38,39,56] This conditioning process involves electrochemical cycling of the electrolyte until desirable plating/stripping behaviour is achieved, which can require upward of 100 cycles (Figure 1.8).[56] Gewirth and co-workers found that this conditioning process results in electrodeposition of the Al on the anode from the Al-containing anion. The deposition of Al is evidenced by both significant cathodic current at potentials expected for Al reduction (>0 V vs. Mg) during initial stages of conditioning as well as the presence of Al on the Mg surface as observed by SEM and EDX analysis.[39,56] The deposition of Al results in a re-equilibration of species in solution, liberating free chloride from the $AlCl_2EtBu^-$ or $AlCl_4^-$ anions while still retaining the $[Mg_2(\mu_2\text{-}Cl)_3{\cdot}6THF]^+$ cation. Further, Gewirth and co-workers propose that the free chloride present in the conditioned electrolyte decorates the Mg electrode and displaces pre-existing THF-Mg passivating surface interactions, creating a lower energy barrier to Mg electrodeposition.

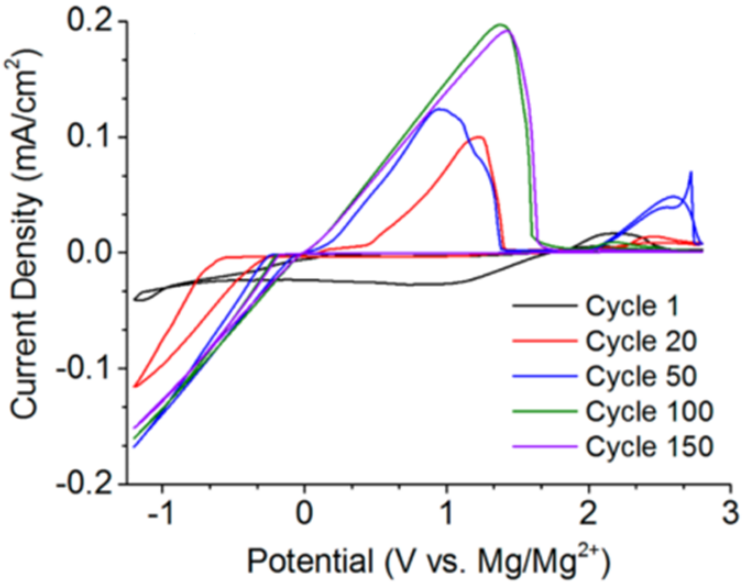

Figure 1.8 Cyclic voltammograms of MACC in THF on a Pt electrode showing the progress of the conditioning process over 150 cycles, leading to efficient plating/stripping. Figure adapted with permission from reference 56. Copyright 2014 American Chemical Society.

In contrast to Gewirth and co-workers who propose that contaminant removal through electrolyte conditioning is not a major factor in enabling efficient cycling, Markovic and co-workers believe that the conditioning process of the aforementioned systems is important for the removal of trace amount of water from the electrolyte system.[55] Using CV and X-ray photoelectron spectroscopy (XPS), the authors report that the electrochemical behaviour of $Mg(TFSI)_2$ in diglyme with trace amounts of water also benefit from the addition of $MgCl_2$. While trace amounts of water (ca. 3 ppm) can passivate the Mg surface and inhibit Mg deposition, the presence of chloride in the electrolyte can preferentially adsorb on the Mg electrode surface to form a protective layer that permits plating/stripping of Mg with low overpotentials.

While many studies have suggested that the dimeric $[Mg_2(\mu_2\text{-}Cl)_3 \cdot 6THF]^+$ cation is the electrochemically active species in chloride-containing electrolytes, which facilitates efficient electrodeposition of Mg, other monocationic Mg-Cl complexes have also been proposed as active species. These other species include solvated $MgCl^+$ cations as well as higher-order clusters like the solvated trinuclear $[Mg_3(\mu_2\text{-}Cl)_3(\mu_3\text{-}Cl)_2]^+$ cation.[57,58] To gain further understanding of the Mg plating mechanism and the species involved, Gewirth and co-workers conducted variable scan rate CV experiments (Pt electrode) on several chloride-containing electrolytes known to contain the $[Mg_2(\mu_2\text{-}Cl)_3 \cdot 6THF]^+$ cation as evidenced by single crystal X-ray diffraction of crystals extracted from chloride-containing electrolyte solutions.[59] The authors note that as the scan rate is increased, from 2 to 20 $mV \cdot s^{-1}$ the current densities measured for plating/stripping decrease. They propose that this scan rate dependency results from a 'chemical' step prior to the transfer of electrons from the electrode to the Mg complex in solution. In addition, they found a temperature dependence to the Mg deposition process, where larger current densities were measured at higher temperatures which further supports the proposed chemical-electrochemical deposition mechanism. As these experiments were conducted using a pristine Pt electrode, the authors propose that the chemical step is related to the active species in solution rather than a chemical step involving a change or breakdown of a passivating surface layer. For this chemical-electrochemical mechanism it is suggested that a disproportionation of the $[Mg_2(\mu_2\text{-}Cl)_3 \cdot 6THF]^+$ cation into a solvated $MgCl^+$ cation occurs, which then adsorbs on the electrode surface before being reduced to Mg^0 (Figure 1.9).

The exact nature of the reduction step, whether it proceeds via successive single electron processes or a concerted double electron transfer, continues to be debated.

Electrochemical kinetics studies conducted by Levi and co-workers suggest that successive single electron processes are involved in the reduction of Mg^{2+}, via a proposed $MgCl^{\cdot}$ radical, with the first electron transfer being the rate determining step.[60] Using X-ray absorption near-edge spectroscopy (XANES), Arthur and co-workers have studied the Mg electrode-electrolyte interface during electrodeposition from solutions containing the $[Mg_2(\mu_2\text{-}Cl)_3{\cdot}6THF]^+$ cation.[61] From the XANES data the authors hint at the possible involvement of a radical species in the reduction process but do not offer a potential formula for this intermediate. While theoretical calculations are in agreement with a process involving the adsorption of the $MgCl^+$ cation on the electrode surface, they have yet to shed light on the electron transfer process.[62] We note here that electrodeposition mechanisms for chloride-free systems are less well developed but it is proposed that electrons are transferred in two successive reduction steps.[63,64]

As the solution structure of the Mg cation is crucial to the Mg electrodeposition behaviour of the electrolyte, Robertson and co-workers have investigated new synthetic methods by which specific nuclearity and coordination environments surrounding Mg can be obtained.[58] By adding different Lewis bases, such as 2-methyltetrahydrofuran (MeTHF), tetramethylethylenediamine (TMEDA), and tris(2-dimethylaminoethyl)amine (Me_6TREN),

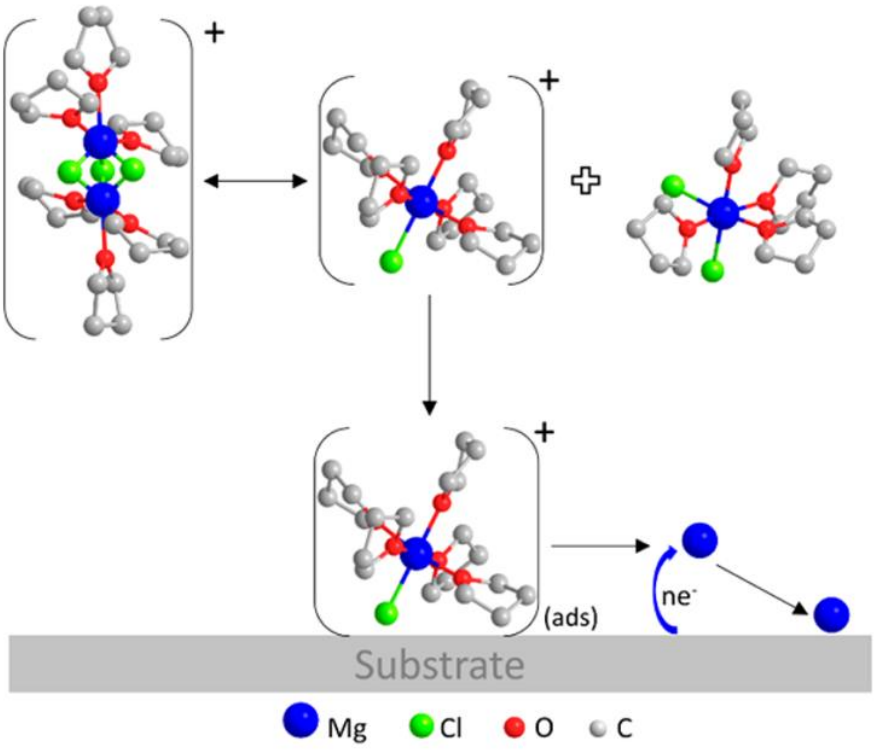

Figure 1.9 Schematic of the proposed chemical-electrochemical Mg deposition mechanism. Figure adapted with permission from reference 59. Copyright 2018 American Chemical Society.

the authors were able to direct the formation of both a $[Mg_3(\mu_2\text{-}Cl)_3(\mu_3\text{-}Cl)_2]^+$ cation and a $MgCl^+$ cation using TMEDA and Me_6TREN/MeTHF, respectively. The identification of Lewis bases that promote the formation of these cationic species could encourage their use as additives or solvents in new electrolyte formulations to promote efficient plating/stripping behaviour. Such studies highlight the important role synthetic inorganic chemistry can play in optimizing electrolyte systems and developing next generation Mg battery technology.

1.3.3 Summary

It is clear that Mg batteries have several features that make them attractive alternative battery technologies. Non-dendritic Mg deposition, arising from close packing of Mg atoms, makes Mg systems inherently safer than Li-ion cells. The high natural abundance of Mg, safety, and high theoretical capacity of Mg anodes make Mg cells a potentially less costly and higher capacity alternative to current Li-ion technology. However, the charge density of the Mg^{2+} cation also imposes several challenges in terms of the mobility of the cation in solution and in the solid state (i.e. cathode materials and SEI). The strong interactions typical of the Mg^{2+} cation make it practically impossible for Mg^{2+} cations to penetrate insulating films that can form on electrode surfaces to maintain good cycling behaviour with low overpotentials. Accordingly, it appears to be essential to avoid the formation of SEIs through the decomposition of the Mg electrolyte.

Thus, considerable research has been directed toward the development of highly electrochemically stable Mg electrolyte systems which are both stable towards reduction at the Mg anode as well as oxidatively stable at the cathode. In attempts to obtain energy densities that begin to approach those of Li-ion cells, high voltage Mg cathode materials demand oxidative stability over ca. 3.5 V vs. Mg. A number of electrolyte systems that are both chloride-containing and chloride-free, described above, are approaching this level of oxidative stability. However, their ability to cycle in Mg full cells containing active cathode materials (mostly tested with the low voltage CP cathode) is still limited, with practical issues arising from low cycling rates and substantial capacity fade over tens of cycles. Even with chloride-containing systems attaining high oxidative stabilities, there is still concern that such systems will promote the onset of corrosion of current collectors or cell casings at voltages around 2.2 V vs Mg and ultimately result in cell failure. Despite the possibility for corrosion, many electrolyte systems are found to benefit from the presence of chloride in terms of plating/stripping overpotentials and Coulombic efficiency and detailed studies have found

that the presence of chloride not only influences the solution structure of the electrolyte but also the surface of the electrodes, creating lower barriers to Mg deposition.

While many significant breakthroughs have been made toward the advancement of Mg battery technology, especially in the development of highly stable electrolyte systems, many challenges remain in creating Mg full cells that are competitive with Li-ion technology. Li-ion battery systems have been developed to a degree wherein any component that is being developed or investigated can be tested in isolation with other standard components functioning under established parameters. Electrolyte systems for Li-ion batteries are highly optimized 'working' systems that allow new electrode materials to be tested and understood independent of the electrolyte, and *vice versa* for the study of Li electrolytes. In Mg systems, however, no component of the cell and its function can be isolated from the other components, making the identification of a limiting component very challenging. Even with a model cell consisting of a Mg anode and a CP cathode, system-specific interactions between the electrolyte and electrodes and variance in cycling behaviour between cells and institutions (contingent on cell construction and electrode preparation) still remain.

1.4 Project Aims

The aim of this project is to approach the development of Mg electrolyte systems by using synthetic and chemical expertise based in synthetic inorganic chemistry to develop new electrolyte systems with greater oxidative stability and employing generally accessible methodologies. Combined with expertise in battery materials development and characterization, we hope to identify and analyze electrolyte systems and their electrochemical behaviour in a way that will contribute to and influence the rapidly growing field of Mg battery chemistry as well as multivalent battery technology more broadly. To this end, we have explored the possibility of synthesizing and isolating the first example of $Mg(PF_6)_2$ and have studied its electrochemical behaviour on Mg electrodes as well as extending the methodology to the synthesis of $Ca(PF_6)_2$ (presented in Chapters 2 and 3). Further, we have developed a general synthetic platform for the preparation of a range of stable Mg aluminate salts that do not contain β-hydrogen atoms, precluding possible β-hydride elimination decomposition pathways that are known for similar systems (presented in Chapter 4). These electrolyte systems are then tested using linear sweep voltammetry (LSV) and cyclic voltammetry (CV) to understand both their electrochemical stability and ability to

facilitate the plating/stripping of Mg using various electrodes. Promising systems are tested in model cells containing the CP cathode to investigate the cyclability of the electrolyte in conjunction with an active cathode material. Cycled electrodes are examined using scanning electron microscopy and energy dispersive X-ray spectroscopy to gain further insight into the surface morphology or SEI on the electrodes and how these might relate to the electrolyte as well as their impact on the cycling performance of a cell.

In addition to new electrolyte systems and leading on from species identified in the synthesis of $Mg(PF_6)_2$, NH_4BPh_4 is found to initiate the catalytic and highly selective 1,4-hydroboration of pyridines, molecules that have many pharmacological applications. The mechanism of this reaction and the active catalytic species are identified using a combination of multinuclear NMR and single crystal X-ray diffraction.. Further, this methodology is applicable to the hydroboration of CO_2 to produce a mixture of hydroboration species.

1.5 References

1 M. Armand and J.-M. Tarascon, *Nature*, 2008, **451**, 652–657.

2 R. Van Noorden, *Nature*, 2014, **507**, 26–28.

3 V. Etacheri, R. Marom, R. Elazari, G. Salitra and D. Aurbach, *Energy Environ. Sci.*, 2011, **4**, 3243–3262.

4 T. M. I. Mahlia, T. J. Saktisahdan, A. Jannifar, M. H. Hasan and H. S. C. Matseelar, *Renew. Sustain. Energy Rev.*, 2014, **33**, 532–545.

5 X. Luo, J. Wang, M. Dooner and J. Clarke, *Appl. Energy*, 2015, **137**, 511–536.

6 *WHO Air quality guidelines for particulate matter, ozone, nitrogen dioxide and sulfur dioxide*, 2005.

7 D. Deng, *Energy Sci. Eng.*, 2015, **3**, 385–418.

8 J. W. Choi and D. Aurbach, *Nat. Rev. Mater.*, 2016, **1**, 16013.

9 A. Manthiram, *ACS Cent. Sci.*, 2017, **3**, 1063–1069.

10 J. B. Goodenough and K. S. Park, *J. Am. Chem. Soc.*, 2013, **135**, 1167.

11 K. Ozawa, *Solid State Ionics*, 1994, **69**, 212–221.

12 J. Wen, Y. Yu and C. Chen, *Mater. Express*, 2012, **2**, 197–212.

13 J. Muldoon, C. B. Bucur and T. Gregory, *Chem. Rev.*, 2014, **114**, 11683–11720.

14 H. D. Yoo, I. Shterenberg, Y. Gofer, G. Gershinsky, N. Pour and D. Aurbach, *Energy Environ. Sci.*, 2013, **6**, 2265–2279.

15 J. Muldoon, C. B. Bucur, A. G. Oliver, J. Zajicek, G. D. Allred and W. C. Boggess, *Energy Environ. Sci.*, 2013, **6**, 482–487.

16 R. Zhang and C. Ling, *MRS Energy Sustain.*, 2016, **3**, E1.

17 C. Ling, D. Banerjee and M. Matsui, *Electrochim. Acta*, 2012, **76**, 270–274.

18 M. Jäckle and A. Groß, *J. Chem. Phys.*, 2014, **141**, 174710.

19 J. Muldoon, C. B. Bucur, A. G. Oliver, T. Sugimoto, M. Matsui, H. S. Kim, G. D. Allred, J. Zajicek and Y. Kotani, *Energy Environ. Sci.*, 2012, **5**, 5941–5950.

20 T. D. Gregory, R. J. Hoffman and R. C. Winterton, *J. Electrochem. Soc*, 1990, **137**, 775–780.

21 Y. Viestfrid, M. D. Levi, Y. Gofer and D. Aurbach, *J. Electroanal. Chem.*, 2005, **576**, 183–195.

22 J. Muldoon, C. B. Bucur and T. Gregory, *Angew. Chem. Int. Ed.*, 2017, **56**, 12064–12084.

23 T. Hughbanks and R. Hoffmann, *J. Am. Chem. Soc.*, 1983, **105**, 1150–1162.

24 A. Mitelman, M. D. Levi, E. Lancry, E. Levi and D. Aurbach, *Chem. Commun.*, 2007, 4212–4214.

25 L. W. Gaddum and H. E. French, *J. Am. Chem. Soc.*, 1927, **49**, 1295–1299.

26 D. M. Overcash and F. C. Mathers, *Trans. Electrochem. Soc.*, 1933, **64**, 305–311.

27 R. Schwarz, M. Pejic, P. Fischer, M. Marinaro, L. Jörissen and M. Wachtler, *Angew. Chem. Int. Ed.*, 2016, **55**, 14958–14962.

28 A. Mayer, *J. Electrochem. Soc.*, 1990, **137**, 2806–2809.

29 D. Aurbach, Z. Lu, A. Schechter, Y. Gofer, H. Gizbar, R. Turgeman, Y. Cohen, M. Moshkovich and E. Levi, *Nature*, 2000, **407**, 724–727.

30 D. Aurbach, G. S. Suresh, E. Levi, A. Mitelman, O. Mizrahi, O. Chusid and M. Brunelli, *Adv. Mater.*, 2007, **19**, 4260.

31 N. Pour, Y. Gofer, D. T. Major and D. Aurbach, *J. Am. Chem. Soc.*, 2011, **133**, 6270–6278.

32 H. S. Kim, T. S. Arthur, G. D. Allred, J. Zajicek, J. G. Newman, A. E. Rodnyansky, A. G. Oliver, W. C. Boggess and J. Muldoon, *Nat. Commun.*, 2011, **2**, 427.

33 Z. Zhao-Karger, X. Zhao, D. Wang, T. Diemant, R. J. Behm and M. Fichtner, *Adv. Energy Mater.*, 2015, **5**, 1401155.

34 T. Liu, Y. Shao, G. Li, M. Gu, J. Hu, S. Xu, Z. Nie, X. Chen, C. Wang and J. Liu, *J. Mater. Chem. A*, 2014, **2**, 3430–3438.

35 P. Canepa, S. Jayaraman, L. Cheng, N. N. Rajput, W. D. Richards, G. S. Gautam, L. A. Curtiss, K. A. Persson and G. Ceder, *Energy Environ. Sci.*, 2015, **8**, 3718–3730.

36 M. Salama, I. Shterenberg, L. J. W. Shimon, K. Keinan-Adamsky, M. Afri, Y. Gofer and D. Aurbach, *J. Phys. Chem. C*, 2017, **121**, 24909–24918.

37 J. Luo, S. He and T. L. Liu, *ACS Energy Lett.*, 2017, **2**, 1197–1202.

38 C. J. Barile, R. Spatney, K. R. Zavadil and A. A. Gewirth, *J. Phys. Chem. C*, 2014, **118**, 10694–10699.

39 K. A. See, K. W. Chapman, L. Zhu, K. M. Wiaderek, O. J. Borkiewicz, C. J. Barile, P. J. Chupas and A. A. Gewirth, *J. Am. Chem. Soc.*, 2016, **138**, 328–337.

40 E. G. Nelson, S. I. Brody, J. W. Kampf and B. M. Bartlett, *J. Mater. Chem. A*, 2014, **2**, 18194–18198.

41 J. T. Herb, C. A. Nist-Lund and C. B. Arnold, *ACS Energy Lett.*, 2016, **1**, 1227–1232.

42 I. Krossing and A. Reisinger, *Coord. Chem. Rev.*, 2006, **250**, 2721.

43 S. Tsujioka, B. G. Nolan, H. Takase, B. P. Fauber and S. H. Strauss, *J. Electrochem. Soc.*, 2004, **151**, A1418–A1423.

44 J. T. Herb, C. A. Nist-Lund and C. B. Arnold, *J. Mater. Chem. A*, 2017, **5**, 7801–7805.

45 R. Mohtadi, M. Matsui, T. S. Arthur and S. J. Hwang, *Angew. Chem. Int. Ed.*, 2012, **51**, 9780–9783.

46 Z. Zhao-Karger, M. E. Gil Bardaji, O. Fuhr and M. Fichtner, *J. Mater. Chem. A*, 2017, **5**, 10815–10820.

47 T. J. Carter, R. Mohtadi, T. S. Arthur, F. Mizuno, R. Zhang, S. Shirai and J. W. Kampf, *Angew. Chem. Int. Ed.*, 2014, **53**, 3173–3177.

48 O. Tutusaus, R. Mohtadi, T. S. Arthur, F. Mizuno, E. G. Nelson and Y. V. Sevryugina, *Angew. Chem. Int. Ed.*, 2015, **54**, 7900–7904.

49 T. T. Tran, W. M. Lamanna and M. N. Obrovac, *J. Electrochem. Soc.*, 2012, **159**, A2005–A2009.

50 N. Sa, B. Pan, A. Saha-Shah, A. a. Hubaud, J. T. Vaughey, L. a. Baker, C. Liao and A. K. Burrell, *ACS Appl. Mater. Interfaces*, 2016, **8**, 16002–16008.

51 N. Sa, H. Wang, D. L. Proffit, A. L. Lipson, B. Key, M. Liu, Z. Feng, T. T. Fister, Y. Ren, C. J. Sun, J. T. Vaughey, P. A. Fenter, K. A. Persson and A. K. Burrell, *J. Power Sources*, 2016, **323**, 44–50.

52 Z. Ma, M. Kar, C. Xiao, M. Forsyth and D. R. MacFarlane, *Electrochem. Commun.*, 2017, **78**, 29–32.

53 I. Shterenberg, M. Salama, Y. Gofer, E. Levi and D. Aurbach, *MRS Bull.*, 2014, **39**, 453–460.

54 J. L. Esbenshade, C. J. Barile, T. T. Fister, K. L. Bassett, P. Fenter, R. G. Nuzzo and A. A. Gewirth, *J. Phys. Chem. C*, 2015, **119**, 23366–23372.

55 J. G. Connell, B. Genorio, P. P. Lopes, D. Strmcnik, V. R. Stamenkovic and N. M. Markovic, *Chem. Mater.*, 2016, **28**, 8268–8277.

56 C. J. Barile, E. C. Barile, K. R. Zavadil, R. G. Nuzzo and A. A. Gewirth, *J. Phys. Chem. C*, 2014, **118**, 27623–27630.

57 T. Liu, J. T. Cox, D. Hu, X. Deng, J. Hu, M. Y. Hu, J. Xiao, Y. Shao, K. Tang and J. Liu, *Chem. Commun.*, 2015, **51**, 2312–2315.

58 E. V Brouillet, A. R. Kennedy, K. Koszinowski, R. Mclellan, R. E. Mulvey and S. D. Robertson, *Dalt. Trans.*, 2016, **45**, 5590–5597.

59 K. Ta, K. A. See and A. A. Gewirth, *J. Phys. Chem. C*, 2018, **122**, 13790–13796.

60 Y. Viestfrid, M. D. Levi, Y. Gofer and D. Aurbach, *J. Electroanal. Chem.*, 2005, **576**, 183–195.

61 T. S. Arthur, P.-A. Glans, M. Matsui, R. Zhang, B. Ma and J. Guo, *Electrochem. commun.*, 2012, **24**, 43–46.

62 P. Canepa, G. S. Gautam, S. Gautam, R. Malik, S. Jayaraman, Z. Rong, K. R. Zavadil, K. Persson and G. Ceder, *Chem. Mater.*, 2015, **27**, 3317–3325.

63 N. N. Rajput, X. Qu, N. Sa, A. K. Burrell and K. A. Persson, *J. Am. Chem. Soc.*, 2015, **137**, 3411–3420.

64 A. F. Chadwick, G. Vardar, S. Dewitt, A. E. S. Sleightholme, C. W. Monroe, D. J. Siegel and K. Thornton, *J. Electrochem. Soc.*, 2016, **163**, 1813–1821.

2. Synthesis and Electrochemical Analysis of Magnesium Hexafluoropnictogenate Salts

2.1 Introduction

Owing to the considerable interest that Li-ion batteries have received in recent years, many Li electrolyte systems have been developed and studied involving a wide range of Li salts including $LiBF_4$, $LiClO_4$, LiTFSI, $LiPF_6$, $LiAsF_6$, and $LiSbF_6$ as well as others.[1,2] Due to a balance of a range of properties that no other common Li salt was found to possess, $LiPF_6$ ultimately became the preferred electrolyte and was commercialised in 1990 by SONY.[3] $LiPF_6$ exhibits low thermal stability, decomposing to LiF and PF_5 at elevated temperatures, which limits its operating temperature to below 70 °C, and is also highly susceptible to hydrolysis, forming HF, LiF, and POF_3 when exposed to water. [4,5] Accordingly, rigorously dry conditions are required when using $LiPF_6$ electrolytes. The relatively labile P-F bonds and resulting decomposition of the PF_6^- anion in mixed carbonate solvents at the electrodes during cycling results in the formation of an integral component of Li-ion battery chemistry: the surface electrolyte interphase (SEI). As discussed in Chapter 1, the SEI in Li-ion cells is composed of both organic (carbonate-derived oligomers and polymers) and inorganic (LiF, Li_2O, Li_2CO_3) components which are Li-permeable and can prevent continual decomposition of the electrolyte at the electrode surfaces.[6] In addition, PF_6^--based electrolytes are able to form passivating layers on aluminium, a metal commonly used as a current collector in battery systems.[7] Electrolyte stability at the current collector under battery operating conditions is highly important to prevent continuous breakdown of the electrolyte and eventual device failure. As a result, this passivation layer on the Al current collector is crucial for protecting the electrolyte from continuous reactions with Al. Despite the thermal and hydrolytic instability of the PF_6^- anion, $LiPF_6$ has been found to be electrochemically stable to 5.1 V vs. Li/Li^+ in ethylene carbonate-dimethyl carbonate mixtures, allowing for the construction of Li-ion batteries with cathode operating potentials of 4 V.[8,9] $LiPF_6$-carbonate solutions are also highly conductive Li-ion electrolytes, with conductivities of up to 10.7 $mS \cdot cm^{-1}$ measured in 1:1 ethylene carbonate-dimethyl carbonate mixtures.[1]

Non-aqueous electrolytes containing the AsF_6^- and SbF_6^- anions have been investigated for both Li-ion batteries as well as capacitors owing to their very wide electrochemical stability windows. Paired with a Et_4N^+ cation, AsF_6^- and SbF_6^- in propylene

carbonate exhibited electrochemical stability windows of 6.8 V and 7.0 V, respectively.[9] $LiAsF_6$ in mixed carbonate solvents is also reported to have molar conductivities up to 15.6 $mS \cdot cm^{-1}$.[10] Although electrolyte systems containing these anions exhibit desirable electrochemical properties, they were ultimately dismissed in favour of PF_6-based systems as AsF_6^- and SbF_6^- anions do not contribute to a robust SEI and are considerably more toxic. Nonetheless, AsF_6^- and SbF_6^- salts of Mg have not been studied in the context of Mg batteries and their chemistry in that respect, both in terms of synthesis and electrochemistry, is unknown.

Despite the ubiquity of $LiPF_6$ in Li-ion systems, as well as the high stability of the AsF_6^- and SbF_6^- salts, the related Mg salts have not received the same attention and to the best of our knowledge no direct synthesis of $Mg(PF_6)_2$, $Mg(AsF_6)_2$ or $Mg(SbF_6)_2$ has been reported. It is generally thought that the PF_6^- anion decomposes on Mg anodes, forming passivating MgF_2 layers that render the Mg surface electrochemically inactive.[11,12] However, no detailed study of the electrochemistry or potential passivating or corrosive nature of $Mg(PF_6)_2$ has been conducted to date. In this chapter, the synthesis and characterization of several new Mg electrolyte systems are reported, including the Lewis base complexes $Mg(CH_3CN)_6(PF_6)_2$ (**2**), $Mg(CH_3CN)_6(SbF_6)_2$ (**3**), and $Mg(CH_3CN)_6(AsF_6)_2$ (**5**). The electrochemical stabilities of electrolytes based on **2**, **3**, and **5** are also investigated by linear sweep voltammetry (LSV) using various working electrodes. The ability of these electrolytes to facilitate the plating and stripping of Mg using Mg electrodes is also explored. Focusing primarily on the PF_6-based systems, Mg deposition on electrodes facilitated by these electrolyte mixtures was further investigated using scanning electron microscopy (SEM), and energy dispersive X-ray spectroscopy (EDX). Additionally, the use of a $Mg(PF_6)_2$-based electrolyte in a Mg-ion battery is demonstrated using a Mg anode and the Chevrel phase (Mo_6S_8) cathode material.

2.2 Results and Discussion

*2.2.1 Synthesis and Characterization of $(Py_2H)PF_6$ (**1**)*

Our initial strategy for the preparation of $Mg(PF_6)_2$ was to employ the 'ammonium salt route' used for an early synthesis of $LiPF_6$ involving the deprotonation of the ammonium cation of NH_4PF_6 with a basic metal source such as ^{n}BuLi.[13] Preliminary attempts to form

$Mg(PF_6)_2$ involved the treatment of a suspension of NH_4PF_6 in dry toluene with $^nBu_2Mg$ in a 2:1 ratio at room temperature (Scheme 2.1).

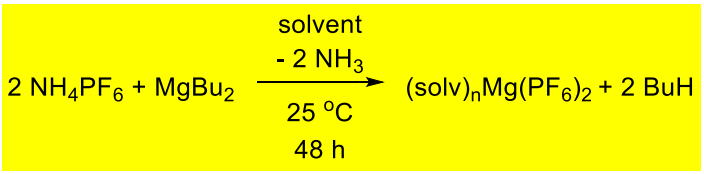

Scheme 2.1 Ammonium salt route for the synthesis of $Mg(PF_6)_2$.

However, the white solid obtained after concentrating the reaction mixture to dryness was found to contain a significant amount of NH_4PF_6 starting material by ^1H NMR spectroscopy, indicated by an N-H resonance at δ = 5.9 ppm (400 MHz, CD_3CN). The poor conversion of the starting material was attributed to the decreased reactivity of $^nBu_2Mg$ in non-donor solvents and the low solubility of NH_4PF_6. Accordingly, the reaction was tried in the donor solvents THF, DME, and Et_3N. In each solvent NH_4PF_6 largely remained as a suspension and the reaction product, isolated after 48 hours, contained a significant amount of starting material, again identified by ^1H NMR spectroscopy. Although conversion may indeed be possible in these solvents with the application of heat, this was avoided due to the known thermal instability of the PF_6^- anion and the desire for a product uncontaminated with MgF_2 or PF_5 species.

Dry pyridine (ca. 10 mL) was found to completely dissolve 500 mg of NH_4PF_6. Stirring the ammonium salt in pyridine for 10 minutes followed by the slow addition of $^nBu_2Mg$ at room temperature and stirring for 24 hours resulted in a pale yellow solution. After solvent removal and subsequent washes with toluene and pentane, the reaction afforded a white solid. The ^1H NMR spectrum of this solid powder in CD_3CN exhibited three resonances consistent with pyridine at δ = 8.58, 7.88, and 7.44 ppm. Importantly, no signals resulting from unreacted starting material are observed in the spectrum. Furthermore, the ^{19}F and ^{31}P NMR spectra, showing the characteristic PF_6^- doublet and heptet, respectively, indicate that no decomposition of the anion occurs during the reaction. Colourless crystals suitable for single-crystal X-ray analysis were obtained by layering toluene onto a solution of the reaction mixture in pyridine at room temperature after one week. Surprisingly, these crystals were found to be composed of a pyridinium hexafluorophosphate, $(Py_2H)PF_6$, **1**, having two pyridine molecules hydrogen-bonded to a central proton in the cation (Figure 2.1). The pyridinium fragment exhibits a N···N distance of 2.638(4) Å, and an N-H-N angle of 171.8°. The short N-N distance as well as the near-linear N-H-N fragment suggests that the

proton is bound by a strong hydrogen-bonding interaction.[14] Very few compounds containing a comparable $(Py\text{-}H\text{-}Py)^+$ motif are known.[15–19] A similar species having a $(Py\text{-}H\text{-}Py)^+$ motif composed of two molecules of 4-methylpyridine in the cation with a BPh_4^- counter anion has previously been reported.[15] As observed for **1**, the crystal structure of [bis(4-methylpyridine)H]$^+$ BPh_4^- exhibits a symmetrical hydrogen bond between the two pyridines with a very short N···N distance (2.610(15) Å) as well as an N-H-N angle of 180°. The identification of this pyridinium species indicates that NH_4^+ is deprotonated by pyridine, providing an explanation for the high solubility of NH_4PF_6 in pyridine. Furthermore, it is possible that the strongly nucleophilic $^nBu_2Mg$, preferentially reacts with the excess pyridine to form alkyl-functionalized dihydropyridine species, which could be washed away during the purification step.[20]

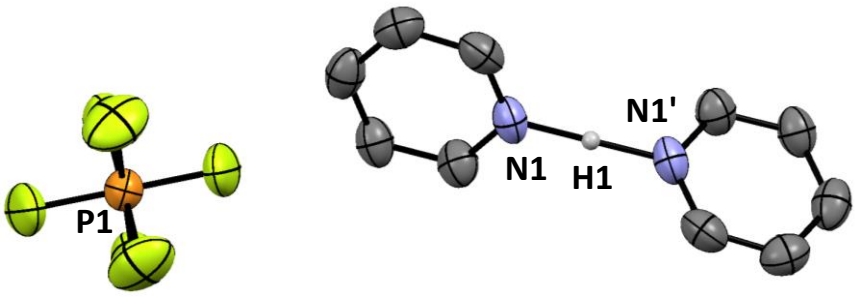

Figure 2.1 Crystal structure of **1**, displaying thermal ellipsoids at 50% probability. Selected protons have been omitted for clarity (C, grey; N, blue; P, orange; F, yellow; H, white). Selected atom distances (Å) and angles (°): N1···N1' 2.638(4), N1-H1-N1' 180. As H1 lies on an inversion centre, the angle of 180° is fixed and given without associated estimated standard deviation.

To verify the hypothesis that NH_4PF_6 is indeed deprotonated by pyridine to form **1**, NH_4PF_6 was stirred in pyridine for 24 hours at room temperature (Scheme 2.2). Colourless crystals could be grown by vapour diffusion of Et_2O into a concentrated pyridine solution of the crude compound, allowing unambiguous confirmation that **1** is formed from the deprotonation of NH_4PF_6 by pyridine. The solid-state structure of **1** obtained from the reaction of NH_4PF_6 with pyridine is a different polymorph from the previous reaction, but exhibits a similar N···N distance of 2.667(3) Å and an N-H-N bond angle of 177(2)°. The ^1H NMR spectrum of this crystalline material in CD_3CN exhibits a doublet and two triplets arising from the pyridine moieties at δ = 8.65, 8.29, and 7.79 ppm, respectively, as well as a very broad downfield resonance centred at δ = 10.2 ppm believed to arise from the pyridinium proton.

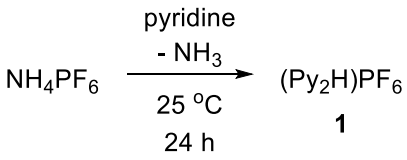

Scheme 2.2 Synthesis of **1** via the deprotonation of NH_4PF_6 by pyridine.

The apparent stability of **1**, limiting deprotonation of NH_4PF_6 by $^{n}Bu_2Mg$ at room temperature in the presence of pyridine, prompted further investigation into the formation of pure $Mg(PF_6)_2Py_n$. In attempts to destabilise **1** as well as increase the rate of reaction with $^{n}Bu_2Mg$, the reaction between NH_4PF_6 and $^{n}Bu_2Mg$ was conducted at 60 °C over 18 hours. However, despite relatively mild heating, the ^{19}F NMR spectrum (400 MHz, CD_3CN) of the solid retrieved from the reaction exhibited the doublet characteristic of the PF_6^- anion (δ = −72.9 ppm) as well as a doublet of doublets (δ = −64.8 ppm) and a doublet of quintets (δ = −82.2 ppm), both having a shared coupling constant of J = 57.0 Hz. The splitting pattern of the latter two peaks is characteristic of a PF_5 structure with a square-pyramidal geometry and is in good agreement with the known $PyPF_5$ adduct, involving $N_{Py}\rightarrow P$ dative interaction.[21] The isolated product also contains an insoluble material presumed to be MgF_2, further supporting the proposed decomposition. We thus concluded that the ammonium salt method was not a practical route for the generation of pure $Mg(PF_6)_2$ species.

*2.2.2 Synthesis and Characterization of $Mg(CH_3CN)_6(PF_6)_2$ (**2**)*

With the aim of obtaining a pure and crystalline $Mg(PF_6)_2$ material, an alternative method was investigated. Previously, a number of first-row transition metal (TM^{2+}) PF_6 salts have been formed from the reaction of the metals with $NOPF_6$ in a 1:2 ratio.[22] The NO^+ cation is highly oxidising and is able to abstract an electron from the metal, forming neutral NO gas. It was hypothesised that $NOPF_6$ could be used in a similar way to oxidise Mg metal and afford $Mg(PF_6)_2$. Accordingly, Mg metal, activated with a small amount of I_2 in dry CH_3CN, was treated with a solution of $NOPF_6$ in dry CH_3CN at room temperature under an atmosphere of N_2 (Scheme 2.3). Very rapidly, the mixture was observed to turn brown and evolve a colourless gas. After gas evolution had subsided at room temperature, the solution was heated at 45 °C for ca. 20 hours. After stirring at 45 °C the CH_3CN was removed *in vacuo* to afford an off-white solid which was then recrystallized twice from hot acetonitrile, affording a white crystalline powder of $Mg(CH_3CN)_6(PF_6)_2$ (**2**) in 52% yield.

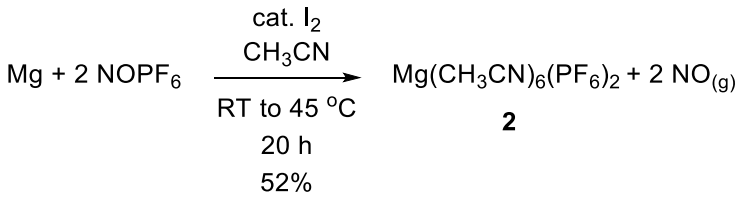

Scheme 2.3 Synthesis of $Mg(CH_3CN)_6(PF_6)_2$ (**2**) from magnesium metal and $NOPF_6$.

The room temperature ^1H NMR spectrum of **2** in CD_3CN showed a single CH_3CN resonance and the ^{19}F and ^{31}P NMR spectra exhibited a doublet and heptet, respectively, characteristic of the PF_6^- anion. X-ray analysis of a crystal obtained from the diffusion of Et_2O in to a CH_3CN solution of **2** confirmed the complex to be the desired $Mg(CH_3CN)_6(PF_6)_2$ salt (Figure 2.2).

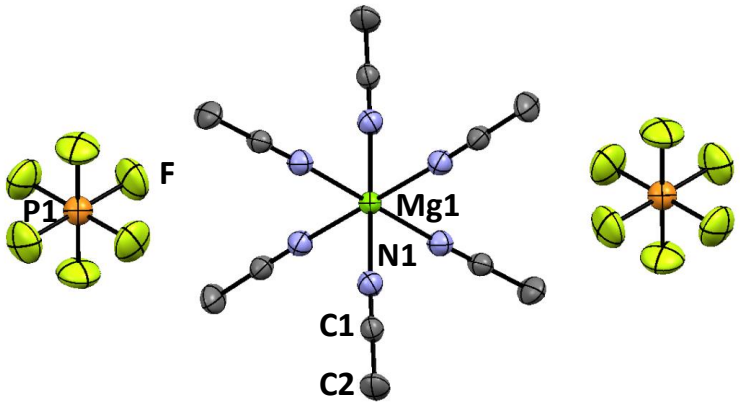

Figure 2.2 Crystal structure of **2**, displaying thermal ellipsoids at 50% probability. Protons and anion disorder have been omitted for clarity (C, grey; N, blue; P, orange; F, yellow; Mg, green). Selected bond distances (Å) and angles (°): N1-Mg1, 2.1439(18); N1-Mg-N1, 87.62(6) and 92.38(6).

As was observed in the structure of $Fe(CH_3CN)_6(PF_6)_2$,[23] Mg is coordinated in an octahedral geometry by CH_3CN molecules and is ion-separated from the counter anion. Bulk purity of **2** was confirmed by elemental analysis which was in good agreement with predicted values (calc'd for $C_{12}H_{18}N_6F_{12}P_2Mg$: C, 25.71; H, 3.25; N, 14.99; found: C, 25.79; H, 3.17; N, 14.16). Furthermore, the infrared (IR) spectrum of **2** exhibits a sharp band at 2299 cm^{-1}, corresponding to the acetonitrile C≡N stretching band (Figure 2.3).

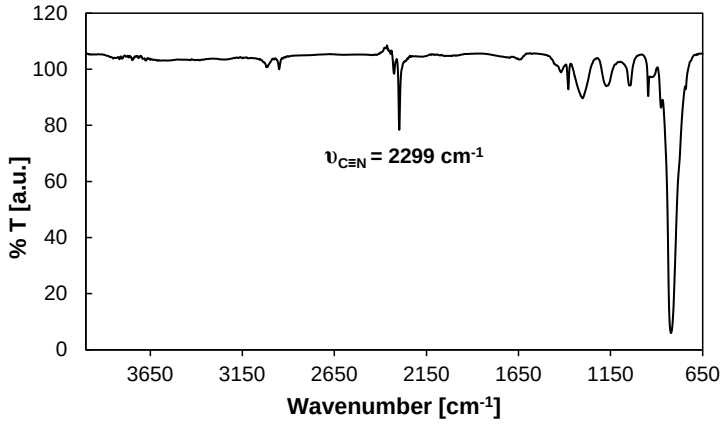

Figure 2.3 IR spectrum of **2** exhibiting the characteristic CH_3CN stretching frequency at 2299 cm^{-1}.

Complex **2** could be dissolved in CH_3CN to a maximum concentration of 0.12 M at 25 °C. Interestingly, it was found to be significantly more soluble in a 1 : 1 mixture of THF-CH_3CN, reaching a maximum concentration of ca. 0.71 M at 25 °C. The ionic conductivity of the 0.12 M electrolyte solution in CH_3CN is 18.7 $mS \cdot cm^{-1}$ at 25 °C while those of the 0.12 and 0.71 M solutions in 1 : 1 THF-CH_3CN are 10.0 and 28.3 $mS \cdot cm^{-1}$, respectively. These conductivities are of the same order of magnitude as those reported for $LiPF_6$ in CH_3CN,[24,25] and significantly higher than those measured for MACC in THF (0.26 $mS \cdot cm^{-1}$, 0.04 M)[26] and $Mg(TFSI)_2$ in 1 : 1 glyme-diglyme (5.22 $mS \cdot cm^{-1}$, 0.5 M).[27]

2.2.3 Electrochemistry of $Mg(CH_3CN)_6(PF_6)_2$ Solutions and Electrode Surface Analysis

Having successfully isolated a complex of $Mg(PF_6)_2$ in gram quantities, attention was turned to its use as an electrolyte salt. The ability of many Mg-ion electrolytes to facilitate the plating and stripping of Mg is typically studied using cyclic voltammetry (CV), employing an inert working electrode (WE) such as Pt, glassy carbon (GC), or Au working electrode for voltammetric cycling.[28] Electrolyte solutions of **2** were initially studied using a three-electrode flooded cell composed of a Pt-wire working electrode and Mg ribbon pseudo-reference and counter electrodes, referred to herein as a Pt|Mg|Mg cell, submerged in 0.5-1 mL of electrolyte solution (see Experimental, Figure 7.3). The use of Mg as a pseudo-reference, a reference not electrochemically isolated from the cell, ideally places the cross-over between plating and stripping, the transition from negative (cathodic) to positive (anodic) current densities, J [$A \cdot cm^{-2}$], at around 0 V versus the Mg^0/Mg^{2+} redox couple. During the CV experiments the potential, controlled by a potentiostat, was swept at a given

rate [$V \cdot s^{-1}$] towards negative potentials versus the Mg reference electrode to a specified negative voltage boundary before being swept toward positive potentials to a positive voltage boundary, while measuring the flow of electrons into or out of the system.

CV measurements conducted on 0.12 M solutions of **2** in CH_3CN as well as 0.71 M solutions of **2** in 1:1 THF-CH_3CN using a Pt working electrode between −0.5 and 3 V vs. Mg at a number of scan rates showed no voltammetric features consistent with plating or stripping behaviour. However, CV showed that a 0.12 M solution of **2** in 1:1 THF-CH_3CN could be cycled reversibly between −0.5 and 1.5 V vs. Mg over at least 20 cycles at a rate of 25 $mV \cdot s^{-1}$ using a GC working electrode (Figure 2.4a). The electrolyte could be cycled for at least 20 cycles with only moderate loss in plating/stripping current density, exhibiting a small stripping overpotential (ca. 0.25 V vs. Mg) and a plating onset at 0 V vs. Mg. While the voltammogram clearly demonstrates plating and stripping behaviour, we note that the broad cathodic features and multiple anodic peaks are not typical of Mg electrolytes and indicate additional processes to plating and stripping. Further, these broad features prevented the determination of meaningful cycling efficiency values.

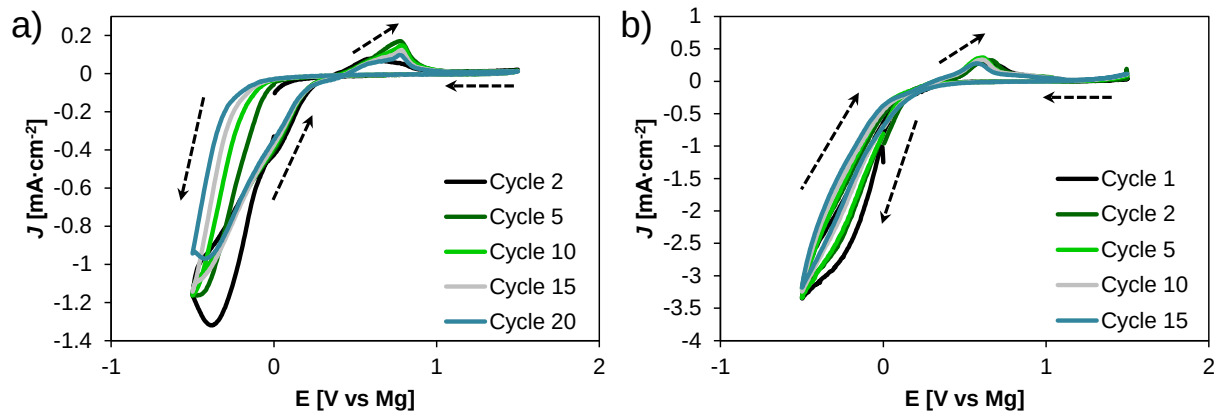

Figure 2.4 Selected cyclic voltammograms of solutions of **2** in 1:1 THF-CH_3CN measured in a WE|Mg|Mg cell, cycling at a rate of 25 $mV \cdot s^{-1}$. a) 0.12 M electrolyte solution cycled using a GC working electrode. b) 0.06 M electrolyte solution cycled using a ss-316 WE.

CV measurements conducted on a 0.06 M solution of **2** in 1:1 THF-CH_3CN using a stainless steel (ss-316) working electrode at a scan rate of 25 $mV \cdot s^{-1}$ showed similar Mg plating and stripping behaviour between −0.5 and 1.5 V vs. Mg (Figure 2.4b). Again, Mg plating is evidenced by anodic features from ca. 0.1 to −0.5 V vs. Mg as well as by clear stripping features observed during the anodic sweeps from ca. 0.4 to 1 V vs. Mg. The large cathodic current densities observed below 0 V vs. Mg, which are not balanced by anodic

current densities during stripping, suggest that processes additional to Mg plating, such as corrosion of the ss-316 (*vide infra*), are occurring at reductive potentials.

The electrochemical stabilities of both the 0.12 and 0.71 M solution of **2** in 1:1 THF-CH_3CN were further studied by performing linear sweep voltammetry (LSV) using Pt, GC, ss-316, and Al working electrodes (solid lines, Figure 2.5a). For the LSV measurement the potential of the working electrode was swept from 0 to 4 V vs. Mg at a rate of 25 $mV \cdot s^{-1}$. For LSV measurements conducted on the 0.12 M solution using Pt and GC electrodes, the onset of electrolyte oxidation was observed to begin with a minor anodic process around 2 V vs. Mg followed by more significant processes at 2.5 and 3 V vs. Mg, respectively. On ss-316, the 0.12 M solution exhibits oxidative processes at much lower potentials of around 1.5 V vs. Mg. Significantly, only very little current is observed with the Al working electrode out to 4 V vs. Mg, suggesting that the Al surface is passivated toward the breakdown of the electrolyte.

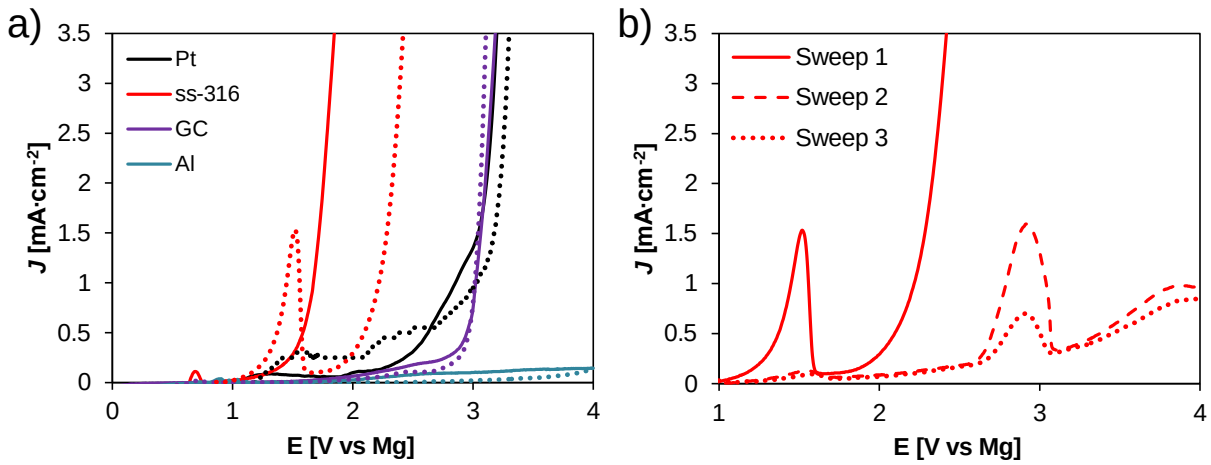

Figure 2.5 LSV of solutions of **2** in 1:1 THF-CH_3CN measured in a WE|Mg|Mg cell, cycling at a rate of 25 $mV \cdot s^{-1}$. a) LSV of the 0.12 (solid lines) and 0.71 (dotted lines) M electrolyte solutions on Pt, ss-316, GC, and Al WEs. b) Consecutive LSV measurements on a ss-316 WE conducted using a 0.71 M electrolyte solution.

LSV measurements conducted using the 0.71 M solution again showed the onset of oxidation of the electrolyte to be significantly lower on ss-316 than on Pt, GC, or Al (dotted lines, Figure 2.5a). On Pt, the 0.71 M solution exhibits minor anodic processes beginning around 1 V vs. Mg before undergoing a more significant oxidation process at ca. 2.7 V vs. Mg. The LSV trace of the 0.71 M solution on the GC working electrode is nearly identical to that obtained from the 0.21 M solution. A comparison of the LSV traces obtained from the two different concentrations shows that, except for ss-316, the electrolyte concentration has little effect on the onset of oxidation potential. On ss-316 the 0.71 M solution exhibits a

current spike around 1.5 V vs. Mg that is followed by large oxidative feature beginning around 1.75 V vs. Mg. The origin of the current spike is not clear but it does not appear to be associated with a bulk passivation of the electrode surface as further anodic current is observed during the same measurement. However, subsequent sweeps using the same ss-316 electrode showed significantly attenuated current densities up to 4 V vs. Mg (Figure 2.5b), suggesting that the electrolyte reacts with the surface of the ss-316 electrode to form an insulating film.

As MgF_2 passivation on Mg electrodes resulting from $Mg(PF_6)_2$ decomposition is believed to hinder Mg plating/stripping, CV measurements conducted in a symmetric cell (Mg|Mg|Mg) with Mg as the working electrode was used to study the stability of the electrolyte at a Mg anode around 0 V vs Mg. Both the 0.12 and 0.71 M solutions of **2** in 1:1 THF-CH_3CN were cycled between −0.5 and 0.5 V vs. Mg at a rate of 50 $mV{\cdot}s^{-1}$ for 10 cycles. The voltammograms of the 0.12 and 0.71 M electrolyte solutions exhibit little to no attenuation of current density, suggesting that the Mg electrode remains free of insulating films after cycling at potentials where Mg plating is expected (Figure 2.6a and b). Furthermore, that these anodic processes begin around 0 V vs. Mg (i.e. with very small overpotentials) suggests that Mg is being removed directly from the metal surface, rather than through the breakdown of a surface film followed by Mg removal.[11] A higher current is observed in the more concentrated electrolyte, most likely reflecting its higher conductivity.

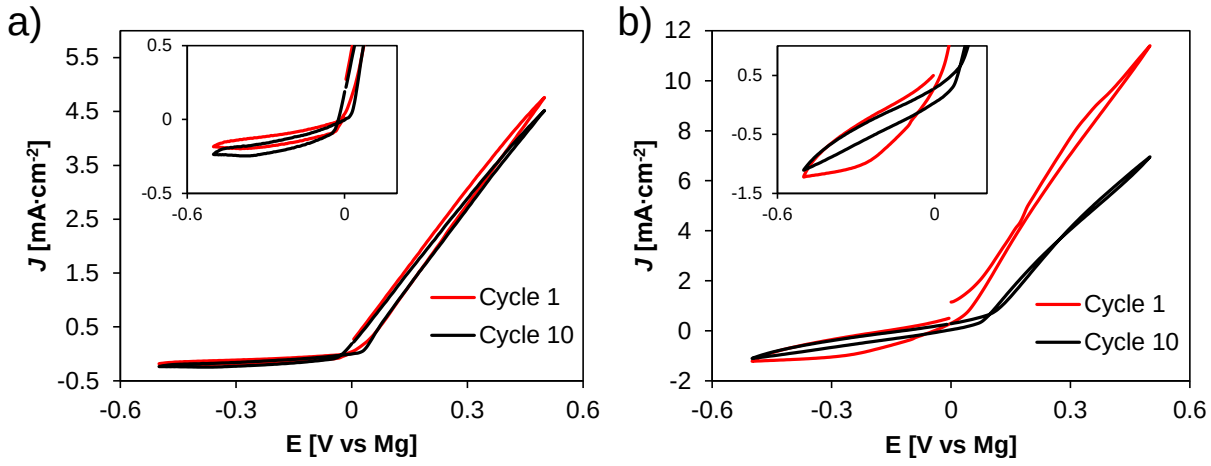

Figure 2.6 Selected cyclic voltammograms of a) 0.12 and b) 0.71 M solutions of **2** in 1:1 THF-CH_3CN in a Mg|Mg|Mg cell, cycling at a rate of 50 $mV{\cdot}s^{-1}$ (insets: expansion of the regions showing Mg plating).

Extended cycling in Mg symmetric cells was studied by galvanostatic plating and stripping experiments in coin cells constructed with Mg on both the anode and cathode sides of the cell separated by a glass fibre separator material soaked in electrolyte. In the

galvanostatic experiment constant currents of ±5 mA·cm^{-2} were applied to the cell for 30 minutes in each direction and the cell potential was measured versus the Mg^0/Mg^{2+} redox coupled. Here, the potential can give a measure of the potential required to plate/strip Mg (overpotential) as well as indicate whether processes such as electrolyte decomposition are occurring at the electrodes based on how symmetric the measured voltages appear during the current cycling. Low overpotentials and plateaus in measured voltages indicate that Mg plating and stripping is the predominant process occurring at the electrodes and symmetric voltage profiles show that the processes are occurring stably and with the same overpotentials on both electrodes throughout cycling.[29] Galvanostatic cycling of symmetric cells containing the 0.71 M electrolyte solution was conducted using either ss-316 or Al as current collectors in the cells (Figure 2.7). These galvanostatic measurements show that the overpotential for both stripping and plating grows steadily over the first 10 hours but stabilizes around 0.6 V, the overpotential remaining constant for more than 250 hours of cycling. The low cell overpotentials as well as the symmetry of the overpotentials observed after the first 10 hours of cycling are consistent with stripping and plating rather than processes dominated by electrolyte decomposition or electrode passivation.

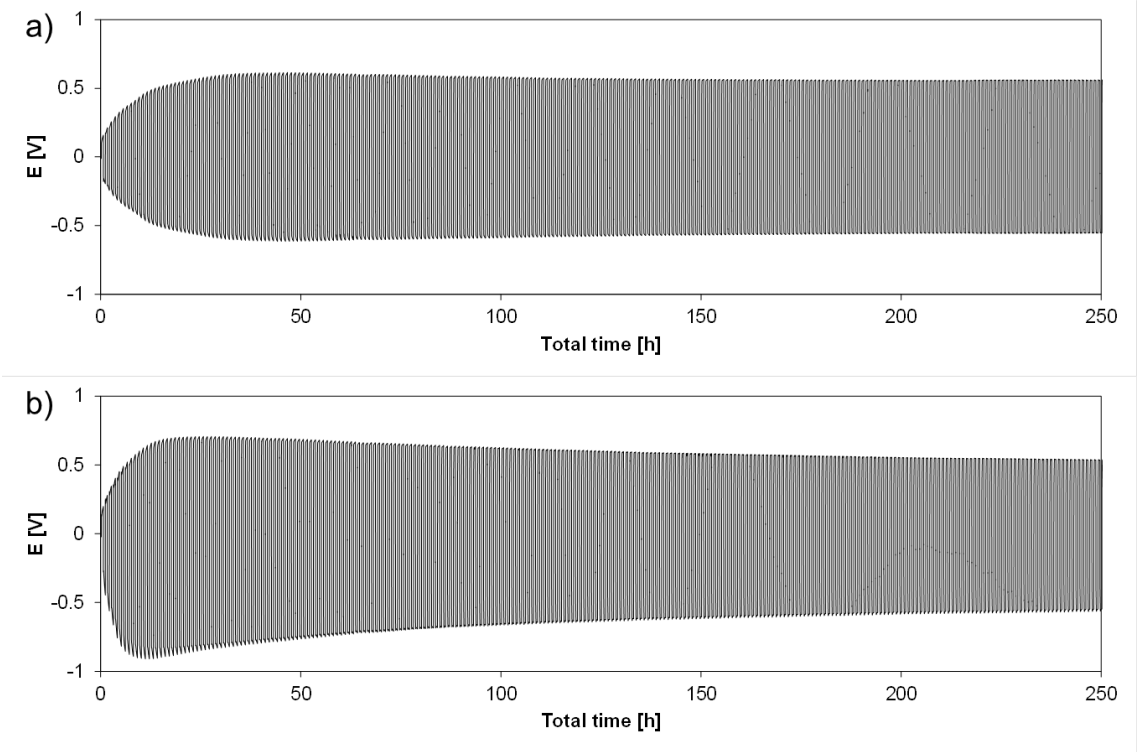

Figure 2.7 Galvanostatic cycling of a Mg symmetric cells containing 0.71 M **2** in 1:1 THF-CH_3CN and using a) ss-316 and b) Al current collectors (anodic and cathodic current densities of 5 mA·cm^{-2} applied for 30 minute periods).

Visual inspection and SEM images of ss-316 current collectors extracted from the Mg symmetric cells discussed above, cycled with 0.71 M solutions of **2** in 1:1 THF-CH_3CN, show large discoloured areas on the surface of the material, features that are not present on pristine ss-316 current collectors (Figures 2.8a-d). These features suggest that some corrosion or electrolyte breakdown has occurred on the ss-316 surface during cycling. Corrosion or electrolyte breakdown resulting in surface passivation is consistent with the LSV measurements shown in Figure 2.5b (above) which shows the attenuation of current density upon subsequent voltammetric sweeps of the ss-316 working electrode.

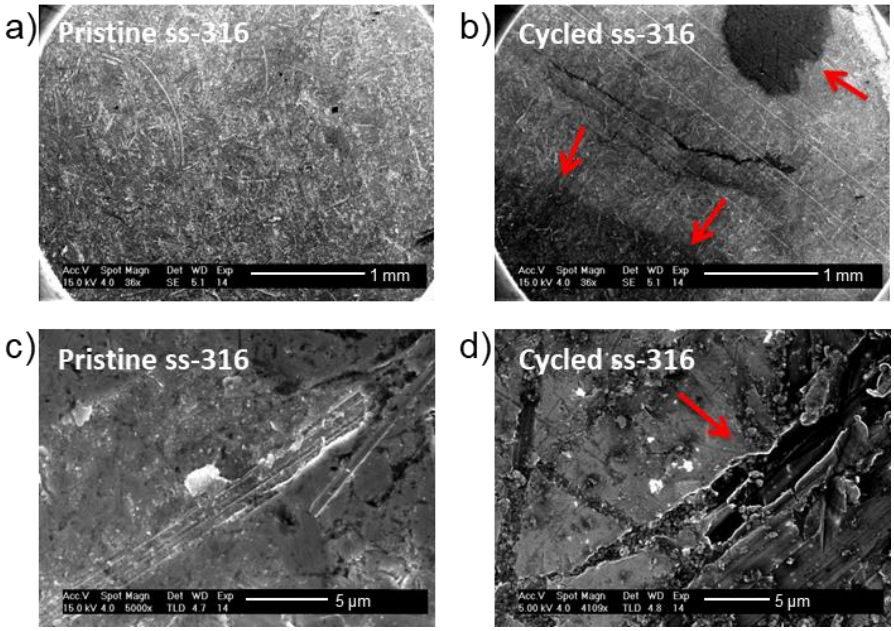

Figure 2.8 Corrosion of ss-316 electrodes cycled with a 0.71 M solution of **2** in 1:1 THF-CH_3CN. a) SEM of the pristine ss-316 current collector and c) a 5000x magnification of the surface. b) SEM of the cycled ss-316 current collector showing large areas of corroded material and d) a 4109x magnification of the corroded area.

SEM images and EDX measurements conducted on Al current collectors taken from the cycled Mg symmetric cell discussed above show much less evidence of corrosion or electrolyte decomposition on the Al surface (Figure 2.9). There are a few isolated areas that display pits in the surface that are rich in F, O, and Fe when compared to the pristine material, possibly resulting from minor reactivity with the electrolyte and corrosion of the ss-316 cell casing during cycling (Figure 2.8c and d). The lack of a significant measureable surface film or electrolyte decomposition products on the Al current collector is consistent with the stability of the electrolyte solution indicated by the LSV measurements displayed in Figure 2.5a.

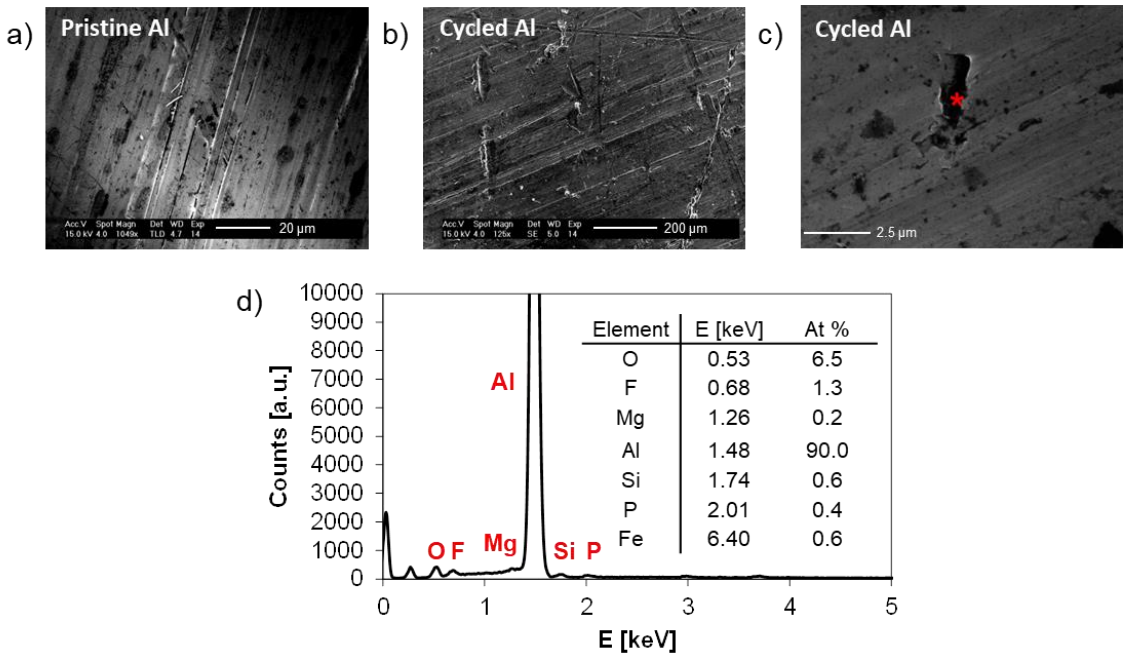

Figure 2.9 SEM images of Al current collectors a) before and b)-c) after being cycled with a 0.71 M solution of **2** in 1:1 THF-CH_3CN and d) EDX analysis of spot shown in red in Figure 2.9c.

SEM images of the Mg metal ribbon taken from these cycled cells, containing both ss-316 and Al current collectors, show the presence of globular masses on the surface of the Mg ribbon (Figure 2.10). These Mg spheres, which appear on the majority of the Mg surface, are a clear indication of Mg plating.[27,30] Additionally, EDX analysis of these spheres show that they are composed almost exclusively of Mg and are not present on the as-prepared Mg electrodes (Figure 2.10f). EDX measurements and element mapping conducted on these large areas of plated Mg exhibit little to no evidence of fluorine being present on the surface, contradicting established wisdom regarding the formation of passivating fluoride-rich films on Mg. Compared to the as-prepared Mg electrodes, the cycled material only shows slightly increased amounts of O and element mapping demonstrates that O is not homogeneously distributed over the surface but isolated to specific regions and could arise from THF decomposition or air exposure during SEM sample preparation (Figure 2.11).

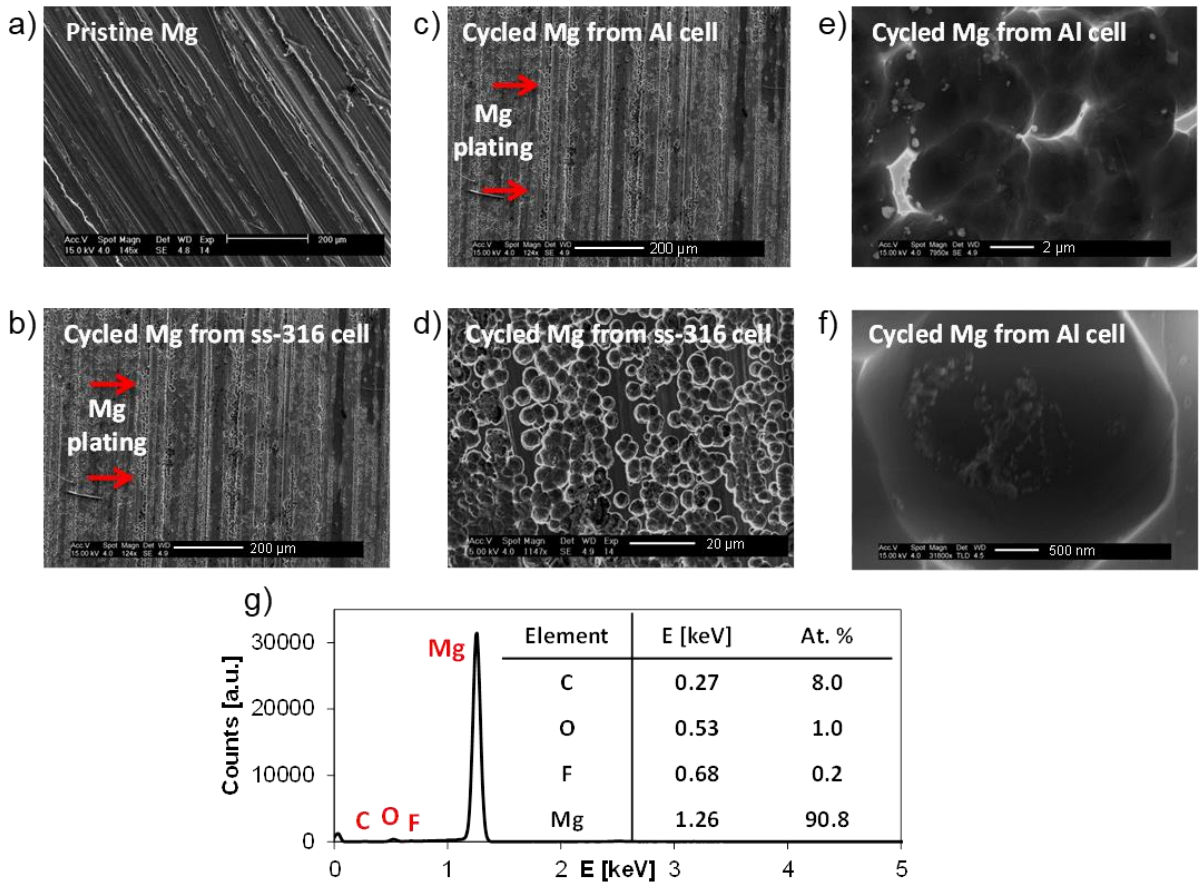

Figure 2.10 Surface analysis of pristine and cycled Mg electrodes. a) SEM of an as-prepared Mg electrode. SEM imaged of Mg electrodes taken from cycled cells containing b) ss-316 and c) Al current collectors showing large areas of Mg deposition. SEM images of cycled Mg electrodes taken from a cell containing d) ss-316 and e) Al current collectors highlighting the globular Mg plating morphology. f) SEM of a single Mg bead deposited on the surface of a Mg electrode cycled with Al current collectors and g) the EDX analysis of the deposited Mg spheres shown in Figure 2.10e.

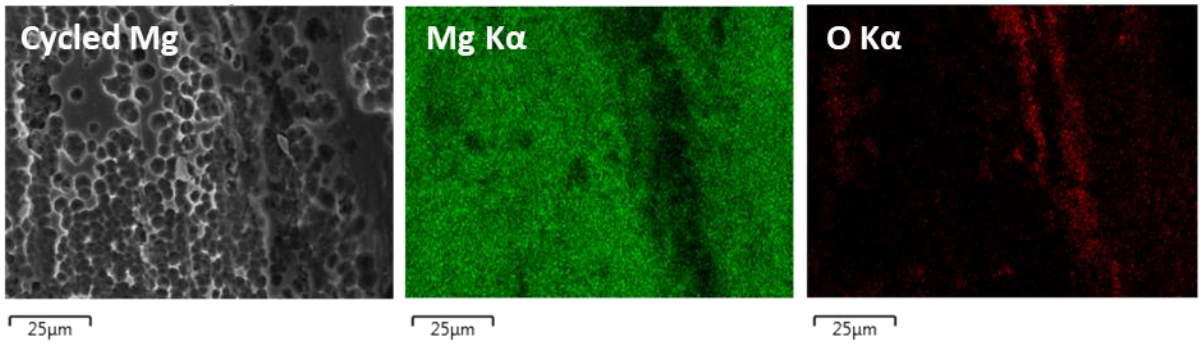

Figure 2.11 SEM image and EDX element mapping of a cycled Mg electrode showing the distribution of Mg and O.

Having demonstrated that the 0.71 M solution of **2** can facilitate the plating and stripping of Mg on Mg electrodes without the formation of a passivating film, the electrolyte solution was employed in coin cells constructed using a Mg anode and a Chevrel (Mo_3S_4) phase cathode. Owing to the observed stability of this electrolyte on Al, current collectors made of Al were employed to limit possible side reactions during battery cycling. The coin

cells, cycled at C/100, showed reversible charge-discharge profiles and could be cycled for at least five cycles reaching a maximum reversible capacity of 51 $mAh \cdot g^{-1}$, roughly half the theoretical capacity of the cell (Figure 2.12). The cell exhibits good capacity retention from cycle two to five and maintains Coulombic efficiencies >90% for these cycles (Figure 2.12b). We note that the measured voltages associated with the two characteristic processes for Mg insertion and removal from the Chevrel phase are associated with overpotentials of >0.4 V, which are likely due to kinetic limitations of both stripping/plating and insertion/removal of Mg^{2+} ions at the positive and negative electrodes, respectively (Figure 2.12a). The observed capacity is similar to that observed for the $LiBH_4/Mg(BH_4)_2$/DME electrolyte (albeit with higher overpotentials),[31] but worse than those typically observed for Al- or B-based electrolytes.[26,32–34] More work is required to explore the role of other solvents beyond CH_3CN and THF to lower the observed overpotentials.

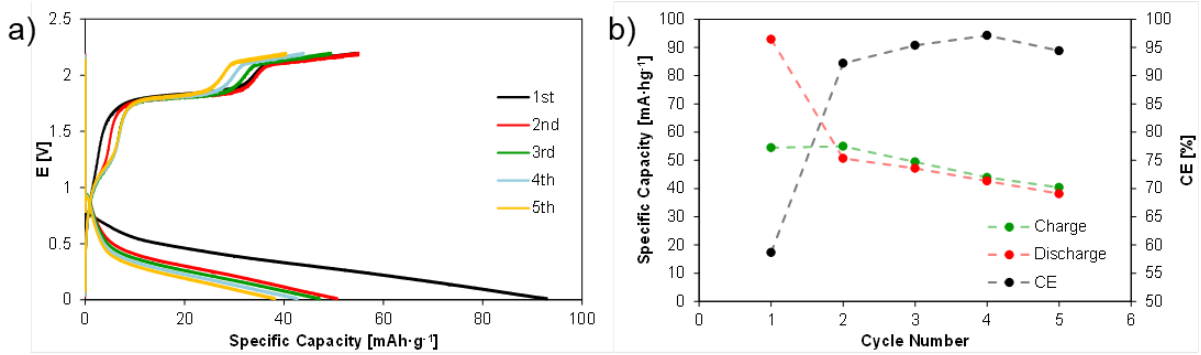

Figure 2.12 Five galvanostatic discharge-charge cycles of a coin cell containing a 0.71 M solution of **2** in 1:1 THF-CH_3CN, a Mg anode, a Chevrel phase cathode, and Al current collectors, cycling at a rate of C/100. a) Cell charge-discharge profiles and b) associated charge/discharge capacities and Coulombic efficiencies.

*2.2.4 Synthesis and Electrochemistry of $Mg(CH_3CN)_6(SbF_6)_2$ (**3**)*[†]

$Mg(CH_3CN)_6(SbF_6)_2$ could be prepared using a similar method to that used for the preparation of **2**. Treatment of Mg metal, activated with a small amount of I_2 in dry CH_3CN, with a solution containing 2 equivalents of $NOSbF_6$ in dry CH_3CN at room temperature resulted in the evolution of a colourless gas (Scheme 2.4). After gas evolution had subsided at room temperature, the reaction mixture was heated to 45 °C and stirred for ca. 18 hours to produce an orange solution. After stirring at 45 °C the CH_3CN was removed *in vacuo* to afford an off-white solid which was then recrystallized twice from hot acetonitrile, affording a white crystalline powder of $Mg(CH_3CN)_6(SbF_6)_2$ (**3**) in 21% yield. We note that the concentration of the reaction has a significant influence on the final outcome of the reaction.

[†]This work was carried out in collaboration with Part III student Ferenc S. Forman.

At concentrations of $NOSbF_6$ in CH_3CN above 0.15 M, large amounts of grey solids are observed to precipitate from the reaction mixture, possibly due to the reduction of SbF_6 to Sb metal upon exposure to fresh Mg metal. However, powder X-ray diffraction analysis was inconclusive in determining the nature of the grey solid.

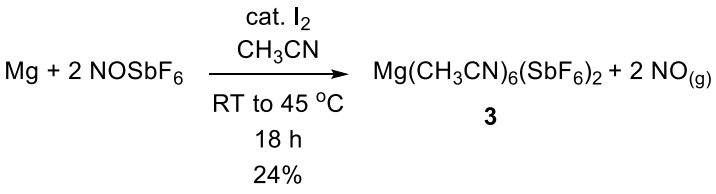

Scheme 2.4 Synthesis of $Mg(CH_3CN)_6(SbF_6)_2$ (**3**) from magnesium metal and $NOSbF_6$.

The ^1H NMR spectrum of **3** in CD_3CN showed a single CH_3CN resonance and the ^{19}F spectrum exhibited a multiplet at $\delta = -120$ ppm, characteristic of the SbF_6^- anion.[35] X-ray analysis of a single crystal obtained from the diffusion of Et_2O in to a CH_3CN solution of **3** confirmed the complex to be the desired $Mg(CH_3CN)_6(PF_6)_2$ salt (Figure 2.13). Lastly, bulk purity of the product was confirmed by elemental analysis which was in good agreement with predicted values (calc'd for $C_{12}H_{18}N_6MgSb_2F_{12}$: C, 19.42; H, 2.44; N, 11.32; found: C, 18.99; H, 2.43; N, 11.39).

Compound **3** could be dissolved in a 1:1 THF-CH_3CN mixture to a concentration of 0.25 M. This electrolyte solution was examined by LSV using Pt, GC, ss-316, Al and Au working electrodes sweeping at a rate of 10 $mV \cdot s^{-1}$ in a three electrode WE|Mg|Mg flooded cell (Figure 2.14). The $Mg(SbF_6)_2$-based electrolyte exhibits onsets of oxidation between 1.2 and 1.5 V vs. Mg on Pt, GC, ss-316, and Au, with the stabilities on Pt and GC lower than the PF_6-based electrolytes by as much 1 V. As with the PF_6-based electrolytes, the SbF_6-based electrolyte exhibits very good stability on Al, with very little current arising up to 4 V vs. Mg.

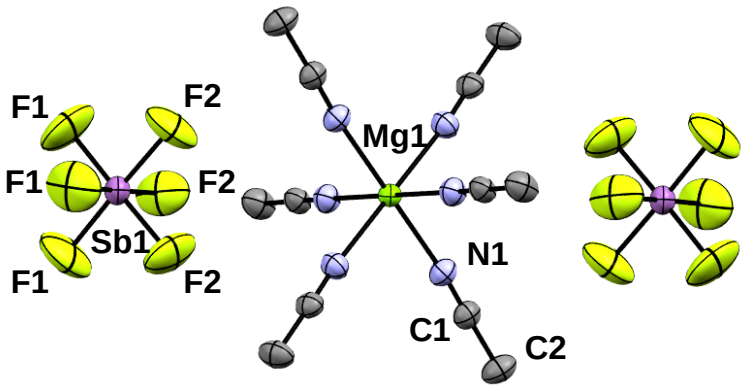

Figure 2.13 Crystal structure of **3**, displaying thermal ellipsoids at 50% probability. Protons have been omitted for clarity (C, grey; N, blue; Sb, purple; F, yellow; Mg, green). Selected bond distances (Å) and angles (°): N1-Mg1, 2.147(3) and 2.148(3); N1-Mg1-N1, 88.06(11)-91.93(11).

Again, this suggests that the Al surface is passivated by the decomposition of the SbF_6^- anion. Other than on the Al electrode, this $Mg(SbF_6)_2$ electrolyte system exhibits relatively poor electrochemical stability compared to many established Mg electrolytes.

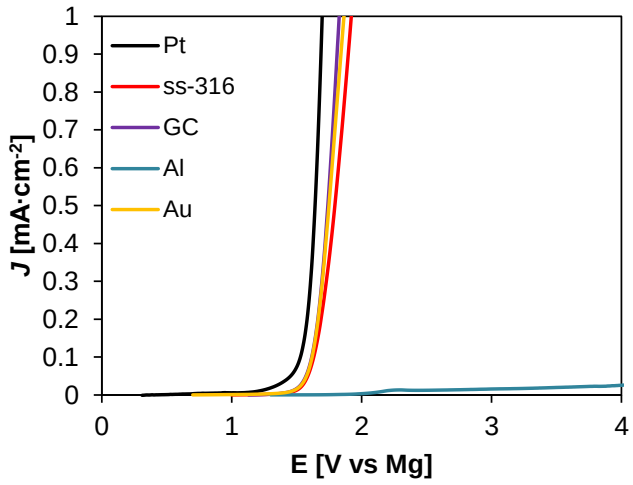

Figure 2.14 LSV of a 0.25 M solution of **3** in 1:1 THF-CH_3CN measured in a WE|Mg|Mg flooded cell, cycling at a rate of 10 $mV \cdot s^{-1}$ on Pt, ss-316, GC, Al, and Au WEs.

Before conducting CV on the 0.25 M solution of **3** in 1:1 THF–CH_3CN, the stability of this mixture on Mg electrodes was examined by galvanostatic cycling in symmetric coin cells. Similar to the galvanostatic cycling experiments described above, the SbF_6-based electrolyte was cycle by passing anodic and cathodic currents of 50 $\mu A \cdot cm^{-2}$, each for a period of 2 hours for a total of 400 hours or 100 cycles (Figure 2.15). Immediately, the symmetric cell exhibited large overpotentials between 1.8 and 2.0 V vs. Mg in response to the applied current, which remained roughly constant and stable for the duration of the experiment (Figure 2.15a). On closer inspection, the measured voltage exhibits two distinct plateaus during both the anodic and cathodic stages which are not typical for Mg symmetric cell cycling (Figure 2.15b). Both the high overpotentials as well as the distinct voltage plateaus indicate that processes additional to Mg plating/stripping are occurring, if plating/stripping is indeed occurring. Yet, the stable nature of the cycling over 400 hours, without a dramatic increase in overpotentials, is not typical of complete electrochemical passivation of the electrode. The origin of the features of the galvanostatic cycling is not understood but it is unlikely that they arise from processes such as Mg alloying with Sb metal plated on the electrode surface as the formation of Mg_3Sb_2 occurs around 0.32 V vs. Mg.[36]

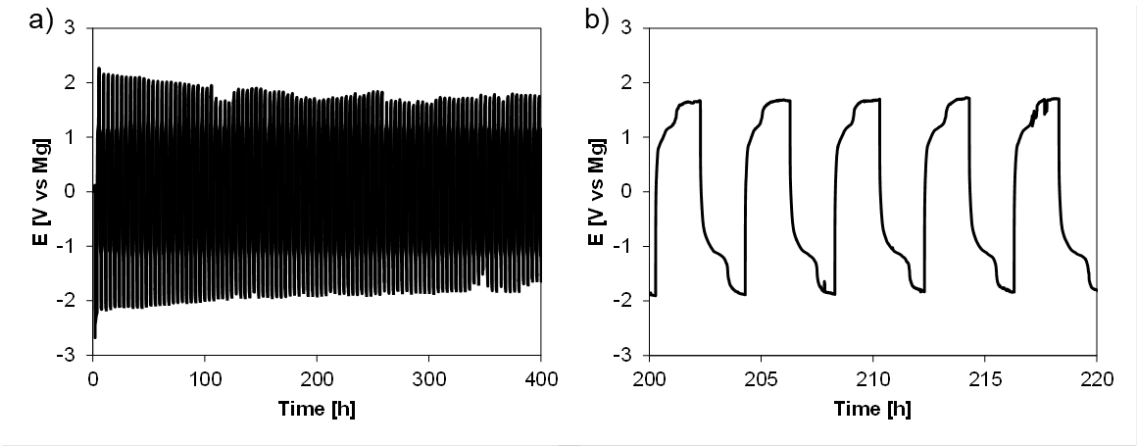

Figure 2.15 Galvanostatic cycling of a Mg symmetric cell containing a 0.25 M solution of **3** in 1:1 THF-CH_3CN (anodic and cathodic currents of 50 $\mu A \cdot cm^{-2}$ applied for 2 hour periods). Expanded region of cycling b) displaying detailed voltage profiles between 200 and 220 hours of cycling.

To investigate this cycling behaviour further, SEM and EDX analysis was conducted on the Mg electrodes taken from the symmetric cell. SEM images of electrode surfaces show large areas of rough morphology, suggesting that the surface is covered in a non-native film (Figure 2.16). This is clear in Figure 2.16b where a film fragment can be seen covering the Mg electrode surface, with the surface remaining relatively unchanged with respect to the as-prepared Mg. These surface coatings were found to be rich in Sb, F, C, O, Ni, and Fe by EDX analysis. The likely origin of the Sb, F, C, and O is from electrolyte decomposition on the electrode while the presence of Ni and Fe could result from corrosion of the stainless steel cell casing. Interestingly, elemental mapping shows that areas rich in Sb and F are not strictly co-localized, indicating that decomposition of the electrolyte affords multiple species rather than a single homogeneous layer (Figure 2.16b). The SEM and EDX data illustrate that the $Mg(SbF_6)_2$-based electrolyte is not stable near Mg plating potentials and large overpotentials observed during galvanostatic cycling likely result in electrolyte decomposition rather than plating/stripping of Mg.

*2.2.5 Synthesis and Electrochemistry of $Mg(CH_3CN)_6(AsF_6)_2$ (**5**)*[†]

Initially, the synthesis of a $Mg(AsF_6)_2$ species using $NOAsF_6$ was impeded by a lack of commercial sources of the nitrosonium salt. Attempts to synthesize $NOAsF_6$ using a modified literature procedure involving metathesis between $NOBF_4$ and $KAsF_6$ in liquid SO_2 in a pressurized vessel were halted by mechanical failure of the reaction vessel.[37]

[†]This work was carried out in collaboration with Part III student Ferenc S. Forman

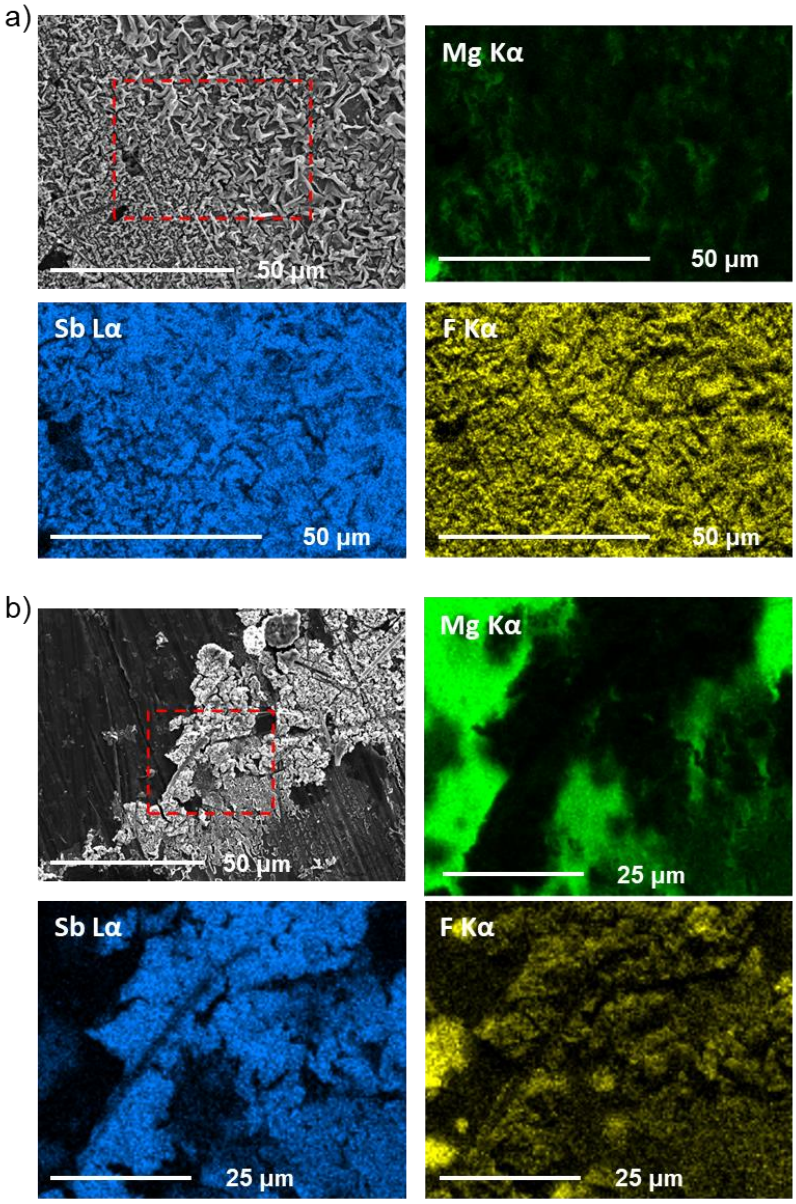

Element	E [keV]	At. %
C	0.28	17.64
O	0.53	9.37
F	0.68	24.43
Mg	1.26	23.29
Si	1.74	1.09
Sb	3.60	13.39
Fe	6.40	2.01
Ni	7.48	8.22

Element	E [keV]	At. %
C	0.28	11.29
O	0.53	6.14
F	0.68	11.29
Mg	1.26	57.55
Si	1.74	0.53
Sb	3.60	7.75
Fe	6.40	2.43
Ni	7.48	3.03

Figure 2.16 SEM and EDX surface analysis of two areas of Mg electrodes extracted from a symmetric cell after galvanostatic cycling in the presence of 0.25 M **3** in 1:1 THF-CH_3CN. EDX element maps and composition taken from the areas highlighted in red boxes.

Accordingly, an alternative metathesis method was investigated. Mixing $KAsF_6$ and either $MgCl_2$ or $MgBr_2$ in dry CH_3CN overnight followed by filtration and evaporation of the filtrates afforded white solids. Low resolution electrospray ionization mass spectrometry (ESI-MS) analysis of these solids showed masses at *m/z* = 135.11, 114.56, 93.64, and 73.36 corresponding to the $Mg(CH_3CN)_6^{2+}$, $Mg(CH_3CN)_5^{2+}$, $Mg(CH_3CN)_4^{2+}$, and $Mg(CH_3CN)_3^{2+}$ complexes, respectively (Figure 2.17). While ESI-MS analysis did not show any evidence of halide contamination in the negative ionization detection mode, positive ion analysis showed contamination of these products by potassium (*m/z* = 38.69). This ESI-MS analysis suggests

that metathesis is incomplete under these conditions and that $KAsF_6$ is carried through in the filtrate together with the $Mg(CH_3CN)_6^{2+}$ salt.

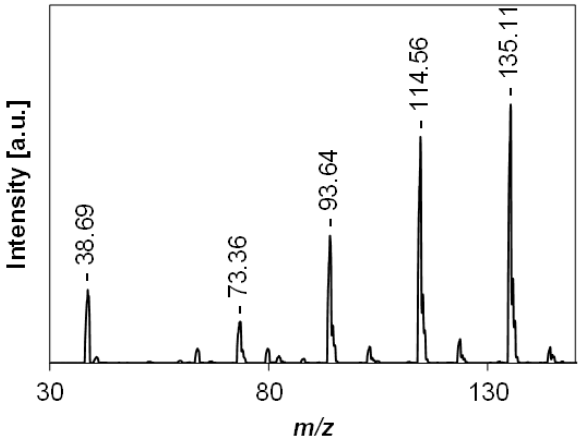

Figure 2.17 Positive low resolution ESI-MS of a $KAsF_6$-$MgBr_2$ metathesis reaction.

In order to avoid metal cation contamination an alternative method, based on the ammonium salt route described above, was explored. First, the ammonium salt Me_3NHAsF_6, **4**, was generated via a metathesis reaction between Me_3NHCl and $KAsF_6$ stirred in CH_3CN for 24 hours (Scheme 2.5). After filtering off the white solids, the filtrate was reduced to dryness and the white solid retrieved was recrystallized from ethanol to afford colourless needles of **4** in 78% yield. Compound **4** could be fully characterized by multinuclear NMR spectroscopy, exhibiting a characteristic N-H resonance at $\delta = 6.98$ ppm in the ^1H domain and a multiplet at $\delta = -66.4$ ppm in the ^{19}F domain. Additionally, the purity of **4** was confirmed by air-free elemental analysis (calc'd for $C_3H_{10}NAsF_6$: C, 14.47; H, 4.05; N, 5.62; found: C, 15.07; H, 4.24; N, 5.68).

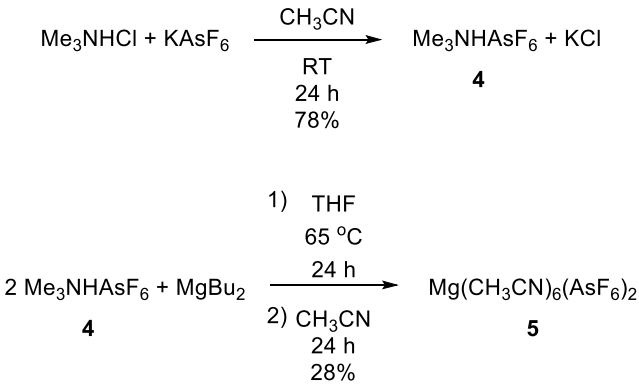

Scheme 2.5 Synthesis of $Mg(CH_3CN)_6(AsF_6)_2$ (**5**) via an ammonium salt route.

Owing to the presence of an acidic N-H proton, **4** could be treated with the basic magnesium organometallic reagent ^{n}Bu^{s}BuMg at 65 °C in dry THF under an inert atmosphere to afford a $Mg(AsF_6)_2$ species. The white solid retrieved from the reaction in THF was washed with hexane, redissolved in dry CH_3CN, and precipitated with dry Et_2O to afford $Mg(CH_3CN)_6(AsF_6)_2$ (**5**) in 28% yield (Scheme 2.5). NMR spectroscopic analysis of **5** displayed only resonances attributed to CH_3CN in the ^{1}H domain and AsF_6^- in the ^{19}F domain. Bulk purity of **5** was confirmed by air-free elemental analysis (calc'd for $C_{12}H_{18}N_6MgAs_2F_{12}$: C, 22.23%; H, 2.80%; N, 12.96%; found: C, 21.42%; H, 2.77%; N, 12.20%). Attempts to isolate single crystals for X-ray analysis by layering Et_2O onto a concentrated CH_3CN solution of **5** were unsuccessful.

Having isolated a pure sample of $Mg(AsF_6)_2$, its electrochemical stability in 1:1 THF-CH_3CN was investigated. LSV was performed on a 0.25 M solution of **5** in 1:1 THF-CH_3CN using Pt, ss-316, GC, Al, and Au working electrodes sweeping at a rate of 10 mV·s^{-1} in a WE|Mg|Mg three electrode flooded cell (Figure 2.18). In general the AsF_6-based electrolyte exhibited higher oxidative stability than the SbF_6 system but similar stability to the PF_6 system, with onsets of oxidation appearing between 1.8 and 2.3 V vs. Mg measured on the Pt, GC, ss-316, and Au electrodes. The AsF_6-based electrolyte solution again exhibits very good electrochemical stability on Al up to 4 V vs. Mg, virtually identical to that measured for the $Mg(PF_6)_2$ and $Mg(SbF_6)_2$ systems.

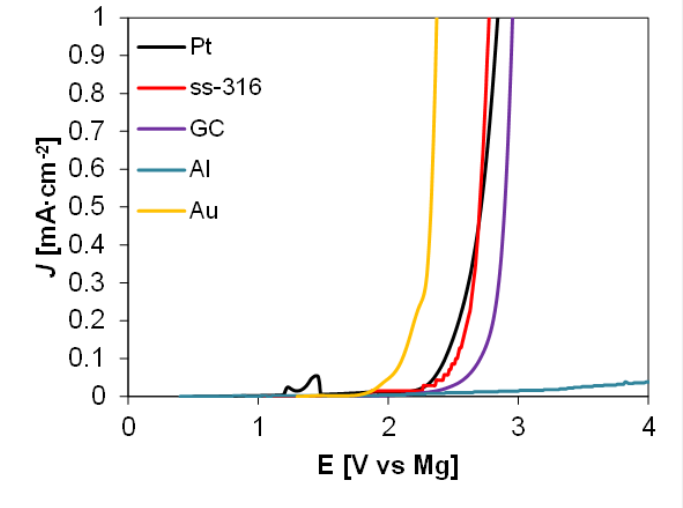

Figure 2.18 LSV of a 0.25 M solution of **5** in 1:1 THF-CH_3CN measured in a WE|Mg|Mg flooded cell, cycling at a rate of 10 mV·s^{-1} on Pt, ss-316, GC, Al, and Au WEs.

To explore the stability of the $Mg(AsF_6)_2$ electrolyte system on Mg electrodes, galvanostatic cycling of a 0.25 M solution of **5** in 1:1 THF-CH_3CN was performed in a Mg symmetric coin cell by applying 5 μA·cm^{-2} anodic and cathodic currents for periods of 2

hours (Figure 2.19). Here we note that smaller currents of 5 $\mu A \cdot cm^{-2}$ were required so as to allow the cell to cycle with reasonable overpotentials; larger currents (10 and 50 $\mu A \cdot cm^{-2}$) gave rise to large overpotentials that rapidly reached the instrument safety cut-off limit. Nonetheless, the cell cycled with lower currents exhibits poor cycling behaviour over the 400 hour (100 cycles) cycling period. During the first 20 hours of cycling large over potentials of −2.8 to −3.3 V and 1.5 to 2.1 V vs. Mg were observed, which likely result from electrolyte decomposition and formation of insulating films. Despite decreasing to between −1.5 and 1.5 V vs. Mg for the remaining cycles, these potentials are still too large to result from the pure plating/stripping of Mg (Figure 2.19a). The variation of these potentials over the cycling period further indicate that stable or reversible processes are not occurring on the Mg electrodes. Owing to this observed instability near Mg plating/stripping potentials, no further experiments using the $Mg(AsF_6)_2$-based electrolyte were carried out.

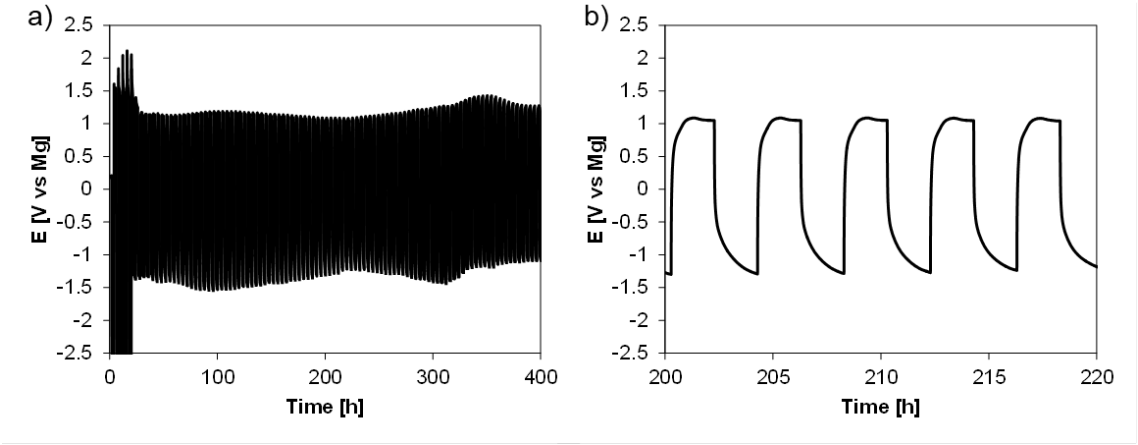

Figure 2.19 Galvanostatic cycling of a Mg symmetric cell containing a 0.25 M solution of **5** in 1:1 THF-CH_3CN (anodic and cathodic currents of 5 $\mu A \cdot cm^{-2}$ applied for 2 hour periods). Expanded region of cycling b) displaying detailed voltage profiles between 200 and 220 hours of cycling.

2.3 Conclusions

In summary, we have for the first time synthesized a $Mg(PF_6)_2$ complex (**2**), providing access to a group 2 complex containing labile CH_3CN ligands and weakly coordinating anions that could be used as a general precursor for the formation of alkaline earth metal catalysts or as a reagent itself.[38,39] Furthermore, we have demonstrated successful plating and stripping of Mg from a $Mg(PF_6)_2$-based electrolyte system. These $Mg(PF_6)_2$-based electrolytes exhibit a large stability window on Al (>4.0 V vs. Mg) and can be cycled on Mg without resulting in any noticeable loss in electrochemical activity of the Mg electrode over at least 10 cycles in flooded CV cells or 250 cycles in Mg symmetric coin cells. LSV and

EDX studies show that these electrolytes react with stainless steel electrodes resulting in corrosion of the electrode surface. Contrary to expectations, SEM and EDX measurements of Mg electrodes taken from cycled symmetric cells show that Mg is plated from $Mg(PF_6)_2$ solutions and that the surface remains electrochemically active after multiple voltammetric cycles as no passivating MgF_2 films are observed to form on the surface of the cycled Mg electrode. Lastly, 0.71 M electrolyte solutions of **2** in 1:1 THF-CH_3CN have been shown to allow the reversible cycling of a coin cell containing a Mg anode, a Chevrel phase cathode, and Al current collectors with a maximum reversible capacity of 51 $mAh \cdot g^{-1}$.

In addition to $Mg(CH_3CN)_6(PF_6)_2$ (**2**), $Mg(CH_3CN)_6(AsF_6)_2$ (**5**) and $Mg(CH_3CN)_6(SbF_6)_2$ (**3**) have also been synthesized using an ammonium salt route and $NOSbF_6$ with Mg metal, respectively. Both compounds can be obtained in high purity and in moderate yields. Again, LSV measurements could be used to investigate the oxidative stability of solutions of **3** and **5** in 1:1 THF-CH_3CN. These LSV measurements showed that the electrolyte based on $Mg(AsF_6)_2$ exhibited higher stability than the SbF_6^- salt on a range of electrodes but similar stabilities to the PF_6^- salt (on Al electrodes both electrolytes exhibited stability up to 4 V vs. Mg). However, galvanostatic cycling of the AsF_6^-- and SbF_6^--based electrolytes in Mg symmetric cells indicated that processes additional to plating/stripping, such as electrolyte decomposition, were occurring on the Mg electrodes. It has been established previously that the heavier hexafluoropnictogenates (i.e. As and Sb) are more susceptible to reduction and are therefore less reductively stable than PF_6^-.[40] This lower reductive stability is thought to result from a decreasing charge density and more polarized E-F bonds, which have a lower antibonding orbital energy that can more easily accept electrons. Decomposition of the electrolyte was confirmed, in the case of the SbF_6^--based electrolyte, by SEM and EDX analysis of the Mg electrodes extracted from the cycled symmetric cell, which showed clear evidence of films on the electrode surface that were rich in Sb, F, and stainless steel corrosion products. The narrower electrochemical stability windows of the $Mg(PnF_6)_2$ systems compared to those of the Et_4N^+ or Li analogues, highlights the importance of electrolyte solvent and its inherent stability. Though previously examined and shown to have wide electrochemical windows, the Et_4NAsF_6 and Et_4NSbF_6 electrolytes comprised carbonate solvents, which could extend the apparent electrochemical stability of these electrolytes through the formation of an insulating and relatively stable SEI. Ultimately, the galvanostatic measurements of **3** and **5** as well as the surface analysis of electrodes extracted from cells cycled with **3** show that Mg electrolytes based on the AsF_6^- and SbF_6^- anions are

not practical for Mg cells employing Mg electrodes as the electrochemical operating voltage of Mg is too reducing for these anions.

2.4 Future Work

One challenge to overcome with these electrolytes is their insolubility in solvents other than CH_3CN or mixtures containing CH_3CN owing to the questionable stability of CH_3CN near 0 V vs. Mg.[41] It has been established that the dinitrile, adiponitrile, is more stable with respect to reduction than CH_3CN.[42] Thus, investigating adiponitrile as an electrolyte solvent for $Mg(PF_6)_2$-based electrolytes may increase the reductive stability of the electrolyte system. However, the bifunctional nature of this solvent may introduce high overpotentials into the cycling of such electrolytes due to the energetically favourable formation of coordination polymers in solution. Alternatively, the new methodology developed for the synthesis of the $Mg(AsF_6)_2$ salt may be applicable more generally to salts such as $Mg(PF_6)_2$ and would allow for its synthesis in solvents other than CH_3CN, such as THF, DME, or glymes. THF, DME, or glyme complexes of $Mg(PF_6)_2$ may be more soluble in non-nitrile solvents and allow this salt to be tested in a greater variety of mixtures. Changing the solvent in such a way may not only influence the stability of the electrolyte systems near 0 V vs. Mg but also influence overpotentials for Mg intercalation into cathode materials. Electrolyte systems employing THF, DME, and glymes have been investigated thoroughly and have been shown to facilitate relatively facile intercalation/de-intercalation of Mg.

2.5 References

1 K. Xu, *Chem. Rev.*, 2004, **104**, 4303–3417.

2 V. Etacheri, R. Marom, R. Elazari, G. Salitra and D. Aurbach, *Energy Environ. Sci.*, 2011, **4**, 3243–3262.

3 K. Ozawa, *Solid State Ionics*, 1994, **69**, 212–221.

4 E. Zinigrad, L. Larush-Asraf, J. S. Gnanaraj, M. Sprecher and D. Aurbach, *Thermochim. Acta*, 2005, **438**, 184–191.

5 T. Kawamura, A. Kimura, M. Egashira, S. Okada and J. I. Yamaki, *J. Power Sources*, 2002, **104**, 260–264.

6 J. B. Goodenough and K. S. Park, *J. Am. Chem. Soc.*, 2013, **135**, 1167.

7 B. Markovsky, F. Amalraj, H. E. Gottlieb, Y. Gofer, S. K. Martha and D. Aurbach, *J. Electrochem. Soc.*, 2010, **157**, A423–A429.

8 D. Guyomard and J. M. Tarascon, *Solid State Ionics*, 1994, **69**, 222–237.

9 M. Ue, M. Takeda, M. Takehara and S. Mori, *J. Electrochem. Soc.*, 1997, **144**, 2684–2688.

10 M. Ue and S. Mori, *J. Electrochem. Soc.*, 1995, **142**, 2577–2581.

11 Z. Lu, A. Schechter, M. Moshkovich and D. Aurbach, *J. Electroanal. Chem.*, 1999, **466**, 203–217.

12 J. Muldoon, C. B. Bucur, A. G. Oliver, J. Zajicek, G. D. Allred and W. C. Boggess, *Energy Environ. Sci.*, 2013, **6**, 482–487.

13 D. R. Armstrong, A. H. Khandelwal, L. C. Kerr, S. Peasey, P. R. Raithby, G. P. Shields, R. Snaith and D. S. Wright, *Chem. Commun.*, 1998, 1011–1012.

14 T. Steiner, *Angew. Chem. Int. Ed.*, 2002, **41**, 48–76.

15 C. Glidewell and H. D. Holden, *Acta Crystallogr.*, 1982, **B38**, 667–669.

16 J. V. Brencic, B. Ceh and I. Leban, *Z. Anorg. Allg. Chem.*, 1987, **549**, 233–239.

17 F. A. Mautner and M. A. S. Goher, *Polyhedron*, 1999, **18**, 553–559.

18 D. Braga, S. L. Giaffreda, F. Grepioni, G. Palladino and M. Polito, *New J. Chem.*, 2008, **32**, 820–828.

19 R. Santra, N. Ghosh and K. Biradha, *New J. Chem.*, 2008, **32**, 1673–1676.

20 W. Clegg, L. Dunbar, L. Horsburgh and R. E. Mulvey, *Angew. Chem. Int. Ed.*, 1996, **35**, 753–755.

21 W. S. Sheldrick, *J. Chem. Soc., Dalt.*, 1974, 1402–1405.

22 R. A. Heintz, J. A. Smith, P. S. Szalay, A. Weisgerber and K. R. Dunbar, in *Inorganic Syntheses*, eds. K. Beck and D. Coucouvanis, John Wiley & Sons, Inc., 2002, vol. 33, pp. 75–121.

23 J. K. Clegg, J. Cremers, A. J. Hogben, B. Breiner, M. M. J. Smulders, J. D. Thoburn and J. R. Nitschke, *Chem. Sci.*, 2013, **4**, 68–76.

24 C. O. Laoire, S. Mukerjee, K. M. Abraham, E. J. Plichta and M. A. Hendrickson, *J. Phys. Chem. C*, 2010, **114**, 9178–9186.

25 D. M. Seo, O. Borodin, D. Balogh, M. O'Connell, Q. Ly, S.-D. Han, S. Passerini and W. A. Henderson, *J. Electrochem. Soc.*, 2013, **160**, A1061–A1070.

26 T. Liu, Y. Shao, G. Li, M. Gu, J. Hu, S. Xu, Z. Nie, X. Chen, C. Wang and J. Liu, *J. Mater. Chem. A*, 2014, **2**, 3430–3438.

27 S. Ha, Y. Lee, S. W. Woo, B. Koo, J. Kim, J. Cho, K. T. Lee and N. Choi, *ACS Appl. Mater. Interfaces*, 2014, **6**, 4063–4073.

28 J. Muldoon, C. B. Bucur, A. G. Oliver, T. Sugimoto, M. Matsui, H. S. Kim, G. D. Allred, J. Zajicek and Y. Kotani, *Energy Environ. Sci.*, 2012, **5**, 5941–5950.

29 W. Li, S. Cheng, J. Wang, Y. Qiu, Z. Zheng, H. Lin, S. Nanda, Q. Ma, Y. Xu, F. Ye, M. Liu, L. Zhou and Y. Zhang, *Angew. Chem. Int. Ed.*, 2016, **55**, 6406–6410.

30 M. Matsui, *J. Power Sources*, 2011, **196**, 7048–7055.

31 R. Mohtadi, M. Matsui, T. S. Arthur and S. J. Hwang, *Angew. Chem. Int. Ed.*, 2012, **51**, 9780–9783.

32 D. Aurbach, Z. Lu, A. Schechter, Y. Gofer, H. Gizbar, R. Turgeman, Y. Cohen, M. Moshkovich and E. Levi, *Nature*, 2000, **407**, 724–727.

33 R. E. Doe, R. Han, J. Hwang, A. J. Gmitter, I. Shterenberg, H. D. Yoo, N. Pour and D. Aurbach, *Chem. Commun.*, 2014, **50**, 243–245.

34 Y. Guo, F. Zhang, J. Yang, F. Wang, Y. NuLi and S. Hirano, *Energy Environ. Sci.*, 2012, **5**, 9100–9106.

35 A. Decken, E. G. Ilyin, H. Donald, B. Jenkins, G. B. Nikiforov and J. Passmore, *Dalt. Trans.*, 2005, 3039–3050.

36 T. S. Arthur, N. Singh and M. Matsui, *Electrochem. Commun.*, 2012, **16**, 103–106.

37 T. A. Engesser, C. Friedmann, A. Martens, D. Kratzert, P. J. Malinowski and I. Krossing, *Chem. Eur. J.*, 2016, **22**, 15085–15095.

38 R. Rochat, M. J. Lopez, H. Tsurugi and K. Mashima, *ChemCatChem*, 2016, **8**, 10–20.

39 M. S. Hill, D. J. Liptrot and C. Weetman, *Chem. Soc. Rev.*, 2016, **45**, 972–988.

40 C. Nanjundiah, J. L. Goldman, L. A. Dominey and V. R. Koch, *J. Electrochem. Soc.*, 1988, **135**, 2914–2917.

41 T. T. Tran, W. M. Lamanna and M. N. Obrovac, *J. Electrochem. Soc.*, 2012, **159**, A2005–A2009.

42 G. T. Cheek, *ECS Trans.*, 2014, **58**, 45–51.

3. Synthesis of $Ca(PF_6)_2$, Formed via Nitrosonium Oxidation of Calcium

3.1 Introduction

Alternative battery technologies to Li-ion systems have been the focus of considerable interest in recent years as they present the possibility of achieving higher electron storage capacities, reducing the risk of thermal runaway, and utilizing less expensive and more Earth-abundant elements as transport ions.[1,2] Among these alternative battery technologies (including Na-, Mg-, and Al-ion), development of rechargeable Ca-ion batteries has been largely neglected due to a lack of effective Ca-ion electrolyte systems and poorly understood electrochemistry. In addition to being the fifth most Earth-abundant element, Ca has a theoretical anode-based capacity of 2073 $mAh \cdot cm^{-3}$ and a reduction potential only 0.17 V higher than Li, making it an attractive multivalent ion for the construction of high-voltage batteries.[3] Furthermore, the large ionic radius of Ca^{2+} ion (1.14 Å), and thus lower charge density with respect to Mg^{2+} and Al^{3+}, could permit faster solid-state diffusion into electrode materials, in electrodes with appropriately sized voids within the structure, an issue that has limited the construction of efficient Mg-ion batteries so far.[3]

The electrochemical behaviour of the Ca-based electrolyte $Ca(AlCl_4)_2$ has been studied in primary cells in $SOCl_2$ using a Ca anode, but rapid passivation or corrosion of the electrodes was observed.[4] Early electrochemical studies of Ca salts in organic solvents identified $Ca(BF_4)_2$ in THF or *N*-methylpyrrolidone as a potential Ca-ion electrolyte candidate due to the stability of the salt towards reduction by Ca anodes.[5] It was not until 2015 that Palacín and co-workers demonstrated the reversible stripping and plating of Ca (over 30 cycles) using electrolytes based on $Ca(BF_4)_2$ and $Ca(ClO_4)_2$.[6] Additionally, $Ca(PF_6)_2$-based electrolytes have been investigated by Ingram and co-workers using manganese hexacyanoferrate-derived cathode materials.[7] These systems exhibited high electrochemical stability and reversible charge/discharge profiles over tens of cycles. Further work on $Ca(PF_6)_2$, in which the salt is dissolved in carbonate solvents, has been conducted by Cheng and co-workers who have developed Ca cells using an Ca-alloying anode and a PF_6^- intercalation cathode.[8] These cells exhibit high operating voltages of 4.45 V and exceptional stability, retaining 95% of the initial capacity over 350 cycles. The reversible electrochemistry and large stability

window (>4.5 V) exhibited by these electrolytes could ultimately lead to the development of competitive rechargeable Ca-ion batteries, given effective Ca cathode materials, although multiple challenges remain. While the aforementioned systems are promising, Ca electrochemistry remains underdeveloped compared to that of Li and even Mg. In particular, very few Ca electrolytes have been studied for their ability to function in electrochemical cells and consequently, the behaviour of potential Ca anode and cathode materials is limited, generally.

Motivated by the success of the electrolytes based on $Ca(BF_4)_2$ and $Ca(PF_6)_2$, we aimed to investigate the formation of $Ca(PF_6)_2$ using a direct anhydrous synthesis developed by our group for the formation of $Mg(PF_6)_2$ (Scheme 3.1).[9] This approach avoids the multiple drying stages required in established preparations of $Ca(BF_4)_2$ and avoids salt metathesis methods employed to prepare $Ca(PF_6)_2$ previously from $AgPF_6$ and $CaCl_2$ in CH_3CN.[7] Such metathesis routes can afford materials that are contaminated with chloride (introducing the possibility of cell corrosion) or other materials resulting from incomplete metathesis.[10,11]

$$M + 2\ NOPF_6 \xrightarrow{L} M(PF_6)_2(L)_n + 2\ NO_{(g)}$$

L = solvent/ligand

Scheme 3.1 Synthesis of Group 2 $M(PF_6)_2(L)_n$ complexes using $NOPF_6$, where M = Mg or Ca.

3.2 Results and Discussion

Having previously reported the isolation of anhydrous $Mg(PF_6)_2(CH_3CN)_6$ through the reaction of Mg metal with $NOPF_6$,[9] preparation of the analogous $Ca(PF_6)_2$ salt was attempted by treating Ca filings with two equivalents of $NOPF_6$ in dry CH_3CN. We found, however, that $Ca(PF_6)_2$ was much more sensitive to decomposition than the Mg analogue, potential sources of oxygen including trace amounts of air and impurities such as CaO. Under inert atmosphere and using freshly distilled CH_3CN, the reaction of Ca with $NOPF_6$ afforded a yellow solution as well as a white precipitate, which could be removed by cannula filtration. Following filtration, the solution was reduced to dryness and the solid was redissolved in a minimum amount of dry CH_3CN. X-ray crystallographic analysis of colorless crystals grown from the saturated CH_3CN solution identified the product as the coordination polymer **6**, composed of repeating $Ca(PO_2F_2)(PF_6)(CH_3CN)_4$ units, obtained in 58% yield (Figure 3.1). The monomer unit of **6** shows a tetrahedral $PO_2F_2^-$ anion, chelating the central Ca^{2+} ion through the oxygen atoms (O1-Ca and O2-Ca bond lengths, 2.600(5) and 2.816(6)

Å), forming CaOPO four-membered rings. Four molecules of CH_3CN occupy the remaining coordination sites on Ca^{2+}, with PF_6^- remaining ion-separated in the lattice. Both of the oxygen atoms of the $PO_2F_2^-$ anion act to bridge the Ca monomer units (in addition to chelating each Ca^{2+}), resulting in a polymeric structure (bridging O1-Ca and O2-Ca bond lengths, 2.340(5) and 2.295(6) Å) and forming CaOCaO four-membered rings.

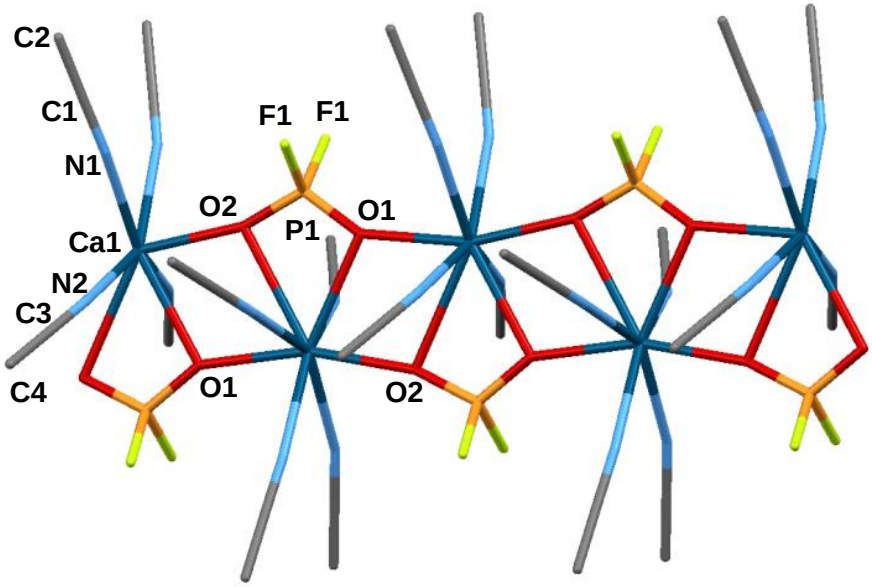

Figure 3.1 Crystal structure of **6** showing several $Ca(PO_2F_2)(CH_3CN)_4$ repeat units. Protons and PF_6^- anions have been omitted for clarity (Ca, dark blue; C, grey; F, yellow; N, light blue; O, red; P, orange). Selected bond distances (Å) and angles (°): O1-Ca1 2.601(5), O1-Ca1 2.340(5), O2-Ca1 2.816(6), O2-Ca1 2.295(6), Ca1-O1-Ca1 111.9(2), Ca1-O2-Ca1 106.1(2), O1-Ca1-O2 54.31(13), O2-Ca1-O1 73.37(18). Structure displayed as a wireframe structure for clarity.

Solution-state ^{19}F and ^{31}P NMR spectra of **6** at room temperature are consistent with the presence of $PO_2F_2^-$, a known PF_6^- hydrolysis product, and PF_6^- anions.[12,13] The ^{19}F NMR spectrum contains two doublets at δ = −86.7 ($^1J_{PF}$ = 929.0 Hz) and −73.0 ($^1J_{PF}$ = 706.4 Hz) ppm and the ^{31}P NMR spectrum contains a triplet at δ = −22.2 ppm ($^1J_{PF}$ = 933.3 Hz) and a heptet at δ = −144.6 ppm ($^1J_{PF}$ = 706.3 Hz), in both cases corresponding to the $PO_2F_2^-$ and PF_6^- anions, respectively. Whether **6** remains polymeric in solution is unknown but, based on the sharp ^{19}F and ^{31}P NMR resonances and the solubility of the complex in organic solvents, it is likely that oligomeric complexes are generated when dissolved in CD_3CN.

In contrast to the relative stability of $Mg(PF_6)_2(CH_3CN)_6$, which is isolated under identical conditions to **6**, decomposition of the PF_6^- anion is more facile in the case of the Ca analogue. To eliminate the possibility that the Ca^{2+} ion was accelerating this conversion of PF_6^-, 15-crown-5 was added to the reaction with the purpose of limiting Ca-F interactions by

occupying coordination sites on Ca^{2+}.[14] The ^{19}F and ^{31}P NMR spectra of the material obtained from the reaction of Ca with $NOPF_6$ in the presence of 15-crown-5 (ca. 1 equiv.) were found to be free of signals attributable to the $PO_2F_2^-$ anion. Crystals of a Ca⊂(15-crown-5)$(PF_6)_2$ species (**7**) were obtained in a yield of 41% by layering dry Et_2O onto a concentrated CH_3CN solution shows the structure of the product. X-ray crystallographic analysis showed the structure of **7**, which consists of two distinct Ca centres: [Ca⊂(15-crown-5)$(CH_3CN)_3$]$(PF_6)_2$ and [Ca⊂(15-crown-5)$_2$]$^{2+}(PF_6)_2$ (Figure 3.2). Once again, no $PO_2F_2^-$ was observed by ^{19}F NMR spectroscopic analysis of the material after crystallization. The bulk purity of this sample was confirmed by elemental analysis [calc'd for $C_{36}H_{69}Ca_2F_{24}N_3O_{15}P_4$ (**7**): C, 29.95; H, 4.82; N, 2.91; P, 8.58; found: C, 28.81; H, 4.83; N, 3.01; P, 8.86].

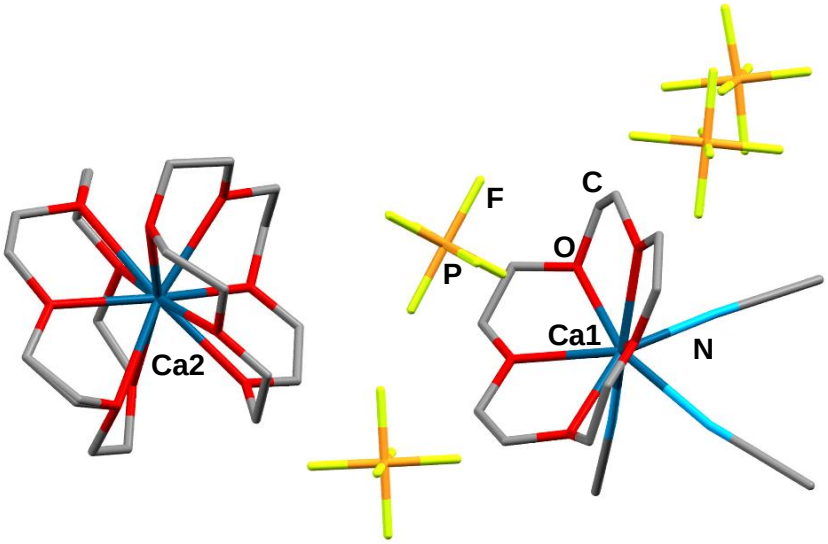

Figure 3.2 Crystal structure of **7**. Protons and disorder have been omitted for clarity (Ca, dark blue; C, grey; F, yellow; N, light blue; O, red; P, orange). Structure displayed as a wireframe structure for clarity.

On one occasion single crystal X-ray analysis of a crystal retrieved from the 15-crown-5 reaction mixture described above identified a Ca complex, [(Ca⊂15-crown-5)$_4$$(SiF_6)_2$$(CH_3CN)_2$]$(PF_6)_4$ (**8**), containing SiF_6^{2-} anions. Originally thought to be an example of Ca$(PF_6)_2$, it was later discovered that the structure in fact contains bridging SiF_6^{2-} anions, likely formed through etching of the glassware by HF (generated by decomposition of the PF_6^- anions) (Figure 3.3).[15] ^{19}F NMR spectroscopic analysis of the bulk crystalline material in CD_3CN did not show evidence of $PO_2F_2^-$ or SiF_6^{2-}, suggesting that the crystal analysed by diffraction represents only a very minor component of the product. However, the presence of SiF_6^{2-} in this sample does suggest that some decomposition of PF_6^- has occurred. In this structure, the four Ca^{2+} ions in the cation are each capped on one 'face' by a 15-crown-5

ligand with the two SiF_6^{2-} anions bridging the four metal ions together using five of the six F atoms. The SiF_6^{2-} anions exhibit two bonding modes, bonding with two Ca^{2+} via two κ^2-interactions (F3/F5-Ca1 and F2/F6-Ca2 range, 2.312(2)-2.368(3) Å) and forming the macrocyclic arrangement via a further κ^1-interaction (F4-Ca1, 2.283(2) Å). SiF_6^{2-} is known to form strong interactions with sodium in an extended lattice;[16] however, only a small number of molecular compounds are known that contain SiF_6^{2-}-metal interactions. In addition to this newly established Ca example, molecular complexes involving SiF_6-metal interactions have only been reported for Na(I),[16] Ag(I),[17,18] Cu(II),[19] and Zn(II).[20] These complexes exhibit a range of SiF_6^{2-} binding modes, from κ^1- to κ^3-interactions, with F-metal bond lengths ranging from 2.107(1)-2.542(2) Å.

Solutions of **7** in wet 'bench-top' CH_3CN and Et_2O and/or under ambient atmosphere result in the formation of only minor amounts of $PO_2F_2^-$, as determined by monitoring the ^{31}P and ^{19}F NMR spectra at various stages of the reaction. In contrast, similar solutions of the reported $Ca(PF_6)_2$,[7] not stabilized by a crown ether, result in significant PF_6^- hydrolysis to $PO_2F_2^-$ and PO_3F^{2-} over a 20 hour period (Figure 3.4a).[13] Treatment of this $Ca(PF_6)_2$ species (**7**) with two equivalents of 15-crown-5 significantly limits conversion of PF_6^- to $PO_2F_2^-$ over a 60 hour period in bench-top solvent, supporting the proposed role of the crown ether in hindering PF_6^- decomposition in our system (Figure 3.4b).

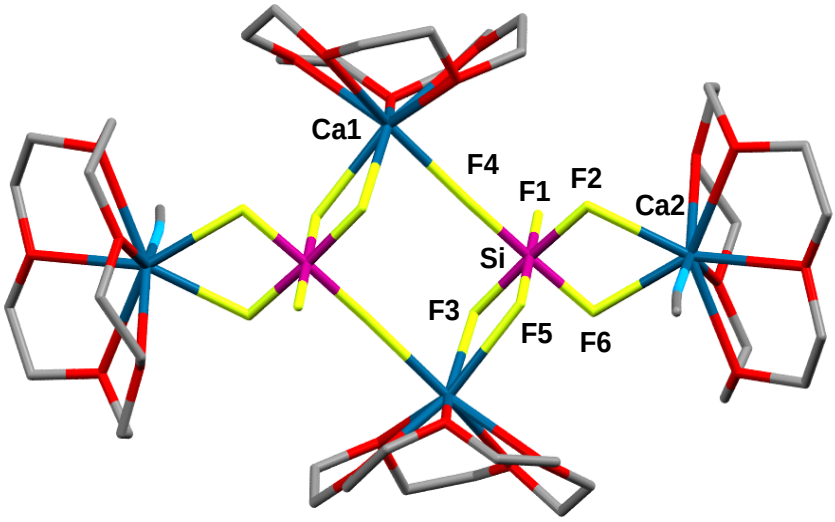

Figure 3.3 The cation of **8**, showing the bridging and chelating bonding modes of the SiF_6^{2-} anions in the $[(Ca\subset 15\text{-crown-}5)_4(SiF_6)_2(MeCN)_2]^{4+}$ cation. Protons, ion separated PF_6^- anions, and solvent molecules have been omitted for clarity (Ca, dark blue; C, grey; F, yellow; N, light blue; O, red; Si, purple). Selected bond distances (Å) and angles (°): F4-Ca1 2.283(2), F5-Ca1 2.346(3), F3-Ca1 2.368(3), F6-Ca2 2.350(2), F2-Ca2 2.312(2), F5-Ca1-F3 58.82(8), Si-F4-Ca1 175.7(2), F6-Ca2-F2 60.30(9). Structure displayed as a wireframe structure for clarity.

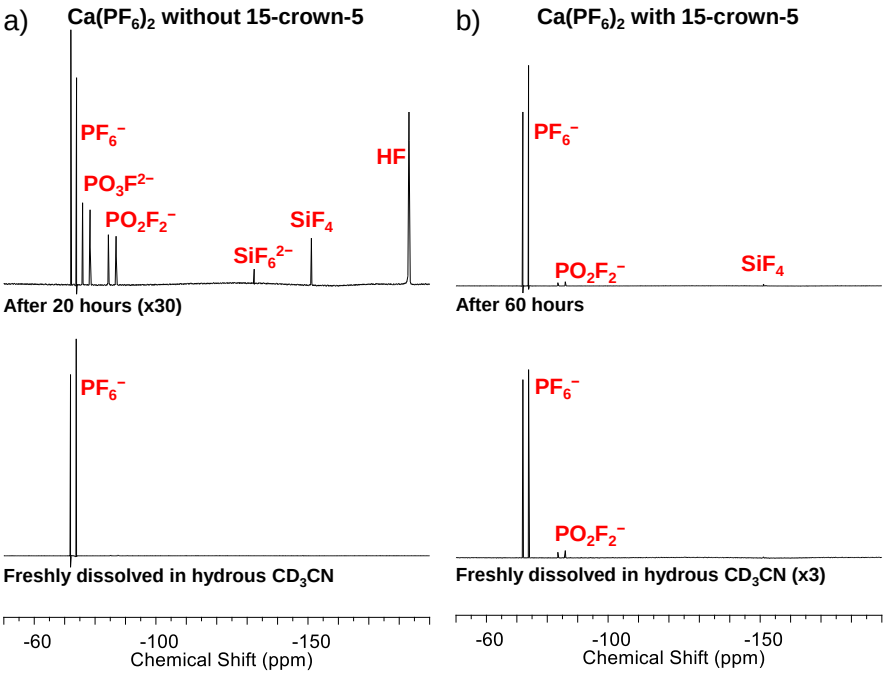

Figure 3.4 ^{19}F NMR (376 MHz, 298 K, CD_3CN) spectroscopic analysis of $Ca(PF_6)_2$ hydrolysis in a) the absence of and b) the presence of 2 equivalents of 15-crown-5 (bottom spectra: $Ca(PF_6)_2$ species freshly exposed to hydrous CH_3CN; top spectra: sample after prolonged exposure to hydrous CD_3CN). Values contained in parentheses represent intensity multiplication factors. Note: Si species are likely generated through HF etching of the glassware.

As the presence of the crown ether permitted the isolation of $Ca(PF_6)_2$ complex **7** under inert conditions and stabilized it toward hydrolysis, we were interested in the extent to which the crown ether ligands influenced the stability of the complex with respect to other decomposition pathways. The reaction of $NOPF_6$ (2 equiv.) with Ca metal in the presence of 15-crown-5 (ca. 1 equiv.) in CH_3CN which was exposed to moist air throughout the reaction period by way of a needle open to the atmosphere, produced a yellow solution along with a white solid. The ^{19}F and ^{31}P NMR spectra of the isolated yellow solution exhibited resonances attributable to both $PO_2F_2^-$ and PF_6^- anions. The same reactivity was observed for analogous reactions of $NOPF_6$ and Ca in the presence of excess 18-crown-6. Colorless crystals of the 18-crown-6 product, $[(Ca\subset 18\text{-crown-6})(PO_2F_2)(PF_6)]_n$ (**9**), could be obtained in 15% yield by layering saturated CH_3CN solutions of the crude solid residue with dry Et_2O. Single crystal X-ray analysis of **9** shows a polymeric structure containing $[(Ca\subset 18\text{-crown-6})(PO_2F_2)(PF_6)]$ units bridged by κ^1-interactions of the two O-atoms of the $PO_2F_2^-$ anions (O1-Ca and O2-Ca, 2.267(7) and 2.282(7) Å; Figure 3.5). In the 18-crown-6 example, the crown ether binds to Ca in an equatorial fashion whereas the 15-crown-5 examples adopt a

facial-type coordination mode. The nature of **9** in solution is not definitively known but, again, the sharp ^{19}F and ^{31}P NMR resonances suggest an oligomeric species. The bulk purity of the sample was confirmed by elemental analysis [calc'd for $C_{12}H_{24}CaF_8O_8P_2$ (**9**): C, 26.19; H, 4.40; N, 0.00; found: C, 26.09; H, 4.33; N, 0.00].

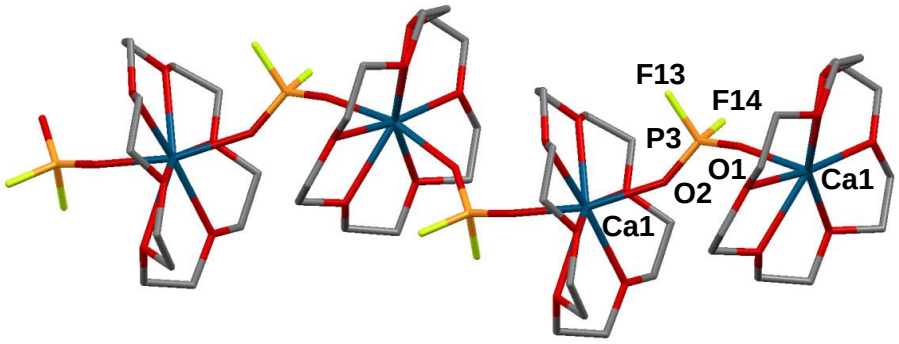

Figure 3.5 Crystal structure of the $PO_2F_2^-$-containing Ca⊂(18-crown-6) coordination polymer **9**. Protons, ion separated PF_6^- anions, and disorder have been omitted for clarity (Ca, dark blue; C, grey; F, yellow; N, light blue; O, red; P, orange). Selected bond distances (Å) and angles (°): Ca1-O1 2.267(7), Ca1-O2 2.282(7), O1-P3-O2 122.3(4), O1-Ca1-O2 164.5(3). Structure displayed as a wireframe structure for clarity.

Accordingly, we believe that $PO_2F_2^-$ does not result solely from the hydrolysis of PF_6^- in all cases. This is based on the formation of **6** (in 58% yield) under inert conditions as well as the formation of **9** in the presence of 18-crown-6, which contradicts NMR experiments described above in which crown ether-containing systems did not show appreciable formation of $PO_2F_2^-$ (observations summarized in Scheme 3.2). It is possible that NO or NO_2 (generated from NO and O_2) participate in the decomposition of the PF_6^- anion by acting as oxidants. One potential pathway could involve the generation of CaO on the activated Ca surface which subsequently reacts with the PF_6^- anion to form PO-containing compounds along with CaF_2. However, the exact mechanism of decomposition, as well as the species involved, is not yet fully understood.

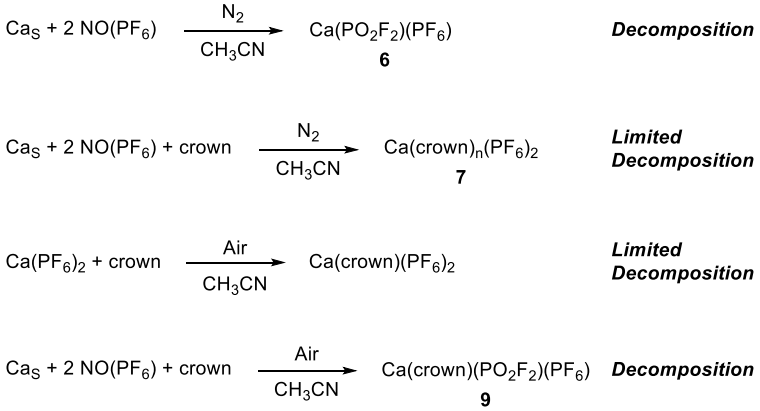

Scheme 3.2 Summary of reactions and observations involving $Ca(PF_6)_2$.

Solid-state NMR spectroscopic analysis[†] of residues taken from reaction mixtures containing 15-crown-5 that were exposed to air exhibits signals corresponding to CaF_2 in the ^{19}F domain ($\delta = -108$ ppm, Figure 3.6), confirming the generation of calcium fluoride in these systems (eq. 1). Interestingly, a new species, $[(15\text{-crown-}5)_3(Ca_4F_4)(PF_6)](PF_6)_3$ (**10**), can be identified in the solid-state ^{19}F NMR spectrum as well as by *in situ* solution-state NMR spectroscopic measurements conducted during air exposure of the mixtures containing Ca, $NOPF_6$ and 15-crown-5 in CH_3CN (Figure 3.6). A resonance attributed to this new species appears as a broad peak centred around $\delta = -98$ ppm in the solid-state ^{19}F NMR spectrum.

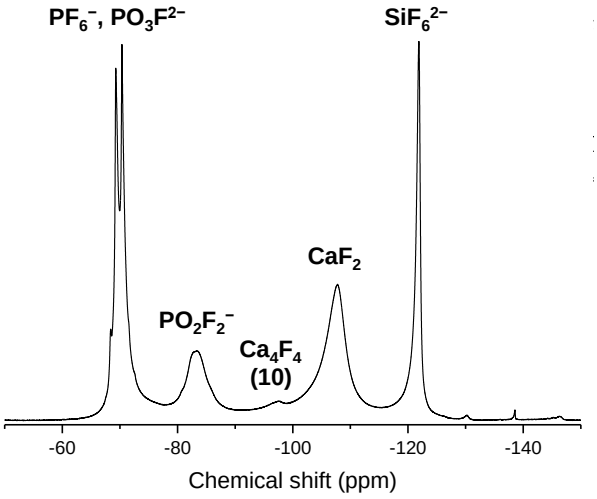

Figure 3.6 Solid-state ^{19}F NMR spectrum (659 MHz, 1.3 mm probe, 50 kHz spinning rate) of the air-exposed reaction mixture containing both CaF_2 and the Ca_4F_4 cubanoid (**10**, *vide infra*).

Single crystal X-ray analysis conducted on crystals of **10**, grown by layering Et_2O onto a concentrated CH_3CN solution of the compound and obtained in 27% yield, reveal a $[(15\text{-crown-}5)_3(Ca_4F_4)(PF_6)]^{3+}$ cation, composed of a central Ca_4F_4 cubane-type structure [core F-Ca bond length range, 2.247(2)-2.313(3) Å; core Ca-F-Ca and F-Ca-F bond angle ranges, 101.95(9)- 105.4(1)° and 73.23(8)-76.77(8)°, respectively] and three ion-separated PF_6^- anions (Figure 3.7a). The solution ^{19}F NMR spectrum (CD_3CN) of isolated crystals of **10** exhibits a broad singlet at $\delta = -98.3$ ppm and a quartet at $\delta = -106.6$ ppm. ^{19}F-^{19}F COSY analysis ($^2J_{F\text{-}F} = 17.4$ Hz) confirms that these two signals are coupled and arise from the

[†] Solid-state NMR spectroscopy conducted by Dr. Zigeng Liu in the Department of Chemistry at the University of Cambridge.

distinct ^{19}F environments within the cationic cluster (Figure 3.7b). These distinct environments arise from three F atoms that are bridging the $Ca(CH_3CN)_2PF_6$ fragment to two Ca⊂(15-crown-5) fragment as well as from a single F atom that bridges three C⊂(15-crown-5) fragments (Figure 3.7). From the ^{19}F NMR spectroscopic data it is clear that this Ca_4F_4 cation is retained in solution. While transition metal fluoride cubanoid structures are known,[21] this structure is not only unprecedented for CaF species, but soluble molecular Group 2

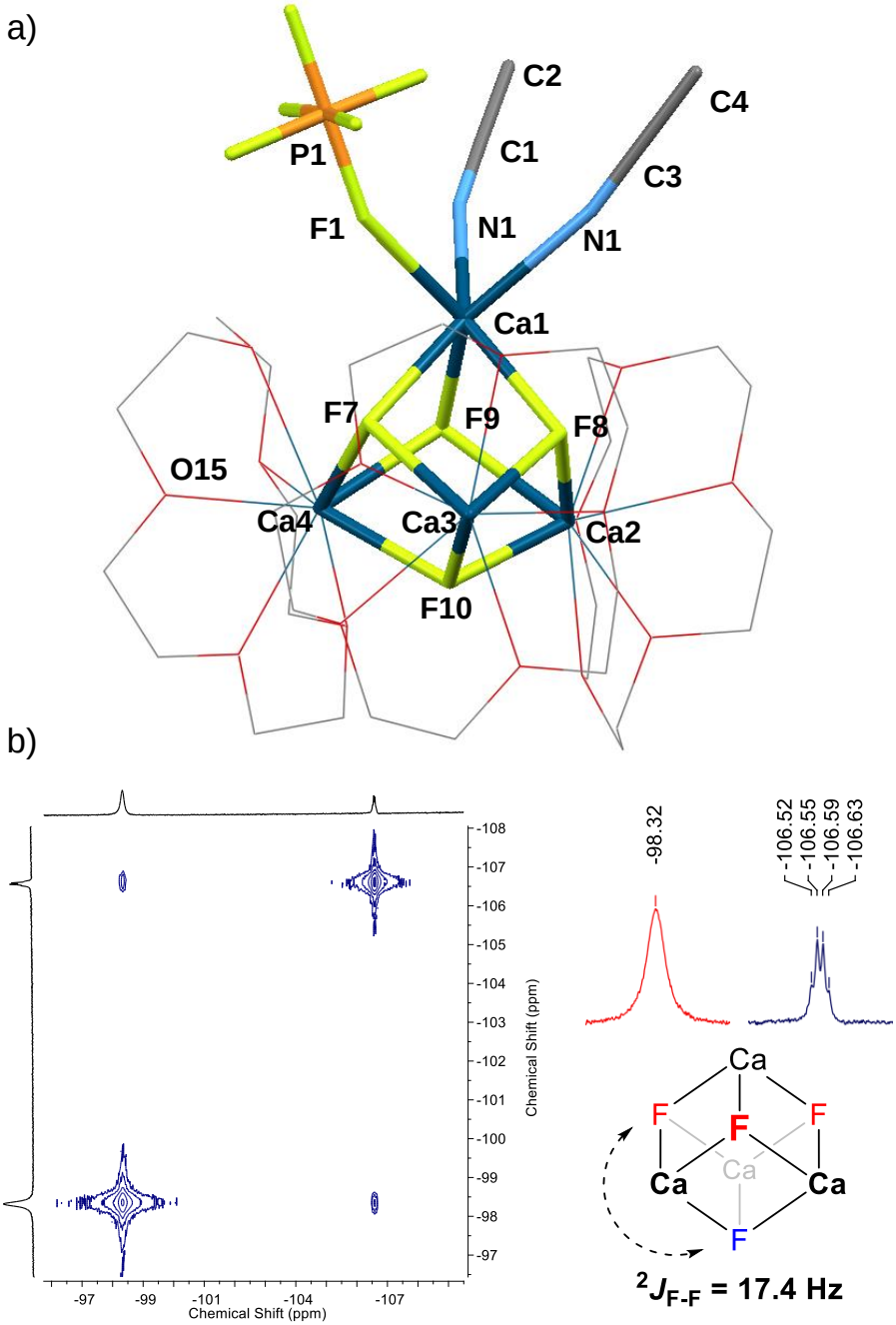

Figure 3.7 Solid- and solution-state analysis of Ca_4F_4 cubanoid **10**. a) Crystal structure of **10** with protons and ion separated PF_6^- anions omitted for clarity (Ca, dark blue; C, grey; F, yellow; N, light blue; O, red; P, orange). b) Solution-state ^{19}F-^{19}F COSY analysis of **10** showing the ^2J F-F coupling. Selected bond distances (Å) and angles (°):core Ca-F 2.247(2)-2.313(3), Ca1-F1 2.354(3), core Ca-F-Ca 101.95(9)- 105.4(1), core F-Ca-F 73.23(8)-76.77(8), Ca1-F1-P1 151.4(2). Structure displayed as a wireframe structure for clarity.

fluorides are rare, in general.[22]

Owing to the unique nature of the Ca_4F_4 cubanoid and the low yield in which it was isolated, several attempts were made to generate a similar cluster using more direct methods. To avoid concomitant generation of $PO_2F_2^-$ with the Ca_4F_4 species, fluoride sources other than PF_6^- were utilized. In an initial attempt, $Ca(NO_3)_2$, used as a soluble Ca^{2+} source, was combined with NH_4F in the presence of 15-crown-5 in either bench-top CH_3CN or EtOH. ^{19}F NMR analysis of aliquots taken from these mixtures under reflux showed no emergence of resonances attributable to the formation of new CaF species. In 1977 Reedijk and co-workers reported a series of transition metal (TM = Mn, Co, and Cd) fluoride cubanoid structures formed from the decomposition of the $TM(H_2O)_6(BF_4)_2$ complexes in the presence of the N-donor ligands *N*-ethylimidazole and *N*-propylimidazole in EtOH-triethylorthoformate solutions.[21] In their work, the presence of water prompted the hydrolysis of the BF_4^- anion, resulting in the release of F^- for the generation of the TM_4F_4 structures, which were supported by three imidazole ligands at each metal vertex. A similar approach was attempted using $Ca(BF_4)_2{\cdot}xH_2O$ with 15-crown-5 or *N*-ethylimidazole in both EtOH-triethylorthoformate and CH_3CN. These reactions were carried out at room temperature, under reflux, and under solvothermal conditions in Teflon-lined autoclaves at 150 °C. However, ^{19}F NMR analysis of the reaction mixtures again showed no evidence of BF_4^- hydrolysis or Ca_4F_4 formation.

3.3 Conclusions

In summary, we have shown that the formation of $Ca(PF_6)_2$ complexes is possible using Ca metal and $NOPF_6$ in the presence of a chelating ligand. Further, the reactivity of these complexes in the presence of ambient atmosphere has been investigated. These complexes are prepared using an efficient route that does not require extra drying steps or salt metathesis methods. $Ca(PF_6)_2$ is stabilized by crown ethers under the reaction conditions employed, limiting decomposition of the PF_6^- anion to $PO_2F_2^-$ or other decomposition products. Investigations of the selective oxidation of the PF_6^- anion suggest that the formation of the $PO_2F_2^-$ anion from the PF_6^- anion does not occur simply via hydrolysis or aerobic oxidation, but occurs in the reaction system itself and possibly involves NO or NO_2. Our initial studies demonstrate the relative sensitivity of $Ca(PF_6)_2$ species compared to the Mg analogue. This reactivity is likely related to the lower charge density of Ca^{2+} and weaker

solvent-cation interactions of the complex, which could permit Ca^{2+}-PF_6^- ion pairing to accelerate the decomposition of the PF_6^- anion. Accordingly, the possible involvement of Ca-PF_6 interactions in the observed reactivity points towards the use of strong donor solvents in electrolyte solutions for the prevention of adventitious PF_6^- decomposition. In addition to the insight gained from studying the behaviour of $Ca(PF_6)_2$, we have been able to structurally characterize several $Ca(PF_6)_2$ decomposition products including an unprecedented $Ca_4F_4^{4+}$ molecular cluster. While, the cubanoid species could not be generated using more direct synthetic methods, this structure type is a target with the potential to emerge as a soluble source of CaF_2.

3.4 Future Work

As Ca^{2+} as well as CaO could be involved in the decomposition of PF_6^-, control reactions involving these species could provide insight into the nature of PF_6^- decomposition. To investigate the role of Ca^{2+} decomposition, the stability of CD_3CN solutions containing $Mg(PF_6)_2$ and $Mg(PF_6)_2$ along with a soluble Ca salt could be compared by monitoring the ^{19}F and ^{31}P NMR spectra of the two solutions over time after exposure to ambient atmosphere. Additionally, the impact of CaO could be probed by stirring a CD_3CN solution of $Ca(PF_6)_2$ over CaO and monitoring the reaction by ^{19}F and ^{31}P NMR or by adding CaO to the reaction of Ca and $NOPF_6$ in the presence of a crown ether.

The isolation of the unique Ca_4F_4 cluster **10** is of interest both as a new type of metal cubanoid and as a source of CaF^+ or CaF_2 that is soluble in non-aqueous solvents. Interest in soluble CaF2 species extends to their use as precursors for the deposition of CaF_2 films. Owing to its low solubility and its transparency over a broad range of wavelengths, from the UV to the IR regions of the electromagnetic spectrum, CaF_2 is an important optical material used to coat certain lenses and optical windows.[23] However, the low solubility of CaF_2 makes its processing and deposition energy intensive.[23] Thus, the identification and investigation of easily processable CaF_2 film precursors is of interest. Previously reported soluble 'CaF' species have required the use of organomercury compounds[22] and organotin fluorides,[23] or have been generated using highly air-sensitive organometallic reagents[24] or through the decomposition of complex fluorinated β-diketiminate ligands.[25] While these methods afford soluble CaF^+ or CaF_2 species, the use of such toxic, unstable, and complex materials limits their practicality as precursors for the deposition of CaF_2 films.

Direct access to the Ca_4F_4 cubanoid using simple supporting ligands, such as crown ethers or N-donors, in high yields is of distinct interest. As it is possible that Ca-bound H_2O in the $Ca(BF_4)_2$ hydrate is not sufficient to hydrolyse the BF_4^- anion, one method of modifying the previously attempted syntheses using $Ca(BF_4)_2 \cdot xH_2O$ would be to titrate known amounts of H_2O into the reaction mixture containing the supporting ligand and monitor the evolution of species formed by ^{19}F NMR spectroscopy or mass spectrometry. Such titration methods have been successful for the formation of titanium-oxo clusters, giving control over speciation based on the stoichiometry of H_2O used.[26] Another method for the formation of CaF species could involve the slow dissolution of Ca^{2+} from Ca metal in THF-NH_3 solutions in the presence of a protic fluoride source and supporting ligands.[27] The generation of Ca^{2+} along with 2 e^- in the presence of NH_4F, for example, could result in the formation of H_2 gas and free F^-. The slow formation of resulting CaF^+ or CaF_2 species could then be trapped in the form of clusters by an appropriate supporting ligand system.

3.5 References

1 H. D. Yoo, I. Shterenberg, Y. Gofer, G. Gershinsky, N. Pour and D. Aurbach, *Energy Environ. Sci.*, 2013, **6**, 2265–2279.

2 J. Muldoon, C. B. Bucur, A. G. Oliver, T. Sugimoto, M. Matsui, H. S. Kim, G. D. Allred, J. Zajicek and Y. Kotani, *Energy Environ. Sci.*, 2012, **5**, 5941–5950.

3 J. Muldoon, C. B. Bucur and T. Gregory, *Chem. Rev.*, 2014, **114**, 11683–11720.

4 A. Meitav and E. Peled, *J. Electrochem. Soc.*, 1982, **129**, 451–457.

5 D. Aurbach, R. Skaletsky and Y. Gofer, *J. Electrochem. Soc.*, 1991, **138**, 3536–3545.

6 A. Ponrouch, C. Frontera, F. Bardé and M. R. Palacín, *Nat. Mater.*, 2016, **15**, 169–172.

7 A. L. Lipson, B. Pan, S. H. Lapidus, C. Liao, J. T. Vaughey and B. J. Ingram, *Chem. Mater.*, 2015, **27**, 8442–8447.

8 M. Wang, C. Jiang, S. Zhang, X. Song, Y. Tang and H. Cheng, *Nat. Chem.*, 2018, **10**, 667–672.

9 E. N. Keyzer, H. F. J. Glass, Z. Liu, P. M. Bayley, S. E. Dutton, C. P. Grey and D. S. Wright, *J. Am. Chem. Soc.*, 2016, **138**, 8682–8685.

10 T. H. Jordan, B. Dickens, L. W. Schroeder and W. E. Brown, *Acta Cryst.*, 1975, **B31**, 669–672.

11 R. Haiges and K. O. Christe, *Z. Anorg. Allg. Chem.*, 2002, **628**, 1717–1718.

12 R. Fernández-Galán, B. R. Manzano, A. Otero, M. Lanfranchi and M. A. Pellinghelli, *Inorg. Chem.*, 1994, **33**, 2309–2312.

13 N. Dupré, M. Cuisinier and D. Guyomard, *Interface*, 2011, **20**, 61–67.

14 E. V Brouillet, A. R. Kennedy, K. Koszinowski, R. Mclellan, R. E. Mulvey and S. D. Robertson, *Dalt. Trans.*, 2016, **45**, 5590–5597.

15 E. N. Keyzer, P. D. Matthews, Z. Liu, A. D. Bond, C. P. Grey and D. S. Wright, *Chem. Commun.*, 2017, **53**, 4573–4576.

16 M.-L. Lehaire, R. Scopelliti and K. Severin, *Chem. Commun.*, 2002, 2766–2767.

17 S. S. Zhu and T. M. Swager, *J. Am. Chem. Soc.*, 1997, **119**, 12568–12577.

18 K. Škoch, F. Uhlík, I. Císařová and P. Štěpnička, *Dalt. Trans.*, 2016, **45**, 10655–10671.

19 J. S. Fleming, K. L. V Mann, S. M. Couchman, J. C. Jeffery, J. A. Mccleverty and M. D. Ward, *J. Chem. Soc. Dalt. Trans*, 1998, 2047–2052.

20 R. W. Seidel, C. Dietz, J. Breidung, R. Goddard and I. M. Oppel, *Acta Cryst.*, 2013, **C69**, 1112–1115.

21 J. C. Jansen, H. van Koningsveld and J. Reedijk, *Nature*, 1977, **269**, 318–319.

22 G. B. Deacon, P. C. Junk and G. J. Moxey, *Dalt. Trans.*, 2010, **39**, 5620–5622.

23 S. Nembenna, H. W. Roesky, S. Nagendran, A. Hofmeister, J. Magull, P.-J. Wilbrandt and M. Hahn, *Angew. Chem. Int. Ed.*, 2007, **46**, 2512–2514.

24 F.-Q. Liu, D. Stalke and H. W. Roesky, *Angew. Chem. Int. Ed.*, 1995, **34**, 1872–1874.

25 A. G. M. Barrett, M. R. Crimmin, M. S. Hill, P. B. Hitchcock and P. A. Procopiou, *Angew. Chem. Int. Ed*, 2007, **46**, 6339–6342.

26 S. D. Pike, E. R. White, M. S. P. Shaffer and C. K. Williams, *Nat. Commun.*, 2016, **7**, 13008.

27 S. R. Drake and D. J. Otway, *J . Chem. Soc., Chem. Commun.*, 1991, 517–519.

4. Magnesium Aluminate Electrolyte Systems for Mg Batteries

4.1 Introduction

As discussed in Chapter 1, despite being an attractive alternative to Li-ion technology, the development of Mg-ion systems continues to be limited by a lack of electrolyte systems that are stable at both Mg plating potentials and at cathode materials that operate at potentials above 3 V vs. Mg. The latter is required to enable the use of cathode materials that operate at higher potentials than the well-established Chevrel phase Mo_6S_8 (CP), which cycles between 0.2 and 2 V vs. Mg.[1] Thus, new synthetic methodologies for electrolyte salt synthesis are required to identify electrolyte systems that are both stable over a wide electrochemical window and facilitate efficient Mg cycling at the anode and cathode. Many established Mg-ion electrolyte systems gradually decompose at the electrode surfaces, resulting in passivating films that ultimately lead to capacity loss and failure of the device. Accordingly, considerable attention has been directed at developing electrolyte systems that are oxidatively stable to at least 3.5 V vs. Mg. Among these, the magnesium aluminium chloride complex (MACC) in THF,[2,3] $Mg(HMDS)_2$-derived (HMDS = hexamethyldisilazide) salts in diglyme,[4] and $Mg(TFSI)_2$ (TFSI = bis(trifluoromethanesulfonyl)imide) in glymes,[5] have shown considerable promise but still do not operate above 3.5 V vs. Mg. Additionally, chloride-free Mg monocarborane in tetraglyme[6] and $Mg(BAr^F)_2$ (BAr^F = tetrakis[3,5-bis(trifluoromethyl)phenyl]borate) in THF exhibit excellent oxidative stability to ca. 3.5 V vs. Mg. However, the latter system has been shown to be unstable at potentials near 0 V vs. Mg, precluding Mg deposition/dissolution at a Mg anode.[7] In addition to oxidative stability, the ability to allow facile desolvation of the highly charge-dense Mg^{2+} and intercalation at one electrode, and Mg plating at the other, represents a considerable challenge.

Recently, Arnold and co-workers have demonstrated the use of the fluorinated Mg alkoxyaluminate $Mg[Al(O^iPr^F)_4]_2$ (O^iPr^F = hexafluoro-*iso*-propoxy) that could be cycled for 500 charge-discharge cycles in DME on a glassy carbon inert electrode while maintaining high Coulombic efficiencies. The oxidative stability of this electrolyte exceeds 4 V vs. Mg on stainless steel and aluminium electrodes in DME.[8]

Despite exhibiting excellent electrochemical properties, the authors site β-hydride elimination oxidative decomposition as a possible limitation to the stability window of this system. When utilized in Mg full cells with the CP cathode, this electrolyte system exhibits poor capacity retention, fading from around 100 to 35 $mAh \cdot g^{-1}$ over 50 cycles. It has been demonstrated in other aluminium-containing systems, such as those employing the $Ph_nAlCl_{3-n}^-$ anion, that the absence of β-hydride elimination pathways can extend the electrochemical stability window of this class of electrolytes by up to 1 V vs. Mg.[9,10] Furthermore, the synthetic strategy used by Arnold and co-workers to prepare the electrolyte, formed *in situ* by treating $Al(O^iPr^F)_3$ with $Mg(O^iPr^F)_2$ in a 2:1 ratio in DME, may limit the use of less nucleophilic Mg alkoxides (i.e. bulky alkoxides or those with strong electron withdrawing groups), which limits exploration of this class of anion. The analogous Li salt, $LiAl(O^iPr^F)_4$, also exhibits high oxidative stability (>5 V vs. Li) in DME.[11]

Zhao-Karger and co-workers recently investigated the analogous magnesium borate system, $Mg[B(O^iPr^F)_4]_2$. This Mg alkoxyborate, along with a series of others, was synthesized through the treatment of $Mg(BH_4)_2$ with the corresponding alcohol in ethereal solvent, affording the borate in high yield. The $^iPr^F$-based borate was shown to facilitate the reversible plating and stripping of Mg on Pt and Mg electrodes and exhibited oxidative stability over 4 V vs. Mg on stainless steel and aluminium electrodes. This electrolyte could also be cycled in Mg full cells containing a sulfur cathode, further confirming the potential advantages of these and similar salts such as the aluminates as viable electrolyte components.[12]

Given the reported performance of the $Mg[Al(O^iPr^F)_4]_2$-DME electrolyte as well as that of the analogous borate system, we were interested in developing a general route to Mg aluminate salts having the formula $Mg[Al(OR)_4]_2$, where R is an alkyl- or aryl-group, and investigating their electrochemistry. The formation and electrochemical analysis of a broad range of such aluminates would provide a better understanding of their behaviour and structural factors that influence their stability. $LiAlH_4$ is a widely-used precursor and methodologies using $LiAlH_4$ have produced an extensive range of Li aluminates.[11,13–16] Thus, $Mg(AlH_4)_2$ should offer a versatile platform for the synthesis of Mg aluminates. Here we present the use of $Mg(AlH_4)_2$ as a general precursor for the generation of a number of previously unreported Mg aluminates. These Mg aluminates are retrieved as isolated solids which can be used directly to form electrolyte systems. A number of these Mg aluminates do not contain

β-hydrogen atoms, eliminating possible β-hydride elimination decomposition pathways previously proposed for the $Mg[Al(O^iPr^F)_4]_2$ and Mg organohaloaluminate systems.[8,17] In this study we demonstrate that electrolyte mixtures based on these new aluminate salts exhibit very stable cycling on inert electrodes (Pt and Au) and Mg electrodes as well as in cells containing CP cathodes. We also show that the presence of chloride in the electrolyte solutions impacts their electrochemical performance by both increasing cycling coulombic efficiencies and lowering plating/stripping overpotentials.

4.2 Results and Discussion

*4.2.1 Synthesis of Magnesium Aluminate Salts **11-15***

$Mg(AlH_4)_2$ can be synthesized in one step by ball-milling $NaAlH_4$ and $MgCl_2$ in a 2:1 ratio for 1 hour.[18] The resulting material is composed of a 1:2 mixture of $Mg(AlH_4)_2$ and NaCl (Scheme 4.1). A series of Mg aluminates, ^{t}Bu = *tert*-butyl (**11**); ^{t}Bu^F = perfluoro-*tert*-butyl (**12**); ^{i}Pr^F = hexafluoro-*iso*-propyl (**13**); Ph = phenyl (**14**); Ph^F = pentafluorophenyl (**15**), was synthesized by treating $Mg(AlH_4)_2$ with various fluorinated/non-fluorinated alkyl and aryl alcohols in dry THF (Scheme 4.1). These reactions were followed by filtration under inert atmosphere to remove insoluble impurities (i.e. NaCl and Al-containing by-products). The resulting Mg aluminates were retrieved as THF solvates in high yields (77–94%) and were characterized by multinuclear NMR spectroscopy, mass spectrometry, and elemental analysis. The isolated compounds were found to contain 0.24-3.2 wt% Cl by elemental analysis (0.24, 2.64, 3.20, 1.68, and 1.9 wt% for **11**-**15**, respectively), likely resulting from dissolved NaCl being carried through filtration (*vide infra*). These materials are termed 'chloride-containing' in the following discussion. Chloride by-products could be removed from aluminates **12** (^{t}Bu^F) and **14** (Ph) by suspending the dried reaction mixtures in dichloromethane and filtering the colourless solution containing the aluminates through glass fibre filter paper. The resulting products were found to contain 0.05 and 0.11 wt% Cl, respectively, by elemental analysis and are hereafter referred to as the 'chloride-free' compounds. The chloride levels found in our work for **12** and **14** are comparable to those found in $Mg[Al(O^iPr^F)_4]_2$ samples synthesised in our laboratory according to the method reported by Arnold and co-workers (0.10 wt%). Aluminate **13**, the $Mg[Al(O^iPr^F)_4]_2$ salt studied by the Arnold group, exhibits

poor solubility in dichloromethane and could not be purified in this way. Note that compound **14** has been previously synthesized by combining Mg, phenol, and $Al(OPh)_3$ in THF with $HgCl_2$ under reflux.[19]

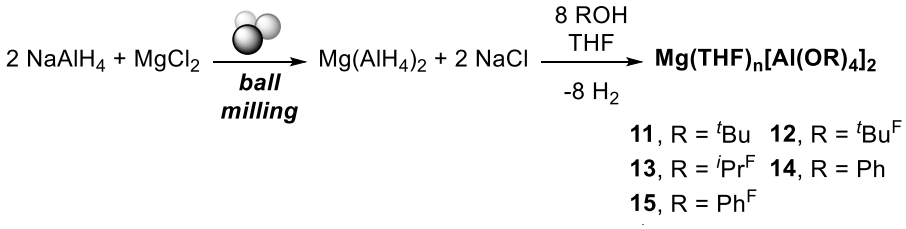

Scheme 4.1 Synthesis of $Mg(AlH_4)_2$ and subsequent reaction with alcohols to afford Mg aluminates **11**-**15** (^{t}Bu = *tert*-butyl; ^{t}Bu^F = perfluoro-*tert*-butyl; ^{i}Pr^F = hexafluoro-*iso*-propyl; Ph = phenyl; Ph^F = pentafluorophenyl).

Single crystals of aluminates **11** (^{t}Bu) and **14** (Ph) could be grown from concentrated solutions at −20 °C and their solid-state structures were determined by single-crystal X-ray diffraction (Figure 4.1). Magnesium *tert*-butoxyaluminate **11** was found to exist as an ion-paired structure with the formula $Mg[Al(O^tBu)_4]_2$ in the solid state, wherein Mg is coordinated in a tetrahedral fashion by four oxygen atoms of two separate aluminate anions (Figure 4.1a). ^{1}H NMR analysis of **11** in C_6D_6 shows two distinct *tert*-butoxy- environments, reflecting the environments in the solid-state structure and suggesting the ion-paired structure is retained in solution. Magnesium phenoxyaluminate **14** was also found to exist as an ion-paired structure in the solid state; however, two molecules of THF are observed to coordinate to Mg along with four oxygen atoms of two separate aluminate anions, resulting in an octahedral geometry around Mg, giving the formula $Mg(THF)_2[Al(OPh)_4]_2$. An additional uncoordinated THF molecule is present in the crystal lattice. Both of these structures are consistent with compositions determined by elemental analysis as well as crystal structures of analogous aluminates,[20,21] including the previously reported (unsolvated) crystal structure of **14**.[19] The differences in the Mg coordination geometry and environments between **11** and **14** are thought to arise from the different steric profiles and electron donor ability of the *tert*-butoxy- and phenoxy- groups. Full multinuclear NMR characterization of compounds **11**-**15** is presented in Chapter 7, section 7.2.3.

Additionally, a hydrolysis product of **12**, **12'**, could be identified crystallographically, likely resulting from the introduction of a small amount of air into the vessel during crystallization. The solid-state structure, obtained from crystals grown by layering benzene on a solution of **12** in DME, shows an unusual Mg

aluminate having the formula (^{t}Bu^{F}O)$_3$Al(μ_2-OH)Mg(O^{t}Bu^F)(DME)$_2$, in which a tetrahedral aluminium moiety is connected to a Mg-O^{t}Bu^F fragment by what is proposed to be a bridging hydroxyl group (Figure 4.1c). The presence of a proton was proposed as the ^{1}H NMR spectrum of **12'** in dry d_8-THF exhibits a sharp singlet at δ = 8.98 ppm, which likely arises from an acidic OH proton. To the best of our knowledge, solid-state structural analysis of an Al-O(H)-Mg motif has not been reported previously, making comparisons of bond angles in **12'** difficult. Nonetheless, the measured Al-O-Mg bond angle of 156.6(2)° suggests that the proton resides on the bridging oxygen. The Al-O(H)-Mg angle is larger than bond angles observed for Al-O(H)-Al or Mg-O(H)-Mg motifs, which range from 92.2° to 148.4° and 91.7° to 173.7°, respectively (based on a comprehensive search using the Cambridge Structural Database). However, a perfluoro-*tert*-butoxyaluminate dimer with the formula (^{t}Bu^{F}O)$_3$Al(μ_2-OH)Al(O^{t}Bu^F)$_3$, which is compositionally and structurally similar to **12'**, exhibits the largest reported Al-O(H)-Al bond angle, 148.4(2)°, and supports the placement of the proton on the bridging oxygen.[22] More conclusively, the position of the proton is evidenced by residual electron density next to the bridging oxygen

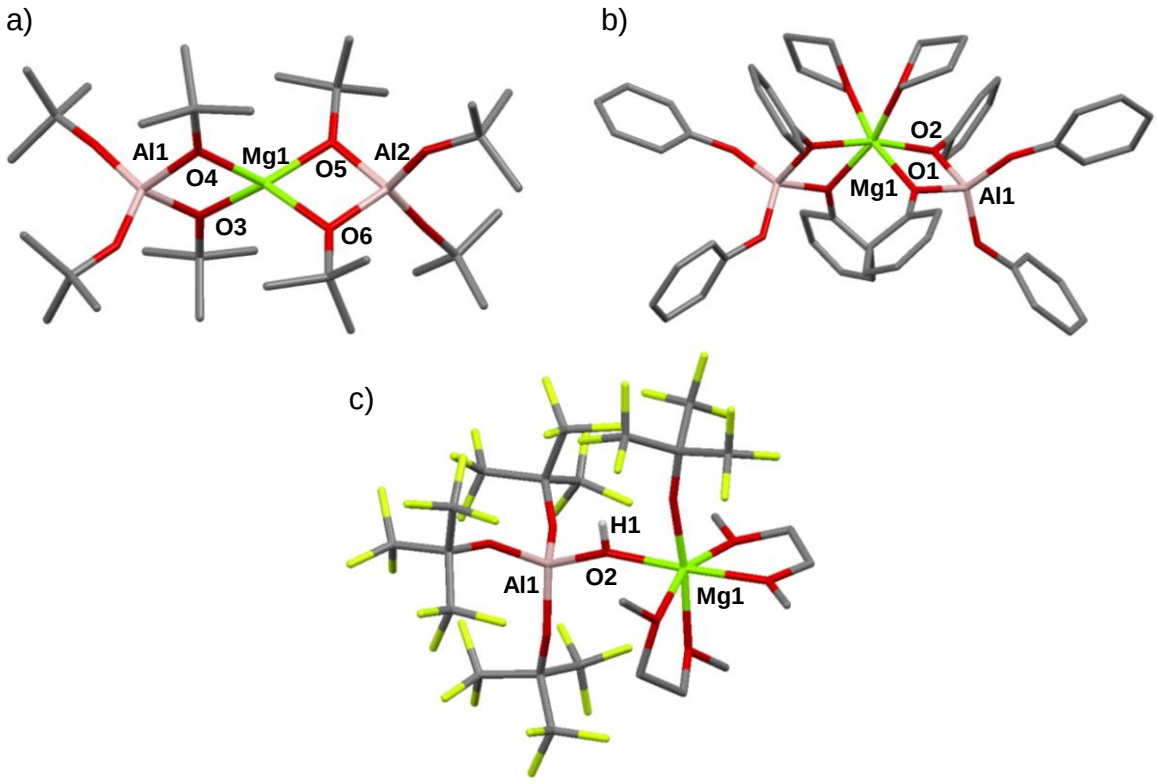

Figure 4.1 Crystal structures of Mg aluminates a) **11** and b) **14** and c) **12'**. Protons (except **12'**, H1), site disorder, and uncoordinated solvent have been removed for clarity (Mg, green; Al, pink; O, red; C, grey; F, yellow). Selected bond lengths (Å) and angles (°): **11**, Mg1-O 1.956(2)-1.961(2), O-Mg1-O 78.13(7)-78.44(8); **14**, Mg1-O 2.069-2.161; O-Mg1-O, 72.3; **12'**, Mg1-O2 2.075(3), Al1-O2 1.755(3), Al1-O2-Mg1 156.6(2). Structures displayed as wireframe structures for clarity.

observed during X-ray structure refinement.

While the structures of aluminates **12**, **13**, and **15** could not be determined by single-crystal diffraction, based on the number of THF molecules determined from elemental analysis it is likely that these highly fluorinated aluminate anions form ion-separated species containing $Mg(THF)_6^{2+}$ cations, of the formulae $Mg(THF)_6[Al(O^tBu^F)_4]_2$ (**12**), $Mg(THF)_6[Al(O^iPr^F)_4]_2$ (**13**), and $Mg(THF)_6[Al(OPh^F)_4]_2$ (**15**) (see Synthetic Procedures and Characterization section in Chapter 7).

*4.2.2 Electrochemistry of Magnesium Aluminates **11-15***

Having established a synthetic protocol for the generation of a series of Mg aluminates, we turned to investigating the electrochemical stability of the chloride-containing compounds (i.e., prior to any further purification steps to remove Cl^-, as detailed above) using linear sweep voltammetry (LSV) at a concentration of 0.25 M. A solution of $Mg[Al(O^tBu)_4]_2$, **11**, in THF is found to exhibit good oxidative stability on stainless steel (ss-316), Cu, Au, and Pt electrodes, with the only minor anodic processes occurring around 2 V vs. Mg on each electrode, and an onset of oxidation on Al at around 1 V vs. Mg (Figure 4.2a). In contrast to **11**, aluminates **12-15** are soluble in DME, the solvent found to facilitate the best electrochemical behaviour by Arnold and co-workers.[8] Chloride-containing solutions of **12-14** in DME exhibit variable stability on the electrodes tested, ranging between 1.5 (**14** on Al, Au, and Pt) and 3 V (**13** on Al) vs. Mg (solid lines, Figure 4.2). We note that the onsets of oxidation exhibited by these systems are generally lower than those reported by Arnold and co-workers, possibly due to the presence of chloride in the electrolyte system interacting with or corroding the electrode surface.[7,23–25] The stability of these electrolytes is particularly reduced on ss-316, Au, and Al. Indeed, chloride-free solutions of **12** and **14** in DME exhibit different onsets of oxidation on a number of electrodes. The chloride-free solution of **12** exhibits similar onsets of oxidation on Cu, ss-316, Au, and Pt but anodic processes observed on Al are suppressed to around 4 V vs. Mg (dotted lines, Figure 4.2b). Chloride-free solutions of **14** show extended stability on Au and Pt electrodes, exhibiting onsets of oxidation around 2.5 V vs Mg. The onset of oxidation on Al is also extended slightly to around 1.8 V vs. Mg, whereas the major onsets on Cu and ss-316 are lowered to 1.5 and 1.8 V vs. Mg, respectively (dotted lines, Figure 4.2d). Again, the onsets of oxidation of the chloride-free solutions are lower than those

previously reported. These differing results highlight the impact of electrolyte preparation methods and the presence of impurities/by-products in either system. Lastly, the solution of $Mg[Al(OPh^F)_4]_2$ (**15**) in DME exhibits onsets of oxidation below 2 V vs. Mg on all electrodes tested, with ss-316 and Al exhibiting the lowest onsets (Figure 4.2e). The low stability of the pentafluorophenyl aluminate **15** may result from Al-O bond cleavage, generating a highly stable pentafluorophenoxy anion.

Owing to the promising stability of the new aluminates **11**, **12**, and **14**, the

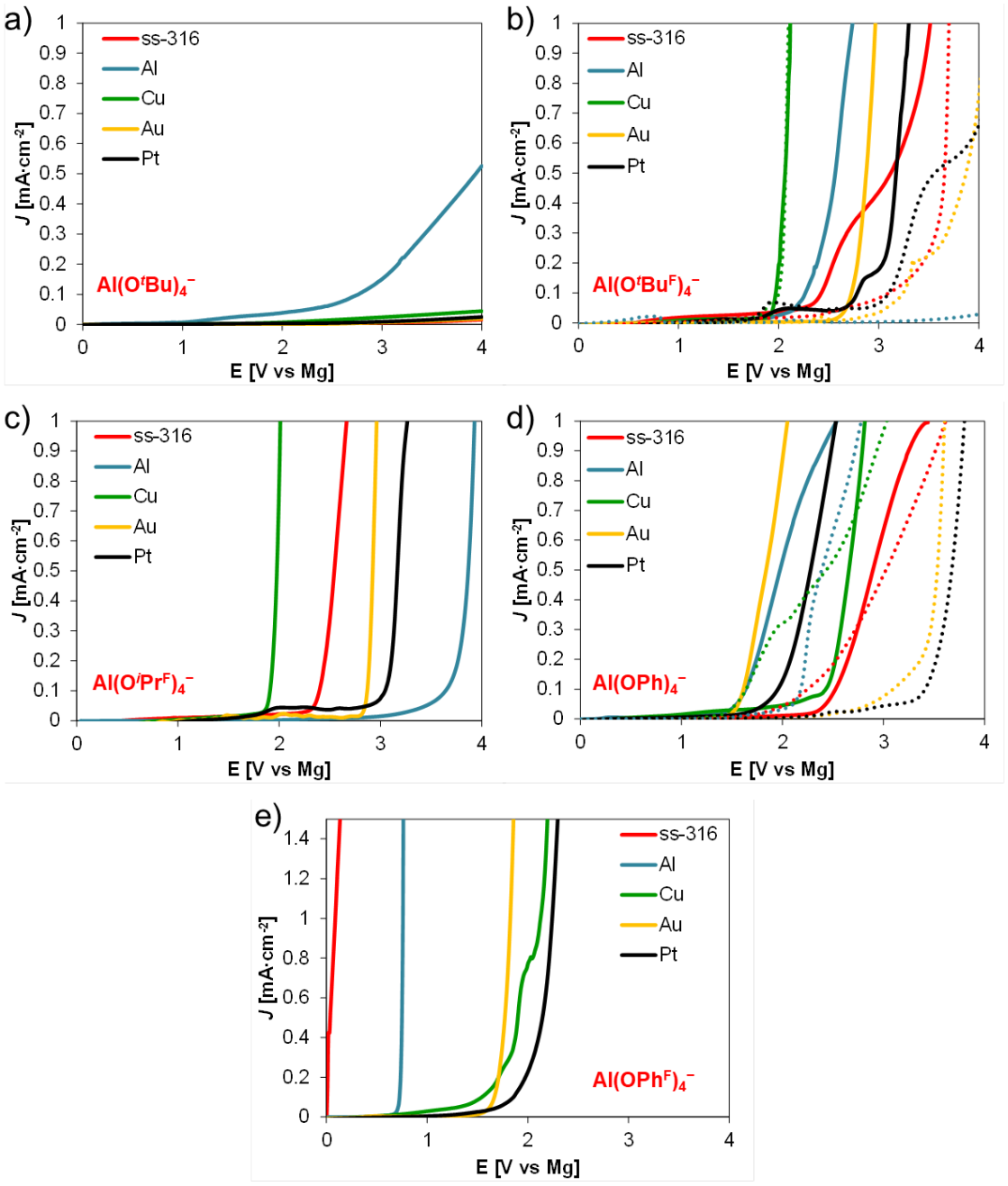

Figure 4.2 LSV measurements of 0.25 M solutions of a) **11** in THF, b) **12** in DME, c) **13** in DME, d) **14** in DME, and e) **15** in DME, scanning at a rate of 10 $mV \cdot s^{-1}$ on ss-316, Al, Cu, Au, and Pt working electrodes. Dotted lines represent chloride-free electrolyte solutions.

ability of the 0.25 M solutions to facilitate Mg plating and stripping was examined by cyclic voltammetry (CV) using a Pt working electrode. Unfortunately, CV measurements of **11** in THF did not show evidence of Mg plating/stripping behaviour between −0.5 V and 1 V vs. Mg. The inability of this system to plate Mg is possibly due to strong ion-pairing between the chelating anion and hard Mg^{2+} cation in solution, which is consistent with the solution ^{1}H NMR spectra and the solid-state X-ray structure. CV conducted on a solution of **12** in DME using a Pt working electrode at a rate of 10 $mV{\cdot}s^{-1}$, however, shows clear evidence of plating and stripping of Mg over fifty cycles between −0.55 V and 1 V vs Mg (Figure 4.3a). Plating overpotentials decrease over the 50 cycles from ca. −0.45 to −0.15 V vs Mg and stripping current densities are observed to increase from 0.04 to 6.4 $mA{\cdot}cm^{-2}$ from cycle one to cycle 50. Similar CV measurements of **14** in DME demonstrate that Mg can be plated and stripped using a Pt electrode between −0.5 V and 1 V vs Mg over 50 voltammetric cycles (Figure 4.3b). Again, plating overpotentials are observed to decrease from −0.41 V to −0.29 V vs Mg and anodic current densities increase from 0.07 to 0.49 $mA{\cdot}cm^{-2}$ from the first cycle to cycle 50. The small measured overpotentials as well as the increasing current densities suggest that the electrochemical processes are occurring on active electrode surfaces rather than first through the breakdown of a surface film.[26]

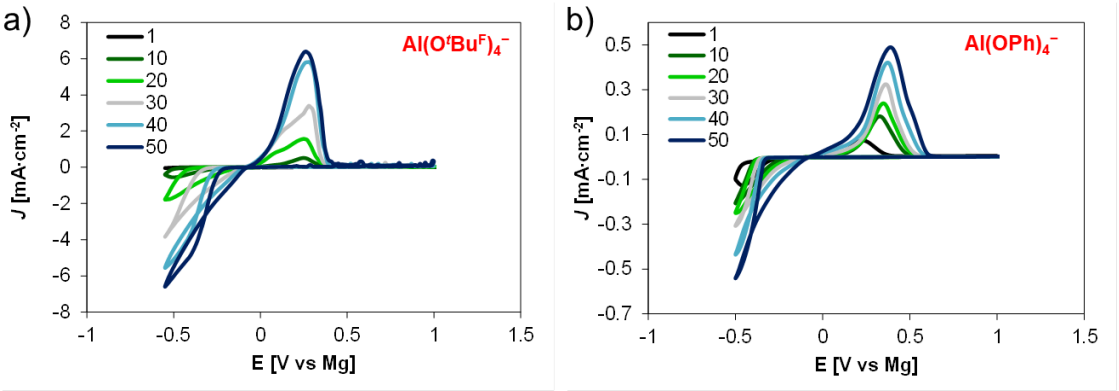

Figure 4.3 CV measurements of 0.25 M DME solutions of a) **12** and b) **14** scanning at a rate of 10 $mV{\cdot}s^{-1}$ using a Pt working electrode.

Coulombic efficiencies of plating and stripping for electrolyte solutions of **12** and **14** were determined using galvanostatic cycling methods reported previously.[8,12,27] Galvanostatic cycling of both chloride-containing and chloride-free 0.25 M solutions of **12** and **14** in DME was performed in a two electrode coin cell using gold-plated stainless steel working electrodes and magnesium ribbon counter electrodes. After a

rest period of 2 hours at open circuit potential, a constant cathodic current of 25 $\mu A \cdot cm^{-2}$ was applied for 1 hour followed by the application of a 25 $\mu A \cdot cm^{-2}$ anodic current until the measured voltage reached a cut-off voltage of 1.0 V vs. Mg. The efficiency was determined by calculating the ratio of the anodic (stripping) period to the 1 hour cathodic (plating) period. The chloride-containing solution of **12** cycled stably for 200 cycles, showing a decrease in both plating and stripping overpotentials, from −0.14 to −0.1 V vs. Mg and 0.2 to 0.07 V vs. Mg, respectively (Figure 4.4a). The chloride-free solution of **12** also showed stable cycling over 200 cycles but exhibited larger plating and stripping overpotentials that decreased over time, from −0.4 to −0.2 V vs. Mg and 0.4 to 0.16 V vs. Mg, respectively (Figure 4.4b). Coulombic efficiencies observed for the chloride-free solution remained significantly lower than the chloride-containing solution over the 200 cycles (Figure 4.4e). The same phenomenon is observed for the chloride-containing and chloride-free solutions of **14**, with the chloride-free mixture beginning to severely decrease in efficiency and develop larger overpotentials around cycle 50, indicative of electrolyte decomposition (Figures 4.4c and 4.4d). The lower overpotentials and higher Coulombic efficiencies observed for the chloride-containing mixtures are likely a result of Mg surface activation in the

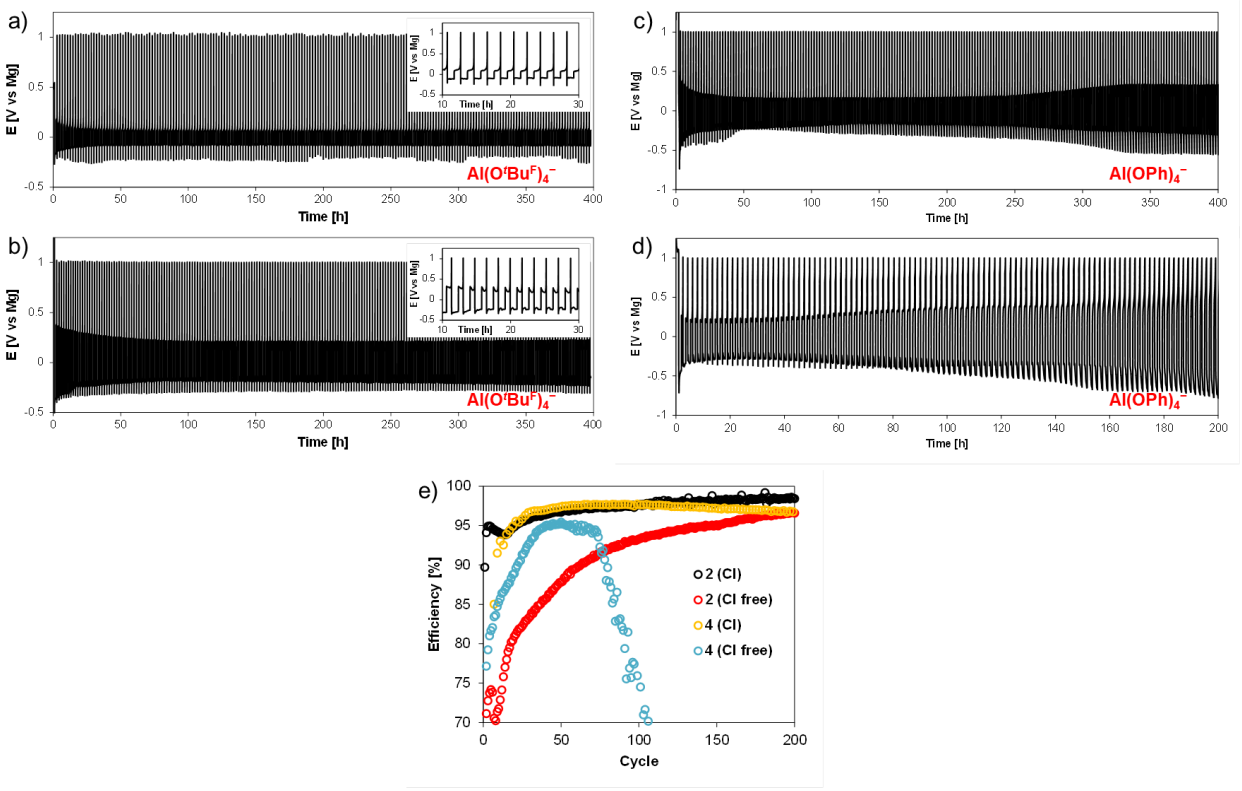

Figure 4.4 Galvanostatic cycling of Au|Mg coin cells using 0.25 M DME solutions of a) chloride-containing **12**, b) chloride-free **12** (insets: expanded chronopotentiograms), c) chloride-containing **14**, d) chloride-free **14**, and e) corresponding cell Coulombic efficiencies.

presence of chloride.[28–30]

Galvanostatic cycling of both mixtures of **12** and **14** in DME was also conducted in Mg symmetric cells by applying cathodic and anodic currents of 50 $\mu A \cdot cm^{-2}$ for 2 hour periods. The chloride-containing solution of **12** in DME shows stable cycling for 250 hours before shorting unexplainably (Figure 4.5a). In the absence of chloride, 0.25 M **12** in DME exhibits a decrease in overpotential over the 100 cycles as well as symmetric voltage profiles between the cathodic and anodic steps, suggesting that processes additional to plating and stripping are minimal on both electrodes (Figure 4.5b).[31] The solutions of **14** in DME exhibit larger overpotentials than **12** which are observed to increase slightly during cycling, but remain between −0.5 and 0.5 V vs Mg (Figures 4.5c and 4.5d). These larger overpotentials could arise from stronger ion-pairing between Mg^{2+} and the more electron rich phenoxyaluminate anion, as observed in the solid-state X-ray structure, creating a barrier to electrodeposition.

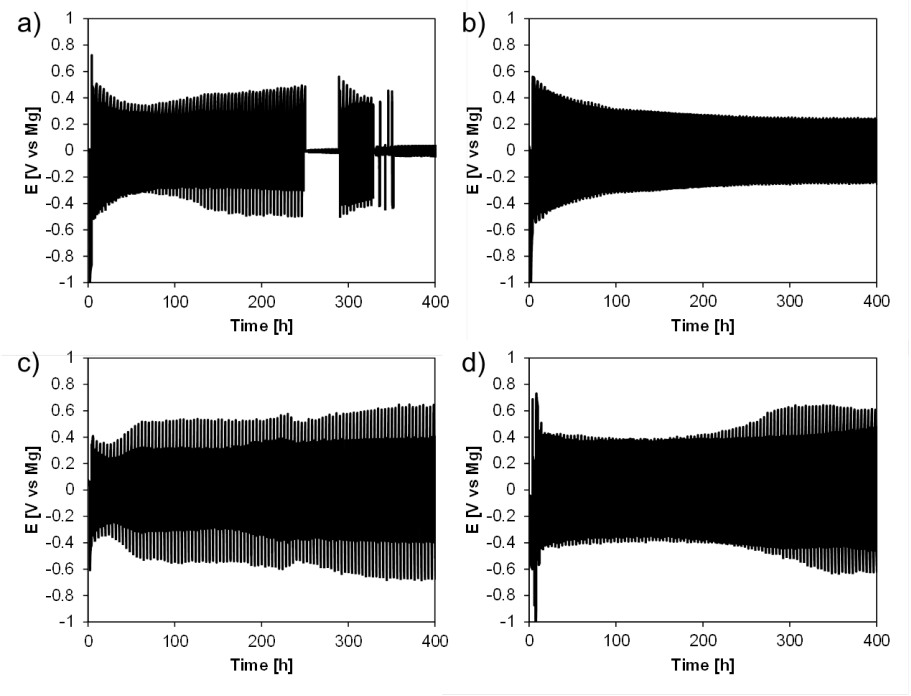

Figure 4.5 Mg symmetric cell galvanostatic cycling of 0.25 M DME solutions of a) chloride-containing **12**, b) chloride-free **12**, c) chloride-containing **14**, and d) chloride-free **14**.

4.2.3 Analysis of Electrodeposited Magnesium

Magnesium electrodeposition in coin cells onto Au at current densities of 25 $\mu A \cdot cm^{-2}$ from solutions of **12** and **14** in DME was found to adhere poorly to the Au working electrode surface and a majority of the Mg was removed on the glass fibre or

Celgard separators. Energy dispersive X-ray spectroscopy (EDX) of Mg deposited on the separator from a chloride-containing solution of **12** shows regions of plated Mg on top of regions of co-localized O and Si as well as F and Al, likely arising from the glass fibre separator and dried aluminate salt, respectively (Figure 4.6a). SEM images of areas of Mg plated from chloride-containing solutions of **14** on the Au electrode show non-dendritic Mg growth and Mg morphologies similar to those deposited using other electrolyte systems (Figure 4.6b).[6,32] Concomitant with these Mg deposits, we note the presence of O and C as determined by EDX analysis, which could arise from a surface-electrolyte interphase (Figure 4.6b) However, the stable cycling of chloride-containing **14**, shown in Figures 4.4c and 4.5c, does not indicate the formation of a passivating film. In addition, the X-ray diffraction (XRD) pattern of Mg deposited from chloride-containing solutions of **12** on a Celgard separator is consistent with that of pure Mg and does not show any Mg or Na halides or other oxides present in the deposited material (Figure 4.6c).[12]

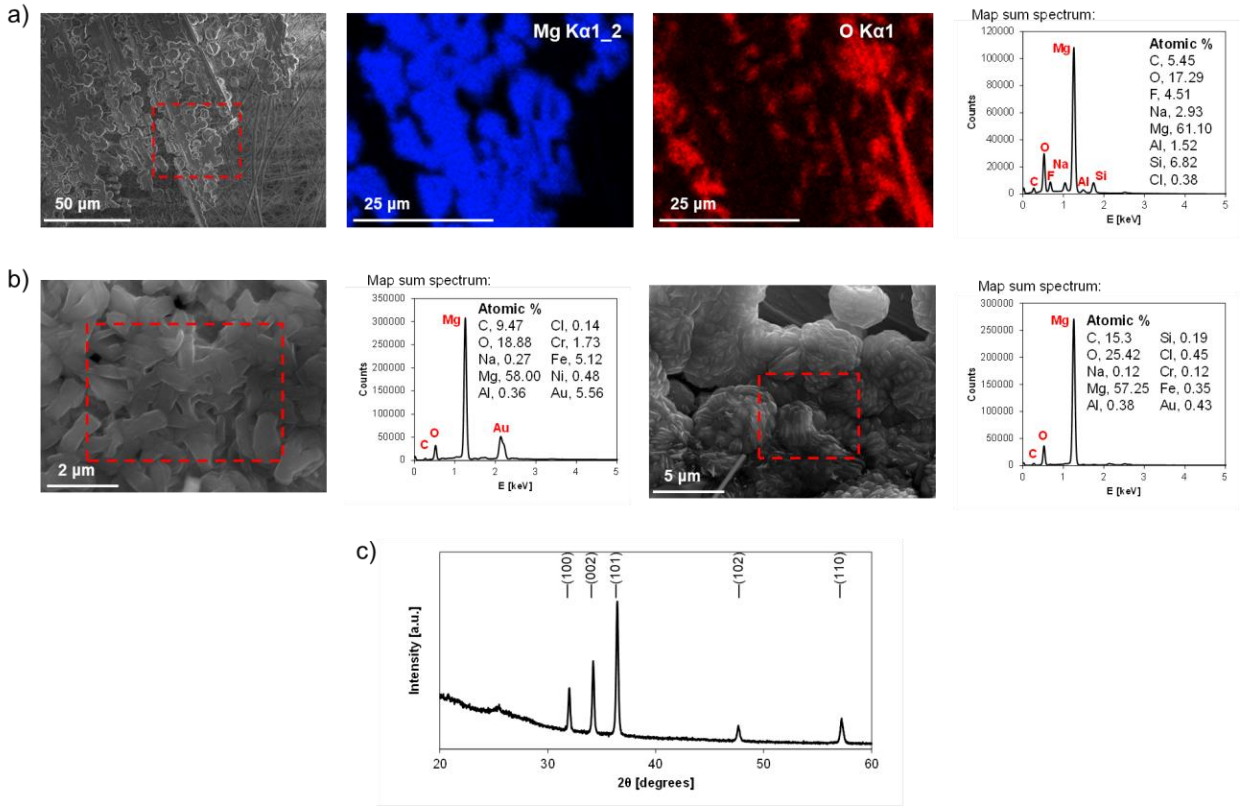

Figure 4.6 Analysis of typical Mg deposits plated from solutions of **12** and **14** in DME at 25 µA·cm^{-2}. a) SEM and EDX (highlighted area) analysis of Mg deposits removed onto a glass fibre separator, b) SEM images and EDX (highlighted area) analysis of Mg deposits on the Au working electrode, and c) XRD pattern of Mg deposited on a Celgard separator.

4.2.4 Battery Cycling and solid-state ^{23}Na NMR Analysis of the Chevrel phase (Mo_6S_8) Cathode[†]

The electrochemical behaviour of 0.25 M DME solutions of aluminates **12** and **14** were further examined in Mg cells against CP cathodes at room temperature at a rate of C/25. The cell employing the chloride-containing mixture of **12** maintained gravimetric capacities of around 90 mAh·g^{-1} over 50 cycles with high Coulombic efficiencies (Figure 4.7a). The chloride-containing mixture of **14** in the CP cell exhibits lower efficiencies in the early stages of cycling as well as a drop in capacity, from around 80 to 60 mAh·g^{-1}, starting roughly after cycle 30 (Figure 4.7b). The cell containing **12** retains capacities similar to those observed for CP cells using Mg carboranes,[6,33] whereas the cell containing **14** shows a fade in capacity typical of a number of Mg electrolytes.[32,34–36] The chloride-free solution of **12** shows poorer cycling behaviour with lower Coulombic efficiencies and lower capacities, fading to around 60 mAh·g^{-1} over 50 cycles (Figure 4.7c). The chloride-free solution of **14**, however, exhibits higher Coulombic efficiencies than the equivalent chloride-containing mixture during the early stages of cycling, decreasing only slightly to around 95%. Further, this cell maintains capacities over 95 mAh·g^{-1} over 50 cycles. Both cells containing the chloride-free electrolytes exhibit better capacity retention than the CP cell reported by Arnold and co-workers over 50 cycles. The retention of capacity in the chloride-free cells may be a result of more kinetically inert electrolyte systems that do not possess β-hydrogen atoms or, conversely, from electrolyte passivation of the current collectors. Cells containing aluminate **15** exhibited very poor charge-discharge behaviour and significant capacity fade within five cycles (Figure 4.7e). This rapid capacity loss is consistent with its apparent instability in LSV measurements.

While the chloride-containing cells cycle with good capacity-retention and high Coulombic efficiencies, this cannot necessarily be attributed to the presence of chloride alone. It is possible that Na, present in the cell in the form of dissolved NaCl as hypothesised above, is inserting into the CP and contributing to the overall capacity. The presence of Na is supported by ^{23}Na solid-state NMR measurements conducted on the CP cathode extracted from the cell shown in Figure 4.7a at the end of discharge

[†] ^{23}Na solid-state NMR measurements and spectral interpretations as well as electronic structure calculations were carried out in collaboration with Jeongjae Lee in the Department of Chemistry at the University of Cambridge.

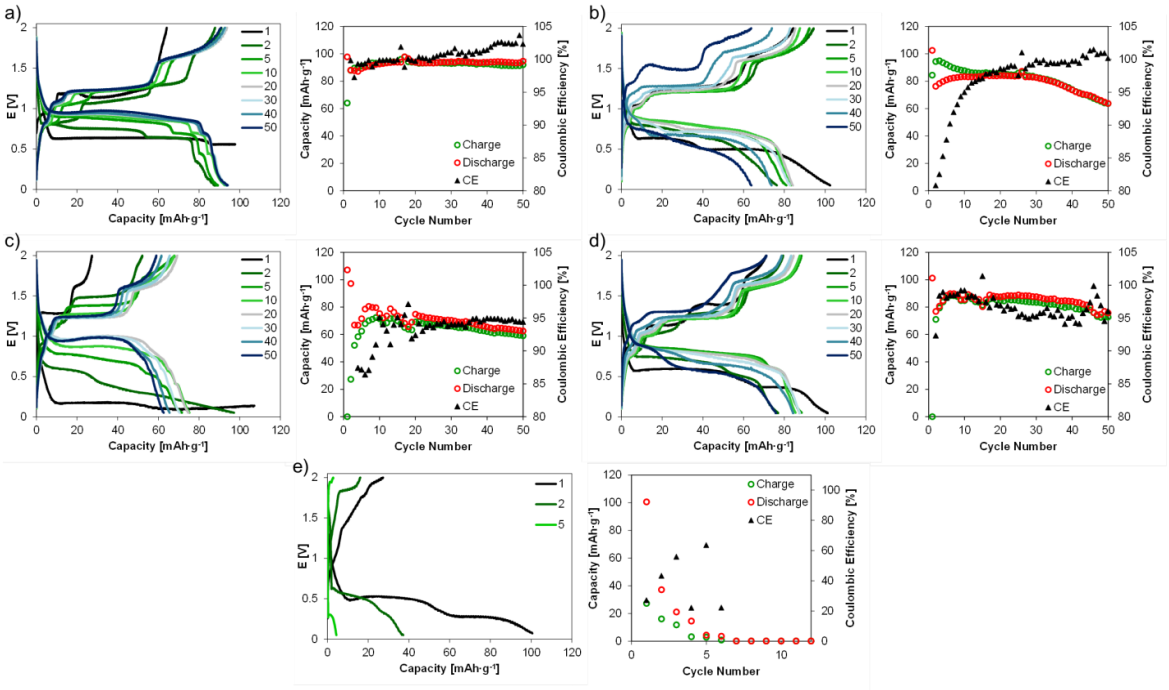

Figure 4.7 Charge-discharge behaviour of Mg cells composed of Chevrel phase cathodes, Mg anodes and solutions of aluminates **12** and **14** at room temperature (rate: C/25). 0.25 M DME solutions of a) chloride-containing **12**, b) chloride-containing **14**, c) chloride-free **12**, d) chloride-free **14**, and e) chloride-containing **15** used as electrolytes.

(Figure 4.8a). Five distinct ^{23}Na resonances are seen in the ^{23}Na NMR spectrum (the fitted spectrum of the centreband region is displayed in Figure 7.1 in the Synthetic Procedures and Characterization section of Chapter 7); the presence of residual NaCl is readily confirmed by the sharp and intense resonance at 7.2 ppm. A saturation-recovery experiment (Figure 7.2) reveals that a broad resonance at −10.8 ppm exhibits fast spin-lattice T_1-relaxation consistent with a Na spin near the paramagnetic molybdenum centre, i.e., inserted into the CP. In addition, the broad resonance at 344.8 ppm is also likely to be associated with the CP, but measurement of the T_1 was not possible due to its low intensity. Two extra resonances are observed at 84.2 and 22.8 ppm in the ^{23}Na NMR spectrum, the former displaying a distinctive quadrupolar lineshape under MAS (C_Q = 3.7 MHz, η = 0). Their long relaxation times suggest that they are from diamagnetic impurity components, such as a Na^+-counterion complex, a Na^+-solvent complex, or an inorganic precipitate.

Regarding the main resonance at −10.8 ppm, this ‘paramagnetic’ shift is much smaller than the typical hyperfine ^{23}Na shifts in paramagnetic transition metal oxide systems, which are of the order of hundreds of ppm. To elucidate the origin of these peaks, the ^{23}Na NMR spectrum of a CP cathode discharged against Na to 145 mAh·g^{-1} (at 0.75 V vs. Na) is also shown in Figure 7.8a (cell discharge profile shown in Figure

7.4). While a ^{23}Na NMR study of cycled Chevrel phases has not been reported previously, diffraction experiments conducted on sodiated Chevrel phases have shown that (i) initial Na intercalation in Mo_6S_8 results in Na occupying the pseudocubic cavity A (cavity with inner-ring arrangement of Na sites) and (ii) subsequent intercalation to occupy the cavity B (cavity with outer-ring arrangement of Na sites) allows up to 3.7 Na per formula unit of Mo_6S_8 (Figure 7.8b).[37–39] Na sites in cavity B can additionally be separated into outer, central, and peripheral sites which have increasing site potential energy in that order.[38] Assuming that the same site preference holds for Na intercalation in Mg-electrolytes, the major paramagnetic ^{23}Na resonance observed in Mg-discharged sample should come from the Na in cavity A. Experimentally, only the -10.8 ppm resonance has significant intensity (apart from the diamagnetic resonances separated by T_1 measurements) on the Mg-discharged sample.

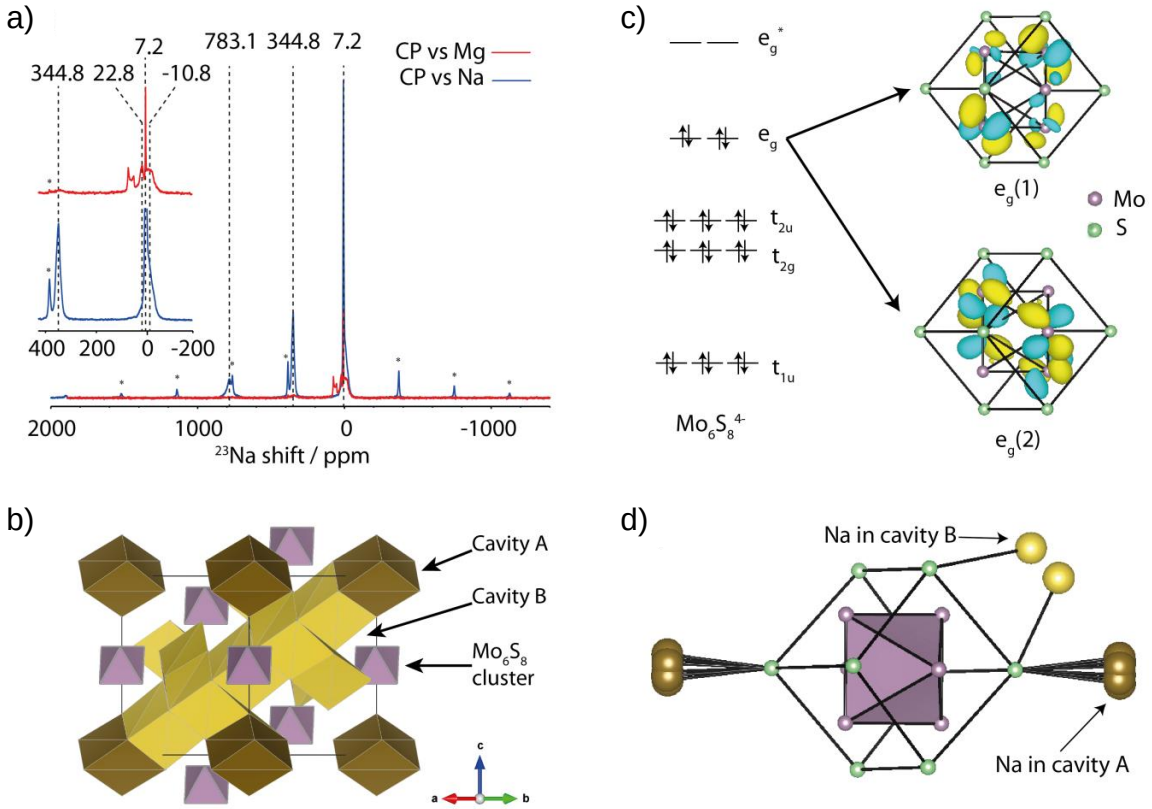

Figure 4.8 Analysis of discharged CP cathodes. a) ^{23}Na solid-state NMR spectra of Mo_3S_4 discharged against Na metal (blue) and discharged against Mg metal (cell shown in Figure 4.7a; red), with the inset showing the enlarged isotropic region. Both spectra were measured at 50 kHz MAS with recycle delays of 1 s. Spectra intensities were scaled to the active material mass and number of scans. Spinning sidebands are marked with asterisks (*). b) Solid-state structure of Mo_6S_8 showing the cavities A (brown) and B (gold). c) Schematic molecular orbital diagram of the $Mo_6S_8^{4-}$ cluster and isosurface plot of the two e_g HOMOs formed by the appropriate combination of the Mo 4d orbitals. Only the Mo dx^2-y^2 orbital (pointing towards the edges of S_8 cube) contributes significantly to this HOMO (orbital phases are indicated by yellow and blue colours). d) Local environment around the Mo_6S_8 cluster with the adjacent Na sites.

Hence, this resonance is assigned to Na in cavity A, and we tentatively assign the ^{23}Na resonances at 344.8 and 783.1 ppm to the outer and central Na sites in cavity B.

To support this assignment, an electronic structure calculation of the Mo_6S_8 molecular cluster was performed. Whereas a full solid-state calculation of sodiated Chevrel phases would be challenging due to the Na disorder in the unit cell, a simple frontier orbital analysis of the Mo_6S_8 cluster should give insights on the nature of orbitals involved in the spin density transfer that are responsible for the observed Na hyperfine shift. The molecular orbital (MO) diagram of the fully reduced $Mo_6S_8^{4-}$ cluster is shown in Figure 4.8c, alongside the MO isosurface plot of the highest occupied MO (HOMO). From the diagram, it is clear that (i) the redox process upon Na (de)insertion should involve the e_g MO, and this orbital should be singly occupied at intermediate levels of sodiation (e.g. $NaMo_6S_8$), and (ii) the lobes of this MO point towards the edges of the S_8 cube. This result is in agreement with a previous report on Chevrel-type molecular clusters.[40] By comparing this MO plot to the local arrangement of Na sites around the Mo_6S_8 cluster (Figure 4.8d), it is clear that the Na atoms in cavity B should either have a direct overlap with the Mo 4d lobes, or have a delocalization-type pathway via Mo-S-Na bonding, both of which should result in positive Na hyperfine shift. Na atoms in cavity A, however, have neither a possibility for a direct overlap nor a delocalization-type pathway since the S-Na bonds point away from the S_8 cube along the threefold rotation axis; this would result in a very small hyperfine contribution to the observed ^{23}Na shift, and subsequently a shift of close to zero is expected, in agreement with the experimental spectra. However, we note that this very simple picture only involves one Mo_6S_8 cluster and the surrounding Na ions. More complex factors such as local ordering of Na ions inside the lattice, which is difficult to observe with diffraction, could also result in multiple resonances. Furthermore, different cation ordering schemes are likely when both Na and Mg intercalate into the lattice.

Comparing the two samples discharged versus Mg and Na, the two spectra share common resonances at 344.8 ppm (weak) and −10.8 ppm (strong), confirming the presence of Na in the CP cycled versus Mg. The resonance at 783.1 ppm is not observed in the Mg-discharged sample, suggesting that the extent of intercalation with Na was not sufficient to fill cavity B. Furthermore, we can compare the peak integrals of the −10.8 ppm resonances of the Na-discharged and Mg-discharged samples to provide a rough estimate of the contribution of Na insertion to the overall capacity. In

the Mg-discharged CP sample, around 22 % (ca. 21 $mAh \cdot g^{-1}$) of the total capacity (94 $mAh \cdot g^{-1}$ at cycle 50) is due to Na insertion, taking the observed discharge capacities and active material masses into account. We do note that possible different relaxation behaviour and quadrupolar parameters in Na-CP and Mg-CP may have non-negligible influence on the final estimation; it is however clear that Na insertion occurs alongside the Mg insertion in these cells due the presence of dissolved Na in the electrolyte solution. This additional capacity due to Na insertion may also be evidenced by the capacities of the cell containing chloride-free **12**, which are consistently lower after the initial stages of cycling (Figure 4.7c). This significant difference in capacities is not observed for cells containing solutions of **14**, possibly indicating that the availability of Na for intercalation is different in these electrolyte systems (Figures 4.7b and 4.7d).

4.3 Conclusions

In summary, we have established a general method for the preparation of Mg aluminate salts having the formula $Mg[Al(OR)_4]_2$ using $Mg(AlH_4)_2$ as a common precursor. This method is effective for producing a range of fluorinated/non-fluorinated alkyl and aryl Mg aluminates that can be isolated as solid materials. Single-crystal X-ray analysis of two of these compounds, **11** (^{t}Bu) and **14** (Ph), shows ion-pairing with Mg, giving insight into their possible interactions in solution and electrochemical behaviour. X-ray analysis also showed a hydrolysis product, **12'**, which highlights the moisture sensitivity of the perfluoro-*tert*-butoxy aluminate **12** and represents the first example of a bridging Al-O(H)-Mg motif. Importantly, this method has provided access to two aluminates, **12** and **14**, that do not contain β-hydrogen atoms, facilitating electrochemical studies of aluminate salts which cannot undergo the β-hydride elimination decomposition pathway reported for $Mg[Al(OC\mathit{H}(CF_3)_2)_4]_2$.

LSV measurements of electrolyte mixtures of **12** and **14** showed variable oxidative stability depending on whether or not chloride was present in the solution, originating from NaCl in the $Mg(AlH_4)_2$ material. Electrolyte solutions of the Mg aluminates **12** and **14** presented here could be cycled reversibly on a Pt working electrode over 50 cycles, showing clear Mg plating and stripping behaviour. Extended galvanostatic cycling measurements (200 cycles) conducted with both chloride containing and chloride-free **12** and **14** using Au working electrodes show that the presence of chloride has a significant influence on the cycling efficiency, with chloride-containing electrolyte mixtures cycling more efficiently and with lower overpotentials within fewer cycles. In addition, galvanostatic cycling of these

electrolyte systems in Mg symmetric cells shows low overpotentials the application of positive and negative potentials, consistent with plating/stripping of Mg and demonstrating the stability of the electrolyte systems on Mg electrodes over 100 cycles. These measurements further reveal that chloride-containing mixtures result in lower plating/stripping overpotentials. These finding are in line with previous reports in which electrolytes have been demonstrated to benefit from the addition of chloride salts.[41,42] Importantly, electrolyte mixtures of **12** and **14** have been demonstrated to cycle in Mg cells containing Chevrel phase cathodes with good capacity retention and high Coulombic efficiencies.

While chloride-free mixtures of **2** exhibit good oxidative stability on Al, Au, and Pt electrodes (ca. 3 V vs. Mg), generally the onsets of oxidation are lower than those exhibited by the $Mg[Al(O^iPr^F)_4]_2$ system investigated by the Arnold group.[8] It is clear that the two synthetic methods used for the generation of the Mg aluminates can result in different by-products, such as chloride in the present systems or the presence of unreacted $Mg(O^iPr^F)_2$ or $Al(O^iPr^F)_3$ from stoichiometric imbalances in the previous report, which could influence electrolyte stability.[8] Thus, it is difficult to conclude whether the absence of β-hydrogen atoms significantly influences the oxidative stability and leads to increased cycling stability in cells containing CP cathodes, or whether the differences originate from the role of impurities, breakdown products, and the salts themselves on electrode passivation.

As is observed in the Au and Mg symmetric cells, it is apparent that the presence of chloride is beneficial to the cycling of the CP cells but their performance cannot be attributed to chloride alone. The presence of Na in the CP cathodes extracted from cells cycled with chloride-containing electrolyte, as indicated by ^{23}Na solid-state NMR measurements, likely influences the operation of the cells on the cathode side, as indicated by ^{23}Na solid-state NMR on CP cathodes extracted from cells cycled with chloride-containing electrolyte. Based on the ^{23}Na NMR analysis, it is apparent that insertion of Na along with Mg contributes to the overall capacity of certain cells but it is not known whether the insertion/removal of the less charge-dense Na^+ cation affects Coulombic efficiencies. The exact influence Na insertion has on Mg cycling bears further investigation as such co-insertion of Na could provide a basis for the development of Mg/Na hybrid battery systems.

4.4 Future Work

Chloride-free **12** is a promising non-corrosive chloride-free electrolyte that exhibits high oxidative stability on Al, stable Mg plating/stripping behaviour using Au and Mg electrodes with low overpotentials, and high Coulombic efficiencies and good capacity retention when cycled against the CP cathode.[7] Accordingly, we are interested in investigating this system in cells containing high voltage cathode materials such as α-MnO_2 or vanadate materials to move toward higher energy density devices or cells containing high-capacity sulfur-based cathodes.

Owing to the versatility of the underlying synthesis, this methodology could be extended to the use of other alcohols, including bidentate diols. One particularly interesting diol that could be employed is the 3,3',5,5'-tetra-*tert*-butyl-2,2'-biphenol shown in Figure 4.9. Reaction of this diol with $LiAlH_4$ and $NaAlH_4$ in Et_2O or THF has been shown to afford the corresponding aluminate, or 'altebate', salts in high yields, which are moderately stable to hydrolysis.[15] The analogous reaction involving $Mg(AlH_4)_2$ in THF or DME could afford a highly soluble and ion-separated electrolyte salt with good electrochemical stability (Figure 4.9). The bidentate nature of the diol could impart stability to the anion through the chelate effect. Even if one Al-O bond is cleaved during cycling, the other Al-O bond of the diol could continue to maintain the integrity of the anion, possibly until the other Al-O bond can reform. Further the large steric profile and insulating nature of the *tert*-butyl groups decorating the biphenol fragment could limit electron transfer to or from the aluminate core, thus providing enhanced electrochemical stability.

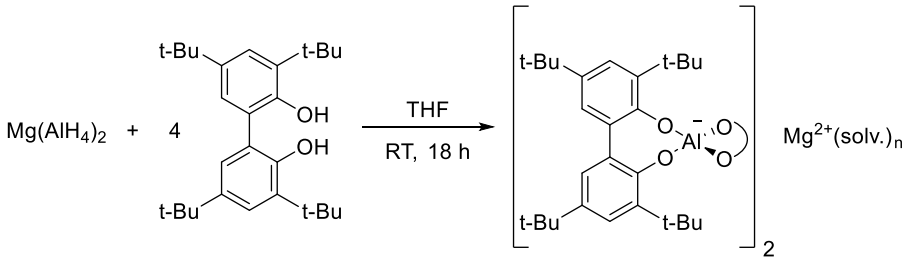

Figure 4.9 Proposed synthesis of a Mg altebate salt.

Additionally, the typically high solubility of salts of weakly coordinating anions (WCAs) in non-polar solvents offers a unique opportunity to study the electrochemistry of some of these salts in non-traditional solvents. Owing to their non-interacting nature, the Gibbs energy of solvation of salts composed of WCAs can easily outweigh the lattice energies of these salts as the WCAs are generally quite large.[43,44] Krossing and co-workers have employed the $Al(O^tBu^F)_4^-$ anion to great effect for the isolation of a number of unstable

cationic complexes where the non-interacting nature of the anion is critical.[44–46] Depending on appropriate solvation of the cation, the electrochemistry of salts such as **12** or the proposed $Mg(altebate)_2$ could be investigated in solvents such as toluene or even alkanes. Electrolyte systems comprising such solvents could allow for the impact of different donor solvents/ligands on cycling behaviour to be studied as the solvents/ligands could be added in a controlled fashion and compared within a common solvent 'matrix'. This would not be limited to Mg salts, as the less charge-dense Na salts could exhibit higher solubility in these solvents.

4.5 References

1 J. Muldoon, C. B. Bucur, A. G. Oliver, T. Sugimoto, M. Matsui, H. S. Kim, G. D. Allred, J. Zajicek and Y. Kotani, *Energy Environ. Sci.*, 2012, **5**, 5941–5950.

2 T. Liu, Y. Shao, G. Li, M. Gu, J. Hu, S. Xu, Z. Nie, X. Chen, C. Wang and J. Liu, *J. Mater. Chem. A*, 2014, **2**, 3430–3438.

3 R. E. Doe, R. Han, J. Hwang, A. J. Gmitter, I. Shterenberg, H. D. Yoo, N. Pour and D. Aurbach, *Chem. Commun.*, 2014, **50**, 243–245.

4 Z. Zhao-Karger, X. Zhao, D. Wang, T. Diemant, R. J. Behm and M. Fichtner, *Adv. Energy Mater.*, 2015, **5**, 1401155.

5 S. Ha, Y. Lee, S. W. Woo, B. Koo, J. Kim, J. Cho, K. T. Lee and N. Choi, *ACS Appl. Mater. Interfaces*, 2014, **6**, 4063–4073.

6 O. Tutusaus, R. Mohtadi, T. S. Arthur, F. Mizuno, E. G. Nelson and Y. V. Sevryugina, *Angew. Chem. Int. Ed.*, 2015, **54**, 7900–7904.

7 J. Muldoon, C. B. Bucur, A. G. Oliver, J. Zajicek, G. D. Allred and W. C. Boggess, *Energy Environ. Sci.*, 2013, **6**, 482–487.

8 J. T. Herb, C. A. Nist-Lund and C. B. Arnold, *ACS Energy Lett.*, 2016, **1**, 1227–1232.

9 D. Aurbach, G. S. Suresh, E. Levi, A. Mitelman, O. Mizrahi, O. Chusid and M. Brunelli, *Adv. Mater.*, 2007, **19**, 4260–4267.

10 N. Pour, Y. Gofer, D. T. Major and D. Aurbach, *J. Am. Chem. Soc.*, 2011, **133**, 6270–6278.

11 S. Tsujioka, B. G. Nolan, H. Takase, B. P. Fauber and S. H. Strauss, *J. Electrochem. Soc.*, 2004, **151**, A1418–A1423.

12 Z. Zhao-Karger, M. E. Gil Bardaji, O. Fuhr and M. Fichtner, *J. Mater. Chem. A*, 2017, **5**, 10815–10820.

13 I. Krossing, *Chem. Eur. J.*, 2001, **7**, 490–502.

14 S. Bulut, P. Klose, M.-M. Huang, H. Weingärtner, P. J. Dyson, G. Laurenczy, C. Friedrich, J. Menz, K. Kümmerer and I. Krossing, *Chem. Eur. J.*, 2010, **16**, 13139–13154.

15 B. F. Straub, M. Wrede, K. Schmid and F. Rominger, *Eur. J. Inorg. Chem.*, 2010, 1907–1911.

16 I. Krossing and I. Raabe, *Angew. Chem. Int. Ed.*, 2004, **43**, 2066.

17 D. Aurbach, H. Gizbar, A. Schechter, O. Chusid, H. E. Gottlieb, Y. Gofer and I. Goldberg, *J. Electrochem. Soc.*, 2002, **149**, A115.

18 Y. Kim, E.-K. Lee, J.-H. Shim, Y. W. Cho and K. B. Yoon, *J. Alloys Compd.*, 2006, **422**, 283–287.

19 J. A. Meese-Marktscheffel, R. E. Cramer and J. W. Gilje, *Polyhedron*, 1994, **13**, 1045–1050.

20 J. Sassmannshausen, R. Riedel, K. B. Pflanz and H. Chmiel, *Z. Naturforsch.*, 1993, **48b**, 7–10.

21 G. Mohammadnezhad, M. M. Amini and H. R. Khavasi, *Dalt. Trans.*, 2010, **39**, 10830–10832.

22 Anne Kraft, Josephine Possart, Harald Scherer, Jennifer Beck, Daniel Himmel and Ingo Krossing, *Eur. J. Inorg. Chem.*, 2013, 3054–3062.

23 D. Lv, T. Xu, P. Saha, M. K. Datta, M. L. Gordin, A. Manivannan, P. N. Kumta and D. Wang, *J. Electrochem. Soc.*, 2013, **160**, A351–A355.

24 S. Yagi, A. Tanaka, Y. Ichikawa, T. Ichitsubo and E. Matsubara, *J. Electrochem. Soc.*, 2013, **160**, C83–C88.

25 C. Wall, Z. Zhao-Karger and M. Fichtner, *ECS Electrochem. Lett.*, 2015, **4**, C8–C10.

26 Z. Lu, A. Schechter, M. Moshkovich and D. Aurbach, *J. Electroanal. Chem.*, 1999, **466**, 203–217.

27 Z. Ma, M. Kar, C. Xiao, M. Forsyth and D. R. MacFarlane, *Electrochem. Commun.*, 2017, **78**, 29–32.

28 J. L. Esbenshade, C. J. Barile, T. T. Fister, K. L. Bassett, P. Fenter, R. G. Nuzzo and A. A. Gewirth, *J. Phys. Chem. C*, 2015, **119**, 23366–23372.

29 K. A. See, K. W. Chapman, L. Zhu, K. M. Wiaderek, O. J. Borkiewicz, C. J. Barile, P. J. Chupas and A. A. Gewirth, *J. Am. Chem. Soc.*, 2016, **138**, 328–337.

30 J. G. Connell, B. Genorio, P. P. Lopes, D. Strmcnik, V. R. Stamenkovic and N. M. Markovic, *Chem. Mater.*, 2016, **28**, 8268–8277.

31 W. Li, S. Cheng, J. Wang, Y. Qiu, Z. Zheng, H. Lin, S. Nanda, Q. Ma, Y. Xu, F. Ye, M. Liu, L. Zhou and Y. Zhang, *Angew. Chem. Int. Ed.*, 2016, **55**, 6406–6410.

32 J. T. Herb, C. A. Nist-Lund and C. B. Arnold, *J. Mater. Chem. A*, 2017, **5**, 7801–7805.

33 T. J. Carter, R. Mohtadi, T. S. Arthur, F. Mizuno, R. Zhang, S. Shirai and J. W. Kampf, *Angew. Chem. Int. Ed.*, 2014, **53**, 3173–3177.

34 R. Mohtadi, M. Matsui, T. S. Arthur and S. J. Hwang, *Angew. Chem. Int. Ed.*, 2012, **51**, 9780–9783.

35 N. Sa, B. Pan, A. Saha-Shah, A. A. Hubaud, J. T. Vaughey, L. A. Baker, C. Liao and A. K. Burrell, *ACS Appl. Mater. Interfaces*, 2016, **8**, 16002–16008.

36 E. N. Keyzer, H. F. J. Glass, Z. Liu, P. M. Bayley, S. E. Dutton, C. P. Grey and D. S. Wright, *J. Am. Chem. Soc.*, 2016, **138**, 8682–8685.

37 E. Levi, G. Gershinsky, D. Aurbach, O. Isnard and G. Ceder, *Chem. Mater.*, 2009, **21**, 1390–1399.

38 E. Levi, G. Gershinsky, D. Aurbach and O. Isnard, *Inorg. Chem.*, 2009, **48**, 8751–8758.

39 P. Saha, P. H. Jampani, M. K. Datta, D. Hong, C. U. Okoli, A. Manivannan and P. N. Kumta, *J. Phys. Chem. C*, 2015, **119**, 5771–5782.

40 T. Hughbanks and R. Hoffmann, *J. Am. Chem. Soc.*, 1983, **105**, 1150–1162.

41 I. Shterenberg, M. Salama, H. D. Yoo, Y. Gofer, J.-B. Park, Y.-K. Sun and D. Aurbach, *J. Electrochem. Soc.*, 2015, **162**, A7118–A7128.

42 N. Sa, B. Pan, A. Saha-Shah, A. A. Hubaud, J. T. Vaughey, L. A. Baker, C. Liao and A. K. Burrell, *ACS Appl. Mater. Interfaces*, 2016, **8**, 16002–16008.

43 I. Krossing and A. Reisinger, *Coord. Chem. Rev.*, 2006, **250**, 2721–2744.

44 T. S. Cameron, A. Decken, I. Dionne, M. Fang, I. Krossing and J. Passmore, *Chem. Eur. J.*, 2002, **8**, 3386–3401.

45 I. Krossing and L. Van Wüllen, *Chem. Eur. J.*, 2002, **8**, 700–711.

46 P. J. Malinowski and I. Krossing, *Angew. Chem. Int. Ed.*, 2014, **53**, 13460–13462.

5. Regioselective 1,4-Hydroboration of Pyridines Catalyzed by an Acid-Initiated Boronium Cation and CO_2 Hydroboration

5.1 Introduction

5.1.1 Dihydropyridines

Dihydropyridines (DHPs) are an important class of compounds with many pharmacological applications. First synthesized by Hantzsch in 1882,[1] the subsequent discovery of the medicinal and synthetic potential of DHPs has led to their being the subject of sustained interest since the 1950s.[2–10] DHPs are found in cells in the reduced form of the coenzyme NAD^+, NADH (Figure 5.1). NADH is a key reductant in biological redox reactions, acting as a source of hydride. The reducing power of NADH lead to many studies on the synthesis of DHPs and their reactivity as enantioselective reductants.[5] Among DHPs, the 1,4-regioisomer has also found use as the centre of many effective calcium-channel modulating agents and various 1,4-DHP derivatives have been used to treat migraines, high blood pressure, Alzheimer's disease, dementia, and multidrug-resistant cancers.[7,11]

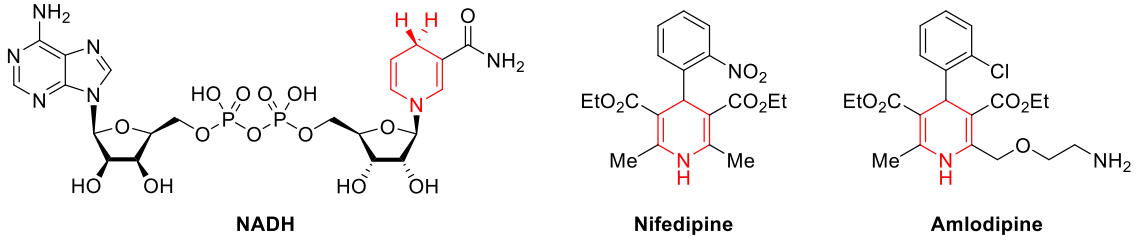

Figure 5.1 Example dihydropyridine derivatives NADH, Nifedipine, and Amlodipine.

5.1.2 Synthesis of Dihydropyridines

A number of stoichiometric methods have been developed for the formation of DHPs, including the Hantzsch synthesis, reduction of pyridines by complex metal hydrides, and nucleophilic additions to pyridines.[12–16] Hantzsch-type reactions permit the generation of a broad range of 1,4-DHPs through the reaction of two equivalents of a β-ketoester or 1,3-diketone with a nitrogen donor and an aldehyde (Scheme 5.1a).[2,17] While these routes are generally robust and high yielding, more intensive challenging synthetic methods are required to form asymmetric 1,4-DHPs. These methods for asymmetric DHP synthesis can require numerous steps, pre-activation of the pyridines, and can result in poor reduction regioselectivity—affording both the 1,2- and 1,4-

regioisomers—which can limit their utility.[8] Reductions of pyridines using hydrides such as $NaBH_4$ have been found to generate DHPs (Scheme 5.1b).[18] These reactions typically require substrates containing electron-withdrawing groups, such as nitriles, in the 3-position to activate the pyridine ring and also suffer from moderate yields as well as poor regioselectivity.[14,19] Another stoichiometric method involves nucleophilic attack on pyridines, resulting in functionalized DHPs (Scheme 5.1c). In these cases the regioselectivity is influenced by the hardness/softness of the nucleophile, with hard and soft nucleophiles selectively undergoing 1,2- and 1,4-additions, respectively.[20–22] Again these reactions typically suffer from relatively poor regioselectivity—the steric profile of the N-functionality directs attack at the 4-position—and require stoichiometric activation of the pyridine substrate.[23]

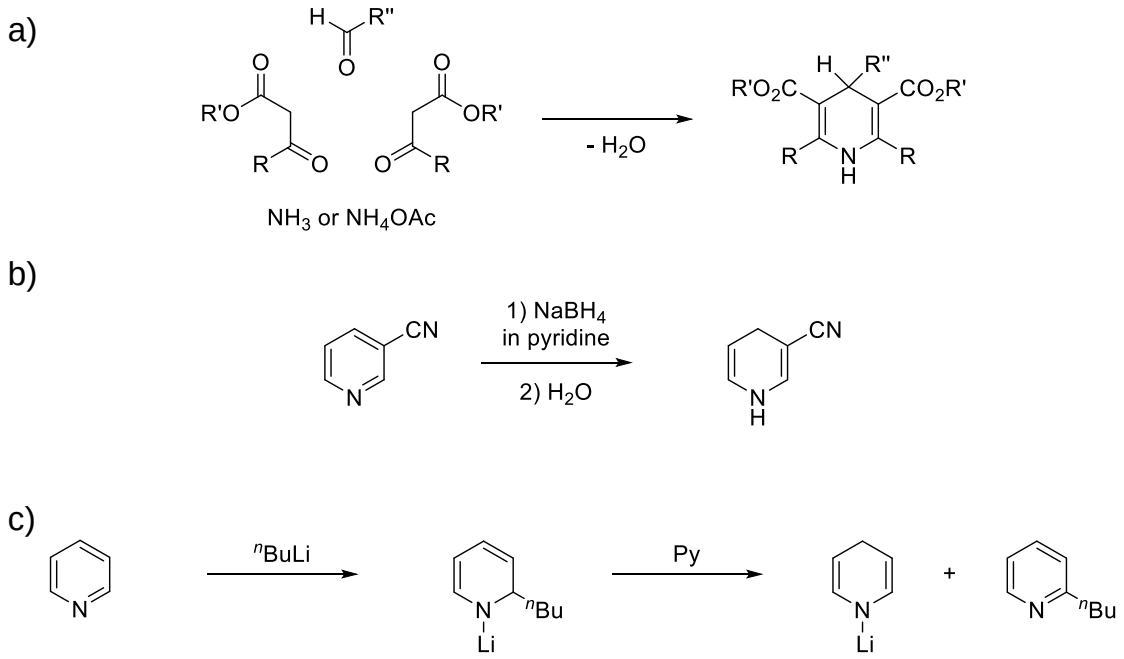

Scheme 5.1 Stoichiometric synthesis of DHPs via a) Hantzsch-type methods, b) hydride reduction, and c) nucleophilic attack on pyridine and subsequent hydride transfer.

Many catalytic reactions have also been developed that enable highly regioselective reductions of a broad range of functionalized pyridines.[24–34] Catalytic hydrogenations of pyridines have been studied using a host of transition metal catalysts.[35] Due to the high activity of these catalysts selective reduction is challenging and multiple reductions of the substrate is common. Other methodologies, which are relevant to the synthesis of a broad scope of DHPs from functionalized pyridines, rely on the addition of an E-H (E = Si or B) bond to the pyridine substrate. Hydrosilylation and hydroboration reactions of pyridines involve the functionalization of the pyridine nitrogen with a silyl or boryl group with concomitant addition of a hydride (typically

from the silyl-/borylating agent) at the 2- or 4-position on the ring (Scheme 5.2). Additionally, heterogeneous catalytic hydrosilylations of pyridines have been investigated since 1966[36] and have been developed significantly by the Harrod, Nikonov, and Oestreich groups.[25,26,31,34]

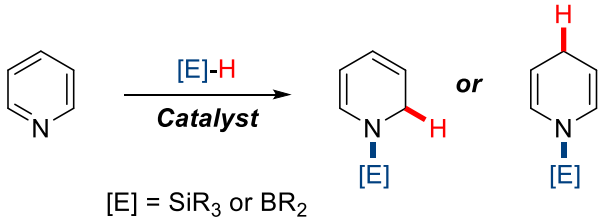

Scheme 5.2 Example of 1,2-/1,4-hydrosilylation and hydroboration.

A number of catalysts have been developed for 1,2- and 1,4-selective pyridine hydroboration reactions. Mg(II)-hydride complexes investigated by Hill and Harder have been shown to promote catalytic hydroboration of pyridines; however, in these systems many substrates reacted to give mixtures of the 1,2- and 1,4-hydroboration products.[37,38] Advances reported by the groups of Suginome and Marks show efficient and functional-group tolerant methods for the 1,2-hydroboration of pyridines using Rh(I)[39] and La(III)[40] catalysts, respectively. While highly selective, the Rh(I) and La(III) catalysts are costly and air sensitive. The Mg(II) and La(III) catalyzed transformations follow similar mechanisms involving metal hydrides (Scheme 5.3). In these mechanisms, pyridine coordinated to a metal hydride undergoes an intramolecular reduction (dearomatization, Scheme 5.3) generating a metal amide. Following reduction it is proposed that pinacol borane (HBpin) associates with the complex and transfers a hydride to the metal and adds Bpin to the pyridyl fragment by way of a four-membered σ-bond metathesis transition state. The Rh catalyzed reaction is proposed to begin with the oxidative addition of the H-B bond of HBpin to give a Rh(III) species with pyridine coordinated (Scheme 5.3). The Py-Rh(III) hydride complex then undergoes an intramolecular dearomatization step to afford the metal amide species, similar to the Mg and La cases. Finally, the 1,2-DHP is generated via reductive elimination of the amide and boryl groups.

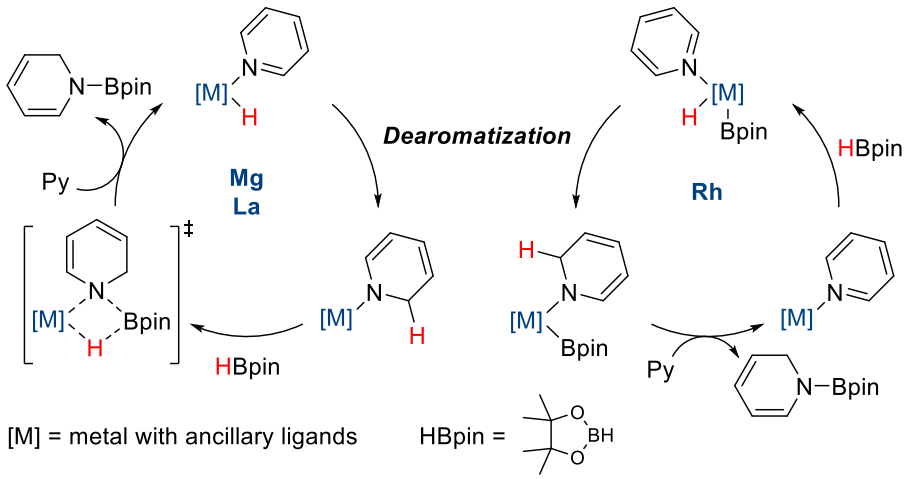

Scheme 5.3 Proposed mechanisms for Mg and La (left), and Rh (right) catalyzed 1,2-hydroboration of pyridine.

In contrast to the catalytic 1,4-selective hydrosilylation reactions developed by Nikonov[31] and Oestreich,[34] general catalytic 1,4-hydroboration reactions have been developed to a lesser extent. In 2015, Wang and co-workers demonstrated a method for regioselective 1,4-hydroboration using a fluoro-organoborane Lewis acid catalyst that affords DHPs in high yields under mild conditions.[41] The highly electrophilic fluoro-organoborane was demonstrated to abstract a hydride from a pyridine-activated HBpin, resulting in a pyridine-stabilized boronium cation that is then reduced by the fluoro-organoborohydride to generate the hydroboration product (Scheme 5.4). Additionally, the groups of Okuda and Gunanathan have used Mg(II) hydridotriphenylborate and Ru(II) catalysts, respectively, for the selective 1,4-hydroboration of pyridines.[42,43] The Mg(II) hydridotriphenylborate work presented by Okuda operates in a very similar manner to that of Wang's fluoro-organoborane whereas the Ru(II) chemistry proceeds via hydride-transfer from a Ru(II)-hydride, generated *in situ*, to pyridine. In each of these examples, selectivity for 1,4-hydroboration is a result of steric effects. The sterically-encumbered hydridic species that are active in these cases are unable to approach the 2-position of the pyridine rings and, therefore, attack at the accessible 4-position.

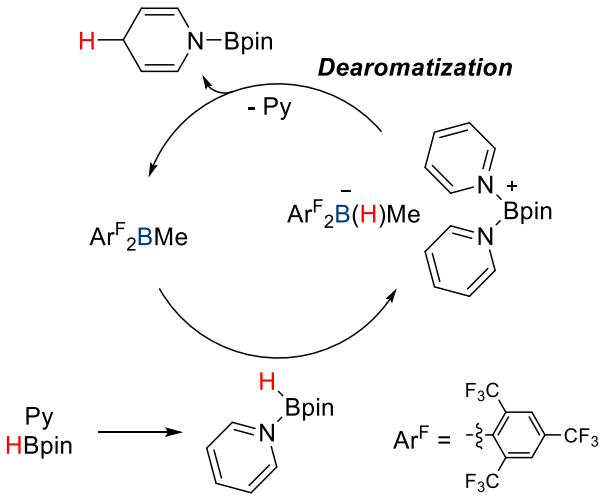

Scheme 5.4 Proposed mechanisms for the fluoro-organoborane catalyzed 1,4-hydroboration of pyridine.

5.1.3 Hydroboration of CO_2

The chemical reduction of CO_2 is an important reaction that acts to both reduce levels of the greenhouse gas from the atmosphere as well as to generate useful carbon-containing chemical feedstocks.[44,45] Homogeneous catalytic hydroborations and hydrosilylations of CO_2 have been extensively investigated and are promising avenues for the conversion of CO_2 to relevant precursors for synthesis and fuels. Many of these catalytic transformations been developed using transition metal,[46–48] frustrated Lewis pair (FLP),[49,50] and main group hydride catalysts.[42,51–55] Four CO_2 reduction products are typically produced from these reactions: the singly reduced formate, the doubly reduced acetal, the triply reduced methoxide, and quadruply reduced methane (Scheme 5.5).[56] The latter two species are formed concomitantly with one (methoxide) or two (methane) equivalents of pinBOBpin when HBpin is used as the reductant. Among these four species, selective isolation of the formate product is challenging as it is easily reduced by subsequent additions of borane or silane, commonly leaving the methoxide as the species obtained selectively.[52] Still, the formate and acetal species are very often observed as transient species during the formation of the methoxide. Both the formate and acetal species have been used for secondary transformations via *in situ* reactions with nucleophiles, affording a host of materials including amides, N-methyl amines, and terminal alkenes.[56–58] Further, reduction to the methoxide species provides access to methanol, a potentially important transportable liquid fuel that can be converted to synthetic combustible hydrocarbons as alternatives to conventional fossil fuels.[44]

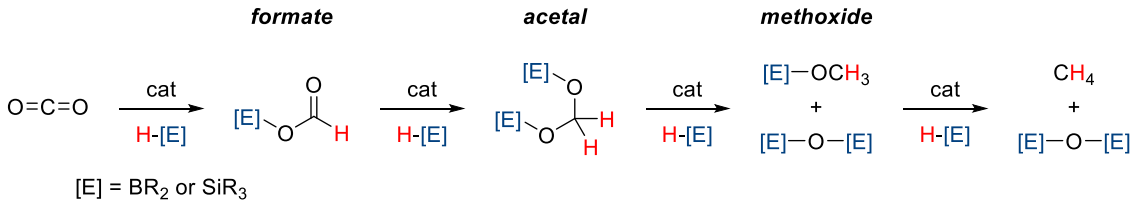

Scheme 5.5 Reduction products from the catalytic hydroboration or hydrosilylation of CO_2.

Many catalysts have been employed to carry out the reduction of CO_2 to the various species described above, including transition metal complexes (Ru,[47,59] Fe,[56] Ni,[46] and Cu[60]), FLPs,[54,61–63] alkaline earth metals (Mg and Ca),[53] and main group hydrides.[42,64] While these catalyst have been shown to be highly effective catalysts for producing various CO_2 reduction products, they are often air/moisture sensitive, costly if commercially available, or, if not, must be synthesized. Of particular relevance to the study presented in this chapter is work reported by Okuda and co-workers on the hydrosilylation of CO_2 using BPh_3 as a catalyst.[52] This reaction involves the reaction of CO_2 with $PhMeSiH_2$ in the presence of 10 mol% BPh_3 to afford selectively the silylformate, $PhMeSiH(O_2CH)$. Okuda and co-workers propose a 'dual activation' mechanism involving a BPh_3-mediated hydride abstraction from $PhMeSiH_2$ along with activation of CO_2 through dynamic coordination to BPh_3 (Scheme 5.6). To support this proposed mechanism, the authors show that the reaction rate increases with increasing solvent dielectric constant (propylene carbonate > CD_3NO_2 > CD_3CN) and that less polar solvents (C_6D_6, d_8-THF) show very little conversion, indicating that stabilization of the polarized transient species is crucial.

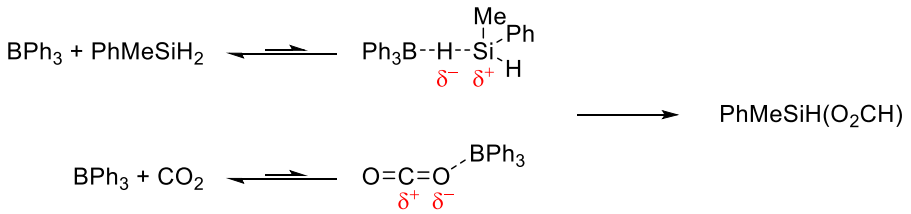

Scheme 5.6 Dual activation mechanism for the BPh_3-catalyzed hydrosilylation of CO_2 proposed by Okuda and co-workers, showing the polarization of transient species.

In this chapter, an efficient and practical metal-free catalytic method for the highly regioselective 1,4-hydroboration of pyridines is presented, using only pyridines, pinacolborane, and low loadings of an inexpensive and commercially available ammonium salt initiator (NH_4BPh_4). This method relies on the formation of a boronium cation through the reaction between pyridine-activated HBpin and NH_4BPh_4, releasing H_2 and NH_3. Borocations have been well established as effective catalysts for the reduction and boration of various substrates;[65–69] a number of these

cations have been similarly generated using Brønsted acids.[70–72] In addition to generating the active boronium catalyst, the pyridine-activated HBpin acts as the hydride source for pyridine reduction. This reaction provides access to 1,4-DHPs containing reactive functional groups and the active hydridic species affords 1,4-hydroboration products that are not easily accessible through other metal-free methods. Further, solvent polarity has been found to play a significant role in the regioselectivity of the reaction, whereby tuning the solvent system of the reaction permits 1,2-hydroboration reactivity with high ratios of the 1,2- regioisomer.

We also demonstrate that the same ammonium salt can be used to initiate the hydroboration of CO_2 with HBpin. Mechanistic studies show that the reaction in THF proceeds through the decomposition of NH_4BPh_4 to BPh_3 and C_6H_6 along with NH_3. ^{1}H NMR spectroscopic analysis shows that both NH_4BPh_4 and BPh_3 result in very similar species during catalysis.

5.2 Results and Discussion

5.2.1 Catalytic 1,4-Hydroboration of Pyridines[†]

The work presented here follows on from a chance discovery during unrelated studies in which we found that the reaction of 10 mol% $(Py_2H)BPh_4$, synthesized in a similar manner to $(Py_2H)PF_6$, **1**, presented in Chapter 2, to equimolar amounts of dry pyridine and HBpin in dry CD_3CN resulted in the formation of a colourless gas at room temperature, determined to be H_2 by ^{1}H NMR spectroscopy (δ = 4.57 ppm in CD_3CN). After heating the reaction mixture at 70 °C for 24 hours, ^{1}H NMR spectroscopic analysis showed the formation of 1,2- and 1,4-DHPs in a ratio of 97:3, with a conversion of >95% from pyridine. Intrigued by this result, we decided to explore this reaction in its own right. On reflection, the pyridinium initiator was deemed unsuitable for the investigation of the substrate tolerance of the reaction as the reaction products could be contaminated by amounts of hydroboration products originating from the pyridinium initiator. Accordingly, the mildly acidic ammonium salt NH_4BPh_4 was investigated as an initiator. NH_4BPh_4 acts as both a proton source and introduces a weakly coordinating anion, precluding the formation of unwanted anion-HBpin interactions. Reactions involving **1** were found to result in the transfer of fluoride to the HBpin species, inhibiting the progress of the reaction. The addition of 10 mol% of NH_4BPh_4 to a solution of HBpin (1.5 equiv.) and pyridine (1 equiv.) in dry CD_3CN was again observed to result in the

[†]This work was carried out in collaboration with Part III student Sky S. Kang.

formation of H_2 at room temperature from the reaction of NH_4^+ and hydridic HBpin species. Heating the mixture to 90 °C over a 15 hour period yielded the 1,4-dihydropyridine as the major product along with the 1,2-dihydropyridine as a minor product, as identified by characteristic signals in the ^{1}H NMR spectrum (Table 5.1, entry 1).[38] The loading of NH_4BPh_4 could be lowered to 2.5 mol% while maintaining high yields and selective hydroboration reactivity over reasonable timescales (1,2-:1,4- product ratio of 2:98; Table 5.1, entry 2). In the absence of NH_4BPh_4 minimal conversion to the hydroboration products was observed over a 96 hour period, verifying its role as an initiator (Table 5.1, entries 3). Lowering the reaction temperature to 70 °C required longer reaction times to achieve similar conversions (Table 5.1, entry 4). Interestingly, solvent polarity was found to have a significant effect on the regioselectivity of the reaction, whereby conducting the reaction in C_6D_6 or heptane afforded 1,2- and 1,4-hydroboration products in ratios of 15:85 and 22:78, respectively (Table 5.1, entries 5 and 7). In contrast, the use of the non-donating polar solvent 1,2-difluorobenzene (1,2-DFB) results in excellent 1,4- selectivity (6:94) and high conversion from the starting material (Table 5.1, entry 9).[73] The reaction can also be conducted in pure pyridine (0.5 mL) using 0.015 mmol NH_4BPh_4 and 0.89 mmol HBpin at 90 °C to produce a

Table 5.1 Optimization of reaction conditions for the 1,4-hydroboration of pyridine.

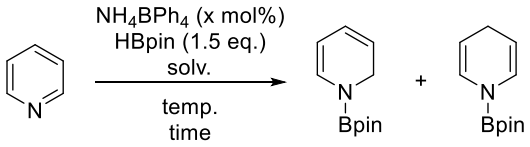

1,2- 1,4-

Entry	NH_4BPh_4 [mol%]	solv.	temp. [°C]	time [h]	conv. [%][a]	1,2-:1,4-
1	10	CD_3CN	90	15	87[b]	2:98
2	2.5	CD_3CN	90	20	>95(72)[c]	2:98
3	0	CD_3CN	90	96	<1	-
4	2.5	CD_3CN	70	72	93	2:98
5	2.5	C_6D_6	90	78	>95	15:85
6	0	C_6D_6	90	96	0	-
7[d]	2.5	heptane	90	96	64	22:78
8[d]	0	heptane	90	96	<1	-
9[d]	2.5	1,2-DFB	90	8	>95	6:94

NMR tube scale reactions performed in a sealed J. Young NMR tube. [a] Determined by ^{1}H NMR spectroscopy. [b] Conversion increased to 90% over a 24 hour period. [c] Isolated yield determined using 3.36 mmol pyridine in a sealed J. Young-type bomb. [d] ^{1}H NMR referenced to DMSO-d_6 in an isolated glass capillary.

mixture of 1,2- and 1,4-hydroboration products in a 4:96 ratio in >95% conversion over a 12 hour period.

Based on the work by Wang[41] and Crudden,[68] we propose a pyridine hydroboration mechanism involving a boronium cation as the active catalyst (Figure 5.2a). In this mechanism, coordination of pyridine to HBpin in acetonitrile increases the hydricity of the borane, allowing it to react with NH_4^+, generating H_2 and NH_3 as well as the pyridine-stabilized boronium-BPh_4 salt (Figure 5.2a, initiation). Both H_2 and the boronium cation are observed by ^1H and ^{11}B NMR spectroscopy, respectively, with the boronium species exhibiting a characteristic resonance at δ = 7.1 ppm in the ^{11}B NMR spectrum (Figure 5.2b).[41] The formation of the boronium cation and H_2 does not occur in the absence of pyridine, suggesting that pyridine donation is crucial for the activation of the B-H bond. Further, ^1H and ^{11}B NMR spectroscopy of the reaction mixture containing only HBpin and NH_4BPh_4 in acetonitrile show decomposition of the system at 90 °C over a 24 hour period, giving moderate amounts of C_6H_6, NH_3, and possibly B_2pin_3.[74,75] This decomposition is not observed in the presence of pyridine. Once formed, the boronium cation activates the coordinated pyridine toward reduction by a second pyridine-HBpin adduct, regenerating the catalytic boronium species after loss of the hydride. On a few occasions minor amounts of pyridine-BH_3 adduct were observed by ^{11}B NMR spectroscopy in the solvents tested,

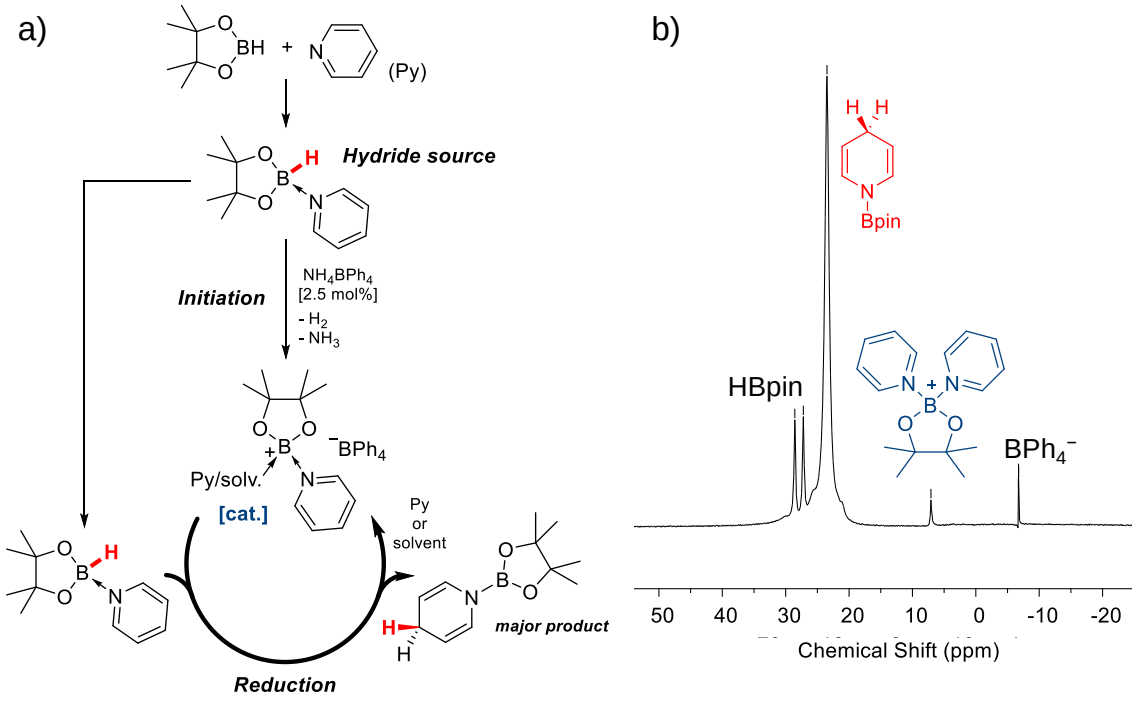

Figure 5.2 a) Proposed mechanism for the boronium-catalyzed hydroboration of pyridine. b) ^{11}B NMR spectrum of the hydroboration reaction mixture showing the presence of the pinBPy_2BPh_4 boronium salt.

possibly formed through the decomposition of HBpin. This species may be active in the reduction of pyridine but does not appear to affect the regioselectivity of the reaction as no differences were observed in CH_3CN reactions with or without BH_3 present. Based on this mechanism, the lower conversion obtained using 10 mol% NH_4BPh_4 compared to 2.5 mol% may be attributed to pyridine being retained in the boronium complex; however, this could not be confirmed conclusively by ^{1}H NMR spectroscopy.

The structure of the boronium salt, pinBPy_2BPh_4 (**16**), was confirmed by single crystal X-ray diffraction conducted on crystals grown from a stoichiometric reaction of HBpin, pyridine (2 equiv.), and NH_4BPh_4 in CD_3CN by layering the solution with dry $(Me_3Si)_2O$ (Figure 5.3). The boronium cation exhibits a tetrahedral geometry around boron and comprises two pyridine molecules and pinacolate bound to the boron centre. The ^{11}B NMR spectrum of the isolated crystals in CD_3CN exhibits the same resonances that are observed in the catalytic reactions at δ = 7.1 and −6.8 ppm, corresponding to the boronium cation and BPh_4^- anion, respectively.

Having optimized the system for pyridine, the substrate tolerance of the reaction was examined using a variety of 2- and 3-substituted pyridines (Scheme 5.7). The boronium-catalyzed reaction has been found to be remarkably successful in facilitating the regioselective 1,4-hydroboration of 3-substituted pyridines (Scheme 5.7, **17a**-**g**). The reaction

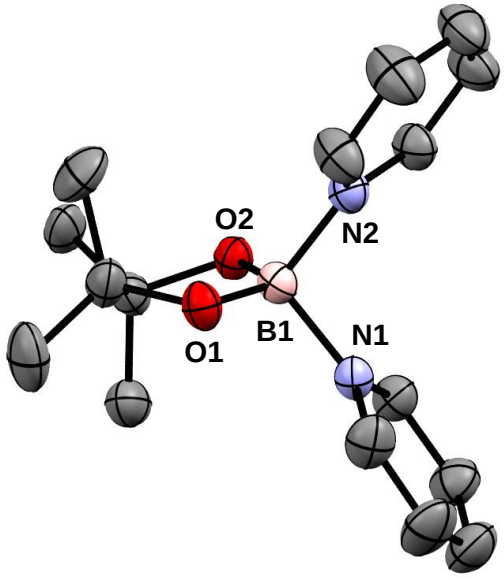

Figure 5.3 Cation structure of the pinBPy_2BPh_4 boronium salt, **16**. Thermal ellipsoids shown at the 50% probability level; hydrogen atoms, disorder, and ion-separated BPh_4^- omitted for clarity (B, pink; N, blue; O, red; C, grey). Selected bond lengths (Å) and angles (°): N1-B1 1.621(3), N2-B1 1.619(3), N1-B1-N2 104.8(2), O1-B1-O2 111.0(2).

is amenable to dehalogenation-prone bromide in the 3-position (Scheme 5.7, **17c**) as well as Lewis basic and reducible cyano, ester, and amide substituents in the 3-position (Scheme 5.7, entries **17d-e**). Furthermore, the hydroboration of 3,5-lutidine, a sterically demanding substrate that failed to undergo hydroboration with Wang's bulkier fluoro-organoborane hydride, can be achieved with excellent regioselectivity (1,2-:1,4- product ratio of 4:96, Scheme 5.7, entry **17g**).[41]

Regioselective hydroboration of 2-substituted pyridines was found to be less successful than those substituted in the 3-positon. The hydroboration of 2-methylpyridine can be achieved with good selectivity for the 4-position using two equivalents of HBpin to ensure complete reactivity (Scheme 5.7, **17h**). However, 2-phenylpyridine and 2-bromopyridine were found not to undergo hydroboration under the optimized reaction conditions (Scheme 5.7, **17i-j**). The steric profile of 2-phenylpyridine and the reduced donor ability of 2-bromopyridine are likely to limit coordination of the pyridine to HBpin, preventing these substrates from activating the B-H bond sufficiently.[41] Additionally, the use of 2-cyanopyridine resulted in a red precipitate along with a complex mixture of nitrile and

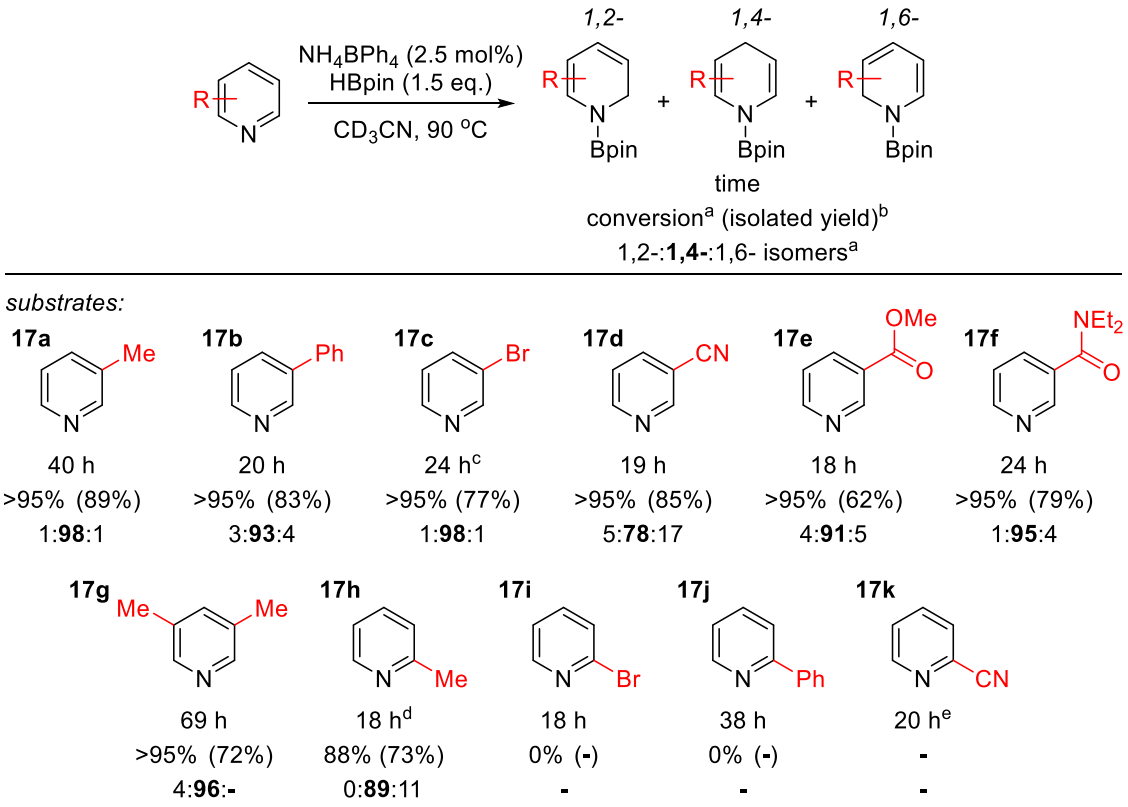

Scheme 5.7 Catalytic 1,4-regioselective hydroboration of substituted pyridines. NMR tube scale reactions performed in a sealed J. Young NMR tube using 0.015 mmol NH_4BPh_4. [a] Determined by ^1H NMR spectroscopy. [b] Isolated yield using 3.36 mmol pyridine in a sealed J. Young-type bomb. [c] Performed at 60 °C. [d] Conducted using 2 equivalents of HBpin. [e] Complex mixture of pyridine and nitrile reduction products.

pyridine reduction products that could not be fully assigned by ^{1}H NMR spectroscopy (Scheme 5.7, **17k**).

The results listed in Table 5.1 show that the regioselectivity of this reaction exhibits a significant solvent dependence; conducting the hydroboration reaction in non-polar solvents (i.e. heptane and benzene) affords a greater proportion of the 1,2-hydroboration product (Table 5.1, entries 5 and 7). This solvent-dependent regioselectivity can also be observed for the hydroboration of substituted pyridines. Comparing the regioselectivity of the hydroboration of 4-methylpyridine conducted in heptane and acetonitrile, the reaction conducted in heptane shows a dramatic increase in conversion of the starting material as well as in selectivity for the 1,2-isomer (Scheme 5.8, **17l**). Very little conversion is observed in CD_3CN when the 4-position is 'blocked' with a methyl group suggesting that for the catalytic reduction of pyridine, the 1,4-product is produced directly and that regioselectivity is not exclusively the result of thermodynamic interconversion from the 1,2-product. The hydroboration of 3-methylpyridine, a substrate that exhibits a strong preference for reduction in the 4-position in acetonitrile, shows a significant increase in the 1,2-hydroboration product when the reaction is conducted in heptane (Scheme 5.8, **17a**). This solvent effect is less pronounced in the hydroboration of quinoline, where reactions conducted in heptane and acetonitrile afford nearly identical 1,2- : 1,4- regioisomer ratios (Scheme 5.8, **17m**). The similar reactivity of quinoline observed in CD_3CN and heptane presumably results from greater charge delocalization causing 1,2- and 1,4-hydroboration to be less energetically distinct. The same reduction of isoquinoline results exclusively in the 1,2-hydroboration product in both heptane and acetonitrile as the 4-position is inaccessible (Scheme 5.8, **17n**). Further, we note the presence of a minor product formed during the hydroboration of isoquinoline (ca. 6% and 11% in heptane and acetonitrile, respectively) that exhibits signals in the ^{1}H NMR spectrum consistent with a 1,2,3,4-tetrahydroisoquinoline species.

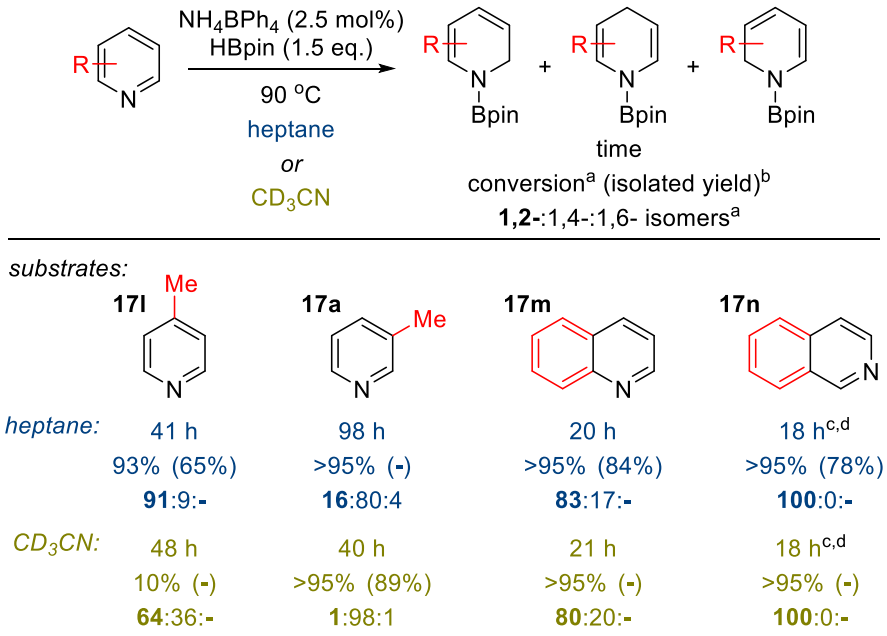

Scheme 5.8 Catalytic 1,2-regioselective hydroboration of pyridines and quinolines. NMR tube scale reactions performed in a sealed J. Young NMR tube using 0.015 mmol NH_4BPh_4. ^{1}H NMR of heptane reactions referenced to DMSO-d_6 in an isolated glass capillary. [a] Determined by ^{1}H NMR spectroscopy. [b] Isolated yield using 3.36 mmol pyridine in a sealed J. Young-type bomb. [c] Reactions conducted at 60 °C. [d] Unknown by-product formed during the reaction (6-11%).

While reactions in heptane afford a greater proportion of the 1,2-regioisomer, 1,4-hydroboration is observed in most cases. Even 4-methylpyridine forms the 1,4-DHP as a minor product in heptane despite steric hindrance in the 4-position. It has been established that, in general, formation of a 1,4-dihydropyridine is more thermodynamically favourable than formation of a 1,2-dihydropyridine and several reports have noted superior regioselectivity for the 1,4-DHP as the reaction temperature is increased.[22,38,76,77] In our system, hydroboration of 4-methylpyridine results in a 91:9 ratio of 1,2-:1,4- isomers when heated to 90 °C in heptane (Scheme 5.8, **17l**). Further heating of the resulting mixture of DHPs at 110 °C for 72 hours results in a 1,2-:1,4- ratio of 24:76, giving the 1,4-isomer as the major product.

Based on the observations in polar and non-polar solvents, it is likely that conditions favouring the thermodynamic 1,4-product are reached at lower temperatures in polar solvents. Thus, larger proportions of the 1,2-product are observed at 90 °C in benzene or heptane compared to reactions conducted in acetonitrile, 1,2-DFB, or pyridine. One possible explanation is that the electron density of the hydride in the pyridine-activated HBpin species is more contracted (harder) in non-polar solvents than in polar solvents, where the hydride electron density can be solvated and remains more diffuse. Such differences in hydride hardness/softness, and their respective site selectivity, would be in agreement with the

established reactivity of pyridines with nucleophiles discussed in Section 5.1.2. In addition, the intramolecular 1,2-hydroboration mechanism established previously likely proceeds with a lower build-up of charge compared to the 1,4- mechanism, which would be favoured in non-polar solvents.[37,38] Similarly, sterics could drive the selectivity since the pyridine-activated HBpin species is solvated in polar solvent and is therefore more sterically encumbered and more likely to attack at the less crowded 4-position of the pyridine substrate. Further, as the reaction occurs more quickly in 1,2-DFB than acetonitrile or pyridine, it is likely that polar donor solvents inhibit the reaction through coordination to boron during the reaction cycle.

5.2.2 Hydroboration of CO_2, Initiated by NH_4BPh_4

Having demonstrated the successful hydroboration of pyridines using the NH_4BPh_4 system we turned to investigate the hydroboration of carbonyl moieties using the same system. Initially, benzaldehydes were chosen as a potential substrate class; however, treatment of benzaldehyde with HBpin (1.5 equiv.) in CD_3CN was found to result in hydroboration at room temperature in the absence of an initiator. Further, control experiments involving the reaction of HBpin with SO_2 in d_8-THF resulted in full reduction of the SO_2 to S_8 as determined by ^1H and ^{11}B NMR spectroscopy as well as single crystal X-ray diffraction. Accordingly, more challenging carbonyl-containing substrates were sought out.

As discussed above, efficient and selective hydroboration of CO_2 represents an important and challenging reaction and thus CO_2 was investigated as a potential substrate using the NH_4BPh_4 initiator. HBpin (1 equiv.) and 10 mol% NH_4BPh_4 were combined in CD_3CN in a J. Young NMR tube under 1 atm of dry CO_2 and the reaction mixture was heated at 70 °C. After 30 minutes at 70 °C, decomposition of the BPh_4^- anion, giving rise to C_6H_6, as well the formation of new resonances, were observed in both the ^1H and ^{11}B NMR spectra in CD_3CN. However, as these new resonances could not be unambiguously assigned or compared to previous literature, the reaction was repeated in d_8-THF, a common solvent used in the hydroboration of CO_2. For the same reaction conducted in d_8-THF at 70 °C, resonances attributed to BPh_4^- were observed to vanish completely within 30 minutes, being replaced by C_6H_6 and another set of aromatic signals in the ^1H NMR spectrum (Figure 5.4). After 1.5 hours a new set of aromatic signals, and ^1H NMR peaks corresponding to the formate and acetal CO_2 hydroboration species at 8.40 and 5.15 ppm, respectively, are observed to grow in.[47] At this stage a broad peak in the ^{11}B NMR spectrum was noted at around 50 ppm.

Further heating at 70 °C for 5 hours results in full consumption of the HBpin, giving the formate, acetal, and methoxide species in yields of 5%, 15%, and 60%, respectively.

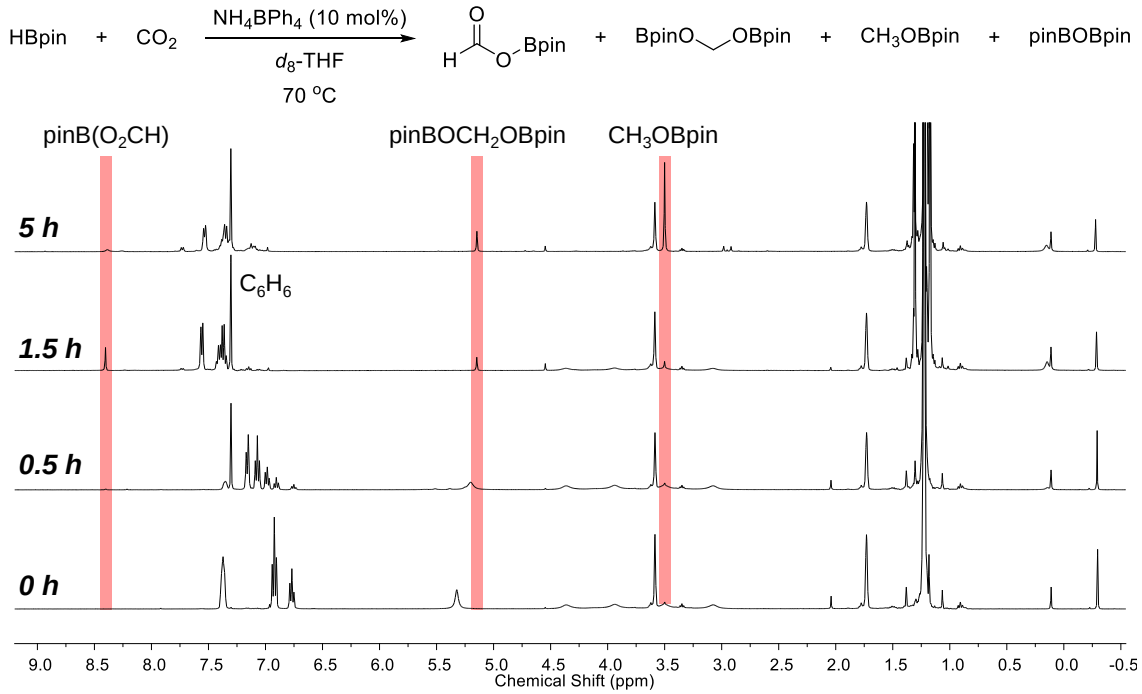

Figure 5.4 ^{1}H NMR spectroscopic monitoring of the catalytic hydroboration of CO_2 using NH_4BPh_4 (10 mol%) in d_8-THF at 70 °C showing the formation of the formate, acetal, and methoxide species (tetramethylsilane in $CDCl_3$ in a sealed glass capillary used as an internal integration standard).

Noting the formation of C_6H_6 as well as the development of new sets of aromatic signals during the progress of the reaction by ^{1}H NMR spectroscopy, it was postulated that the BPh_4^- anion could be decomposing to BPh_3, which forms the active hydroboration catalyst. To test this, HBpin (1 equiv.) and 10 mol% BPh_3 were heated at 70 °C in d_8-THF under 1 atm of CO_2 in a J. Young NMR tube and the reaction was monitored by ^{1}H and ^{11}B NMR spectroscopy. The aromatic region of the initial ^{1}H NMR spectrum (Figure 5.5a) showed resonances attributed to BPh_3 and the ^{11}B NMR spectrum exhibited a broad resonance around 52 ppm. After 5 hours at 70 °C, all of the HBpin had been consumed to give CH_3OBpin in >95% yield, confirming that BPh_3 can indeed efficiently catalyze the hydroboration of CO_2. The aromatic region in the ^{1}H NMR spectrum of this mixture showed that at least two major products had formed from the starting BPh_3 mixture (Figure 5.5b). Notably, the BPh_3 doublet at 7.86 ppm (J = 6.9 Hz) disappears during the reaction period; however, other major aromatic peaks are consistent between the two spectra (highlighted in red, Figure 5.5a and b). The similarity between the two spectra at the end of catalysis suggests that the BPh_3 fragment remains intact but that during the reaction it forms an adduct with some species other than THF, possibly one of the CO_2 reduction products. An anionic

formate adduct, $BPh_3(O_2CH)^-$, can be ruled out as these resonances are not consistent with those of the reported by Okuda and co-workers in d_8-THF.[64] In each of these cases the ^{11}B NMR spectra show resonances generally attributable to pinBOR/pinBO$_2$R species but the broadness of the peaks and the similarity of chemical shifts, which is characteristic of these types of boron environments, make any firm assignment difficult.

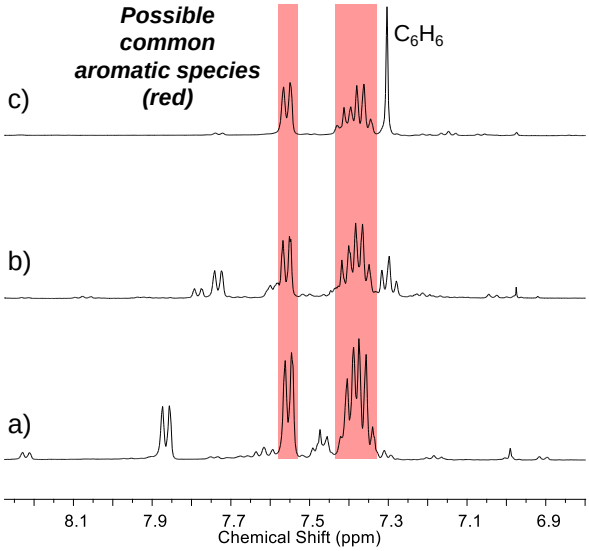

Figure 5.5 Aromatic region of the ^1H NMR spectra of catalytic CO_2 hydroboration reactions in d_8-THF. a) BPh_3 reaction mixture before heating. b) BPh_3 reaction mixture after heating for 5 hours at 70 °C. c) NH_4BPh_4 reaction mixture after heating for 5 hours at 70 °C.

Further, comparing the ^1H NMR spectrum of the BPh_3 reaction after 5 hours to that of the BPh_4^- reaction at 5 hours (Figure 5.5c) it is clear that the aromatic regions bear strong similarities, wherein a doublet at 7.56 ppm and a more complex multiplet at 7.39 ppm are present in both. From these initial NMR monitoring experiments we tentatively propose that the hydroboration reaction involving NH_4BPh_4 proceeds via the decomposition of the BPh_4^- anion to a BPh_3 species which is active in the catalytic reduction of CO_2. As yet, no further insight into the compositional or structural nature of the aromatic-containing species, observed in either the BPh_4^- reaction at 0.5 or 5 hours (Figure 5.4) or the BPh_3 reaction at 5 hours, has been gained.

To study whether NH_4BPh_4 indeed represents a more economical alternative to BPh_3 for the effective hydroboration of CO_2, the two systems were compared and reaction conditions were varied in attempts to optimize the reaction. In each case a J. Young NMR tube was loaded with a catalytic amount of either NH_4BPh_4 or BPh_3 along with HBpin in d_8-THF and placed under 1 atm of CO_2. The mixtures were allowed to react until all of the

HBpin was consumed as observed by ^{1}H and ^{11}B NMR spectroscopy (Table 5.2). We note that it has been established that the hydroboration of CO_2 does not proceed in polar donor solvents in the absence of a catalyst at 40 °C but we have yet to demonstrate this under conditions used here.[52] At lower temperatures of 40 and 45 °C the reactions using 10 mol% of both BPh_3 and NH_4BPh_4 proceeded slowly, consuming all HBpin after 66 and 18 hours, respectively (Table 5.2, entries 1 and 2). While the reaction containing BPh_3 resulted in >95% conversion to the methoxide product, the reaction initiated by NH_4BPh_4 resulted in the formate, acetal, and methoxide species in yields of 27%, 12%, and 8%, respectively.‡ Increasing the temperature to 70 °C results in full consumption of HBpin within 5 hours in both cases (Table 5.2, entries 3 and 4). Again, the BPh_3-catalyzed reaction affords the methoxide species in >95% yield but the reaction involving NH_4BPh_4 affords the formate, acetal, and methoxide species in yields of 5%, 15%, and 60%, respectively, with the remaining 20% consisting of unidentified products. Lowering the loading of NH_4BPh_4 to 2.5 mol% again resulted in full consumption of HBpin over a 5 hour period and gave the methoxide species exclusively, but only in 65% yield (Table 5.2, entry 5).

For results involving the NH_4BPh_4 initiator it is clear that side reactions are taking place which remove HBpin from the reaction mixture but do not afford CO_2 hydroboration products or result in hydroboration products that have not yet been identified by NMR spectroscopy. It is possible that the presence of NH_4^+ or NH_3 influence the product distribution through the formation of aminated species. However, no such products could be identified by ^{1}H NMR spectroscopy nor could they account for the difference in HBpin conversion and the measured yield of CO_2 hydroboration products. Thus, a significant proportion of the reaction products still remain unidentified in the system at the end of the reaction using NH_4BPh_4.

The CO_2 hydroboration reactions times and HBpin consumption we observe with both NH_4BPh_4 and BPh_3 in d_8-THF at 70 °C are similar to those reported by Okuda and co-workers in CD_3CN at 40 °C suggesting that the NH_4BPh_4 system could be a viable and more economical alternative to the use of the BPh_3 catalyst. Nonetheless, that the degree of HBpin consumption does not equal the total amount of products observed when NH_4BPh_4 is used as a catalyst remains an issue. Thus, for the NH_4BPh_4 system to be truly viable as a metal-free CO_2 hydroboration method, further experiments are required to fully understand this

‡Yields determined by ^{1}H NMR spectroscopy using peak integrals, calibrated to a tetramethylsilane internal standard, and balanced chemical equations for each individual species.

difference between HBpin consumption and conversion to products and whether full conversion can be achieved by changing reaction conditions.

Table 5.2 Comparison of reaction conditions for NH_4BPh_4- and BPh_3-catalyzed hydroboration of CO_2.

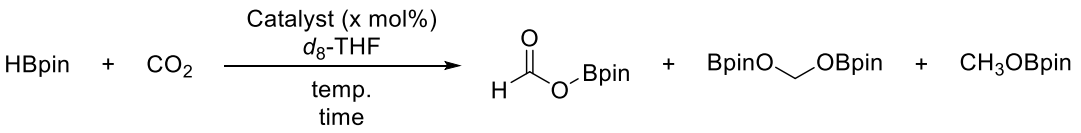

Entry	Catalyst [mol%]	temp. [°C]	time [h]	HBpin consumed [%][a]	Yield of products [%][a]	TOF [h^{-1}]
1	BPh_3 (10)	40	66	100	>95	0.13
2	NH_4BPh_4 (10)	45	18	100	47	0.86
3	BPh_3 (10)	70	5	100	>95	1.93
4	NH_4BPh_4 (10)	70	5	100	80	0.65
5	NH_4BPh_4 (2.5)	70	5	100	65	5.21

NMR tube scale reactions performed in a sealed J. Young NMR tube in d_8-THF. [a] Determined by ^{1}H NMR spectroscopy using tetramethylsilane/$CDCl_3$ in an isolated glass capillary as an internal integration standard.

5.3 Conclusions

In conclusion, we have demonstrated a practical methodology for the regioselective 1,4-hydroboration of pyridines based on a boronium-catalyzed reaction, initiated by the readily available ammonium salt, NH_4BPh_4. Additionally, the proposed active boronium species in this reaction, pinBPy_2BPh_4 (**16**), could be isolated and characterized in the solid state. This reaction is tolerant to a variety of substituents in the 3-position and exhibits high conversions to the hydroboration products. The regioselectivity of this transformation can be altered by changing solvent polarity, where polar solvents (acetonitrile, 1,2-DFB, pyridine) favour selective 1,4-hydroboration and non-polar solvents (benzene, heptane) result in poor regioselectivity or favour the generation of the 1,2-regioisomer for certain substituted pyridine substrates.

Further, the NH_4BPh_4 initiator system can be extended to the hydroboration of CO_2; however, in this case catalytic hydroboration appears to be mediated by a BPh_3 species, generated through the decomposition of BPh_4^-, rather than by a boronium cation. Preliminary studies of this system show that the use of both NH_4BPh_4 and BPh_3 result in very similar species during catalysis, indicated by ^{1}H NMR spectral features in the aromatic region. Despite the similarity in the ^{1}H and ^{11}B NMR spectra between the two catalysts, reactions involving NH_4BPh_4 exhibit discrepancies between the amounts of HBpin consumed during

the reaction and the yield of CO_2 hydroboration products measured spectroscopically. As such, these studies represent only an initial investigation into the initiation of CO_2 hydroboration by NH_4BPh_4 and further work is required.

5.4 Future Work

The origin of the solvent effect observed for the catalytic hydroboration of pyridines remains unclear and further investigations into the solvent-dependant regioselectivity could be gained using computational methods. Calculations to find energy-minimized structures, especially transition states, could help establish a more rigorous understanding of the reaction mechanisms that give rise to the 1,2- and 1,4-DHPs. In addition, if the energy minimizations are conducted with an implicit solvent dielectric field it is possible that energy differences in various steps along the reaction pathway may be highlighted and give insight into the solvent-dependent regioselectivity.

It is clear that NH_4BPh_4 is acting as an initiator for the hydroboration of CO_2 with HBpin; however, the active catalytic species operating in the reaction has not yet been identified. Accordingly, multinuclear and multidimensional NMR studies on stoichiometric reactions of NH_4BPh_4 and HBpin under CO_2 could help elucidate the proposed BPh_3 species present during catalysis. Following the identification of the catalytic species or catalyst resting state, detailed NMR and gas chromatography-mass spectrometry (GC-MS) studies could be conducted on catalytic reaction mixtures to provide insight into the observed loss of hydroboration products though the identification of possible side products or even methane. If such species could be identified steps could then be taken to avoid their formation, either through changing reaction conditions or through the use of a different cation.

Beyond the hydroboration of pyridines and CO_2, we are currently working to extend this methodology to use of other pinacol boranes. Similar to HBpin, pinacol boranes of the more general type RBpin, with sufficiently nucleophilic R groups, could be used in other boronium-catalyzed transformations (Scheme 5.6). These boranes could give rise to hydropyridines functionalized in the 4-position with judicious choice of R group (Scheme 5.6). Such RBpin species may not be limited to carbon nucleophiles but could be extended to reactants where the negatively polarized group, R, comprises a borane, such as in B_2pin_2, or a silane, such as in $pinBSiPhMe_2$ (Scheme 5.6).[78] Owing to the reducing character of DHPs and

their ability to convert back to their respective pyridines when exposed to H_2O, it is possible that treating the proposed hydropyridines, functionalized in the 4-positions, could afford new functionalized pyridines after an aqueous work-up (Scheme 5.6).[37]

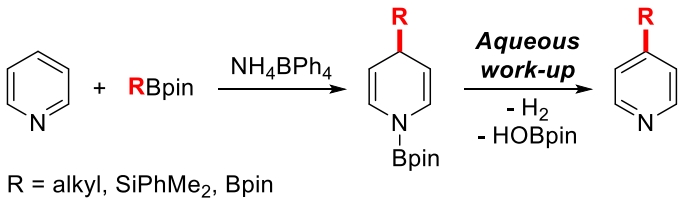

Scheme 5.6 Proposed extension of the boronium catalyzed formation of hydropyridines with boranes of the type RBpin and subsequent rearomatization to afford functionalized pyridines.

The formation of boronium cations or the initiation of catalytic reactions similar to those described above using other more acidic initiators is of interest to expand the scope of this chemistry. The generation of a boronium cation using bis(trifluoromethane)sulfonimide ($HNTf_2$) or its use as an initiator in the presence of Lewis base such as a carbonyl substrate (e.g. aliphatic ketones) may open up new opportunities for boronium catalysis that were not possible with the ammonium salt owing to the much lower pKa of $HNTf_2$ (0.3 in CH_3CN vs. 10.5 for NH_4^+ in DMSO, Figure 5.7).[79,80] Initiators which are strong acids of weakly coordinating anions may result in the formation of boronium species in the presence of Lewis bases that are poorer donors than pyridine. This approach has been used successfully by Vedejs and co-workers in the generation of highly electrophilic boronium species supported by 1,8-bis(dimethylamino)naphthalene.[81] In addition, the substitution of BPh_4^- for NTf_2^- would preclude the possibility of BPh_3 formation and any side reactions that result from its presence. Similar to the $HNTf_2$ approach would be to use chiral BINOL-derived phosphoric acid initiators. Chiral phosphoric acids have received considerable attention for their ability to enantioselectively catalyze Brønsted acid mediated transformations.[82] The transition states of many reactions involving these chiral phosphoric acids involve the weak association of the phosphate group to the substrate through the donated proton, thus transmitting chiral information. Accordingly, it may possible, with sufficiently bulky R groups on the BINOL fragment to prevent strong phosphate-boronium interactions, that association of the phosphate with a boron-bound substrate could afford enantioselective transformations, such as asymmetric carbonyl or imine reductions (Figure 5.7). In both cases it is possible that association of the anion with the boronium could occur to give neutral boron species (i.e. L = A, Figure 5.7). However, provided the interactions are weaker than those of the Lewis base substrate, these neutral species could act as latent sources of a boronium cation.

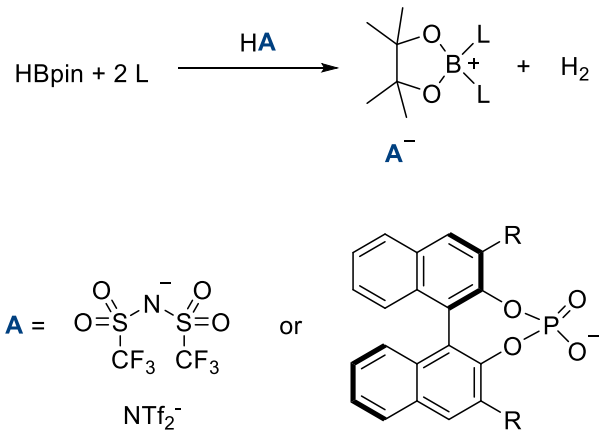

Figure 5.7 Proposed formation of boronium cations with other weakly coordinating or chiral anions.

5.5 References

1 A. Hantzsch, *Justus Liebigs Ann. Chem.*, 1882, **215**, 1–82.

2 U. Eisner and J. Kuthan, *Chem. Rev.*, 1972, **72**, 1–42.

3 D. M. Stout and A. I. Meyers, *Chem. Rev.*, 1982, **82**, 223–243.

4 R. Lavilla, *J. Chem. Soc., Perkin Trans. 1*, 2002, 1141–1156.

5 S. G. Ouellet, A. M. Walji and D. W. C. Macmillan, *Acc. Chem. Res.*, 2007, **40**, 1327–1339.

6 N. Satoh, T. Akiba, S. Yokoshima and T. Fukuyama, *Angew. Chem. Int. Ed.*, 2007, **46**, 5734–5736.

7 N. Edraki, A. R. Mehdipour, M. Khoshneviszadeh and R. Miri, *Drug Discov. Today*, 2009, **14**, 1058–1066.

8 J. A. Bull, J. J. Mousseau, G. Pelletier and A. B. Charette, *Chem. Rev.*, 2012, **112**, 2642–2713.

9 C. Zheng and S.-L. You, *Chem. Soc. Rev.*, 2012, **41**, 2498–2518.

10 G. W. Zamponi, *Nat. Rev. Drug Discov.*, 2016, **15**, 19–34.

11 J. M. López-Arrieta and J. Birks, *Cochrane Database Syst. Rev.*, 2002, CD000147.

12 F. W. Fowler, *J. Org. Chem.*, 1972, **37**, 1321–1323.

13 T. Chennat and U. Eisner, *J. Chem. Soc., Perkin Trans. 1*, 1975, 926–929.

14 E. Booker and U. Eisner, *J. Chem. Soc., Perkin Trans. 1*, 1975, 929–931.

15 J. Pabel, C. E. Hösl, M. Maurus, M. Ege and K. T. Wanner, *J. Org. Chem.*, 2000, **65**, 9272–9275.

16 C. E. Hoesl, M. Maurus, J. Pabel, K. Polborn and K. T. Wanner, *Tetrahedron*, 2002, **58**, 6757–6770.

17 A. P. Phillips, *J. Am. Chem. Soc.*, 1951, **73**, 2248–2248.

18 J. Kuthan and E. Janečková, *Collect. Czech. Chem. Commun.*, 1964, **29**, 1654–1662.

19 S. Yamada, M. Kuramoto and Y. Kikugawa, *Tetrahedron Lett.*, 1969, **36**, 3101–3104.

20 D. L. Comins and A. H. Abdullah, *J. Org. Chem.*, 1982, **47**, 4315–4319.

21 T.-L. Ho, *Tetrahedron*, 1985, **41**, 1–86.

22 W. Clegg, L. Dunbar, L. Horsburgh and R. E. Mulvey, *Angew. Chem. Int. Ed.*, 1996, **35**, 753–755.

23 R. Yamaguchi, Y. Nakazono and M. Kawanisi, *Tetrahedron Lett.*, 1983, **24**, 1801–1804.

24 O. Abril and G. M. Whitesides, *J. Am. Chem. Soc.*, 1982, **104**, 1552–1554.

25 L. Hao, J. F. Harrod, A. M. Lebuis, Y. Mu, R. Shu, E. Samuel and H. G. Woo, *Angew. Chem. Int. Ed.*, 1998, **37**, 3126–3129.

26 J. F. Harrod, R. Shu, H.-G. Woo and E. Samuel, *Can. J. Chem.*, 2001, **79**, 1075–1085.

27 P. S. Wagenknecht, J. M. Penney and R. T. Hembre, *Organometallics*, 2003, **22**, 1180–1182.

28 F. Glorius, N. Spielkamp, S. Holle, R. Goddard and C. W. Lehmann, *Angew. Chem. Int. Ed.*, 2004, **43**, 2850–2852.

29 A. P. Shaw, B. L. Ryland, M. J. Franklin, J. R. Norton, J. Y. C. Chen and M. L. Hall, *J. Org. Chem.*, 2008, **73**, 9668–9674.

30 Q. A. Chen, M. W. Chen, C. Bin Yu, L. Shi, D. S. Wang, Y. Yang and Y. G. Zhou, *J. Am. Chem. Soc.*, 2011, **133**, 16432–16435.

31 D. V. Gutsulyak, A. Van Der Est and G. I. Nikonov, *Angew. Chem. Int. Ed.*, 2011, **50**, 1384–1387.

32 K. Osakada, *Angew. Chem. Int. Ed.*, 2011, **50**, 3845–3846.

33 Y. Maenaka, T. Suenobu and S. Fukuzumi, *J. Am. Chem. Soc.*, 2012, **134**, 367–374.

34 C. D. F. Königs, H. F. T. Klare and M. Oestreich, *Angew. Chem. Int. Ed.*, 2013, **52**, 10076–10079.

35 Y. G. Zhou, *Acc. Chem. Res.*, 2007, **40**, 1357–1366.

36 N. C. Cook and J. E. Lyons, *J. Am. Chem. Soc.* , 1966, **88**, 3396–3403.

37 M. Arrowsmith, M. S. Hill, T. Hadlington, G. Kociok-Köhn and C. Weetman, *Organometallics*, 2011, **30**, 5556–5559.

38 J. Intemann, M. Lutz and S. Harder, *Organometallics*, 2014, **33**, 5722–5729.

39 K. Oshima, T. Ohmura and M. Suginome, *J. Am. Chem. Soc.*, 2012, **134**, 3699–3702.

40 A. S. Dudnik, V. L. Weidner, A. Motta, M. Delferro and T. J. Marks, *Nat. Chem.*, 2014, **6**, 1100–1107.

41 X. Fan, J. Zheng, Z. H. Li and H. Wang, *J. Am. Chem. Soc.*, 2015, **137**, 4916–4919.

42 D. Mukherjee, S. Shirase, T. P. Spaniol, K. Mashima and J. Okuda, *Chem. Commun.*, 2016, **52**, 13155–13158.

43 A. Kaithal, B. Chatterjee and C. Gunanathan, *Org. Lett.*, 2016, **18**, 3402–3405.

44 G. A. Olah, *Angew. Chem. Int. Ed.*, 2005, **44**, 2636–2639.

45 Q. Liu, L. Wu, R. Jackstell and M. Beller, *Nat. Commun.*, 2015, **6**, 5933.

46 S. Chakraborty, J. Zhang, J. A. Krause and H. Guan, *J. Am. Chem. Soc.*, 2010, **132**, 8872–8873.

47 S. Bontemps and S. Sabo-Etienne, *Angew. Chem. Int. Ed.*, 2013, **52**, 10253–10255.

48 F. J. Fernández-Alvarez, A. M. Aitani and L. A. Oro, *Catal. Sci. Technol*, 2014, **4**, 611–624.

49 M.-A. Courtemanche, M.-A. Légaré, L. Maron and F.-G. Fontaine, *J. Am. Chem. Soc.*, 2013, **135**, 9326–9329.

50 T. Wang and D. W. Stephan, *Chem. Commun.*, 2014, **50**, 7007–7010.

51 Y. Yang, M. Xu and D. Song, *Chem. Commun.*, 2015, **51**, 11293–11296.

52 D. Mukherjee, D. F. Sauer, A. Zanardi and J. Okuda, *Chem. Eur. J.*, 2016, **22**, 7730–7733.

53 M. D. Anker, M. Arrowsmith, P. Bellham, M. S. Hill, G. Kociok-Köhn, D. J. Liptrot, M. F. Mahon and C. Weetman, *Chem. Sci.*, 2014, **5**, 2826–2830.

54 C. Das Neves Gomes, E. Blondiaux, P. Thuéry and T. Cantat, *Chem. Eur. J.*, 2014, **20**, 7098–7106.

55 I. Knopf and C. C. Cummins, *Organometallics*, 2015, **34**, 1601–1603.

56 G. Jin, C. G. Werncke, Y. Escudié, S. Sabo-Etienne and S. Bontemps, *J. Am. Chem. Soc.*, 2015, **137**, 9563–9566.

57 O. Jacquet, C. Das, N. Gomes, M. Ephritikhine and T. Cantat, *J. Am. Chem. Soc.*, 2012, **134**, 2934–2937.

58 Y. Li, X. Fang, K. Junge and M. Beller, *Angew. Chem. Int. Ed.*, 2013, **52**, 9568–9571.

59 M. J. Sgro and D. W. Stephan, *Angew. Chem. Int. Ed.*, 2012, **51**, 11343–11345.

60 R. Shintani and K. Nozaki, *Organometallics*, 2013, **32**, 2459–2462.

61 G. Ménard and D. W. Stephan, *J. Am. Chem. Soc.*, 2010, **132**, 1796–1797.

62 M. A. Courtemanche, J. Larouche, M. A. Légaré, W. Bi, L. Maron and F. G. Fontaine, *Organometallics*, 2013, **32**, 6804–6811.

63 M. A. Courtemanche, M. A. Légaré, L. Maron and F. G. Fontaine, *J. Am. Chem. Soc.*, 2014, **136**, 10708–10717.

64 D. Mukherjee, H. Osseili, T. P. Spaniol and J. Okuda, *J. Am. Chem. Soc.*, 2016, **138**, 10790–10793.

65 P. Eisenberger and C. M. Crudden, *Dalt. Trans.*, 2017, **46**, 4874–4887.

66 Z. Zhang, P. Jain and J. C. Antilla, *Angew. Chem. Int. Ed.*, 2011, **50**, 10961–10964.

67 J. M. Farrell, J. A. Hatnean and D. W. Stephan, *J. Am. Chem. Soc.*, 2012, **134**, 15728–15731.

68 P. Eisenberger, A. M. Bailey and C. M. Crudden, *J. Am. Chem. Soc.*, 2012, **134**, 17384–17387.

69 E. R. Clark, A. Del Grosso and M. J. Ingleson, *Chem. Eur. J.*, 2013, **19**, 2462–2466.

70 D. McArthur, C. P. Butts and D. M. Lindsay, *Chem. Commun.*, 2011, **47**, 6650–6652.

71 A. Prokofjevs, A. Boussonnièe Re, L. Li, H. Ne Bonin, E. Lacô, D. P. Curran and E. Vedejs, *J. Am. Chem. Soc.*, 2012, **134**, 12281–12288.

72 K. Chernichenko, M. Lindqvist, B. Koai, M. Nieger, K. Sorochkina, I. Paai and T. Repo, *J. Am. Chem. Soc.*, 2016, **138**, 4860–4868.

73 S. D. Pike, M. R. Crimmin and A. B. Chaplin, *Chem. Commun.*, 2017, **53**, 3615–3633.

74 C. A. G. Carter, C. M. Vogels, D. J. Harrison, M. Karen, J. Gagnon, D. W. Norman, R. F. Langler, R. T. Baker and S. A. Westcott, *Organometallics*, 2001, **20**, 2130–2132.

75 M. Arrowsmith, M. S. Hill and G. Kociok-Köhn, *Chem. Eur. J.*, 2013, **19**, 2776–2783.

76 N. Bodor and R. Pearlman, *J. Am. Chem. Soc.*, 1978, **100**, 4946–4953.

77 E. C. Ashby and A. B. Goel, *J. Organomet. Chem.*, 1981, **204**, 139–145.

78 A.-F. Pécharman, A. L. Colebatch, M. S. Hill, C. L. Mcmullin, M. F. Mahon and C. Weetman, *Nat. Commun.*, 2017, **8**, 15022.

79 T. Rodima, J. Saame, E. Raamat, I. Kaljurand, I. A. Koppel, R. Yu Garlyauskayte, Y. L. Yagupolskii, L. M. Yagupolskii, E. Bernhardt, H. Willner and I. Leito, *J. Org. Chem*, 2011, **76**, 391–395.

80 F. G. Bordwell, *Acc. Chem. Res*, 1988, **21**, 456–463.

81 A. Prokofjevs, J. W. Kampf and E. Vedejs, *Angew. Chem. Int. Ed.*, 2011, **50**, 2098–2101.

82 D. Parmar, E. Sugiono, S. Raja and M. Rueping, *Chem. Rev.*, 2014, **114**, 9047–9153.

6. Conclusions and Outlook

6.1 Conclusions

The aim of this work has been to develop new magnesium-containing salts for use in electrolyte systems in Mg batteries that exhibit large electrochemical stability windows in attempts to preclude the formation of insulating surface electrolyte interphases. Conception and development of these salts was approached from a synthetic inorganic background with the aim of designing new and accessible synthetic routes to form stable compounds so as to make an impactful contribution to the field of Mg electrochemistry. We have shown that at least eight such salts could be synthesized using robust methodologies in moderate to high yields. Further we have demonstrated, both in terms of their fundamental electrochemical stability and their ability to be cycled with active cathode materials, that the electrolytes we have developed are functioning systems and are promising for the further development of Mg battery technology.

The syntheses of the $Mg(CH_3CN)_6(PnF_6)_2$ complexes (Pn = P, As, and Sb) represent the first syntheses and characterization of pure Mg hexafluoropnicogenate salts. In particular, our exploration of the electrochemical stability and cyclability of the electrolyte based on $Mg(PF_6)_2$ was the first to demonstrate that this system can be cycled stably on a Mg electrode without rendering the surface electrochemically inactive though the formation of a MgF_2 film. These observations, based on a combination of electrochemical analysis and Mg surface analysis using SEM imaging and EDX analysis, are contrary to previous perceptions about the stability of $Mg(PF_6)_2$-based systems, which were deemed unstable near 0 V vs. Mg but had not received detailed electrochemical analysis.[1] While the AsF_6^- and SbF_6^- analogues were proposed to exhibit desirable electrochemical stability based on their established behaviour in Li-ion electrochemistry, these systems exhibit poor cyclability and are found to be more susceptible to reduction than the PF_6 salt. Further, this work highlighted the importance of solvent, owing to the tenuous stability of CH_3CN (a necessary and major electrolyte component in our systems) the decomposition of CH_3CN could lead to the formation of an undesirable surface electrolyte interphase and high overpotentials.[2]

Not only were we able to develop a methodology for the synthesis of $Mg(PF_6)_2$ and $Mg(SbF_6)_2$ using $NOPF_6$ and $NOSbF_6$, respectively, we were able to extend this method to

the synthesis of $Ca(PF_6)_2$, a salt relevant as a Ca battery electrolyte. Interestingly, the Ca system was found to be much more prone to decomposition, resulting in $Ca(PO_2F_2)(PF_6)$ complexes in dry CH_3CN. It was hypothesized that the more diffuse nature of Ca^{2+} and the weaker CH_3CN-Ca^{2+} interactions allowed for better interactions between Ca^{2+} and the PF_6^- anion, which could polarize and weaken the P-F bond. In order to prevent such interactions, the crown ethers 15-crown-5 and 18-crown-6 were added to the reaction so as to strongly complex to Ca^{2+} and limit Ca-F interaction. By doing so it was possible to isolate a sample of $Ca(PF_6)_2$ bound by 15-crown-5. This synthetic method circumvents the use of CaX_2 (X = halide) salts as a metathesis partners with $AgPF_6$ used in a previously reported synthesis, preventing contamination of the final electrolyte with halides (i.e. Cl), which could result in corrosion in a Ca battery.[3]

In another case we were able to develop a general methodology for the preparation of Mg aluminate salts, $Mg[Al(OR)_4]_2$, using $Mg(AlH_4)$ and various alcohols. Mg aluminates are an important and widely studied class of Mg electrolytes but have largely been investigated as organohaloaluminates ($R_{4-n}AlCl_n^-$) or as tetrachloroaluminates ($AlCl_4^-$). Amongst these systems, it has been shown that Mg aluminates that do not contain β–hydrogens, such as those comprising the $AlPh_4^-$ anion, exhibit better electrochemical stability as they are not susceptible to β–hydride elimination decomposition pathways.[4] However, Mg aluminates of the type $Mg[Al(OR)_4]_2$, a promising class of Mg electrolyte, which do not contain a β-hydrogen had not yet been investigated despite the suspected presence of the elimination pathway.[5] We were able to synthesize a number of aluminate salts that do not contain β-hydrogens and demonstrate that electrolyte systems based on a number of these salts exhibit good electrochemical stability and facilitate the plating/stripping of Mg using inert electrodes as well as full cells containing a Chevrel phase (Mo_6S_8) cathode. While it was difficult to determine conclusively whether the absence of a β-hydrogen increased the stability and cyclability of these electrolytes, the presence of chloride, in the form of NaCl, was found to decrease the overpotential and increase the Coulombic efficiency of plating/stripping using these electrolytes in combination with a gold electrode. Importantly, the systems we developed exhibited better capacity retention over 50 charge-discharge cycles when cycled with the Chevrel phase cathode than the previously reported $Mg[Al(OR)_4]_2$ electrolyte.[5] Further, we note that solid-state ^{23}Na NMR experiments show evidence of co-intercalation of Na into the Chevrel phase cathode in cells cycled with chloride-containing electrolytes, with Na insertion constituting up to ca. 22% of the overall capacity after 50 cycles. Not only does

this study highlight potential consequences (whether beneficial or detrimental) of synthetic routes that employ salt metathesis but also demonstrates the importance of full elemental characterization of the electrolyte system, which is not always conducted in the literature.

Table 6.1 Comparison of our electrolyte systems (red) with state-of-the-art Mg electrolytes.

Electrolyte	Stability [V vs. Mg]	Cyclability	Notes
$Mg(PF_6)_2$ in 1:1 THF-CH_3CN[6]	4	Stable on Mg. Limited with CP.	High overpotentials in CP cell. Poor stability of CH_3CN near 0 V vs. Mg.
$Mg[Al(O^tBu^F)_4]_2$ in DME	4 (Cl^--free)	Stable on Mg and Au. Stable with CP.	Stable cycling with low overpotentials with CP (Na insertion with Cl^--containing electrolytes). Does not contain β-hydrogens.
$Mg(AlCl_2EtBu)_2$ in THF[7]	2.4	Stable on Mg and Pt. Stable with CP.	Cycling above 2.4 V vs. Mg results in β-hydride elimination. Nucleophilic.
$Mg(AlPh_4)_2$ in THF[4]	3.3	Stable on Mg and Pt. Stable with CP.	Does not contain β-hydrogens.
$Mg(HMDSAlCl_3)_2$ in THF[8,9]	3.2	Stable on Mg. Stable with sulfur.	Non-nucleophilic and compatible with sulfur cathodes.
MACC[10–13]	3.4	Stable on Mg, Cu, and Pt. Stable with CP.	High Cl^- content could give rise to corrosion. Requires electrochemical conditioning.
$Mg[Al(O^iPr^F)_4]_2$ in DME[5]	3.5	Stable on Mg and Al. Limited with CP.	Possible β-hydride elimination decomposition. Capacity fade over 50 cycles in CP cells.
$Mg(CB_{11}H_{12})_2$ in DME[14]	3.5	Stable on Mg and Pt. Stable with CP. Limited with α-MnO_2.	Cl^--free, limiting corrosion. Good oxidative stability on Ni and Al. Carboranes are currently high cost materials.
$Mg(BAr^F)_2$ in THF[15]	4	Not stable on Mg	High oxidative stability but anion is not stable near 0 V vs. Mg.
$Mg[B(O^iPr^F)_4]_2$ in DME[16]	4	Stable on Mg and Pt. Stable with sulfur.	High oxidative stability on stainless steel and Al. Possible β-hydride elimination decomposition.
$Mg(TFSI)_2$ in diglyme with $MgCl_2$[17,18]	3	Stable on Mg and Pt Not stable with CP	Diglyme electrolyte cannot be cycled in CP cells. Less stable THF electrolyte enables cycling in CP cells.

The synthetic development of these Mg electrolyte salts also gave rise to several new species that are interesting and useful in their own right. This is highlighted by the discovery that NH_4BPh_4 is able to initiate highly selective and catalytic 1,4-hydroborations of pyridines. In studying this reaction using a combination of multinuclear NMR and single-crystal X-ray diffraction, it was found that the addition of catalytic quantities of NH_4BPh_4 to various pyridines along with HBpin in CH_3CN gave rise to H_2 and a boronium species with the formula $pinBPy_2BPh_4$. This boronium species is proposed as the catalytic species in the reaction which affords 1,4-dihydropyridine species in excellent yields and with excellent regioselectivity. A methodology based on the use of NH_4BPh_4 as an initiator was also found to be successful in the hydroboration of CO_2. It is proposed in this case, however, that NH_4BPh_4 decomposes to NH_3, C_6H_6, and BPh_3, which comprises part of the catalytically active species. Further, this reaction is not selective and affords a mixture of CO_2 hydroboration products, in contrast to pure BPh_3 which affords the pinBOMe species selectively. The origin of this difference in selectivities between the NH_4BPh_4 and BPh_3 reactions remains unclear.

As the Mg electrolyte remains a crucial limiting factor in the development of competitive Mg batteries, a technology that has really only received significant attention since 2000, development of new systems and deeper understanding of structure-property behaviour is still required to progress this post-lithium ion technology.[7] Whether or not a new electrolyte system is highly electrochemically stable and exhibits stable cycling both on inert electrodes and with active cathode materials, the detailed study of these systems only adds to our understanding of which cation/anion structural motifs or features of electrolyte composition (i.e. solvent system, additives, etc.) result in effective electrolytes. This work has contributed new synthetic methodologies as well as new electrolyte systems to the field of nonaqueous Mg battery electrochemistry and adds to the larger understanding of how anion structure and electrolyte composition influences Mg battery electrochemistry on various electrodes. Further, these electrolytes are competitive with state-of-the-art electrolytes presented in the literature (Table 6.1). In particular, our Mg aluminate system in DME offers a large electrochemical stability window and exhibits stable cycling in cells containing CP cathodes, promising features for its utilization in the development of next generation Mg batteries. In terms of commercial cell development, other electrolyte systems are less practical due to high costs (carborane-based electrolytes), the requirement for electrolyte conditioning (MACC), high chloride content (MACC), or capacity loss within a few tens of

cycles ($Mg[Al(O^iPr^F)_4]_2$). Ultimately, we hope our findings will contribute to the identification of electrolyte systems with electrochemical stability windows of >4 V vs. Mg that can be cycled with high voltage cathode materials to begin to access the high theoretical energy densities proposed for Mg batteries. The development of such batteries, while extremely challenging, could alleviate pressures on Li resources and reduce the demand for Co, used commonly in Li-ion cathodes, which is mined using unethical labour practices and is a significant human rights concern.[19]

6.2 Outlook

Since our work on Mg electrolytes began in 2014, a number of electrolyte systems that exhibit stability up to ca. 3.5 V vs. Mg have been developed (see Introduction). However, these electrolytes are largely tested with the Chevrel phase cathode and those that are examined with higher voltage materials, such as α-MnO_2 or Mn_2O_4 that operate at ca. 2.8 and 2.9 V vs. Mg, respectively, exhibit poor capacity retention and poor ion mobility with nonaqueous electrolytes.[20] One of the biggest challenges in Mg battery development is overcoming the effects of the high charge density of Mg^{2+}, which limits ion diffusion in solution, at the electrolyte-electrode interface (caused by the large energy penalty associated with the desolvation of Mg^{2+} ions), and in the cathode. This limited ion diffusion can result in high electrochemical overpotentials and consequently electrolyte decomposition as well as trapped Mg within the cathode material lattice which can manifest as capacity loss. Thus, a trade-off arises between using high voltage cathode materials—often metal oxides which bind Mg^{2+} strongly—and reasonable ion mobility, which is typically achievable with softer metal chalcogenides (e.g. Mo_6S_8, sulfur, TiS_2, etc.). With relatively high voltage electrolytes now available, the next stage of Mg battery development lies in the discovery or identification of new high voltage cathode material that possess structural features (e.g. layered materials, materials with clearly defined ion channels, and/or materials containing polarizable atoms), that facilitate the facile transport of Mg^{2+}. Emerging candidates of this type include fluorinated polyanion structures such as $FePO_4F$,[21] VPO_4F,[22] and $FeSO_4F$[23] which operate above ca. 2.5 V vs. Mg and have been predicted to have increased Mg^{2+} mobility due to the introduction of fluorine which reduces the Mg-anion interaction strength.[20]

A recent report by Ban and co-workers, in which they demonstrate the preparation and utilization of an ‘artificial’ SEI for Mg anodes, will likely contribute significantly to the

development of high voltage Mg batteries.[24] This SEI is composed of polyacrylonitrile which has been thermally cyclized in the presence of Mg powder, conductive carbon, and $Mg(TFSI)_2$ to form a composite anode that can be cycled stably over 1000 cycles using 0.5 M $Mg(TFSI)_2$ in propylene carbonate. The discovery of this composite is extraordinary in that is permits reversible plating/stripping of Mg from a metallic anode with small overpotentials (ca. 0.1 V) while preventing the reductive decomposition of a solvent that would typically be unstable near 0 V vs. Mg. The use of this anode material could allow for the use of many electrolyte systems that have excellent oxidative stability but which have been considered unsuitable for Mg electrochemistry due to poor reductive stability, such as $Mg(BAr^F)_2$ (BAr^F = tetrakis[3,5-bis(trifluoromethyl)phenyl]borate) in THF.[15] Such an anode material could be used to study the behaviour of the $Mg(PF_6)_2$ system in both CH_3CN and carbonate solvents in conjunction with various high voltage cathode materials without concern for undesirable reactivity at the anode.

Another cell configuration that would exploit the high theoretical capacity of the Mg electrode while achieving high voltages could be to combine a Mg anode (treated with the artificial SEI described above) with an anion intercalation cathode such as graphite. Cheng, Tang, and co-workers recently reported a Ca-ion battery that exhibits a working voltage of 4.45 V with 95% capacity retention over 350 cycles.[25] This cell was constructed using an alloying Sn anode (to form Ca_7Sn_6), a graphite cathode and a $Ca(PF_6)_2$-carbonate electrolyte. Above 4.2 V, reversible intercalation of PF_6^- anions into the graphite cathode was observed with capacities remaining between 60 and 80 $mAh \cdot g^{-1}$, capacity values similar to those observed currently for Mg batteries. Applying the approaches used in the Ca battery to a Mg cell by exchanging the alloying Sn anode for the composite Mg anode described above would increase the theoretical anode capacity from 526 $mAh \cdot g^{-1}$ (for Ca_7Sn_6) to 2205 $mAh \cdot g^{-1}$ for Mg metal. While the limiting capacity in the Ca-ion battery likely comes from the cathode where PF_6^- intercalation typically affords capacities below 120 $mAh \cdot g^{-1}$, the use of a Mg metal anode in a Mg battery would alleviate the 137% volume expansion observed during the formation of the Ca-Sn alloy which could result in fracturing of the anode or delamination from the current collector over prolonged cycling periods which could lead to device failure.[26] The higher voltage of such cells would ultimately result in higher energy densities while preserving the inherent safety and cost benefits of Mg systems. More generally, the use of anion intercalation cathodes could provide a method for investigating the high voltage

cycling stability of some proposed high voltage electrolytes without depending on a functioning metal-based material.

In addition to the nitrosonium method, which we have demonstrated to be applicable to the synthesis of multiple electrolyte salts, the general methodology established for the preparation of the Mg aluminates should be equally applicable to other battery chemistries. In particular, this methodology could easily provide access to a wide range of stable Na or K aluminates, or even borates. Both of Na and K battery systems are emerging alternative battery technologies that offer many benefits over established Li-ion systems (e.g. high natural abundance of the transport ion) but which lack extensive electrolyte development.[27,28] The treatment of precursors such as $NaAlH_4$, $KAlH_4$, $NaBH_4$, or KBH_4 with alkyl-/aryl-alcohols as well as highly fluorinated alcohols could provide access to new, highly stable electrolyte systems for Na and K batteries.

6.3 References

1 Z. Lu, A. Schechter, M. Moshkovich and D. Aurbach, *J. Electroanal. Chem.*, 1999, **466**, 203–217.

2 T. T. Tran, W. M. Lamanna and M. N. Obrovac, *J. Electrochem. Soc.*, 2012, **159**, A2005–A2009.

3 A. L. Lipson, B. Pan, S. H. Lapidus, C. Liao, J. T. Vaughey and B. J. Ingram, *Chem. Mater.*, 2015, **27**, 8442–8447.

4 N. Pour, Y. Gofer, D. T. Major and D. Aurbach, *J. Am. Chem. Soc.*, 2011, **133**, 6270–6278.

5 J. T. Herb, C. A. Nist-Lund and C. B. Arnold, *ACS Energy Lett.*, 2016, **1**, 1227–1232.

6 E. N. Keyzer, H. F. J. Glass, Z. Liu, P. M. Bayley, S. E. Dutton, C. P. Grey and D. S. Wright, *J. Am. Chem. Soc.*, 2016, **138**, 8682–8685.

7 D. Aurbach, Z. Lu, A. Schechter, Y. Gofer, H. Gizbar, R. Turgeman, Y. Cohen, M. Moshkovich and E. Levi, *Nature*, 2000, **407**, 724–727.

8 H. S. Kim, T. S. Arthur, G. D. Allred, J. Zajicek, J. G. Newman, A. E. Rodnyansky, A. G. Oliver, W. C. Boggess and J. Muldoon, *Nat. Commun.*, 2011, **2**, 427.

9 Z. Zhao-Karger, X. Zhao, D. Wang, T. Diemant, R. J. Behm and M. Fichtner, *Adv. Energy Mater.*, 2015, **5**, 1401155.

10 T. Liu, Y. Shao, G. Li, M. Gu, J. Hu, S. Xu, Z. Nie, X. Chen, C. Wang and J. Liu, *J. Mater. Chem. A*, 2014, **2**, 3430–3438.

11 P. Canepa, S. Jayaraman, L. Cheng, N. N. Rajput, W. D. Richards, G. S. Gautam, L. A. Curtiss, K. A. Persson and G. Ceder, *Energy Environ. Sci.*, 2015, **8**, 3718–3730.

12 M. Salama, I. Shterenberg, L. J. W. Shimon, K. Keinan-Adamsky, M. Afri, Y. Gofer and D. Aurbach, *J. Phys. Chem. C*, 2017, **121**, 24909–24918.

13 J. Luo, S. He and T. L. Liu, *ACS Energy Lett.*, 2017, **2**, 1197–1202.

14 O. Tutusaus, R. Mohtadi, T. S. Arthur, F. Mizuno, E. G. Nelson and Y. V. Sevryugina, *Angew. Chem. Int. Ed.*, 2015, **54**, 7900–7904.

15 J. Muldoon, C. B. Bucur, A. G. Oliver, J. Zajicek, G. D. Allred and W. C. Boggess, *Energy Environ. Sci.*, 2013, **6**, 482–487.

16 Z. Zhao-Karger, M. E. Gil Bardaji, O. Fuhr and M. Fichtner, *J. Mater. Chem. A*, 2017, **5**, 10815–10820.

17 N. Sa, B. Pan, A. Saha-Shah, A. A. Hubaud, J. T. Vaughey, L. A. Baker, C. Liao and A. K. Burrell, *ACS Appl. Mater. Interfaces*, 2016, **8**, 16002–16008.

18 N. Sa, H. Wang, D. L. Proffit, A. L. Lipson, B. Key, M. Liu, Z. Feng, T. T. Fister, Y. Ren, C. J. Sun, J. T. Vaughey, P. A. Fenter, K. A. Persson and A. K. Burrell, *J. Power Sources*, 2016, **323**, 44–50.

19 *Time to recharge: Corporate action and inaction to tackle abuses in the cobalt supply chain*, Amnesty International, Index number: AFR 62/7395/2017, 2017.

20 P. Canepa, G. Sai Gautam, D. C. Hannah, R. Malik, M. Liu, K. G. Gallagher, K. A. Persson and G. Ceder, *Chem. Rev.*, 2017, **117**, 4287–4341.

21 Z.-D. Huang, T. Masese, Y. Orikasa, T. Mori, T. Minato, C. Tassel, Y. Kobayashi, H. Kageyama and Y. Uchimoto, *J. Mater. Chem. A*, 2014, **2**, 11578–11582.

22 J. Wu, G. Gao, G. Wu, B. Liu, H. Yang, X. Zhou and J. Wang, *Phys. Chem. Chem. Phys.*, 2014, **16**, 22974–22978.

23 J. Wu, G. Gao, G. Wu, B. Liu, H. Yang, X. Zhou and J. Wang, *RSC Adv.*, 2014, **4**, 15014–15017.

24 S. B. Son, T. Gao, S. P. Harvey, K. X. Steirer, A. Stokes, A. Norman, C. Wang, A. Cresce, K. Xu and C. Ban, *Nat. Chem.*, 2018, **10**, 532–539.

25 M. Wang, C. Jiang, S. Zhang, X. Song, Y. Tang and H. Cheng, *Nat. Chem.*, 2018, **10**, 667–672.

26 M. Zhang, X. Song, X. Ou and Y. Tang, *Energy Storage Mater.*, 2019, **16**, 65–84.

27 J.-Y. Hwang, S.-T. Myung and Y.-K. Sun, *Chem. Soc. Rev*, 2017, **46**, 3529–3614.

28 X. Wu, D. P. Leonard and X. Ji, *Chem. Mater.*, 2017, **29**, 5031–5042.

7. Experimental

7.1 General Experimental Details

All reactions were carried out under a dry, oxygen free nitrogen atmosphere using standard Schlenk and glovebox techniques in dry degassed solvents unless otherwise specified. All solvents were collected freshly distilled over sodium wire/benzophenone (THF), sodium metal (toluene), activated molecular sieves (DME) or CaH_2 (acetonitrile, pyridine). Deuterated NMR solvents were dried over activated molecular sieves and degassed with dry nitrogen (CD_3CN, C_6D_6, d_8-THF, heptane). In Chapter 2, NH_4PF_6 was dried under vacuum for 24 hours at room temperature and Me_3NHCl was dried under vacuum prior to use. In Chapter 3, 15-crown-5 and 18-crown-6 were distilled prior to use. In Chapter 4, ^{t}BuOH was distilled and stored over activated molecular sieves, $^{t}Bu^{F}OH$ and $^{i}Pr^{F}OH$ were dried over activated molecular sieves, C_6F_5OH was dried in a desiccator with P_2O_5. In Chapter 5, NH_4BPh_4 was dried under vacuum for 24 hours, all pyridines were stirred over CaH_2 for 24 hours and distilled by bulb-to-bulb vacuum distillation or sublimed, HBpin was distilled by bulb-to-bulb vacuum distillation and stored under dry nitrogen in a Young's flask, and 1,2-difluorobenzene was stirred over alumina followed by bulb-to-bulb vacuum distillation from CaH_2 and finally stored over activated molecular sieves. All other reagents and solvents were used as received. Dry ice/acetone cooling baths were used to obtain a temperature of −78 °C.

NMR spectra were recorded at 298.0 K on a Bruker 500 MHz AVIII HD Smart Probe Spectrometer (^{1}H at 500 MHz, ^{31}P 202 MHz, ^{13}C 125 MHz, ^{19}F 471 MHz) or a Bruker 400 MHz AVIII HD Smart Probe spectrometer (^{1}H at 400 MHz, ^{31}P 162 MHz, ^{11}B 128 MHz, ^{27}Al 104 MHz, ^{13}C 101 MHz, and ^{19}F 376 MHz) unless otherwise specified. Chemical shifts (δ, ppm) are given relative to residual solvent signals for ^{1}H and ^{13}C, to 85% H_3PO_4 for ^{31}P, to BF_4-Et_2O for ^{11}B, to $Al(NO_3)_3$ in D_2O for ^{27}Al, and to CCl_3F for ^{19}F, with coupling constants reported in Hz. The multiplicities of NMR resonances are denoted by the abbreviations s (singlet), d (doublet), t (triplet), q (quartet), hept (heptet), m (multiplet), and combinations thereof for highly coupled systems.

In Chapter 3, solid-state NMR spectra were recorded on a Bruker 700 MHz AvanceIII spectrometer using a 1.3 mm probe and spinning at a rate of 50 kHz. All experiments were employed a rotor-synchronised Hahn-echo pulse sequence. The 90° pulse length for ^{19}F and

^{31}P are 2.95 μs and 1.35 us and recycle delay for ^{19}F and ^{31}P are 10 s and 50 s, respectively. ^{19}F and ^{31}P shifts were referenced to LiF powder (−204 ppm) and NH_4HPO_4 powder (1 ppm), respectively. In Chapter 4, solid-state NMR spectra were recorded on a Bruker 500 MHz Avance III spectrometer using a 1.3mm probe. ^{23}Na radiofrequency strength of 162 kHz and a CT-selective π/4-pulse were employed. All experiments employed a rotor-synchronised Hahn-echo pulse sequence. For the saturation-recovery experiment, a simple excitation-delay-acquisition pulse sequence was used. ^{23}Na shifts were referenced to NaCl powder (7.2 ppm). MAS spin rates and recycle delays are as shown in figure captions. Figure 7.2 shows a saturation-recovery experiment conducted on the Chevrel phase cathode extracted from the cell shown in Figure 4.7a at the end of discharge (Figure 4.8). Of the four resonances present in the spectrum, only one resonance (spanning 3 to −53 ppm; denoted −8.7 ppm in the main text) shows fast T_1-relaxation of 9.1 ms, thus confirming the paramagnetic nature of this resonance. The other resonances, despite not being fully recovered in the saturation-recovery experiment, clearly shows much slower relaxation (>150 ms) and are likely to be diamagnetic in nature. The exact nature of these resonances is not clear, apart from the narrow resonance at 7.2 ppm (NaCl); possible sources could be unrinsed Na-solvent complex or Na-electrolyte complex. Isotropic resonances were also extracted from two variable-spin rate spectra as shown in Figure 7.3. As expected from paramagnetic shifts following a Curie-Weiss type law ($\delta_{iso} \propto 1/(T-\Theta)$, where δ_{iso} is the isotropic shift, T is the sample temperature, and Θ is the Curie-Weiss constant of the system), larger frictional heating from faster MAS results in reduced paramagnetic shifts.

FT-IR spectroscopic measurements were conducted using a PerkinElmer universal ATR sampling accessory. Elemental microanalytical data were obtained from the University of Cambridge, Department of Chemistry microanalytical service. High-resolution mass spectra (HRMS) were collected using a Waters Xevo G2-S QTOF mass spectrometer in negative mode using dry THF or CH_3CN.

Single crystal X-ray diffraction was carried out at 180(2) K on a Bruker D8-Quest PHOTON-100 diffractometer equipped with an Incoatec IμS Cu microsource (λ_{ave} = 1.5418 Å) or Nonius KappaCCD diffractometer, using graphite monochromated MoKα radiation (λ_{ave} = 0.7107 Å). Structures were solved using SHELXT[1] and refined using full-matrix least squares on F^2 using SHELXL (ver.2018/1).[2] Powder X-ray diffraction (XRD) data were collected using a PANalytical Empyrean X-ray diffractometer using non-monochromated CuKa radiation (λ_{ave} = 1.5418 Å).

All electrochemical experiments (other than those performed in coin cells) were performed in a glovebox under an atmosphere of dry argon. All solvents used for electrochemical measurements were distilled under or purged with dry argon. Cyclic voltammetry and linear sweep voltammetry were performed using an IVIUM CompactStat. Mg ribbon electrodes (99.9%, Sigma Aldrich) were polished using a blade to remove surface oxides. Pt wire working electrodes (99.95% purchased from Alfa Aesar) were polished sequentially with 800 and 1200 grit Emory paper and finally washed with dry CH_3CN or DME. The glassy carbon working electrode (glassy carbon electrode purchased from Alvatek Limited) was polished with fibre paper and dried under vacuum. Stainless steel (316 grade purchased from Advent Research materials) and Al mesh (purchased from Dexmet corp.) working electrodes were used as received and dried under vacuum. Gold wire electrodes were prepared in-house by plating gold onto titanium wire (99.99%, Alfa Aesar) according to a literature procedure.[3] Conductivity measurements were conducted in a conductivity dip cell with a cell constant of 1.27 (calibrated using 0.01 M KCl in distilled H_2O) using a Solartron SI 2160 impedance/gain-phase analyzer.

Coin cell batteries were constructed using Mg ribbon anodes, Al or stainless steel current collectors, a Mo_3S_4/carbon/PTFE composite cathode, and a glass fibre separator soaked in electrolyte. Gold-plated stainless steel disk electrodes (PI-KEM) were used in galvanostatic plating/stripping experiments in Chapter 4. The Chevrel phase was synthesized as follows: stoichiometric amounts of MoS_2, Cu, and Mo powders were combined, ground and formed into a pellet. The pellet was placed in a graphite crucible and heated to 1100 °C under flowing 5% H_2 in Argon. The resultant $Cu_xMo_3S_4$ with 2 wt% Mo impurity was then stirred in a 6M HCl solution for 24 hours. The now pure product was washed with deionised water and successful synthesis was confirmed by powder XRD.

In Chapter 4, electronic structure calculations on the $Mo_6S_8^{4-}$ cluster was performed with the Gaussian16 quantum chemistry package by Jeongjae Lee in the Department of Chemistry at the University of Cambridge.[4] The cluster was relaxed at B3LYP[5] level of theory with Def2SVP basis functions[6] and the MO energies and isosurface plots were generated from a final single point calculation.

Scanning electron microscopy (SEM) images and energy-dispersive X-ray spectroscopy (EDX) spectra were obtained using a FEI Philips XL30 sFEG scanning electron

microscope or a TESCAN MIRA3 FEG-SEM. SEM images were captured at a 5 or 15 kV accelerating voltage and EDX spectra were collected at 15 kV.

7.2 Synthetic Procedures and Characterization

7.2.1 Chapter 2

$H(py)_2PF_6$ (1):

In a Schlenk flask, NH_4PF_6 (500 mg, 3.07 mmol) was dissolved in freshly distilled pyridine (ca. 10 mL) under inert atmosphere and stirred overnight. The solvent was removed *in vacuo* to afford a white solid. The solid was then crystallized from a minimum of dry pyridine by Et_2O diffusion, giving colourless crystals (224 mg, 24%). ^{1}H NMR (500 MHz, 298.0 K, CD_3CN) δ 8.65 (d, J = 5.0 Hz, 4H), 8.29 (td, J = 7.8, 1.5 Hz, 2H), 7.79 (dd, J = 7.6, 6.5 Hz, 4H); ^{13}C NMR (101 MHz, 298.0 K, CD_3CN) δ 145.55, 144.44, 127.26; ^{19}F NMR (471 MHz, 298.0 K, CD_3CN) δ −73.20 (d, J_{F-P} = 706.4 Hz); ^{31}P NMR (202 MHz, 298.0 K, CD_3CN) δ −144.63 (hept, J_{P-F} = 706.0 Hz). Anal. calc'd for $C_{12}H_{11}N_2F_6PO$ (**1** + H_2O): C, 37.28; H, 4.07; N, 8.69; found: C, 37.74; H, 3.64; N, 8.71.

$Mg(PF_6)_2(CH_3CN)_6$ (2):

In a Schlenk flask Mg (100 mg, 4.12 mmol) was suspended in freshly distilled CH_3CN (ca. 10 mL) along with a granule of iodine and stirred at room temperature under a nitrogen atmosphere. In a separate Schlenk flask, $NOPF_6$ (1.44 g, 8.22 mmol) was dissolved in freshly distilled CH_3CN (10 mL) under a nitrogen atmosphere. After the brown colour of the iodine in the Mg suspension had dissipated the $NOPF_6$ solution was added slowly at room temperature. When gas evolution had subsided, the mixture was heated to 45 °C overnight. The orange-brown solution was then filtered through a cannula using a glass fibre filter and dried *in vacuo*. The off-white solid was then recrystallized from hot CH_3CN (ca. 8 mL) to afford a white crystalline solid (1.19 g, 52%). ^{1}H NMR (400 MHz, 298.0 K, CD_3CN) δ 1.96 (s, 1H); ^{13}C NMR (101 MHz, 298.0 K, CD_3CN) δ 118.48, 1.76; ^{19}F NMR (471 MHz, 298.0 K, CD_3CN) δ −73.15 (d, J = 706.4 Hz); ^{31}P NMR (202 MHz, 298.0 K, CD_3CN) δ −144.63 (hept, J_{P-F} = 706.4 Hz). Anal. calc'd for $C_{12}H_{18}N_6F_{12}P_2Mg$ (**2**): C, 25.71; H, 3.24; N, 14.99; found: C, 25.79; H, 3.17; N, 14.16.

$Mg(SbF_6)_2(CH_3CN)_6$ (3):

In a Schlenk flask Mg (100 mg, 4.12 mmol) was suspended in freshly distilled CH_3CN (ca. 10 mL) along with a granule of iodine and stirred at room temperature under a nitrogen atmosphere. In a separate Schlenk flask, $NOSbF_6$ (775 mg, 2.92 mmol, 0.7 equivalent) was dissolved in freshly distilled CH_3CN (20 mL) under a nitrogen atmosphere and added slowly to the flask containing Mg. The reaction mixture was stirred at room temperature briefly and finally stirred at 45 °C for 20 hours. The orange-brown solution was then filtered through a cannula using a glass fibre filter and dried *in vacuo*. The off-white solid was then recrystallized twice from hot CH_3CN (2x ca. 7mL) to afford a white solid (524 mg, 24%). ^{1}H NMR (400 MHz, 298.0 K, CD_3CN) δ 1.96 (s, 1H); ^{13}C NMR (101 MHz, 298.0 K, CD_3CN) δ 118.48, 1.76; ^{19}F NMR (471 MHz, 298.0 K, CD_3CN) δ −120 (m). Anal. calc'd for $C_{12}H_{18}N_6MgSb_2F_{12}$ (**3**): C, 19.42; H, 2.44; N, 11.32; found: C, 18.99; H, 2.43; N, 11.39.

Me_3NHAsF_6 (4):

Me_3NHCl (524 mg, 5.55 mmol) and $KAsF_6$ (1.125 g, 5 mmol, 0.9 equivalent) were combined in a Schlenk flask and suspended in CH_3CN (ca. 15 mL) and stirred for 24 hours under nitrogen. The white precipitate was filtered off using filter paper and recrystallized from ethanol (ca. 10 mL) to afford colourless needles of Me_3NHAsF_6 (963 mg, 78%). ^{1}H NMR (400 MHz, 298.0 K, CD_3CN) δ 2.83 (s, 9H), 6.98 (s, 1H); ^{13}C NMR (101 MHz, 298.0 K, CD_3CN) δ 45.1; ^{19}F NMR (471 MHz, 298.0 K, CD_3CN) δ −65.89 (dd, J = 1864.7, 932.7 Hz). Anal. calc'd for $C_3H_{10}NAsF_6$ (**4**): C, 14.47; H, 4.05; N, 5.62; found: C, 15.07; H, 4.24; N, 5.68.

$Mg(AsF_6)_2(CH_3CN)_6$ (5):

Me_3NHAsF_6 (397 mg, 1.61 mmol) dissolved in THF (ca. 10 mL) in a Schlenk flask under nitrogen and solution of ^{n}Bu^{s}BuMg in hexane (0.7 M, 1.5 mL, 1.05 mmol, 1.3 equivalent) was added dropwise. After stirring briefly at room temperature, the mixture was stirred under reflux for 20h. The white suspension was dried *in vacuo* and washed with hexane (ca. 20 mL). The white solid obtained was precipitated by layering Et_2O onto a concentrated solution the white solid in CH_3CN, affording a white solid (145 mg, 28%). ^{1}H NMR (400 MHz, 298.0 K, CD_3CN) δ 1.96 (s); ^{13}C NMR (101 MHz, 298.0 K, CD_3CN) δ 118.48, 1.76; ^{19}F NMR (471 MHz, 298.0 K, CD_3CN) δ −65.89 (dd, J = 1864.7, 932.7 Hz). Anal. calc'd for $C_{12}H_{18}N_6MgAs_2F_{12}$ (**5**): C, 22.23; H, 2.80; N, 12.96; found: C, 21.42; H, 2.77; N, 12.20.

7.2.2 Chapter 3

$[Ca(PO_2F_2)(PF_6)(CH_3CN)_4]_n$ (6):

In a Schlenk flask, Ca (60 mg, 1.5 mmol, excess) was suspended in freshly distilled CH_3CN (ca. 5 mL) and stirred at room temperature under a nitrogen atmosphere. In a separate Schlenk flask, $NOPF_6$ (327 mg, 1.9 mmol) was dissolved in freshly distilled CH_3CN (ca. 5 mL) under a nitrogen atmosphere. The $NOPF_6$ solution was then added slowly to the Ca granules using a dry syringe. The reaction mixture was stirred at room temperature for ca. 4 days. The yellow solution was then filtered through a cannula using a glass fibre filter and dried *in vacuo*. The resulting solid was dissolved in a minimum amount of dry CH_3CN and placed in a freezer at -26 °C for 72 hours. The supernatant was then decanted to afford colourless crystals of **6** (248 mg, 58%). ^{19}F NMR (376 MHz, 298.0 K, CD_3CN) δ −72.90 (d, $^1J_{F\text{-}P}$ = 706.2 Hz), −86.65 (d, $^1J_{F\text{-}P}$ = 928.8 Hz); ^{31}P NMR (162 MHz, 298.0 K, CD_3CN) δ −22.71 (t, $^1J_{P\text{-}F}$ = 928.8 Hz), −144.62 (hept, $^1J_{P\text{-}F}$ = 706.4 Hz); sufficient elemental analysis could not be obtained likely due to de-solvation of **6**.

$[Ca\subset(15\text{-crown-}5)(CH_3CN)_3]^{2+}[Ca\subset(15\text{-crown-}5)_2]^{2+}(PF_6^-)_4$ (7):

In a Schlenk flask, Ca (60 mg, 1.5 mmol, excess) was suspended in freshly distilled CH_3CN (ca. 5 mL) along with 15-crown-5 (0.2 mL, 1.0 mmol) and stirred at room temperature under a nitrogen atmosphere. In a separate Schlenk flask, $NOPF_6$ (327 mg, 1.9 mmol) was dissolved in freshly distilled CH_3CN (ca. 5 mL) under a nitrogen atmosphere. The $NOPF_6$ solution was then added slowly to the Ca granules using a dry syringe. The reaction mixture was stirred at room temperature for ca. 3 days. The off-white solution was then filtered through a cannula using a glass fibre filter and dried *in vacuo*. The resulting solid was dissolved in a minimum amount of dry CH_3CN, layered with dry Et_2O, and left undisturbed for several days. The supernatant was then decanted to afford colourless crystals of **7** (235 mg, 41%). ^1H NMR (400 MHz, 298.0 K, CD_3CN): δ 3.80 (s, 15-crown-5), 1.96 (s, CH_3CN); ^{19}F NMR (376 MHz, 298.0 K, CD_3CN): δ −72.91 (d, $^1J_{F\text{-}P}$ = 706.6 Hz); ^{31}P NMR (162 MHz, 298.0 K, CD_3CN): δ −144.62 (hept, $^1J_{P\text{-}F}$ = 706.5 Hz). Anal. calc'd for $C_{36}H_{69}Ca_2F_{24}N_3O_{15}P_4$ (**7**): C, 29.95; H, 4.82; N, 2.91; P, 8.58; found: C, 28.81; H, 4.83; N, 3.01; P, 8.86

$[Ca\subset 18\text{-crown-}6(PO_2F_2)(PF_6)]_n$ (9):

In a Schlenk flask, Ca (60 mg, 1.5 mmol, excess) was suspended in freshly distilled CH_3CN (ca. 5 mL) along with 18-crown-6 (362.7 mg, 1.4 mmol, excess) and stirred at room temperature under a nitrogen atmosphere. In a separate Schlenk flask, $NOPF_6$ (327 mg, 1.9

mmol) was dissolved in freshly distilled CH_3CN (ca. 5 mL) under a nitrogen atmosphere. The $NOPF_6$ solution was then added slowly to the Ca granules using a dry syringe. The reaction mixture was stirred at room temperature for ca. 3 days under nitrogen with a needle pierced through a rubber septum to allow a small amount of ambient atmosphere into the reaction flask. The needle was then removed and the remaining procedure carried out using standard air sensitive techniques. The yellow solution was filtered through a cannula using a glass fibre filter and dried *in vacuo*. The resulting solid was dissolved in a minimum amount of dry CH_3CN, layered with dry Et_2O, and left undisturbed for several days. The supernatant was then decanted to afford colourless crystals of **9** (77 mg, 15%). ^{1}H NMR (400 MHz, 298.0 K, CD_3CN): δ 3.79 (s, 18-crown-6); ^{19}F NMR (376 MHz, 298.0 K, CD_3CN): δ −72.89 (d, $^1J_{F\text{-}P}$ = 706.5 Hz), −83.55 (d, $^1J_{F\text{-}P}$ = 938.9 Hz); ^{31}P NMR (162 MHz, 298.0 K, CD_3CN): δ −22.09 (t, $^1J_{P\text{-}F}$ = 938.8 Hz), −144.61 (hept, $^1J_{P\text{-}F}$ = 706.5 Hz). Anal. calc'd for $C_{12}H_{24}CaF_8O_8P_2$ (**9**): C, 26.19; H, 4.40; N, 0.00; found: C, 26.09; H, 4.33; N, 0.00.

[(15-crown-5)$_3$(Ca$_4$F$_4$)(PF$_6$)CH$_3$CN](PF$_6$)$_3$ (10):

In a Schlenk flask, Ca (60 mg, 1.5 mmol, excess) was suspended in freshly distilled CH_3CN (ca. 5 mL) along with 15-crown-5 (0.2 mL, 1.0 mmol) and stirred at room temperature under a nitrogen atmosphere. In a separate Schlenk flask, $NOPF_6$ (327 mg, 1.9 mmol) was dissolved in freshly distilled CH_3CN (ca. 5 mL) under a nitrogen atmosphere. The $NOPF_6$ solution was then added slowly to the Ca granules using a dry syringe. The reaction mixture was stirred at room temperature for ca. 3 days under nitrogen with a needle pierced through a rubber septum to allow a small amount of ambient atmosphere into the reaction flask. The needle was then removed and the remaining procedure carried out using standard air sensitive techniques. The yellow solution was filtered through a cannula using a glass fibre filter and dried *in vacuo*. The resulting solid was dissolved in a minimum amount of dry CH_3CN, layered with dry Et_2O, and left undisturbed for several days. The supernatant was then decanted to afford a mixture of colourless crystals of **10** and a colourless precipitate (138 mg, 27%). ^{1}H NMR (400 MHz, 298.0 K, CD_3CN) δ 3.81 (m, 15-crown-5), 1.96 (s, CH_3CN); ^{19}F NMR (376 MHz, 298.0 K, CD_3CN) δ −72.88 (d, $^1J_{F\text{-}P}$ = 706.8 Hz), −84.78 (d, $^1J_{F\text{-}P}$ = 923.7 Hz), −98.32 (s), −106.57 (q, $^2J_{F\text{-}F}$ = 17.4 Hz); ^{31}P NMR (162 MHz, 298.0 K, CD_3CN) δ −22.87 (t, $^1J_{P\text{-}F}$ = 923.9 Hz), −144.61 (hept, $^1J_{P\text{-}F}$ = 706.6 Hz); sufficient elemental analysis could not be obtained likely due to contamination by $PO_2F_2^-$-containing species.

7.2.3 Chapter 4

General procedure for the synthesis of magnesium alkoxyaluminates 11-15:

In a N_2- or Ar-filled glovebox, a Schlenk tube was loaded with 50-100 mg of the light grey $Mg(AlH_4)_2$-containing solid (42.5 wt% $Mg(AlH_4)_2$) along with dry THF (ca. 5 mL). The alcohol (7.9 equiv.) was then added, resulting in vigorous bubbling and the release of H_2 gas. Once gas-release had subsided, the reaction vessel was sealed and removed from the glovebox to stir for 16-18 hours. The chloride-containing mixtures could be isolated by filtering reaction mixture through glass fibre cannula filter. The clear colourless solution obtained was taken to dryness *in vacuo*, affording a white solid. The electrolyte salts could be further purified by suspending the dried crude reaction mixture in freshly distilled DCM and filtering through a glass fiber cannula filter to remove chloride-containing by-products.

$Mg[Al(O^tBu)_4]_2$ (11):

250 mg, 32% crystalline yield. ^{1}H NMR (400 MHz, 298.0 K, C_6D_6) δ 1.48 (s, 1H), 1.46 (s, 1H) ppm; ^{13}C NMR (101 MHz, 298.0 K, C_6D_6) δ 71.82, 68.62, 34.20, 33.24 ppm; ^{27}Al NMR (104 MHz, 298.0 K, DME) δ 49.17 ppm. Anal. calc'd for $C_{32}H_{72}Al_2Cl_{0.2}MgNa_{0.2}O_8$ (**11**+0.2 NaCl): C, 56.95; H, 10.75; N, 0.00; Cl, 1.05; found: C, 55.77; H, 10.63; N, 0.00; Cl, 0.24.

$Mg(THF)_6[Al(O^tBu^F)_4]_2$ (12):

500 mg, 91%. ^{1}H NMR (400 MHz, 298.0 K, d_8-THF) δ 3.62 (m, THF), 1.79 (m, THF) ppm; ^{13}C NMR (101 MHz, 298.0 K, d_8-THF) δ 122.75 (q, J = 293.5 Hz), 68.39, 26.54 ppm; ^{19}F NMR (376 MHz, 298.0 k, C_6D_6) δ −75.77 ppm; ^{27}Al NMR (104 MHz, 298.0 K, DME) δ 52.40 ppm. HRMS m/z calc'd for $C_{16}AlF_{36}O_4$ $[Al(O^tBu^F)_4^-]$: 966.9037; found: 966.9148. Anal. calc'd for $C_{64}H_{63}Al_2Cl_2F_{72}MgNa_2O_{16}$ (**12**+2 NaCl+2 THF): C, 28.99; H, 2.40; N, 0.00; Cl, 2.67; found: C, 28.84; H, 2.43; N, 0.00; Cl, 2.64.

$Mg(THF)_6[Al(O^iPr^F)_4]_2$ (13):

330 mg, 74% with chloride. ^{1}H NMR (400 MHz, 298.0 K, d_8-THF) δ 4.53 (hept, J = 6.4 Hz), 3.62 (m, THF), 1.78 (m, THF) ppm; ^{13}C NMR (126 MHz, 298.0 K, d_8-THF) δ 128.92-119.27 (m), 73.06-71.06 (m), 68.39, 26.54; ^{19}F NMR (376 MHz, 298.0 K, d_8-THF) δ −77.73 (m) ppm; ^{27}Al NMR (104 MHz, 298.0 K, d_8-THF) δ 60.70 ppm. HRMS *m/z* calc'd for $C_{12}H_4AlF_{24}O_4$ $[Al(O^iPr^F)_4^-]$: 694.9542; found: 694.9530. Anal. calc'd for $C_{50}H_{60}Al_2Cl_2F_{48}MgNa_2O_{14}$ (**13**+2 NaCl): C, 29.37; H, 2.82; N, 0.00; Cl, 3.61; found: C, 29.38; H, 2.92; N, 0.00; Cl, 3.20.

$Mg(THF)_2[Al(OPh)_4]_2$ (14):

390 mg, 84% crystalline yield. ^{1}H NMR (400 MHz, 298.0 k, C_6D_6) δ 7.08-6.99 (m, 32H), 6.76 (t, *J* = 7.2 Hz, 8H), 3.64 (s, THF), 1.27 (s, THF) ppm; ^{13}C NMR (101 MHz, 298.0 K, C_6D_6) δ 156.89, 129.99, 121.16, 120.44, 69.99, 25.11 ppm; ^{27}Al NMR (104 MHz, 298.0 K, DME) δ 54.46 ppm. HRMS *m/z* calc'd for $C_{24}H_{20}AlO_4$ $[Al(OPh)_4^-]$: 399.1177; found: 399.1232. Anal. calc'd for $C_{56}H_{56}Al_2Cl_{0.5}MgNa_{0.5}O_{10}$ (**14**+0.5 NaCl): C, 67.56; H, 5.70; N, 0.00; Cl, 1.78; found: C, 66.46; H, 5.42; N, 0.00; Cl, 1.68.

$Mg(THF)_6[Al(OPh^F)_4]_2$ (15):

370 mg, 78% with chloride. ^{1}H NMR (400 MHz, 298.0 K, d_8-THF) δ 3.67-3.63 (m, THF), 1.84-1.78 (m, THF); ^{13}C NMR (126 MHz, 298.0 K, d_8-THF) δ 142.93-132.60 (m), 68.27, 26.43; ^{19}F NMR (376 MHz, 298.0 K, d_8-THF) δ −163.80 (d, *J* = 22.0 Hz), −169.85 (dd, *J* = 21.5, 19.6 Hz), −177.40 (tt, *J* = 22.5, 7.0 Hz); ^{27}Al NMR (104 MHz, 298.0K, d_8-THF) δ 47.32. HRMS *m/z* calc'd for $C_{24}AlF_{20}O_4$ $[Al(OPh^F)_4^-]$: 758.9293; found: 758.9385. Anal. calc'd for $C_{72}H_{48}Al_2Cl_{1.5}F_{40}MgNa_{1.5}O_{14}$ (**15**+1.5 NaCl): C, 41.94; H, 2.30; N, 0.00; Cl, 2.58; found: C, 42.08; H, 2.47; N, 0.00; Cl, 2.52.

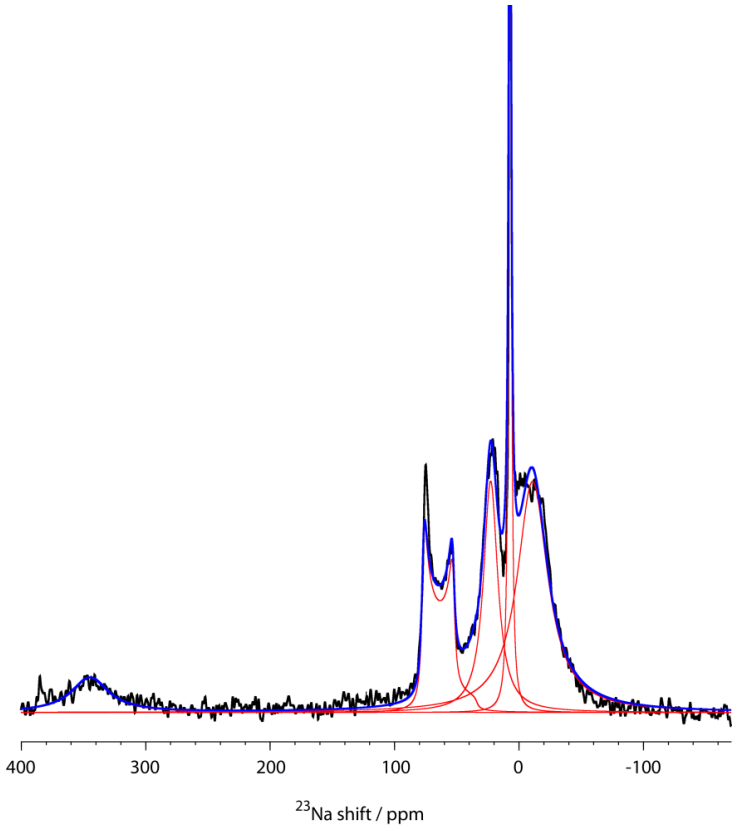

Figure 7.1 Fitted centreband region of the ^{23}Na NMR spectrum of Mo_3S_4 discharged against Mg metal (Figure 4.7a, main text; spectrum reproduced from Figure 4.8, red line) Spectrum was measured at 50 kHz MAS with a recycle delay of 1 s. Fitted parameters are displayed in Table S1.

Table 7.1 Fitted parameters of spectrum shown in Figure 7.1.

	Site 1	**Site 2**	**Site 3**	**Site 4**	**Site 5**
δ_{iso} [ppm]	344.8	−10.8	7.2	84.2	22.8
C_Q [MHz]	-	-	-	3.7	-
η	-	-	-	0	-
Lorentzian broadening [Hz]	4785	3961	300	503	1848
Assignment	Chevrel Na2	Chevrel Na1	NaCl	Unknown	Unknown

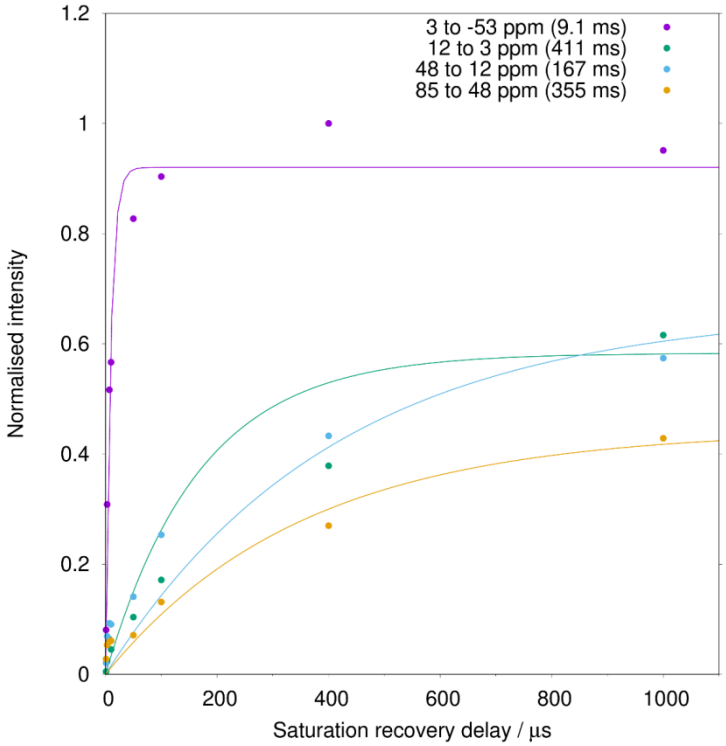

Figure 7.2 ^{23}Na saturation-recovery data of Mo_3S_4 discharged against Mg metal (Figures 7a and 8, Chapter 4) at 50 kHz MAS. Fitted T_1-values are indicated for each peak.

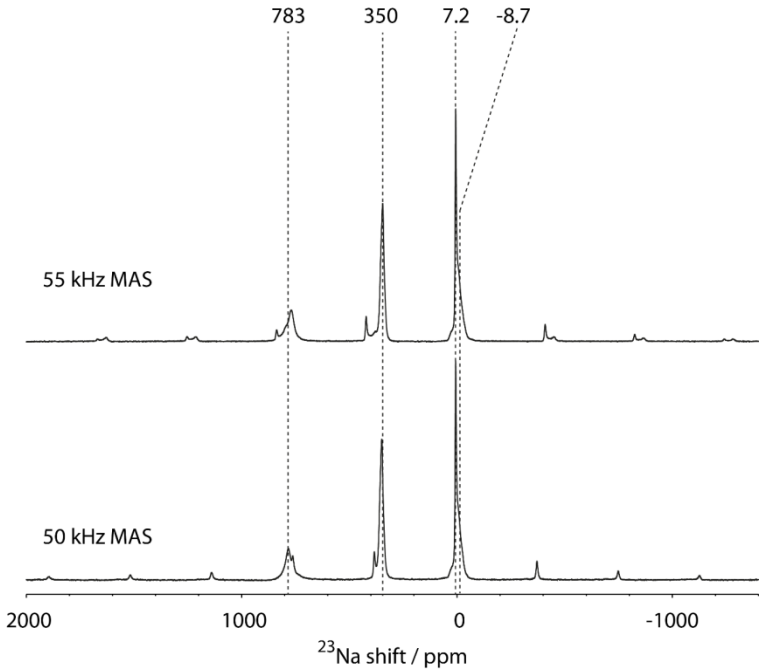

Figure 7.3 ^{23}Na solid-state NMR spectra of Mo_6S_8 discharged against Na metal, taken at 55 and 50 kHz MAS, respectively. Both spectra were measured with recycle delays of 0.1 s. Values of the isotropic resonances are taken from the 50 kHz MAS spectrum for consistency with the rest of the discussion.

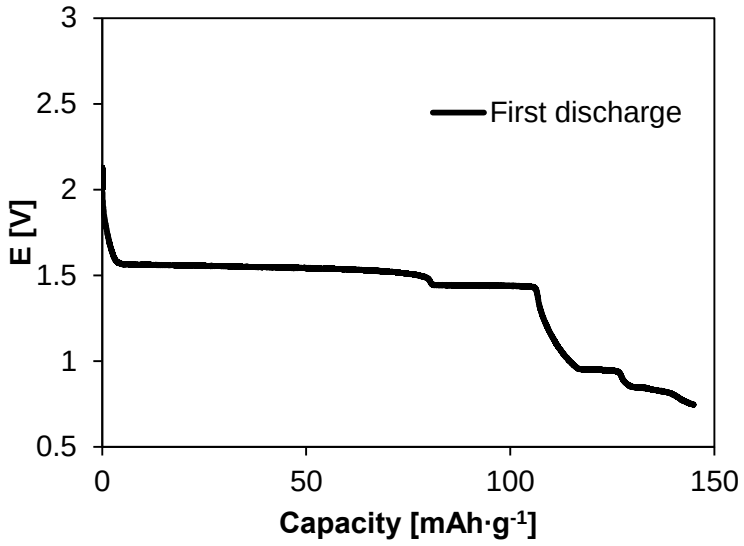

Figure 7.4 First discharge of a Na cell containing a Chevrel phase cathode, a Na anode, and a 1 M solution of $NaBPh_4$ in 2-methyltetrahydrofuran at room temperature (rate: C/25).

7.2.4 Chapter 5

$pinBPy_2BPh_4$ (16):

HBpin (0.045 mL, 0.296 mmol), pyridine (0.05 mL, 0.592 mmol), and NH_4BPh_4 (100 mg, 0.296 mmol) were combined in CH_3CN (ca. 5 mL) in a Young's flask in a glovebox. The mixture was heated to 70 °C until all solids had dissolved. The solution was allowed to cool

to room temperature and stirred overnight. The solution was then layered with $(Me_3Si)_2O$ and left unperturbed, which afforded colourless crystals. ^{1}H NMR (400 MHz, 298.0 K, CD_3CN) δ 7.28 (bs, 4H), 7.00 (t, *J* = 7.2 Hz, 4H), 6.84 (t, *J* = 6.9 Hz, 2H), 1.24 (s, 12H); ^{11}B NMR (128 MHz, 298.0 K, CD_3CN) δ 7.1 (s), −6.8 (s).

General procedure for NMR-scale reactions:

In a glove box, ammonium tetraphenylborate (5mg, 2.5 mol%, 0.0148 mmol) was dissolved/suspended in dry solvent (0.5 mL CD_3CN, C_6D_6, or heptane). This solution was transferred to a J. Young NMR tube. For reactions conducted in heptane, a DMSO-d_6 capillary was included. The desired pyridine (0.593 mmol) was then added, followed by 1.5 equivalents HBpin (0.13 mL, 0.890 mmol). The NMR tube was sealed, removed from the glove box, shaken and placed in a preheated oil bath.

General procedure for preparative-scale reactions:

In a glove box, ammonium tetraphenylborate (28.3 mg, 0.08 mmol) was transferred to an oven-dried J. Young flask equipped with a magnetic stir bar along with the desired pyridine (3.36 mmol) and HBpin (0.73 mL, 5.04 mmol). Dry CH_3CN, heptane, or benzene (5ml) was then added outside of the glovebox. The reaction was then heated in an oil bath. Following heating the volatiles were removed *in vacuo*, and the remaining reaction mixture was suspended in dry pentane (5ml). The solution was then filtered through paper via a cannula filter into a pre-dried Schlenk flask. After removal of the pentane the 1,2- and 1,4-dihydropyridine products were retrieved as oils or waxy solids which can be purified further by reported methods if necessary. Due to the high moisture sensitivity of the products, the reaction was frequently contaminated with a small amount of pinBOH.

N-boryl-1,4-dihydropyridine:[7]

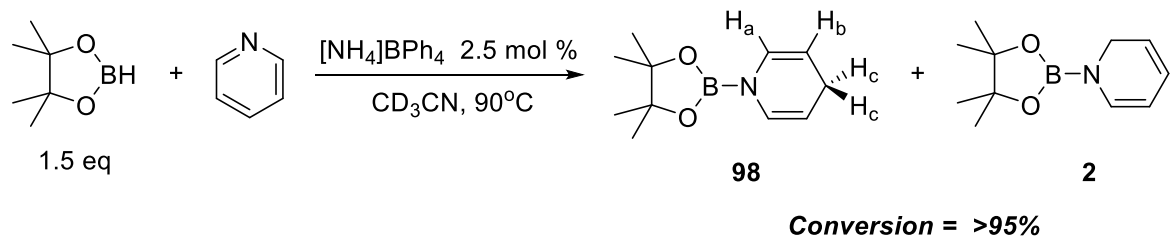

^{1}H NMR (400 MHz, 298.0 K, CD_3CN) δ 6.11 (dt, *J* = 8.5, 1.6 Hz, 2H, $\mathbf{H_a}$), 4.64 – 4.56 (m, 2H, $\mathbf{H_b}$), 2.84 – 2.80 (m, 2H, $\mathbf{H_c}$), 1.23 (s, 12H, pin). *N*-boryl-1,2-dihydropyridine could not

be fully assigned due to its low concentration in solution. However, it can be identified by the characteristic multiplet at δ 3.92 (dd, *J* = 4.2, 1.7 Hz, 2H, **H_d**).

N-boryl-3-methyl-1,4-dihydropyridine (17a):[8,9]

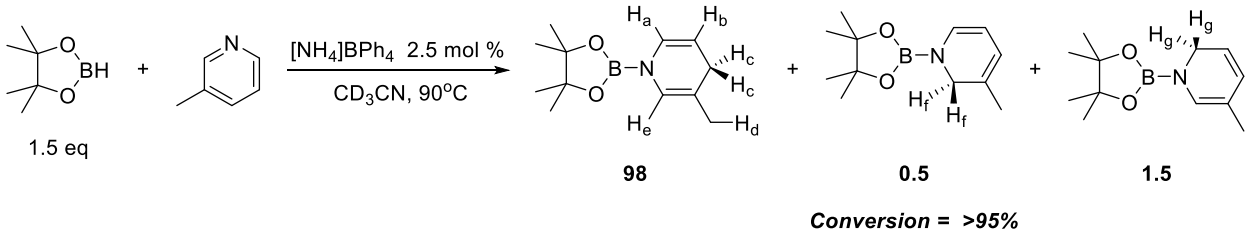

^{1}H NMR (400 MHz, 298.0 K, CD_3CN) δ 6.15 (dd, *J* = 8.1, 1.3 Hz, 1H, **H_a**), 5.97 – 5.95 (m, 1H, **H_e**), 4.63 (dt, *J* = 8.1, 3.3 Hz, 1H, **H_b**), 2.77 – 2.68 (m, 2H, **H_c**), 1.51 (s, 3H, **H_d**), 1.22 (s, 12H, pin). *N*-boryl-3-methyl-1,2-dihydropyridine and *N*-boryl-3-methyl-1,6-dihydropyridine could not be fully assigned due to their low concentration in solution. However, they can be identified as the 1,2- and 1,6-isomers by characteristic multiplets at δ 3.86 (m, 2H, **H_f**) and 3.83 (dd, *J* = 4.2, 1.7 Hz, 2H, **H_g**), respectively.

N-boryl-3-phenyl-1,4-dihydropyridine (17b):[7,10]

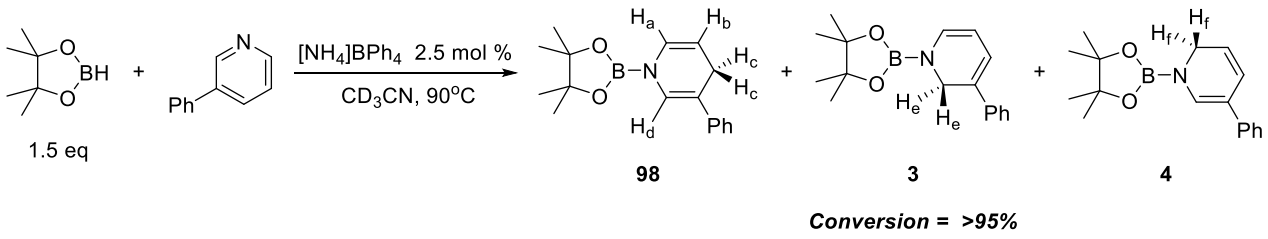

^{1}H NMR (400 MHz, 298.0 K, CD_3CN) δ 7.34 – 7.16 (m, 5H, Ph), 6.81 (s, 1H, **H_d**), 6.29 (dd, *J* = 8.1, 0.8 Hz, 1H, **H_a**), 4.93 – 4.85 (m, 1H, **H_b**), 3.21 – 3.18 (m, 2H, **H_c**), 1.25 (s, 12H, pin). *N*-boryl-3-phenyl-1,2-dihydropyridine and *N*-boryl-3-phenyl-1,6-dihydropyridine could not be fully assigned due to their low concentration in solution. However, they can be identified as the 1,2- and 1,6-isomers by characteristic peaks at δ 4.35 (s, 1H, **H_e**) and 4.01 (dd, *J* = 4.1, 1.6 Hz, 1H, **H_f**), respectively.

N-boryl-3-bromo-1,4-dihydropyridine (17c):[7,10]

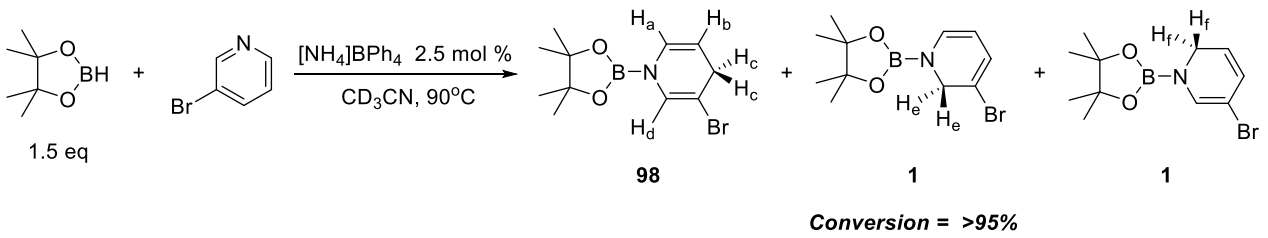

^{1}H NMR (400 MHz, 298.0 K, CD_3CN) δ 6.48 (d, *J* = 1.1 Hz, 1H, **H_d**), 6.17 (dd, *J* = 8.1, 1.1 Hz, 1H, **H_a**), 4.63 (dt, *J* = 8.1, 3.3 Hz, 1H, **H_b**), 3.18 (dt, *J* = 3.2, 1.5 Hz, 2H, **H_c**), 1.24 (s, 12H, pin). *N*-boryl-3-bromo-1,2-dihydropyridine and *N*-boryl-3-bromo-1,6-dihydropyridine could not be fully assigned due to their low concentration in solution. However, they can be identified as the 1,2- and 1,6-isomers by characteristic peaks at δ 4.18 (d, *J* = 1.3 Hz, 2H, **H_e**) and 3.91 (dd, *J* = 4.3, 1.8 Hz, 2H, **H_f**), respectively.

N-boryl-3-cyano-1,4-dihydropyridine (17d):[7]

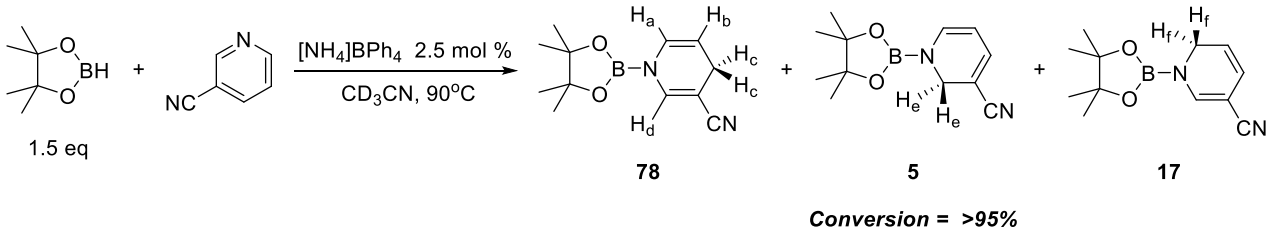

Conversion = >95%

^{1}H NMR (400 MHz, 298.0 K, CD_3CN) δ 6.86 (s, 1H, **H_d**), 6.10 (dd, *J* = 8.3, 1.4 Hz, 1H, **H_a**), 4.82 (dt, *J* = 8.1, 3.4 Hz, 1H, **H_b**), 3.00 – 2.98 (m, 2H, **H_c**), 1.24 (s, 12H, pin). *N*-boryl-3-cyano-1,2-dihydropyridine and *N*-boryl-3-cyano-1,6-dihydropyridine could not be fully assigned due to their low concentration in solution. However, they can be identified as the 1,2- and 1,6-isomers by characteristic peaks at δ 4.03 (s, 2H, **H_e**) and 4.08 (dd, *J* = 3.8, 1.8 Hz, 2H, **H_f**), respectively.

N-boryl-1,4-dihydropyridine-3-methylcarboxylate (17e):[7]

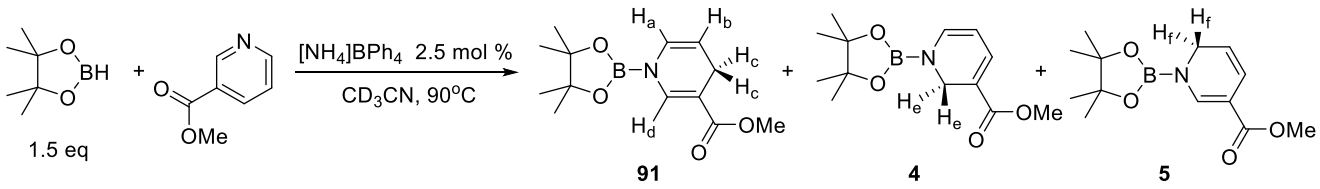

Conversion = >95%

^{1}H NMR (400 MHz, 298.0 K, CD_3CN) δ 7.25 (d, *J* = 0.7 Hz, 1H, **H_d**), 6.11 (ddd, *J* = 8.1, 3.1, 1.7 Hz, 1H, **H_a**), 4.89 (dt, *J* = 8.0, 3.4 Hz, 1H, **H_b**), 3.65 (s, 3H, OCH_3), 3.00 – 2.92 (m, 2H, **H_c**), 1.26 (s, 12H, pin). *N*-boryl-1,2-dihydropyridine-3-methylcarboxylate and *N*-boryl-1,6-dihydropyridine-3-methylcarboxylate could not be fully assigned due to their low concentration in solution. However, they can be identified as the 1,2- and 1,6-isomers by characteristic peaks at δ 4.12 (d, *J* = 0.7 Hz, **H_e**) and 4.05 (dd, *J* = 3.7, 1.9 Hz, **H_f**), respectively.

N-boryl-1,4-dihydropyridine-3-(N,N-diethylamide (17f):

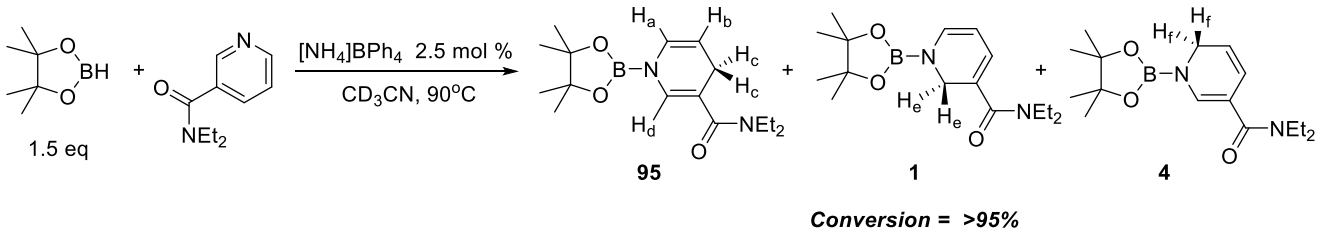

^{1}H NMR (400 MHz, 298.0 K, CD_3CN) δ 6.33 (s, 1H, **H_d**), 6.13 (dd, *J* = 8.2, 1.2 Hz, 1H, **H_a**), 4.76 (dt, *J* = 8.0, 3.3 Hz, 1H, **H_b**), 3.35 (q, *J* = 7.1 Hz, 4H, Et), 3.00 – 2.94 (m, 2H, **H_c**), 1.23 (s, 12H, pin), 1.10 (t, *J* = 7.1 Hz, 6H, Et); ^{13}C NMR (101 MHz, 298.0 K, CD_3CN) δ 171.62, 128.06, 126.65, 110.71, 104.20, 84.90, 83.98, 41.88, 24.86, 24.76, 24.45, 14.04; ^{11}B NMR (128 MHz, 298.0 K, CD_3CN) δ 23.70. HRMS (positive mode, CH_3CN) *m/z* calcd for $C_{16}H_{28}BN_2O_3$ (**17f**+H^+): 307.2187, found: 307.2177. *N*-boryl-1,2-dihydropyridine-3-(*N'*,*N'*-diethylamide) and *N*-boryl-1,6-dihydropyridine-3-(*N'*,*N'*-diethylamide) could not be fully assigned due to their low concentration in solution. However, they can be identified as the 1,2- and 1,6-isomers by characteristic peaks at δ 3.98 (d, *J* = 0.5 Hz, **H_e**) and 3.95 (dd, *J* = 4.1, 1.6 Hz, **H_f**), respectively.

N-boryl-1,4-dihydro-3,5-lutidine (17g):[8]

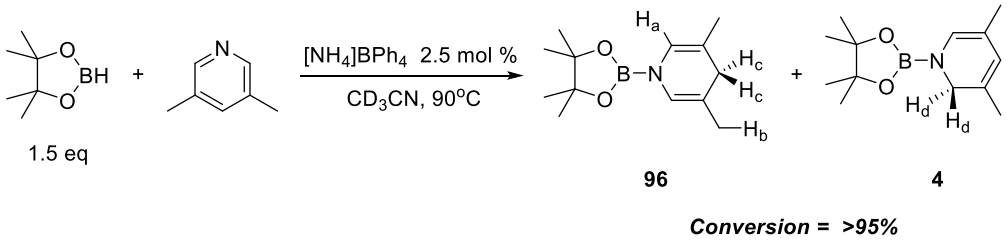

^{1}H NMR (400 MHz, 298.0 K, CD_3CN) δ 5.99 (s, 2H, **H_a**), 2.60 (s, 2H, **H_c**), 1.55 (s, 6H, **H_b**), 1.22 (s, 12H, pin). *N*-boryl-1,2-dihydro-3,5-lutidine could not be fully assigned due to its low concentration in solution. However, it can be identified by the characteristic peak at δ 3.77 (s, 2H, **H_d**).

N-boryl-2-methyl-1,4-dihydropyridine (17h):[8]

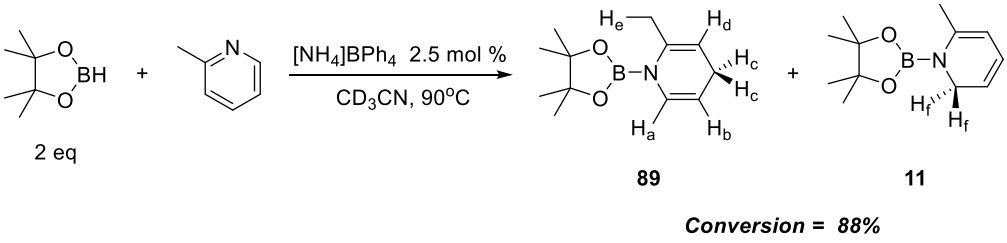

^{1}H NMR (400 MHz, 298.0 K, CD_3CN) δ 6.30 (d, *J* = 8.2 Hz, 1H, **H$_a$**), 4.63 (m, 1H, **H$_b$**), 4.42 (m, 1H, **H$_d$**), 2.77 – 2.71 (m, 2H, **H$_c$**), 1.86 (d, *J* = 1.2 Hz, 3H, **H$_e$**), 1.22 (s, 12H, pin). *N*-boryl-2-methyl-1,2-dihydropyridine could not be fully assigned due to its low concentration in solution. However, it can be identified by a characteristic multiplet at δ 3.79 (d, *J* = 4.2 Hz, 2H, **H$_d$**).

N-boryl-4-methyl-1,2-dihydropyridine (17l):[8]

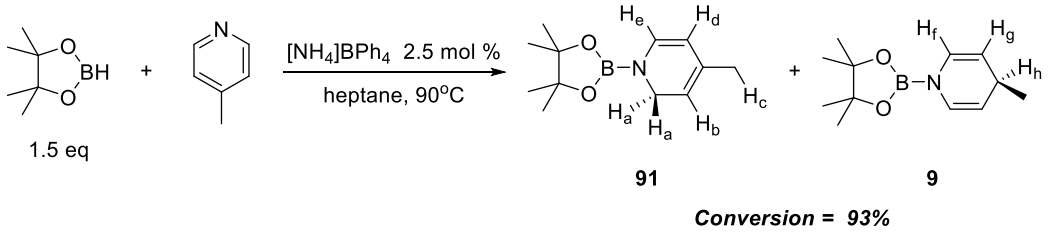

^{1}H NMR (400 MHz, 298.0 K, heptane) δ 6.23 (d, *J* = 7.4 Hz, 1H, **H$_e$**), 4.78 (m, 1H, **H$_b$**), 4.71 (dd, *J* = 7.5, 1.4 Hz, 1H, **H$_d$**), 3.85 (dd, *J* = 3.8, 1.7 Hz, 2H, **H$_a$**), 1.54 (d, *J* = 1.4 Hz, 3H, **H$_c$**), 1.12 (s, 12H, pin). *N*-boryl-4-methyl-1,4-dihydropyridine could not be fully assigned due to its low concentration in solution. However, it can be identified by characteristic peaks at δ 6.08 (d, *J* = 7.4 Hz, 2H, **H$_f$**), 4.39 (dd, *J* = 8.4, 3.2 Hz, 2H, **H$_g$**), 2.95 – 2.89 (m, 1H, **H$_h$**).

N-boryl-1,2-dihydroquinoline (17m):[8,11]

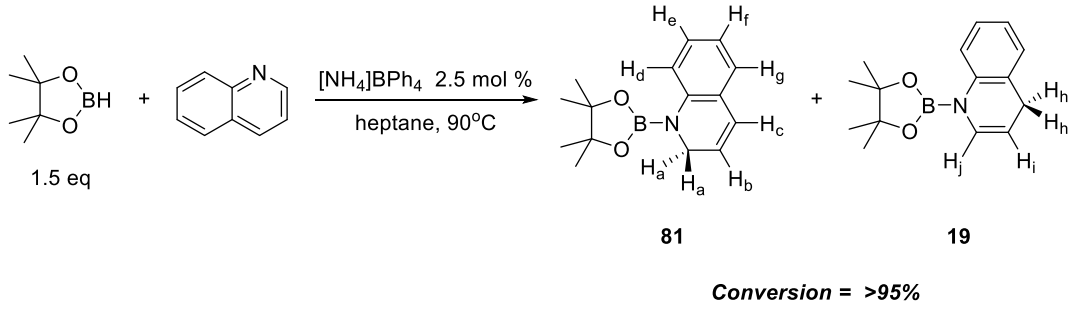

^{1}H NMR (400 MHz, 298.0 K, heptane) δ 7.24 (d, *J* = 8.2 Hz, 1H, **H$_g$**), 6.83 – 6.77 (m, 1H, **H$_f$**), 6.66 (m, 1H, **H$_d$**), 6.58 (td, *J* = 7.4, 1.1 Hz, 1H, **H$_e$**), 6.13 (d, *J* = 9.6 Hz, 1H, **H$_c$**), 5.55 (dt, *J* = 9.4, 4.2 Hz, 1H, **H$_b$**), 3.90 (dd, *J* = 4.2, 1.7 Hz, 2H, **H$_a$**), 1.07 (s, 12H, pin). *N*-boryl-1,4-dihydroquinoline could not be fully assigned due to its low concentration and overlapping signals in solution. However, it can be identified by characteristic peaks at δ 6.43 (dt, *J* = 8.1, 1.7 Hz, 1H, **H$_j$**), 4.64 – 4.60 (m, 1H, **H$_i$**), 3.25 (dd, *J* = 3.3, 1.4 Hz, 2H, **H$_h$**).

N-boryl-1,2-dihydroisoquinoline (17n):[8]

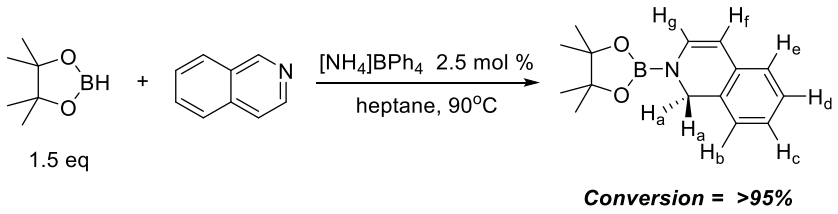

^{1}H NMR (400 MHz, 298.0 K, heptane) δ 6.79 (td, *J* = 7.5, 1.3 Hz, 1H, $\mathbf{H_d}$), 6.73 (d, *J* = 7.4, 1.3 Hz, 1H, $\mathbf{H_c}$), 6.62 (d, *J* = 7.3 Hz, 1H, $\mathbf{H_x}$), 6.58 (dd, *J* = 7.4, 0.8 Hz, 1H, $\mathbf{H_x}$), 6.31 (d, *J* = 7.5 Hz, 1H, $\mathbf{H_g}$), 5.31 (d, *J* = 7.5 Hz, 1H, $\mathbf{H_f}$), 4.27 (s, 2H, $\mathbf{H_a}$), 1.00 (s, 12H, pin).

7.3 Electrochemical apparatus

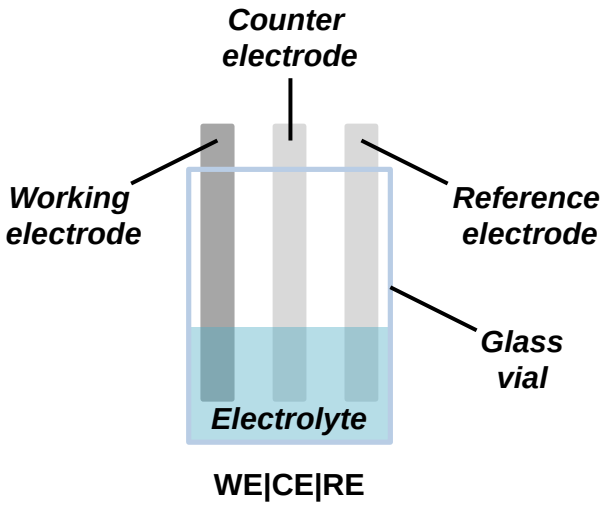

Figure 7.5 Schematic of a three-electrode flooded cell.

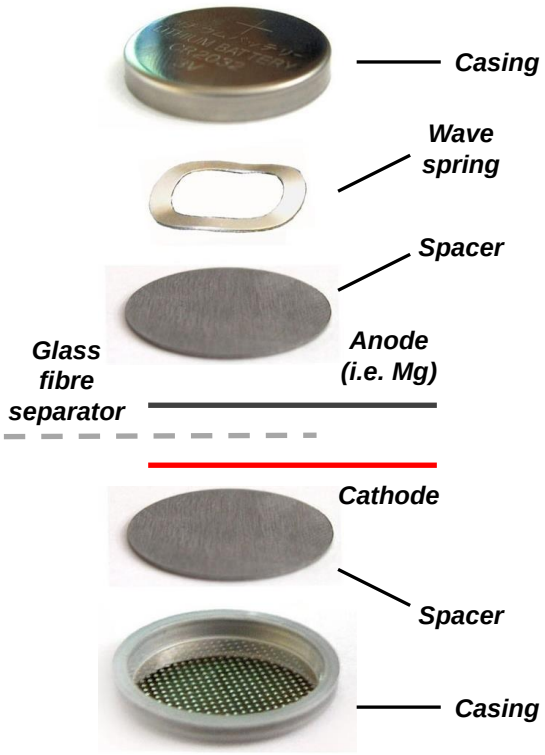

Figure 7.6 Schematic of coin cell comprising an anode, a glass fibre separator, and a cathode.

7.4 Crystallographic Data[†]

Table 7.2 Crystal data and structure refinement details for **1**-**3**

Empirical formula	$C_{10}H_{11}F_6N_2P$ (**1**)	$C_{12}H_{18}F_{12}MgN_6P_2$ (**2**)	$C_{12}H_{18}F_{12}MgN_6Sb_2$ (**3**)
Formula weight	304.18	560.57	742.13
Temperature/K	180(2)	180(2)	180(2)
Crystal system	Monoclinic	Trigonal	Trigonal
Space group	*C*2/*c*	R-3	R-3
a/Å	15.9008(17)	11.1793(2)	11.3574(3)
b/Å	8.9829(7)	11.1793(2)	11.3574(3)
c/Å	9.8963(9)	16.6946(8)	17.4199(5)
α/°	90	90	90
β/°	116.409(9)	90	90
γ/°	90	120	120
Volume/$Å^3$	1266.0(2)	1806.91(11)	1945.96(12)
Z	4	3	3
ρ_{calc} g/cm^3	1.596	1.545	1.900
μ/mm^{-1}	2.566	2.901	2.203
F(000)	924	846.0	1062.0
Crystal size/mm^3	0.300 × 0.060 × 0.030	0.200 × 0.120 × 0.050	0.050 × 0.050 × 0.050
Radiation	CuKα (λ = 1.54178)	CuKα (λ = 1.54178)	MoKα (λ = 0.71073)
2Θ range for data collection/°	5.823 to 58.839	10.562 to 133.022	8.612 to 59.268
Index ranges	$-17 \le h \le 17$, $-7 \le k \le 9$, $-10 \le l \le 10$	$-10 \le h \le 9$, $-8 \le k \le 12$, $-18 \le l \le 16$	$-15 \le h \le 12$, $-14 \le k \le 15$, $-20 \le l \le 24$
Reflections collected	3685	2227	6291
Independent reflections	901 [R_{int} = 0.0463]	640 [R_{int} = 0.0279]	1122 [R_{int} = 0.0454]
Data/restraints/parameters	901/0/ 88	640/4/91	1122/0/53
Goodness-of-fit on F^2	1.058	1.105	1.091
Final R indexes [I>=2σ (I)]	R_1 = 0.0458, wR_2 = 0.1101	R_1 = 0.0354, wR_2 = 0.0831	R_1 = 0.0381, wR_2 = 0.0866
Final R indexes [all data]	R_1 = 0.0642, wR_2 = 0.1197	R_1 = 0.0426, wR_2 = 0.0874	R_1 = 0.0519, wR_2 = 0.0936
Largest diff. peak/hole / e $Å^{-3}$	0.436 and -0.274	0.19/-0.17	0.60/-0.60

[†]Structures refined by Dr. Andrew Bond and Dr. Andrew Peel in the Department of Chemistry at the University of Cambridge.

Table 7.3 Crystal data and structure refinement details for **6**, **7**, **8**, and **9**

Empirical formula	$C_8H_{12}CaF_8N_4O_2P_2$ (**6**)	$C_{36}H_{69}Ca_2F_{24}N_3O_{15}P_4$ (**7**)	$C_{52}H_{98}Ca_4F_{36}N_6O_{20}P_4Si_2$ (**8**)	$C_{12}H_{22}CaF_8O_8P_2$ (**9**)
Formula weight	450.24	1443.98	2151.74	548.31
Temperature/K	180(2)	180(2)	180(2)	180(2)
Crystal system	Orthorhombic	Monoclinic	Triclinic	Orthorhombic
Space group	*Cmc*2_1	P2_1/m	P-1	*Pca*2_1
a/Å	12.9151(14)	12.8822(2)	12.9890(4)	28.1056(10)
b/Å	20.3651(14)	12.0101(2)	13.1082(4)	11.9971(5)
c/Å	7.0543(6)	19.7212(5)	13.8922(4)	13.0595(5)
α/°	90	90	100.3963(11)	90
β/°	90	102.4884(9)	103.0857(11)	90
γ/°	90	90	91.6070(12)	90
Volume/Å^3	1855.4(3)	2979.01(10)	2260.21(12)	4403.5(3)
Z	4	2	1	8
ρ_{calc}g/cm^3	1.612	1.610	1.581	1.654
μ/mm^{-1}	5.405	0.434	4.267	4.827
F(000)	904	1484.0	1104.0	2240
Crystal size/mm^3	0.21×0.07× 0.06	0.250 × 0.250 × 0.100	0.240 × 0.130 × 0.090	0.17×0.13×0.10
Radiation	CuKα (λ = 1.5418)	MoKα (λ = 0.71073)	CuKα (λ = 1.54178)	CuKα (λ = 1.5418)
2Θ range for data collection/°	8.11 to 133.10	7.108 to 54.916	6.874 to 133.74	6.29 to 118.21
Index ranges	-15 ≤ h ≤ 15, -24 ≤ k ≤ 24, -8 ≤ l ≤ 7	-16 ≤ h ≤ 16, -15 ≤ k ≤ 14, -21 ≤ l ≤ 24	-15 ≤ h ≤ 15, -15 ≤ k ≤ 15, -16 ≤ l ≤ 15	-31 ≤ h ≤ 30, -13 ≤ k ≤ 7, -14 ≤ l ≤ 12
Reflections collected	11439	22264	26812	22919
Independent reflections	1669 [R_{int} = 0.039]	6979 [R_{int} = 0.0557]	7970 [R_{int} = 0.0399]	5907 [R_{int} = 0.053]
Data/restraints/ parameters	1669/1/130	6979/368/427	7970/100/562	5907/145/560
Goodness-of-fit on F^2	1.06	2.398	1.079	1.04
Final R indexes [I>2σ(I)]	R_1 = 0.044, wR_2 = 0.117	R_1 = 0.1268, wR_2 = 0.3442	R_1 = 0.0778, wR_2 = 0.2021	R_1 = 0.059, wR_2 = 0.152
Final R indexes [all data]	R_1 = 0.044, wR_2 = 0.117	R_1 = 0.1655, wR_2 = 0.3643	R_1 = 0.0837, wR_2 = 0.2075	R_1 = 0.068, wR_2 = 0.159
Largest diff. peak/hole /e Å^{-3}	0.68/-0.70	1.53/-0.91	1.86/-1.01	0.77/-0.41
Flack parameter	0.31(3)[a]			0.52(2)[a]

[a] Refined as an inversion twin.

Table 7.4 Crystal data and structure refinement details for **10**

Empirical formula	$C_{38}H_{72}Ca_4F_{28}N_4O_{15}P_4$ (**10**)
Formula weight	1641.19
Temperature/K	180(2)
Crystal system	triclinic
Space group	*P*–1
a/Å	12.7225(6)
b/Å	13.4339(6)
c/Å	21.7776(10)
α/°	73.456(2)
β/°	89.794(2)
γ/°	68.867(2)
Volume/Å^3	3307.5(3)
Z	2
ρ_{calc}g/cm^3	1.648
μ/mm^{-1}	5.042
F(000)	1680
Crystal size/mm^3	0.18× 0.14×0.10
Radiation	CuKα (λ = 1.5418)
2Θ range for data collection/°	7.34 to 118.63
Index ranges	-14 ≤ h ≤ 14, -14 ≤ k ≤ 13, -24 ≤ l ≤ 24
Reflections collected	34975
Independent reflections	9471 [R_{int} = 0.041]
Data/restraints/parameters	9471/426/972
Goodness-of-fit on F^2	1.06
Final R indexes [I>2σ(I)]	R_1 = 0.051, wR_2 = 0.133
Final R indexes [all data]	R_1 = 0.059, wR_2 = 0.139
Largest diff. peak/hole / e Å^{-3}	0.55/-0.53

Table 7.5 Crystal data and structure refinement details for **11**, **14**, and **12'**.

Empirical formula	$C_{32}H_{72}Al_2MgO_8$ (**11**)	$C_{60}H_{64}Al_2MgO_{11}$ (**14**)	$C_{30}H_{27}AlF_{36}MgO_9$ (**12'**)
Formula weight	663.16	1039.38	1266.80
Temperature/K	180(2)	180(2)	180(2)
Crystal system	Monoclinic	Orthorhombic	Orthorhombic
Space group	$P2_1/n$	$P2_12_12$	$P2_12_12_1$
a/Å	9.9953(3)	14.1081(4)	10.2705(3)
b/Å	16.5017(5)	21.3826(6)	18.4729(6)
c/Å	25.7252(8)	8.9782(3)	24.1062(8)
α/°	90	90	90
β/°	92.9649(11)	90	90
γ/°	90	90	90
Volume/$Å^3$	4237.4(2)	2708.43(14)	4573.6(3)
Z	4	2	4
$\rho_{calc}g/cm^3$	1.040	1.274	1.840
μ/mm^{-1}	1.077	1.095	2.380
F(000)	1464.0	1100.0	2512.0
Crystal size/mm^3	0.280 × 0.140 × 0.110	0.170 × 0.080 × 0.070	0.160 × 0.140 × 0.060
Radiation	CuKα (λ = 1.54178)	CuKα (λ = 1.54178)	CuKα (λ = 1.54178)
2Θ range for data collection/°	6.366 to 133.158	7.506 to 117.874	6.028 to 133.596
Index ranges	$-11 \le h \le 11$, $-17 \le k \le 19$, $-29 \le l \le 30$	$-13 \le h \le 15$, $-23 \le k \le 18$, $-9 \le l \le 9$	$-12 \le h \le 12$, $-18 \le k \le 21$, $-28 \le l \le 23$
Reflections collected	28916	16436	27209
Independent reflections	7432 [R_{int} = 0.0282]	3857 [R_{int} = 0.0518]	8032 [R_{int} = 0.0455]
Data/restraints/parameters	7432/48/413	3857/10/300	8032/0/702
Goodness-of-fit on F^2	1.035	1.045	1.032
Final R indexes [I>=2σ (I)]	R_1 = 0.0693, wR_2 = 0.1877	R_1 = 0.0487, wR_2 = 0.0987	R_1 = 0.0376, wR_2 = 0.0897
Final R indexes [all data]	R_1 = 0.0757, wR_2 = 0.1942	R_1 = 0.0711, wR_2 = 0.1093	R_1 = 0.0443, wR_2 = 0.0938
Largest diff. peak/hole / e $Å^{-3}$	0.78/-0.80	0.22/-0.25	0.35/-0.31
Flack parameter		0.01(2)	0.02(2)

Table 7.6 Crystal data and structure refinement details for **16**

Empirical formula	$C_{40}H_{42}B_2N_2O_2$ (**16**)
Formula weight	604.37
Temperature/K	180.0
Crystal system	Triclinic
Space group	P-1
a/Å	10.5637(3)
b/Å	10.8714(3)
c/Å	15.2958(4)
α/°	95.1220(10)
β/°	102.8720(10)
γ/°	95.0690(10)
Volume/Å^3	1694.99(8)
Z	2
ρ_{calc}g/cm^3	1.184
μ/mm^{-1}	0.550
F(000)	644.0
Crystal size/mm^3	0.7 × 0.17 × 0.05
Radiation	CuKα (λ = 1.54184)
2Θ range for data collection/°	5.964 to 133.832
Index ranges	$-12 \leq h \leq 12$, $-12 \leq k \leq 12$, $-18 \leq l \leq 17$
Reflections collected	32118
Independent reflections	5953 [R_{int} = 0.0737]
Data/restraints/parameters	5953/74/470
Goodness-of-fit on F^2	1.059
Final R indexes [I>=2σ (I)]	R_1 = 0.0604, wR_2 = 0.1381
Final R indexes [all data]	R_1 = 0.0800, wR_2 = 0.1525
Largest diff. peak/hole / e Å^{-3}	0.22/-0.24

7.5 References

1 G. M. Sheldrick, *Acta Cryst.*, 2015, **A71**, 3–8.

2 G. M. Sheldrick, *Acta Cryst.*, 2015, **C71**, 3–8.

3 A. He, Q. Liu and D. G. Ivey, *J. Mater. Sci. Mater. Electron.*, 2009, **20**, 543–550.

4 Gaussian16, RevisionB.01, M. J. Frisch, G. W. Trucks, H. B. Schlegel, G. E. Scuseria, M. A. Robb, J. R. Cheeseman, G. Scalmani, V. Barone, G. A. Petersson, H. Nakatsuji, X. Li, M. Caricato, A. V. Marenich, J. Bloino, B. G. Janesko, R. Gomperts, B. Mennucci, H. P. Hratchian, J. V. Ortiz, A. F. Izmaylov, J. L. Sonnenberg, D. Williams-Young, F. Ding, F. Lipparini, F. Egidi, J. Goings, B. Peng, A. Petrone and D. J. Henderson, 2016.

5 K. Kim and K. D. Jordan, *J. Phys. Chem*, 1994, **98**, 10089–10094.

6 F. Weigend and R. Ahlrichs, *Phys. Chem. Chem. Phys.* , 2005, **7**, 3297–3305.

7 X. Fan, J. Zheng, Z. H. Li and H. Wang, *J. Am. Chem. Soc.*, 2015, **137**, 4916–4919.

8 M. Arrowsmith, M. S. Hill, T. Hadlington, G. Kociok-Köhn and C. Weetman, *Organometallics*, 2011, **30**, 5556–5559.

9 K. Oshima, T. Ohmura and M. Suginome, *J. Am. Chem. Soc.*, 2012, **134**, 3699–3702.

10 A. S. Dudnik, V. L. Weidner, A. Motta, M. Delferro and T. J. Marks, *Nat. Chem.*, 2014, **6**, 1100–1107.

11 J. Intemann, M. Lutz and S. Harder, *Organometallics*, 2014, **33**, 5722–5729.